Relaxation of Energized Polycyclic Aromatic Hydrocarbons : A Laboratory Astrophysical Study

Gabi Wenzel

UNIVERSITÉ TOULOUSE III PAUL SABATIER

Université Fédérale Toulouse Midi-Pyrénées

THÈSE

En vue de l'obtention du

Doctorat de l'Université de Toulouse

Délivré par : l'Université Toulouse III – Paul Sabatier

Présentée et soutenue le **03/07/2020** par :

Gabi Wenzel

Relaxation de l'énergie de molécules polycycliques aromatiques hydrogénées : Une étude en astrophysique de laboratoire

---

Jury

Adam Walters	Professeur	Président
Gilles Grégoire	Directeur de Recherche	Rapporteur
Dahbia Talbi	Directrice de Recherche	Rapportrice
Laurent Verstraete	Professeur	Rapporteur
Sandra Brünken	Assistant Professeure	Examinatrice
Franck Lépine	Chargé de Recherche	Examinateur
Giacomo Mulas	Astronome	Examinateur
Christine Joblin	Directrice de Recherche	Directrice de Thèse

École doctorale et spécialité :
SDU2E : Astrophysique, Sciences de l'Espace, Planétologie

Unité de Recherche :
Institut de Recherche en Astrophysique et Planétologie (IRAP)

Directrice de Thèse :
Christine Joblin

Rapporteurs :
Gilles Grégoire, Dahbia Talbi et Laurent Verstraete

Doctoral Thesis

Relaxation of Energized Polycyclic Aromatic Hydrocarbons: A Laboratory Astrophysical Study

Author:
Gabi Wenzel

Supervisor:
Dr. Christine Joblin

Institut de Recherche en Astrophysique et Planétologie
SDU2E: Astrophysique, Sciences de l'Espace, Planétologie
Université Toulouse III – Paul Sabatier

3 July 2020

Remerciements

Acknowledgements

Throughout the past three years that I have been working on this PhD project, I have received a great deal of support and assistance. Here I would like to thank everyone who has contributed in many different ways to the success of this work.

Firstly and by far most importantly, I would like to express my deepest gratitude to my *directrice de thèse*, Christine Joblin, who gave me the opportunity to carry out this PhD project under her supervision. An experimental physicist herself, she introduced me to this amazing research field of laboratory astrophysics. Her expertise was invaluable to me, especially in finding connections and seeing the larger picture, but also during numerous hours spent together in the laboratory. Thank you so much, Christine, for that your insightful feedback pushed me to sharpen my thinking and brought this work to the high level it is.

I would like to acknowledge my *rapporteurs*, Gilles Grégoire, Dahbia Talbi, and Laurent Verstraete, for accepting the evaluation of this doctoral thesis during one of the weirdest times. Your comments and questions yielded such fruitful discussions.

Thank you, Adam Walters, for being the *président* of my jury and dealing with all the moderator duties during my defence.

I would also like to thank my *comité de suivi de thèse* consisting of Karine Demyk, Didier Lemoine, and Franck Lépine. You accompanied me along the past years, gave the most useful instructions and asked me the most difficult questions and hence prepared me in the best possible way.

As one will find out reading this PhD manuscript, experimental physicists cannot survive without their theoretical counterparts. Thank you so much, Aude Simon, for explaining even the tiniest details and always being only one email away.

In the same context, I would like to extend my gratitude to Giacomo Mulas, who not only introduced me to quantum chemistry, but also to the beautiful island Sardinia. Giacomo, thank you for your support and valuable guidance in all situations, be it density functional theory, Italian pizza and coffee, or programming codes.

A huge thank you is sent out to Sandra Brünken, who supervised Shreyak Banhatti and me during my time at the FELIX facility in the Netherlands. Pancakes and Haribo will forever be unforgotten.

Shreyak, thanks for being such an awesome lab partner, in Toulouse and in Nijmegen, and thank you so much, Stephan Schlemmer, for making our wonderful collaborations possible.

I am thankful to Alexandre Giuliani and Laurent Nahon for their great support during and after our experiments at the SOLEIL synchrotron.

Thank you, Jérôme Bernard and Serge Martin, for taking me with you to the DESIREE ring experiment in Stockholm and involving me in such a *cool* experience.

I would like to acknowledge my colleagues from the MICMAC work group at IRAP and the University of Toulouse for their friendly reception and helpfulness. I would particularly like to thank Anthony Bonnamy, Loïc Nogues, David Murat, Pavol Jusko, Hassan Sabbah, Shubhadip Chakraborty, MingChao Ji, Alexandre Marciniak, Olivier Berné, Isabelle Ristorcelli, and my office mate Sandrine Bottinelli.

Special thanks go to my fellow PhD student friends, Sarah Rodriguez Castillo, Rémi Bérard, Mickaël Carlos, and Sacha Foschino – C's team! – as well as to all participants of the PhD diary group.

In addition, I would like to thank all members of the EUROPAH consortium, in particular Lindsey St. Mary, Julianna Palotàs, and Evgeny Posenitskiy, for helpful discussions, wise counsel, and their unconditional friendship.

Thank you so much, Tim Kroll and Paul Möllers, for always having my back, and thanks to my few friends outside physics, Kathrin Jostarndt, Franziska Tilse, Lena Schöpp, Pia Grundmann, and Jannik Vogt, for taking my mind off of research sometimes.

A great thank you to my grandparents, Oma and Opa, who never stopped believing in me, and to my uncle Martin and aunt Ramona, for always being in my corner.

Moreover, I will be forever grateful to my stepparents, Anja and Holger Weigel, who

took me in during a pandemic and provided me with happy distractions and a basically unlimited coffee supply during the thesis writing procedure.

And finally, thank you, Mama. For everything.

Tu manques à ma vie.

Acknowledgement

This work acknowledges support by the European Union under the Horizon 2020 framework for the Marie Skłodowska-Curie action EUROPAH, Grant Agreement no. 722346, and funding from the European Research Council under the European Union's Seventh Framework Programme ERC-2013-SyG, Grant Agreement no. 610256, NANOCOSMOS. This research has also received funding from LASERLAB-EUROPE, Grant Agreement no. 654148 under the European Union's Horizon 2020 research and innovation programme, and was granted access to the HPC resources at the CALMIP supercomputing centre under project P20027.

Abstract [en]

As a part of interstellar dust, polycyclic aromatic hydrocarbons (PAHs) in so-called photodissociation regions (PDRs) are processed by the interaction with ultraviolet (UV) photons that are emitted by hot stars. After absorption of a UV photon, an isolated PAH can undergo different relaxation processes: ionization, dissociation, and radiative cooling, including infrared (IR) fluorescence which results in the aromatic infrared bands (AIBs) observed in many astronomical objects. This interaction influences their charge state and photodissociation dynamics, ultimately determining their photostability in space. In return, it impacts the energy balance of the interstellar gas by photoelectric heating. PAHs are also proposed to act as catalysts for the most abundant molecule in space, H_2, and play thus an ubiquitous role in the physics and chemistry of PDRs.

This PhD thesis concentrates on the experimental investigation of cationic PAHs, addressing independently and for different molecular families two major aspects which concern the evolution of PAHs under UV irradiation and the possibility to form several isomers. The experimental measurements are supported by complementary theoretical calculations.

Two main experimental campaigns have been carried out throughout this PhD work. At the SOLEIL synchrotron, large PAH cations ($30-48$ carbon atoms) were submitted to tunable vacuum UV (VUV) radiation in the range of 9.5 to 20.0 eV and their photofragments and dications were mass-analyzed as a function of photon energy. We could derive branching ratios, action spectra, and photoionization and photodissociation cross sections, demonstrating that ionization is the dominant channel in the photoprocessing of these large PAHs by VUV irradiation. Using theoretical photoabsorption cross sections from time-dependent density functional theory (TD-DFT), we were also able to determine photoionization yields and to give recipes which can

directly be implemented in astrochemical modeling studies.

At the FELIX facility, IR predissociation spectroscopy of cold species tagged with Ne atoms was employed to disentangle isomers according to their IR fingerprints. The study focused on the –H fragments of methylated PAH cations in order to investigate the formation of the tropylium-like isomer relative to the benzylium-like isomer, which carries a methylene sidegroup. Theoretical harmonic IR spectra have been calculated from DFT to support the identification of the ions. We found that methylene-PAHs are the only formed structures for PAHs containing more than $2-3$ cycles. Methylated PAHs have been proposed as the carriers of the $3.4\,\mu$m emission feature in PDRs. We conclude that the observed variations of the AIB spectrum are consistent with the photoprocessing of these species by VUV irradiation leading to the formation of methylene sidegroups.

Résumé [fr]

Composantes de la poussière interstellaire, les molécules polycycliques aromatiques hydrogénées (PAH) qui peuplent les régions dites de photodissociation (PDR) sont soumises au rayonnement ultraviolet (UV) provenant des étoiles chaudes. Après l'absorption d'un photon UV, un PAH isolé peut subir différents processus de relaxation: ionisation, dissociation et refroidissement radiatif, y compris la fluorescence infrarouge (IR) qui se traduit par les bandes infrarouges aromatiques (AIB) observées dans de nombreux objets astronomiques. Cette interaction influence l'état de charge du PAH et sa photostabilité via la dynamique de dissociation. D'autre part, elle impacte le bilan énergétique du gaz interstellaire par chauffage par effet photoélectrique. Les PAH pourraient aussi contribuer à la formation de H_2, la molécule la plus abondante et jouent donc un rôle important dans la physique et la chimie des PDR.

Cette thèse se concentre sur l'étude expérimentale de PAH cationiques, traitant de manière indépendante et pour différentes familles de molécules, deux aspects majeurs que sont l'évolution sous irradiation UV et la possibilité de former différents isomères. Les mesures expérimentales sont complétées par des calculs théoriques.

Deux campagnes expérimentales principales ont été menées tout au long de cette thèse. Au synchrotron SOLEIL, des cations PAH de grande taille ($30 - 48$ atomes de carbone) ont été soumis à un rayonnement UV du vide (VUV) accordable dans le domaine de 9,5 à 20,0 eV et leurs photofragments et dications ont été analysés en masse en fonction de l'énergie des photons. Nous en avons déduit des rapports de branchement, des spectres d'action et des sections efficaces de photoionisation et de photodissociation, démontrant que l'ionisation est la voie dominante d'évolution chimique sous irradiation VUV de ces PAH de grande taille. En utilisant des valeurs des sections efficaces d'absorption provenant de la théorie de la fonctionnelle de la densité dépendante du temps (TD-DFT), nous avons également pu déterminer des

rendements de photoionisation et donner des recommandations pour leur utilisation dans des codes de modélisation astrochimique.

L'étude des isomères a été réalisée à l'infrastructure FELIX grâce à une spectroscopie IR de prédissociation par complexation à basse température avec des atomes de Ne. Elle a porté sur les fragments –H de PAH cations méthylés afin de rechercher la formation de l'isomère de type tropylium relativement à celle de l'isomère de type benzylium qui comprend un groupement méthylène. Les fréquences harmoniques théoriques des différentes espèces ont été calculées en utilisant la théorie DFT afin de faciliter l'identification des ions formés. Nous avons montré que seules les espèces PAH-méthylène sont formées pour des PAH plus grands que $2-3$ cycles carbonés. Les PAH méthylés ont été proposés comme porteurs de la bande d'émission à 3,4 μm dans les PDR. Notre étude montre que les variations observées dans le spectre AIB sont cohérentes avec l'évolution de ces espèces sous l'irradiation de photons VUV conduisant à la formation de groupements de type méthylène.

Contents

Description [fr]

Composantes de la poussière interstellaire, les molécules polycycliques aromatiques hydrogénées (PAH) qui peuplent les régions dites de photodissociation (PDR) sont soumises au rayonnement ultraviolet (UV) provenant des étoiles chaudes. Après l'absorption d'un photon UV, un PAH isolé peut subir différents processus de relaxation: ionisation, dissociation et refroidissement radiatif, y compris la fluorescence infrarouge (IR) qui se traduit par les bandes infrarouges aromatiques (AIB) observées dans de nombreux objets astronomiques. L'interaction des PAH avec les photons UV et la compétition entre les processus de relaxation moléculaire influencent l'état de charge des PAH et leur photostabilité dans les PDR. En retour, ces processus ont un impact sur le gaz interstellaire environnant, en particulier par le chauffage du gaz par thermalisation des électrons émis par effet photoélectrique. Dans les PDR, les PAH pourraient aussi contribuer à la formation de la molécule la plus abondante dans l'espace, H_2. Ces PAH jouent donc un rôle important dans la physique et la chimie des PDR, et il est donc important de pouvoir décrire leurs propriétés physico-chimiques dans les modèles de PDR.

L'objectif de ce travail de thèse est de progresser dans notre compréhension des propriétés photophysiques et chimiques des PAH astrophysiques par une approche expérimentale d'astrophysique de laboratoire. Plus spécifiquement, cette thèse se concentre sur le cas de PAH cationiques, traitant de manière indépendante et pour différentes familles de molécules, deux aspects majeurs que sont l'évolution de ces PAH sous irradiation UV et la possibilité de former différents isomères lors de leur fragmentation. Les mesures expérimentales sont complétées par des calculs théoriques.

Les modèles d'astrochimie prédisent que seuls les PAH de grande taille (plus de $50-60$ atomes de carbone) peuvent survivre dans les PDR. Nous avons donc souhaité étudier

en laboratoire les propriétés de ces grands cations PAH sous l'effet du rayonnement UV. Notre campagne expérimentale au synchrotron SOLEIL a utilisé le dispositif de piège à ions linéaire qui est interfacé avec la ligne de lumière DESIRS. Des PAH de taille de 30 à 48 atomes de carbone ont été soumis à des photons de l'UV du vide (VUV) du domaine de 9,5 à 20,0 eV. Les produits de photoionisation et photodissociation ont été analysés en masse en fonction de l'énergie des photons absorbés. Nous en avons déduit des rapports de branchement, des spectres d'action et des sections efficaces de photoionisation et de photodissociation. Nous avons montré que l'ionisation est la voie dominante d'évolution chimique sous irradiation VUV de ces PAH de grande taille. En utilisant des valeurs des sections efficaces d'absorption provenant de la théorie de la fonctionnelle de la densité dépendante du temps (TD-DFT), nous avons également pu déterminer des rendements de photoionisation et donner des recommandations pour leur utilisation dans les codes de modélisation astrochimique. Des PAH sous la forme de dications pourraient être présents dans certains environnements comme dans la cavité autour de l'étoile HD 200775 de la nébuleuse NGC 7023. Cette présence pourrait avoir un impact sur le chauffage du gaz par effet photoélectrique ainsi que sur le spectre des AIB.

Une autre contribution de cette thèse est associée à des aspects plus fondamentaux concernant l'isomérisation du fragment –H de cations PAH méthylés. Ces PAH méthylés sont présents dans les environnements astrophysiques et il est intéressant d'étudier les espèces –H qui résultent de leur fragmentation. La formation de ces espèces peut impliquer des processus d'isomérisation comme prédits pour le fragment du cation de méthylpyrène. Nous avons utilisé le dispositif de piège à ions cryogénique FELion qui est couplé avec le laser à électrons libres FELIX. L'étude des isomères a été réalisée grâce à une spectroscopie IR de prédissociation par complexation à basse température des ions froids avec des atomes de Ne. Cette spectroscopie permet en particulier de rechercher la formation de l'isomère de type tropylium (présence d'un cycle à 7 atomes de carbone) relativement à celle de l'isomère de type benzylium qui comprend un groupement méthylène. Les fréquences harmoniques théoriques des différentes espèces ont été calculées en utilisant la théorie DFT afin de faciliter l'identification des ions formés. Nous avons pu identifier clairement la formation de différents isomères dans le cas du fragment –H du 2-méthylnaphthalène. En plus de la structure comprenant un groupement méthylène qui est habituellement observée,

au moins un isomère de type tropylium avec un cycle à 7 atomes de carbone a été mis en évidence. Avec le méthylanthracène comme précurseur, la présence de l'isomère de type tropylium est restée ambigüe. Dans le cas du 1-méthylpyrène, cependant, cet isomère n'est clairement pas présent. Nous pouvons donc en conclure que seules les espèces PAH-méthylène sont formées pour des PAH plus grands que $2-3$ cycles carbonés. Les PAH méthylés ont été proposés comme porteurs de la bande d'émission à 3,4 μm dans les PDR. Notre étude montre que les variations observées dans le spectre AIB, par exemple dans le cas de la PDR prototype de NGC 7023, sont cohérentes avec l'évolution de ces espèces sous irradiation UV conduisant á la formation de groupements de type méthylène.

Durant ma thèse, l'étude expérimentale des processus d'isomérisation et de leur rôle potentiel dans le refroidissement des PAH photoexcités a également fait l'objet d'une campagne utilisant l'anneau de stockage cryogénique DESIREE. Cette étude à laquelle j'ai eu l'opportunité de participer a porté sur deux isomères de $C_{14}H_{10}^{+}$ que sont l'anthracène (Ant+) et le phénanthrène (Phen+). Ces mesures ont été motivées par une étude publiée dans la littérature qui suggère, par le calcul de chemins de fragmentation, qu'Ant+ peut s'isomériser en Phen+ lors de sa dissociation par perte de C_2H_2. Dans les expériences menées, l'isomérisation peut se produire dans la source d'ions ou ultérieurement lors de la photoexcitation des ions dans l'anneau. Les expériences dans les anneaux de stockage, qui peuvent être réalisées sur des temps longs (secondes) dans le cas d'anneaux cryogéniques, ouvrent la possibilité d'étudier la dynamique de relaxation des ions et de mettre en évidence d'éventuels processus d'isomérisation. L'analyse des résultats de DESIREE est toujours en cours et ne fait pas partie de ce manuscrit. Je décrirai néanmoins la technique utilisée. De plus, en préparation à la campagne DESIREE, j'ai utilisé le dispositif de piège à ions cryogénique PIRENEA à Toulouse afin de mesurer, dans la gamme $420-480$ nm, le spectre d'action de l'ion Phen+ refroidi. Ce spectre est présenté dans l'Annexe A.

Ce manuscrit est divisé en six chapitres. Le chapitre 1 présente le contexte scientifique de la thèse, donnant le contexte astrophysique et une description des processus photophysiques pour des PAH cationiques. Les chapitres 2 et 3 sont consacrés à la description des méthodes expérimentales et théoriques utilisées en synergie tout au

long de ce travail de doctorat, avec néanmoins une plus forte implication dans le travail expérimental. Ils sont suivis de deux chapitres présentant les principaux résultats obtenus. Le chapitre 4 concerne l'étude de l'interaction des cations PAH piégés avec le rayonnement VUV du synchrotron SOLEIL. Il traite plus spécifiquement de la compétition entre l'ionisation et la dissociation en fonction de l'énergie des photons VUV absorbés. Les résultats sur la composition isomérique des fragments –H des cations de PAH méthylés sont présentés dans le chapitre 5, révélant les différentes structures chimiques identifiées pour ces fragments. Le chapitre 6 résume l'impact des données moléculaires obtenues pour les problématiques astrophysiques, telles que l'évolution du potentiel d'ionisation avec la taille moléculaire et le rendement de photoionisation avec l'énergie des phtons UV absorbés. En outre, il discute de perspectives pour des travaux futurs. Enfin, les conclusions énumèrent les principaux résultats obtenus lors de ce travail de doctorat.

1 | Scientific Context and Objectives

Outline

1.1 Astrophysical Background

Containing galaxies, stars, planets, and all other forms of energy and matter, the Universe has always piqued our curiosity. Investigating the evolution of our Universe and the galaxy we live in, the Milky Way, promotes a deeper understanding of our origins, the formation of stars and planets, and the emergence of molecular complexity, potentially leading to life. This study is connected to the physics and chemistry of the interstellar medium (ISM), the space between the stars. In particular, the interaction of starlight with interstellar matter plays a fundamental role in the evolution of the ISM itself.

1.1.1 The Diffuse Interstellar Medium

The diffuse interstellar medium (ISM) comprises a heterogeneous mixture of different phases of gas and dust, containing typically 10 % of the matter of the Milky Way. Observations of the ISM show that different regions can be distinguished with respect to temperature, density and ionization state of the gas. Different cloud types can be classified due to whether hydrogen, the most abundant element in the ISM, is in its neutral atomic, ionized atomic or molecular form.

A classification of cloud types was introduced by Snow and McCall [1], based on the local fraction, f_{X}^{n}, of the key abundant species, X, in the cloud: H/H_2, $\mathrm{C}^+/\mathrm{C}/\mathrm{CO}$, whose relative abundance is indeed dependent on the ultraviolet (UV)[(1)] field (see Section 1.1.3). According to Snow and McCall [1], we can distinguish between diffuse, translucent, and dense molecular clouds (see Table 1.1).

Diffuse Clouds are tenuous, mostly populated by atoms, ions, and small radicals with very low gas density and exposure to the mean interstellar UV radiation field, ionizing or dissociating most of the molecules. Their typical temperatures range from 30 to 100 K. Diffuse atomic clouds contain mainly hydrogen in neutral atomic form and ionized atoms with ionization potentials, IP^+, below the IP^+ of hydrogen, 13.6 eV, such as carbon, providing electrons in this region. Diffuse molecular clouds, however, are characterized by a larger, more substantial fraction of molecular hydrogen, $f_{\mathrm{H}_2}^{n} > 0.1$.

[(1)] The ultraviolet light ranges of the electromagnetic spectrum referred to throughout this thesis are reported in Table B.1 in Appendix B.

Table 1.1: Classification of interstellar cloud types after Snow and McCall [1], distinguishing into diffuse atomic, diffuse molecular, translucent, and dense molecular clouds.

	Diffuse Atomic	**Diffuse Molecular**	**Translucent**	**Dense Molecular**
f^n_{X}	$f^n_{\mathrm{H_2}} < 0.1$	$f^n_{\mathrm{H_2}} > 0.1$ $f^n_{\mathrm{C^+}} > 0.5$	$f^n_{\mathrm{C^+}} < 0.5$ $f^n_{\mathrm{CO}} < 0.9$	$f^n_{\mathrm{CO}} > 0.9$
A_{V}	0	~ 0.2	$\sim 1-2$	$\sim 5-10$
n_{H} [cm^{-3}]	$10-100$	$100-500$	$500-5000$?	$> 10^4$
T [K]	$30-100$	$30-100$	$15-50$?	$10-50$
λ-range	UV/Vis HI line	UV/Vis IR abs mm abs	Vis (UV?) IR abs mm abs/em	IR abs mm em

The UV interstellar radiation field is slightly attenuated, $A_{\mathrm{V}} \approx 0.2$, but strong enough to ionize atomic carbon, C^+, or to photodissociate CO. Carbon is therefore primarily present as C^+ or as small molecules, such as CH, CO, CN, C_2, or C_3.

Translucent Clouds comprise less ionized atomic carbon, C^+, than diffuse clouds. Carbon is mostly abundant in its neutral form or included in molecules, but the local fraction of CO remains below 0.9. They are significantly denser than diffuse clouds, and therefore the interstellar UV radiation is more attenuated. The outer edges of dense molecular clouds might be described as translucent clouds.

Dense Molecular Clouds are the densest clouds from which stars and planets can form. Inside these clouds, the typical temperatures range from 10 to 50 K. They contain predominantly molecular hydrogen and stable molecules, such as CO, but also more complex molecules are formed and survive in regions shielded from the UV field. This is due to the fact that the atoms, molecules, and submicronic particles present in the cloud efficiently absorb the UV/Visible (Vis) light emitted by nearby stars. In addition, gas and dust particles are strongly coupled, as gas-phase elements freeze onto the surface of grains. This leads to the formation of ice mantles which induce a richer chemistry [2]. In particular, in these ice mantles on interstellar grains, the formation

of complex organic molecules, which have been detected in dense clouds, may be favored [3]. The interface of these clouds with hot stars gives rise to photodissociation regions (PDRs) in which the strong interaction with UV photons governs the physical and chemical conditions (see Section 1.1.3).

1.1.2 Cosmic Dust Life Cycle

The most abundant element of the ISM is hydrogen, making up 70.4 % of its mass, followed by helium with 28.1 %. The remaining 1.5 % are composed of heavier elements, for instance, oxygen, carbon, and nitrogen. Typically 99 % of the interstellar matter is in gaseous form and only 1 % is attributed to tiny dust particles of submicronic size.

Interstellar matter lives through continual change which is closely coupled to the formation, life, and death of stars. We can thus name this continual change the cosmic dust life cycle, which is presented in Figure 1.1.

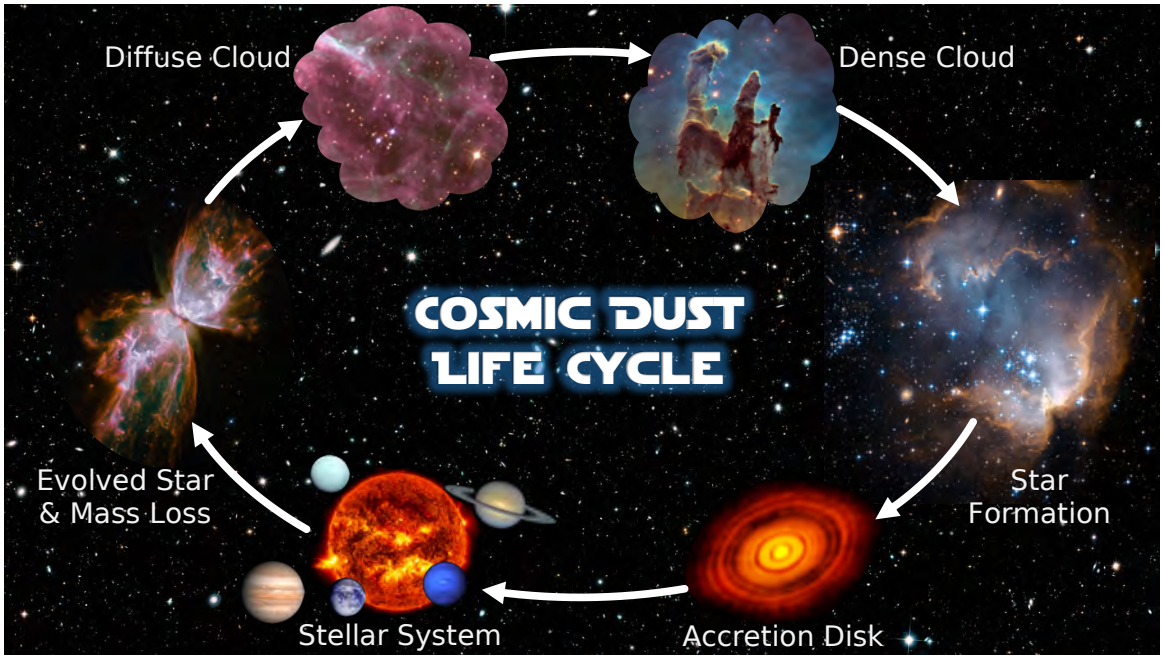

Figure 1.1: The life cycle of the interstellar matter. Credit for the original images to ESA and NASA.

Star forming regions emerge from dense molecular clouds as a natural consequence of their low temperatures and high densities. Containing enough mass to initiate a gravitational collapse, a protostar is formed. Conservation of angular momentum

during the collapse causes the formation of a protoplanetary accretion disk which rotates around the star. Within the high density of the disk, coagulation of dust might lead to the formation of planets, to a stellar system. Massive stars with masses above $8\,M_\odot$ end with explosions called supernovae, during which stellar matter is violently ejected. Evolved low mass stars with masses below $2\,M_\odot$ and intermediate mass stars, $2-8\,M_\odot$, however, lose their mass during their life by stellar winds. The outer layer of such asymptotic giant branch (AGB) stars form expanding circumstellar envelopes and, during the final phases of their evolution, planetary nebulae. The progressive mass loss causes matter being constantly ejected by the stars, feeding the interstellar medium and enriching the interstellar matter which will eventually form new molecular clouds.

1.1.3 Photodissociation Regions

Photodissociation regions (PDRs), sometimes also called photon-dominated regions, are regions of the ISM in which the physical and chemical conditions are governed by the interaction of matter with far UV (FUV)[(2)] photons. In these regions, hydrogen is found in its neutral form and only photons below 13.6 eV are present, the so-called H I regions. Bright PDRs often result from the interaction of young massive stars with their parental cloud [4]. Typical examples are the Orion Bar or the north-west PDR of NGC 7023, for which a recent study has gathered all available observational data to obtain a better understanding of the physical conditions in these environments [5]. These bright PDRs are usually found at the interface with H II regions that surround massive stars and in which hydrogen is ionized and photons above the 13.6 eV limit can therefore penetrate.

The FUV flux in PDRs is usually quantified in units of G_0 given by Habing [6]. It is normalized to the value corresponding to the average interstellar flux integrated between 5.2 and 13.6 eV, which results in an energy flux of $1.6 \cdot 10^{-10}\,\mathrm{W\,cm^{-2}}$ and a photon flux of $10^8\,\mathrm{photons\,cm^{-2}\,s^{-1}}$. In massive star forming regions, values of G_0 of $10^4 - 10^6$ can be found. All of the atomic and most (90 %) of the molecular gas in the Galaxy is contained in PDRs [4]. The interaction of FUV photons with the gas and dust impacts both the thermal balance of the gas and the chemistry, leading

[(2)] We consider here UV photons up to 13.6 eV.

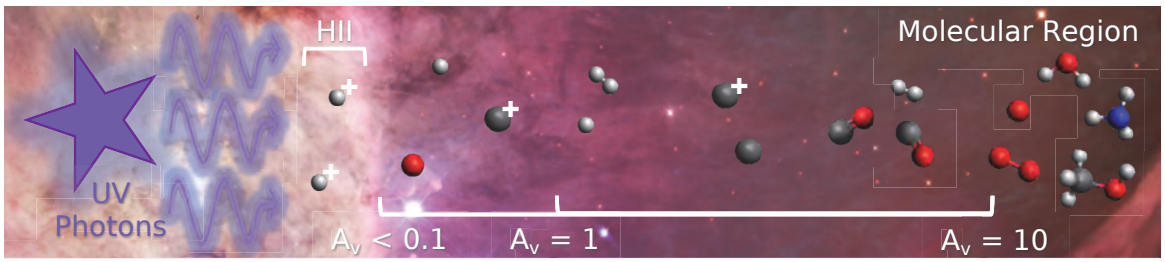

Figure 1.2: Schematic of a typical photodissociation region. The PDR is illuminated by UV photons from the left and extends from where atomic matter dominates to where the photodissociation of O_2 is negligible, at $A_V \approx 10$. This is where, what we consider, the molecular region starts. Credit for the original image of the Orion Nebula to Hubble/ESA/NASA.

to a gas composition which depends on the penetration of the FUV field. H/H_2 and C^+/C/CO interfaces are predicted by models [see 4]. A schematic of a typical PDR is shown in Figure 1.2. Typically one percent of the mass in PDRs is in the form of dust particles (see Section 1.1.2). Dust plays a key role in PDRs by attenuating the FUV field and generating electrons by the photoelectric effect which heat the gas [7, 8]. It also provides surfaces on which molecules adsorb, favoring chemistry and increasing the possibility of chemical reactions. A well-known case is the formation of the most abundant molecule, H_2, as described in a recent review by Wakelam *et al.* [9], but this concerns also complex organic molecules [3]. The physicochemical processes in PDRs are complex and coupled with each other. PDR models have been developed to analyse the emission in the gas lines and to constrain the chemical and physical processes that take place in PDRs [10–14].

1.1.4 Dust Extinction and Emission

When observing the night sky in the visible (Vis) light spectrum range as presented in the top panel of Figure 1.3, dark features are observed in the galactic plane. These dark spots are attributed to cosmic dust in the diffuse ISM, efficiently extinguishing starlight by absorbing and scattering all UV/Vis photons emitted by hot stars, leading to dust extinction [15]. Changing the observational technique to the infrared (IR), in particular to the mid (MIR) and far infrared (FIR), bright emission features are observed where it was dark before (see Figure 1.3, bottom panel). Hence, we conclude that most of the absorbed energy is emitted back to the ISM in the IR.

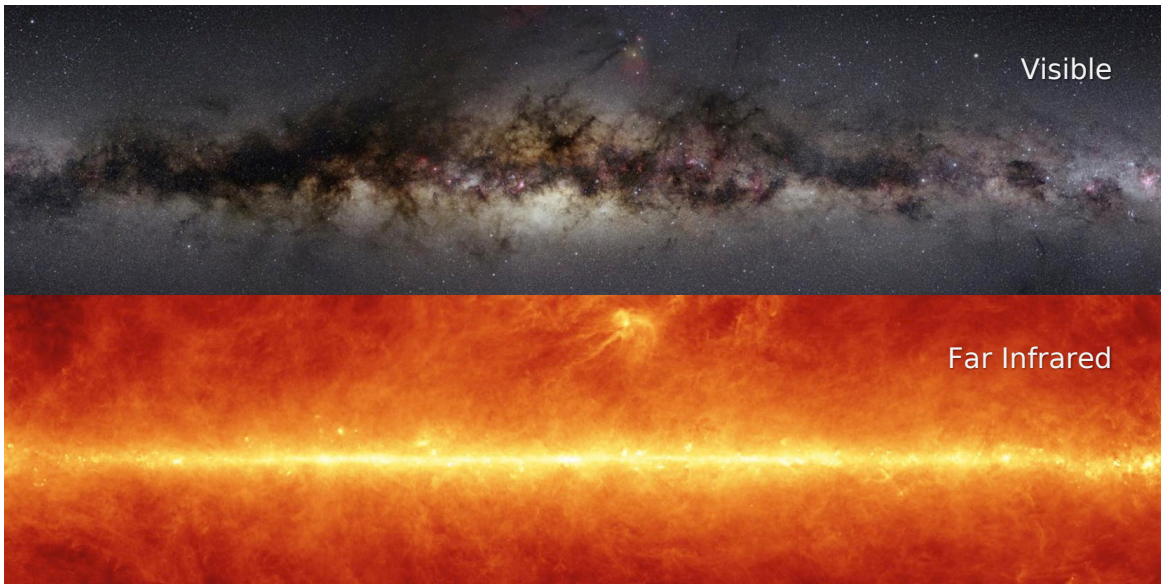

Figure 1.3: Our Galaxy, the Milky Way, observed in the visible and in the far infrared. Where dust extincts starlight in the visible, bright infrared emission can be observed. Credit for the original images to Nick Risinger and IRAS/NASA.

The left panel of Figure 1.4 shows the dust extinction curve of the diffuse ISM as given by Compiègne *et al.* [16]. It represents the extinction cross section expressed per H nuclei as a function of inverse wavelengths, λ^{-1}, *i.e.*, wavenumber, $\tilde{\nu}$, in $\mu\mathrm{m}^{-1}$. Its main characteristics [17] are the gradual rise from the IR to the UV range and the bump at approximately 220 nm ($4.55\,\mu\mathrm{m}^{-1}$ or 5.64 eV) which is attributed to $\pi \rightarrow \pi^*$ electronic transitions in polycyclic aromatic hydrocarbons and very small graphite-like grains [18, 19]. In addition to the main dust features, a set of narrower absorption bands have been observed in several lines of sight when investigating reddened early type stars [20]. These are called diffuse interstellar bands (DIBs) and were first discovered one century ago [21, 22]. The number of observed DIBs has increased over the years, counting over 400 detected DIBs [23, 24]. Arising at optical and near infrared wavelengths in the interstellar gas, the DIBs are thought to be associated with carbonaceous molecules, but their origin has not yet been conclusively revealed. Recently, a couple of bands in the near IR could be attributed to originate from the cationic buckminsterfullerene, C_{60}^{+} [25, 26]. Being an ongoing unsolved mystery in astronomical spectroscopy, new DIBs are discovered regularly. See Geballe [27] for a detailed review on the recent developments on DIBs. Dust reemits the energy it

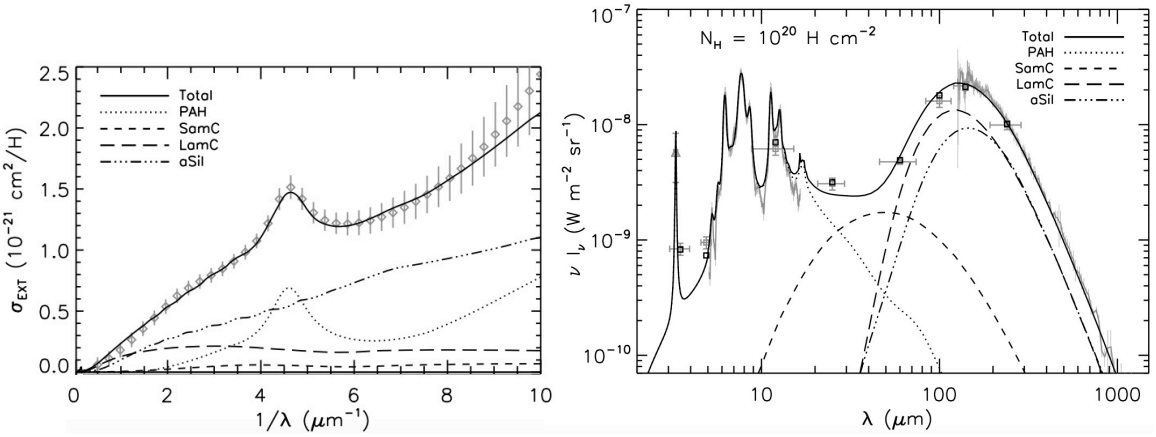

Figure 1.4: Left: Extinction curve for dust in the diffuse ISM at high galactic latitudes. Right: Dust emission for the diffuse ISM at high galactic latitudes. Grey symbols and curves indicate observations from the ISO satellite for the MIR range, $\sim 5 - 15\,\mu$m, and from the COBE satellite for the FIR range, $\sim 100 - 1000\,\mu$m. Black lines correspond to the model output. Both graphs taken from Compiègne *et al.* [16].

has absorbed in the Vis/UV range in the IR to mm range. The characteristics of the emission curve depend on the composition of the interstellar dust population, *i.e.*, the chemical nature of the dust and its size. The spectral energy distribution of dust emission in the galactic interstellar medium has been modeled by Compiègne *et al.* [16], attributing the various emission features to different kinds of dust as depicted in the right panel of Figure 1.4. Different dust models have been built to account for the features of the extinction and emission curves [16, 28–31]. These concentrate mainly on dust made of silicates and carbonaceous grains of varying sizes, typically in the molecular to μm size. Characteristic features in the low wavelength range can be seen from the right panel in Figure 1.4, especially at 3.3, 6.2, 7.7, 8.6, and 11.3 μm. Initially, they were referred to as the Unidentified Infrared Emission (UIR or UIE) bands and were attributed to very small grains (VSGs) with radii in the $\sim 10 - 150$ Å range [32]. After the comparison to laboratory data, another potential carrier was proposed [33, 34].

1.1.5 Astrophysical Polycyclic Aromatic Hydrocarbons

A family of carbonaceous molecules, the polycyclic aromatic hydrocarbons (PAHs), was proposed by Léger and Puget [33] and Allamandola *et al.* [34] to account for the

UIR bands. They introduced the PAH model, suggesting that isolated PAH molecules efficiently absorb starlight in the UV, heat up to high temperatures of about ∼1000 K, and subsequently cool down by slow IR emission. In addition, PAHs have IR bands which can be correlated with the observed UIR bands and their stability makes them good candidates to be abundant in the ISM as a part of interstellar dust. They can survive the interactions with UV photons, whereas other molecules are easily photodissociated by the interstellar UV radiation field.

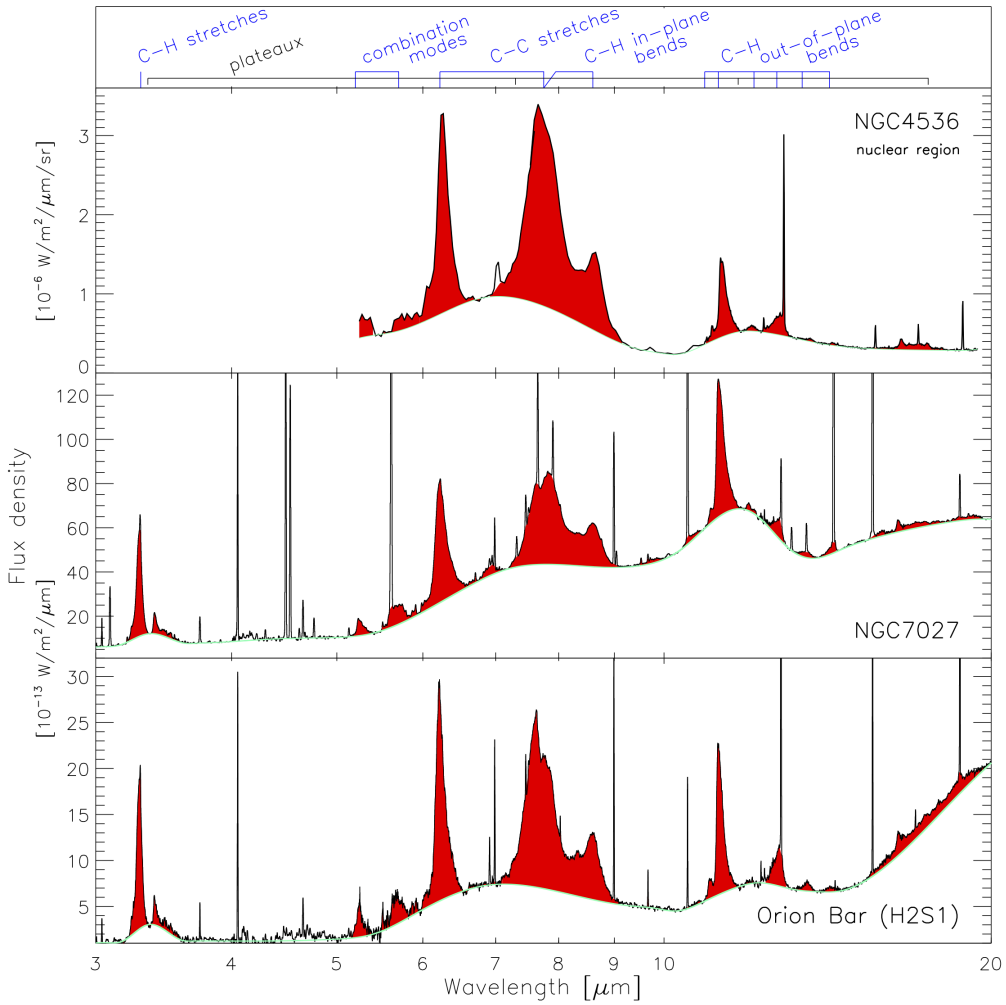

Figure 1.5: The Spitzer-IRS spectrum of the nuclear region of the galaxy NGC 4536 and the ISO-SWS spectra of the planetary nebula NGC 7027 and the photodissociation region at the Orion Bar illustrate the richness and variety of the PAH spectrum. Also indicated are the vibrational mode identifications of the major PAH bands. Taken from Peeters [35].

1.1.5.1 Aromatic Infrared Bands

Due to the PAH model [33, 34] in particular considering the fact that the UIR/UIE bands are at characteristic frequencies of the vibrational modes in aromatic rings, these bands were renamed to aromatic infrared bands (AIBs). AIBs are bright features of the MIR spectrum of many astrophysical objects in which UV photons are abundant, including protoplanetary disks, planetary nebulae, and PDRs. The strongest features are observed at 3.3, 6.2, 7.7, 8.6, 11.3, and 12.7 μm and are associated to the vibrational modes of PAHs, involving C–H and C–C stretches, as well as C–H in-plane and out-of-plane bends.

Figure 1.5 shows AIB spectra observed by the Spitzer-IRS spectrometer of the nuclear region NGC 4536, and by the ISO-SWS spectrometer in the planetary nebula NGC 7027 and in the PDR of the Orion Bar [35]. They all show similar main features, whereas variations of the exact positions, band shapes, and relative intensities can be observed, reflecting differences in the chemical composition and excitation conditions in these astrophysical environments.

1.1.5.2 Characteristics of Astro-PAHs

PAHs belong to the family of organic molecules consisting only of carbon and hydrogen atoms. They contain two or more benzene-like aromatic carbon rings with peripheral hydrogen atoms attached. In PAHs, each carbon has a double bond to another carbon atom, so that each carbon is sp^2 hybridized and therefore has a p orbital accounting for delocalized π-electrons across the rings. The smallest PAH is naphthalene, $C_{10}H_8$, consisting of two aromatic rings. When none of the carbon atoms belongs to more than two aromatic rings, the PAH is classified to be catacondensed or non-compact. If at least one carbon is shared between three aromatic rings, the PAH is denoted pericondensed or compact. Figure 1.6 depicts an excerpt of a few PAHs.

PAHs are a large family of species and since the PAH model proposal there has been numerous studies to constrain the composition of the astrophysical population and its variation with environmental conditions based on the analysis of the AIB spectra Peeters [see 35, for a review]. This analysis is possible thanks to theoretical and experimental spectra obtained for PAHs. More details about the progress on the characterization of astro-PAHs will be given in Section 1.3.

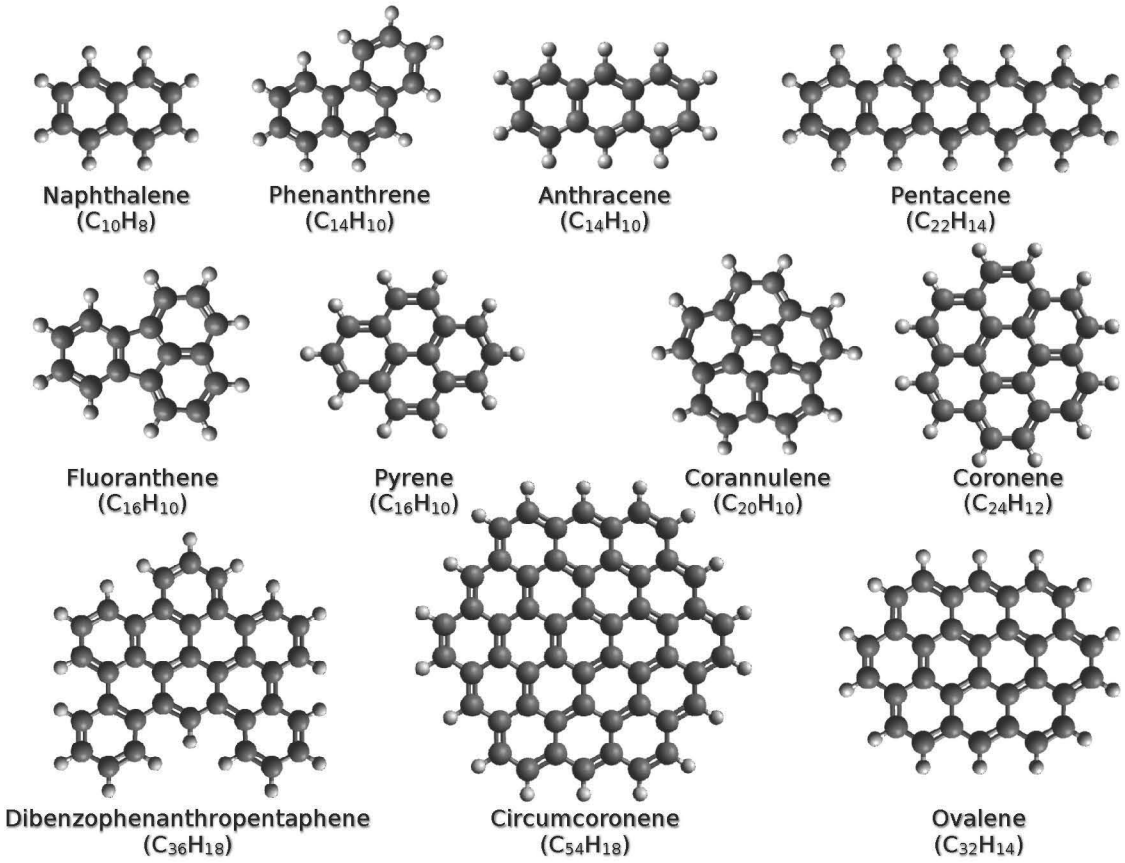

Figure 1.6: Example of PAH molecules. The top row depicts catacondensed PAHs, all other shown PAHs are pericondensed. Phenanthrene and anthracene as well as fluoranthene and pyrene are isomers with chemical formula $C_{14}H_{10}$ and $C_{16}H_{10}$, respectively.

The variation of the relative band intensities of the AIBs (*cf.* Section 1.1.5.1, in particular in the $6-8\,\mu$m range relative to the $11-15\,\mu$m range, has been identified as a good indicator of the charge state of PAHs [e.g 29, 36–42]. The structure and chemical composition were discussed. For instance, the presence of N heteroatoms was proposed to account for the position of the $6.2\,\mu$m band [43]. Moreover, very large compact PAHs were proposed to be the carriers of the $8.6\,\mu$m band [44]. The $3.4\,\mu$m satellite band was attributed to PAHs containing methyl sidegroups [45]. However, no specific PAH has yet been evidently identified in space, with exception of the PAH-related species, buckminsterfullerenes, C_{60}, C_{70}, and C_{60}^{+}, which were unambiguously detected in the ISM [25, 46–50].

Constraint on the PAH sizes was given by chemical models. By using the available molecular data as input, they predict that only PAHs with at least 50 carbon atoms are expected to survive in interstellar conditions [51–55]. It is worth to mention that these large sizes are not the ones which are usually studied in the laboratory.

1.2 Photophysics of Astro-PAHs

When an isolated cationic PAH absorbs a UV photon, it can undergo different deexcitation processes. These processes can be illustrated with an energy level diagram featuring the electronic levels with their vibrational levels, referred to as a Jablonski diagram as depicted in Figure 1.7.

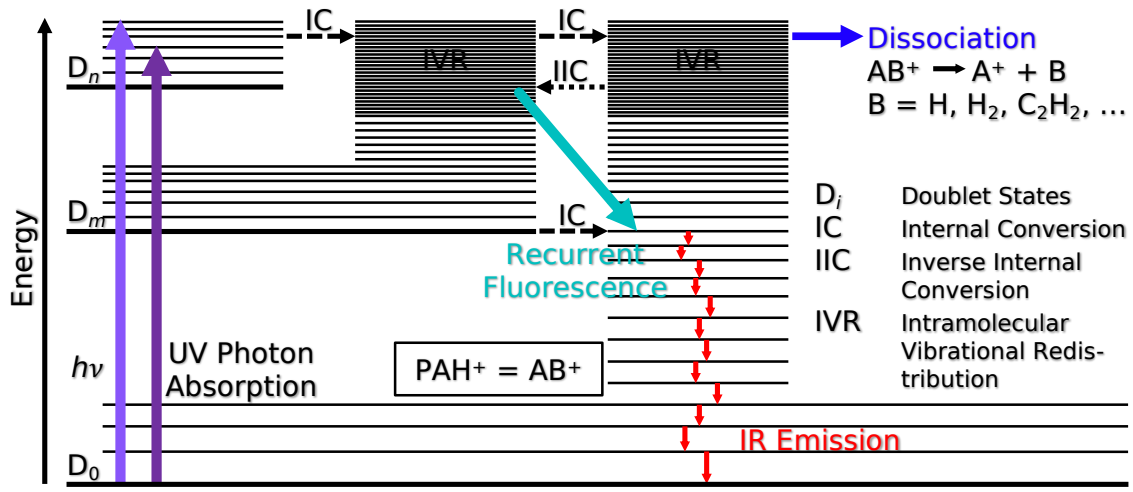

Figure 1.7: Energy level diagram describing the possible processes of a PAH cation upon the absorption of a UV photon with photon energy, $h\nu$. Non-radiative transitions such as internal conversion (IC) and inverse internal conversion (IIC) are depicted as dashed black arrows. Intramolecular vibrational redistribution is indicated as IVR. The radiative transitions, recurrent fluorescence and IR photon emission, are represented by solid colored arrows, as well as dissociation. Ionization is not illustrated.

The absorption of the UV photon induces a transition from the ground electronic state, D_0, to a higher electronic level, here for example D_n, where the D_i refer to doublet states which are associated with PAH cations. The electronic excitation can eventually lead to ionization (not shown in Figure 1.7) or cascade to lower electronic states by internal conversion (IC). This fast process will likely lead to reach D_0 with

a high vibrational energy. The latter will be redistributed over all modes through intramolecular vibrational redistribution (IVR) leading to a hot molecular ion. Statistical processes such as unimolecular dissociation, with H, H_2 and C_2H_2 as usual fragments [56], and infrared cooling [57] will subsequently cool down the ion.

For PAH cations, direct fluorescence from an excited electronic state is usually not observed because of the strong coupling between the D_0 and D_1 states. An exception is the perylene cation, $C_{20}H_{12}^+$, which was isolated in Ne and Ar matrices during luminescence measurements [58]. This can be explained by the absence of a planar conical intersection between the D_0 and D_1 for this radical cation [59]. Direct fluorescence is thus a marginal process in PAH cations and neglected in Figure 1.7. However, the strong coupling between the lowest electronic energy states leads to the possibility to populate D_1 back from D_0, which is made possible through inverse internal conversion (IIC). This conversion leads to the possibility of electronic fluorescence in a process called recurrent fluorescence or Poincaré fluorescence [60, 61].

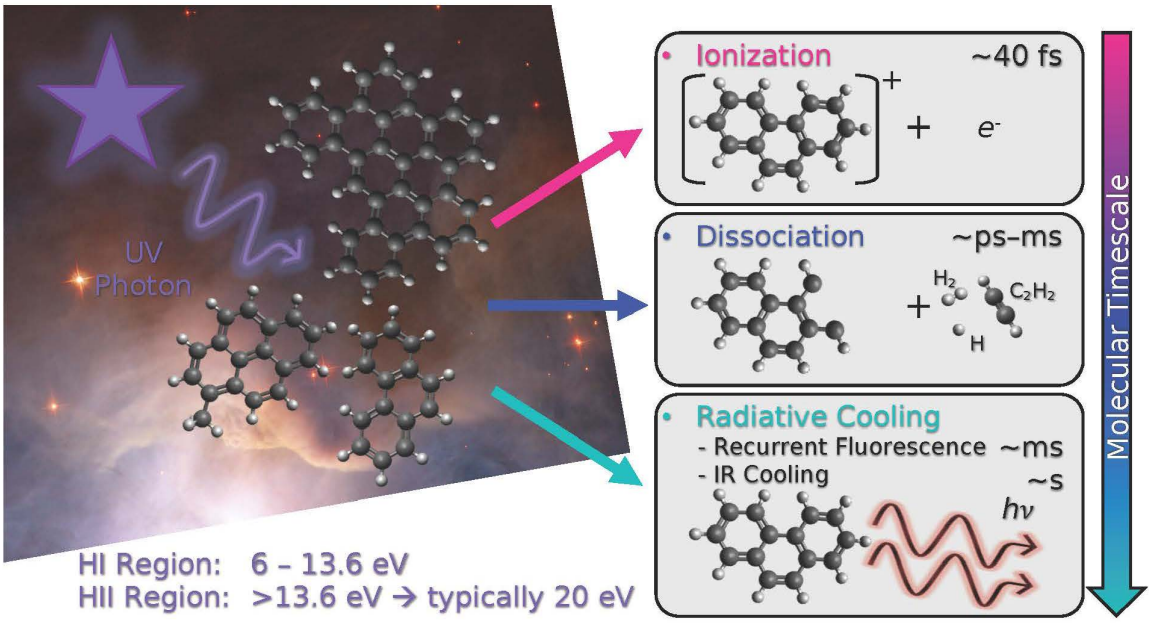

Figure 1.8: Schematic of the different possible relaxation processes of astro-PAHs upon absorption of a UV photon in the ISM and involved characteristic molecular timescales. Credit for the original image of NGC 7023 to Hubble/ESA.

Considering now an isolated PAH cation in the ISM, for example in a PDR, absorbing a single UV photon with photon energy, $h\nu$, it will undergo one of three main relaxation

processes. Ionization is the fastest; the relaxation of the excited electronic states that can eventually lead to ionization was measured to occur at a few tens of fs [62].

The three main relaxation channels for an isolated PAH cation in a PDR, ionization, dissociation, and radiative cooling, are summarized in Figure 1.8. Their characteristic molecular timescales are also presented. This work focuses on the competition between photoionization and photodissociation, and isomerization, which can occur as (i) a consequence of ionization and/or dissociation of a PAH, or (ii) in competition with the presented relaxation processes.

1.3 Laboratory Astrophysics Studies on PAHs

The objective of laboratory astrophysics is to obtain data on physical and chemical processes that are of interest in the astrophysical context. In the case of PAHs, the goal is to acquire spectroscopic information that can be used to identify these species, but also molecular data that can be used in models [e.g 52, 54] to quantify their physical and chemical evolution in astrophysical environments. In particular, the interaction with UV photons and the reactivity with electrons and gas-phase species such as H and H_2 are of interest. The astrophysical conditions differ from the ones which are usually found in the laboratory. Thus, obtaining relevant data may require dedicated setups. In addition, often compromises have to be found because not all physical and chemical conditions that are relevant to astrophysical environments can be accessed at once in a given setup. It is often that experiments and theoretical calculations go together in synergy, complementing and extending each other. More specifically, calculations can be used where experimental data is missing or to predict a specific behavior in a stand-alone study.

1.3.1 Spectroscopy of PAHs

The first theoretical calculations for small molecular ions of astrochemical significance, based on the Hartree-Fock approximation [63–65], were performed in the 1980s by DeFrees and McLean [66] and Yamaguchi *et al.* [67, 68], and were followed by the first theoretical IR spectra of the smallest PAH, ionized naphthalene, by Pauzat *et al.* [69]. Pauzat *et al.* [70] have investigated the effects of ionized and dehydrogenated

PAHs, namely anthracene and pyrene, and their impact on the 3.3 μm band, showing that this band collapses in the case of the cationic species. With calculations based on density functional theory (DFT), Langhoff [71] later connected this band collapse to observations of the AIB spectrum, demonstrating that it originates from ionized PAHs rather than dehydrogenation. DFT became popular and this quantum chemical approach is now widely used in order to optimize geometries and to calculate theoretical IR spectra of astrophysically relevant PAHs [72–74] up to very large PAHs with a number of carbon atoms, N_C, of 384 [75]. In particular, a great wealth of spectra has been computed and is readily available in the NASA Ames PAH IR Spectroscopic Database, PAHdb[(3)] [76–78], or the Theoretical Spectral Database of PAHs[(4)] [79].

Experimental studies have been performed to characterize the IR spectra of PAHs and are key to benchmark these calculations. For example, neutral or ionic PAHs have been isolated in rare gas matrices at low temperatures and their absorption spectra were recorded [80–90]. Since it is hot PAHs which contribute to the AIBs, further efforts were made in the astrophysics laboratory in order to investigate and to quantify the evolution of their IR spectra with temperature [91, 92], which was also the aim of theoretical studies [93, 94].

Another technique conveniently used to obtain information on the IR fingerprints of charged PAHs is IR multiple photon dissociation (IRMPD) spectroscopy in combination with DFT calculations. IRMPD spectroscopy experiments have been employed to measure the IR spectra of PAH cations [95–97] and anions [98] or even protonated species [99, 100] in order to compare them to theoretically calculated IR spectra and ultimately to AIB observations. For instance, Zhen *et al.* [101, 102] have recorded the first IR spectra of larger PAH cations (and one dication) with 32, 42, and 48 carbon atoms.

An additional spectroscopic aspect is the identification of the carriers of the diffuse interstellar bands (DIBs). Possible carriers of the DIBs are considered to be cold species as these are observed in absorption and not in emission. Neutral and cationic PAHs [34, 103–106] but also fullerenes [107] have been proposed as promising candidates. In particular, cationic PAHs are of interest as they have electronic transitions in the spectral region of the DIBs [108]. Extensive laboratory efforts have been made

(3) `http://astrochemistry.org/pahdb/theoretical/`
(4) `http://astrochemistry.ca.astro.it/database/`

over the past years in order to characterize electronic spectral signatures of neutral and ionized PAHs under interstellar conditions. For example, matrix isolation spectroscopy (MIS) can provide low temperatures and low densities and therefore a well-isolated environment to record the spectroscopy of cold PAH neutrals and cations, which can be formed *in situ* by irradiation of the matrix with UV photons [109–111]. However, the interaction with the matrix (usually made of frozen Ne or Ar atoms) can lead to band broadening and spectral shifts (*cf.* Appendix A), which make gas-phase techniques necessary for this task. In this context, cavity ring-down gas-phase spectroscopy experiments have probed the electronic spectra of ionized PAHs [112, 113] and PAH neutrals [114, 115] and found that the vibronic bands of PAH ions are broad in the range of several tens of cm^{-1}, whereas the ones of neutral PAHs range between $2 - 10\,cm^{-1}$. These efforts have been summarized for example by Salama *et al.* [116]. It was in fact gas-phase predissociation spectroscopy of the cold He tagged C_{60}^+ complex which for the first time confirmed C_{60}^+ to be a carrier of at least two DIBs [25, 26], proving the potential of this technique and progressing in the identification of possible DIBs carriers.

As previously mentioned, PAHs are also expected to contribute to the ultraviolet extinction curve, which initiated the investigation of their UV photoabsorption properties from an experimental point of view. Pure PAHs as well as mixtures of PAHs have been probed in the laboratory and Joblin *et al.* [117] have demonstrated that PAHs not only contribute to the bump at approximately 220 nm but also to the rise in the UV range. Such experiments led to theoretical photoabsorption studies performed by time-dependent density functional theory (TD-DFT) computations [74]. TD-DFT is a powerful tool which can as well be used, for example, to explore the effect of PAH dehydrogenation on the UV extinction curve [118]. All these studies led to detailed modeling of the galactic extinction curve including dust [119] and "real" PAHs [120].

1.3.2 Studies on the Photophysics and Chemistry of PAHs

In Section 1.2, we have described the processes that are involved in the photophysics of PAHs. Various experimental studies have enabled the provision of quantitative information on these processes.

The relaxation dynamics of the electronic excited states leading to ionization were

investigated by extreme UV (XUV or EUV) fs experiments. These have shown that it occurs on characteristic timescales of ∼40 fs for small PAHs [62], which increase with molecular size. Another recent theoretical study has investigated the ultrafast dynamics in excited states of neutral polyacenes as a function of molecular size, demonstrating the ability of time-dependent density functional based tight binding (TD-DFTB) methods to address this process [121].

In order to estimate the charge state of PAHs in PDRs, photoionization cross sections and ionization yields are necessary. They are accessible in the laboratory and efforts have been made to measure them for PAH neutrals [122–124] and cations [125–127].

Dissociation has been probed employing imaging photoelectron photoion coincidence (iPEPICO) spectroscopy at synchrotron facilities [128, 129] together with modeling based on the Rice-Ramsperger-Kassel-Marcus (RRKM) theory. This approach was successful to quantify activation energies and dissociation rates in the $1 - 100\,\mu$s range [130]. At longer timescales, radiative cooling enters in competition with dissociation. This is where ion traps and storage rings come into play, providing longer trapping or storing times and hence the possibility of the investigation of the competition between different relaxation processes on this timescale. For example, the cryogenic PIRENEA setup, which will be described in Section 2.2.3, is dedicated to the examination of the photodissociation of PAHs at the threshold where this process is in competition with radiative cooling. The excitation is driven by a multiple photon absorption scheme, which can also be used to record action spectra to characterize electronic transitions [131–133]. Moreover, photodissociation rates in this regime were extracted for the coronene cation, $C_{24}H_{12}^{+}$, and extrapolated to larger PAHs to be used in the model by Montillaud *et al.* [54].

Furthermore, the predicted recurrent fluorescence, also called Poincaré fluorescence [60, 134], was found to be a relevant process in the radiative cooling of hot PAH cations and its study benefits from experiments in storage rings such as the Mini-Ring in Lyon [61, 135]. However, the PIRENEA and Mini-Ring setups are not coupled to synchrotron radiation and therefore cannot be run in the presence of tunable UV light. Other setups consisting of linear ion traps at room temperature available at synchrotron facilities are used to provide us with useful branching ratios, quantifying the competition between ionization and dissociation [126, 127, 136]. These studies also bring information on the fragmentation products and the branching ratio between

them. For instance, Rodriguez Castillo *et al.* [137] have investigated two cationic isomers of dibenzopyrene and demonstrated the impact of the edge structure on the loss of H and H_2. With their laboratory results in combination with DFT, the authors found that the H_2 channel of the planar dibenzo(a,e)pyrene is favored, which, in conclusion, could impact the view of H_2 formation due to PAHs in the ISM. Their work also illustrates how isomerization and dissociation processes can be studied theoretically to model the complex pathways and evolution of energized PAHs. A detailed review on theoretical methods can be found in Simon and Rapacioli [138]. For these studies, the combination of DFT or DFTB with molecular dynamics (MD) approaches are proven to be of interest [see for example 139].

1.4 Objective of this Work

The objective of this work is to progress on our understanding of the properties of energized PAHs. A first aspect concerns the behavior of PAHs under UV photon irradiation in interstellar conditions as has been discussed throughout this chapter. Within the frame of this PhD work, we attempt to characterize the photophysical properties of trapped PAH cations interacting with UV photons. As predicted by models, predominantly PAHs with a size of $50 - 60$ carbon atoms are photostable enough to survive in the ISM. We therefore desire to study large PAH cations which can be experimentally challenging when bringing them into gas-phase in the laboratory. This part of the work has direct impact on our understanding of astro-PAHs.

Another contribution is associated to more fundamental aspects related to the isomerization of the –H fragment of methylated PAH cations. As we have seen, methylated PAHs are present in astrophysical environments and it is of interest to study their –H photofragments [45]. These species can involve isomerization processes as predicted for the fragment of the methylpyrene cation [140]. We will show how the isomerization composition can be probed experimentally by using IR spectroscopy of cold tagged ions.

Studying isomerization processes and their potential role in the cooling of energized PAHs was also the target of a campaign using the DESIREE cryogenic ring in which I had the opportunity to participate. The focus was on the cations of the small PAH species, $C_{14}H_{10}$, which include anthracene (Ant+) and phenanthrene (Phen+).

Calculations demonstrated that Ant+ can likely isomerize to Phen+ while dissociating and losing C_2H_2 [141]. In the experiments, isomerization processes can occur in the ion source or later upon photoexcitation. Experiments in storage rings, which are realized on long timescales in the case of cryogenic rings, open up the possibility to monitor the relaxation dynamics of the ions and probe potential isomerization processes. The analysis of the DESIREE results is still ongoing and is not part of this manuscript. Still, I will describe the technique as part of the scientific approach and my training. Also, in preparation of the DESIREE campaign, I have used the PIRENEA setup in Toulouse to record the action spectrum of cold Phen+ in the $420 - 480\,\mathrm{nm}$ range. This spectrum is reported in Appendix A.

Whereas the majority of the presented work is experimental, theoretical calculations based on quantum chemical computations and molecular dynamics simulations are also used to complement the experimentally obtained data and help to interpret the results.

The present thesis is divided into six main chapters. This first chapter has presented the scientific context of the thesis, introducing the astrophysical background and explaining the photophyscis of PAHs. Chapters 2 and 3 are dedicated to describe the laboratory and theoretical methods, respectively, used in synergy throughout this PhD work with a strong focus on the experimental side. These are followed by two chapters presenting the main results achieved. Chapter 4 concentrates on the interaction of trapped large PAH cations with molecular sizes ranging from 30 to 48 carbon atoms with UV irradiation of the synchrotron SOLEIL, experimentally investigating the competition between two relaxation channels, ionization and dissociation, as a function of photon energy. The results of the isomer composition of the –H fragments of methylated PAH cations are presented in Chapter 5, revealing various chemical structures for these fragments. Chapter 6 summarizes the molecular data being beneficial for astrophysical implications, such as the evolution of ionization potential with molecular size and the photoionization yield with photon energy. Additionally, it gives possible perspectives for future work. Finally, the conclusions list the accomplishments achieved during the completion of this PhD work.

1.5 Implementation within the EUROPAH Network

The Innovative Training Network (ITN) EUROPAH is a Marie Skłodowska-Curie Action (MSCA) funded by the European Union under the Horizon 2020 framework, Grant Agreement number 722346. EUROPAH is short for the '**E**xtensive and **U**biquitous **R**ole **O**f **P**olycyclic **A**romatic **H**ydrocarbons in space' and is a consortium consisting of 13 different research groups at 10 universities in collaboration with 3 companies across 6 European countries. 16 Early Stage Researchers (ESRs) are distributed between these research nodes, each working on a distinct research project and participating in public outreach activities.

As ESR #13 of the EUROPAH network, my scientific goal was to investigate the relaxation processes of energized PAHs as a function of photon energy and molecular properties in order to determine the photostability of PAHs in the interstellar medium. Whereas I will describe my scientific approach as well as my experimental and theoretical results throughout the following chapters of this thesis, I would like to give a brief introduction to the training and tasks fulfilled as an ESR.

In order to be well prepared for the research expected to be conducted by the ESRs, five training events were organized by the research nodes. The introductory training in Aarhus, Denmark, in Spetember 2017 included, among presentations about the EUROPAH ITN in general, a health and safety training, a surface science workshop and a public engagement introduction. During a first summer school named 'PAHs in the Interstellar Medium' at the well known Les Houches School of Physics, France, in April 2018, we were introduced to recent PAH research and useful observational, experimental and computational tools. An innovation training workshop followed in October 2018 in Liverpool, United Kingdom, consisting of presentations about innovative approaches and two company visits. In June 2019 it was Toulouse's responsibility of organizing a summer school which dealt with the subject 'PAHs in extreme environments'. A last training is planned for autumn 2020, a career planning and lead out event in Münster, Germany, which will give guidance and ideas for the ESRs to form their future and career, academic or non-academic, after EUROPAH.

A significant part of my PhD training was to complete secondments within the EUROPAH network. Secondments are placements of the ESRs to other institutes, universities, and/or industrial partners of the consortium in order to be exposed to new

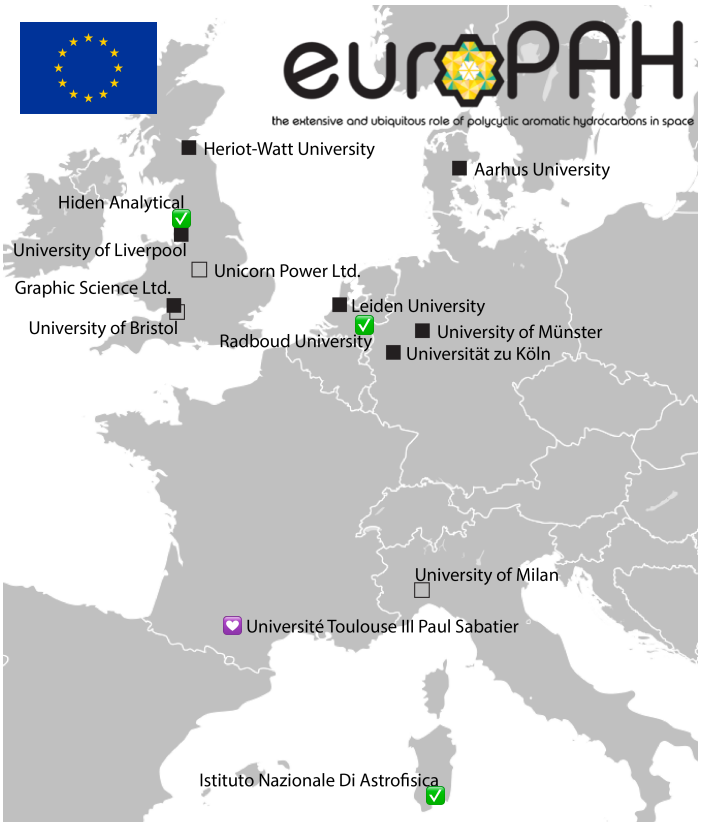

Figure 1.9: Map of Europe showing all research and industrial partners of the EUROPAH consortium. Marked in violet is my host university, Université de Toulouse III – Paul Sabatier, and in green the locations of my secondments to Istituto Nazionale di Astrofisica, the FELIX Laboratory at the Radboud University, and the company Hiden Analytical Ltd. Credit for the original image to europah.eu.

research techniques and work environments and to gain insights and skills in the respective fields as well as to develop collaborations within the network. During my time as an ESR, I was seconded to three institutions, namely to

- Istituto Nazionale di Astrofisica (INAF) at the Osservatorio Astronomico di Cagliari (OAC), Italy,
- Free Electron Laser for Infrared Experiments FELIX Laboratory at the Radboud University (RU), Nijmegen, The Netherlands, and
- Hiden Analytical Ltd., Warrington, United Kingdom.

A collaboration between the astronomer and quantum chemist Dr. Giacomo Mulas from INAF–OAC, Cagliari, and my PhD thesis supervisor, Dr. Christine Joblin, already existed. This connection enabled me to spend one of my secondments in Cagliari. Throughout my PhD we worked closely together in order to theoretically complement experimentally recorded data, by which I learned how to employ the quantum chemical packages Turbomole and OCTOPUS, especially to optimize molecular geometries and to calculate IR spectra as well as photoabsorption cross sections. The efforts made through this collaboration are presented in various sections of this PhD thesis manuscript, in particular in Chapters 3 and 4.

As part of a second secondment, I had the chance to write a successful research beamtime proposal as the principal investigator of the project entitled 'Tracking isomers of the –H fragment of methylated PAH cations by gas-phase IRPD spectroscopy'. The experimental campaign was carried out together with Shreyak Banhatti, ESR #11, Dr. Sandra Brünken from RU/FELIX, and Prof. Dr. Stephan Schlemmer from the University of Cologne (UCO), at the FELIX Laboratory in Nijmegen and the results are presented in detail in Chapter 5. In addition, I compare the experimentally obtained spectra to theoretical infrared spectra which were calculated in collaboration with Dr. Aude Simon, LCPQ/IRSAMC, Toulouse, who utilizes the quantum chemistry package Gaussian09.

Furthermore, I was fortunate to have been involved in a collaboration with the Mini-Ring team consisting of Dr. Jérôme Bernard and Dr. Serge Martin from the University of Lyon (ILM). Together, we spent one week at the DESIREE double ring experiment in Stockholm, Sweden, which enabled me to acquire first experiences with electrostatic storage rings and to get a flavor of the investigation of radiative cooling processes in the laboratory. I will thus briefly describe the DESIREE setup in Section 2.1.2.3.

Finally, I had the opportunity to gain experience working in an industrial environment and to make contact with scientists working outside academia at the quadrupole mass spectrometer manufacturer Hiden Analytical Ltd. I summarized these experiences in a posting which was published on the EUROPAH's public outreach blog europah.com and can be found in Appendix C.

2 | Laboratory Methods

Outline

2.1 Ion Traps and Storage Devices

In order to meet the objective of this work and to examine PAHs and their interaction with light in the laboratory, desirably at interstellar conditions, several different instruments and techniques are employed and presented in this chapter.

All PAHs studied during this PhD work were positively charged, meaning I solely examined PAH cations. The simple reason for this is our ability to guide, select, trap and analyze them using electric or magnetic fields. The production of PAH cations and their storage in traps and rings will be described in the following sections.

2.1.1 Production of Ions

This work is concentrated on the investigation of cationic PAHs, ions with a single positive charge, $z = 1$. The used neutral PAH samples were in the form of solid powder, most of which originated from chemical companies except the largest one studied, dicoronylene, which has been synthesized by one of our collaborators (see Appendix D). The PAH ions of interest were produced using several ionization techniques as described below.

2.1.1.1 Atmospheric Pressure Ionization Source

Atmospheric pressure photoionization (APPI) is a soft technique ionizing molecules by the interaction with UV light in the gas phase preventing strong fragmentation of the precursor. In order to bring the solid PAH powder into gas-phase, neutral PAHs are dissolved in a solvent and pulled up into a syringe. This technique was used in our SOLEIL campaign with toluene and trichlorobenzene as solvents. The neutral PAH solution is then vaporized and enters an ionization chamber at atmospheric pressure in which the PAH gas is irradiated by UV light from a krypton discharge lamp. PAHs have first ionization potentials of around 7 eV which is decreasing with increasing number of carbon atoms [142]. Hence, the energy of the krypton lamp photons at 10.0 and 10.6 eV is sufficient to ionize PAHs without leading to significant fragmentation [143], but too low to ionize air, water or other contaminating molecules [144]. The produced PAH cations can be extracted due to the attraction induced by a voltage difference between the ionization chamber and the exit plate of the ion source.

During the SOLEIL campaign, difficulties were faced in the production of solutions of large PAHs with more than 35 carbon atoms. In order to produce larger PAH cations in the gas-phase, we cannot recommend and employ the APPI technique.

2.1.1.2 Electron Impact Ionization

Electron impact ionization is a technique used in many different setups in order to ionize the surrounding species by electron bombardment. The electrons are generated by glow emission from a tungsten or rhenium cathode. More specifically, in the FELion setup we used two kinds of electron impact ionization source, a non-storage ion source and a radio frequency (RF) storage ion source.

In the non-storage ion source, a cylindrical grating is surrounded by a filament which wraps around the grating in a ring like arrangement. The electrons generated by the filament are accelerated toward the grating which is held at a slight positive potential (3 V) and a negative floating potential is applied to the filament. These accelerated electrons bombard the molecules inside the cylindrical grating region with the energy, E_{e^-}, given by the potential difference between the grating and the filament (usually tuned between 10 and 125 eV). The ions are then extracted via an Einzel lens system connected closely to the ionization region. In this source, ions are generated and neutralized continuously.

In the case of the RF storage source, the ions generated by electron impact are introduced into a radio frequency (RF) trapping field supplied by a push-pull type RF generator at 1.5 MHz. Here, the ions are accumulated for a certain duration in each measurement cycle, typically 1 to 3 s, during which they thermalize. By pulsing the exit electrode with a pulse width of typically 1 to 100 ms once per experiment cycle, the ions are extracted from the source. A detailed discussion of this kind of RF storage ion source can be found in Gerlich [145].

2.1.1.3 Laser Desorption Ionization

An homogeneous solution of neutral PAH powder mixed with toluene is created and dropped successively onto a solid target. Through evaporation of the solvent, a solid

uniform deposit of PAHs is obtained on the target, which then can be transferred via a load lock into the ultra-high vacuum (UHV) experimental setup. Low temperatures and immediate pumping of the load lock prevent the evaporation of the species which might have high vapour pressures. Focusing the fourth harmonic of a Nd:YAG laser at 266 nm (*cf.* Section 2.3.3.1) at the solid sample target, gas-phase neutral and ionized PAHs are produced by laser ablation, realizing the vaporization and the ionization of the sample. The neutral PAHs and other neutral species condense to the low-temperature walls of the setup whereas the ionized PAHs are guided further into the ion trap. Laser desorption ionization (LDI) is therefore a single step technique which can easily be used for higher mass species. PAHs are likely to absorb at this wavelength, $\lambda = 266\,\text{nm}$, yielding a strong ion signal which could also, however, lead to some heating of the ions.

2.1.2 Trapping and Storage of Ions

The possibility of studying molecular processes on long timescales is enabled by the use of ion traps and storage devices which confine ions in space. Ion traps can be realized by applying dynamic electric potentials to electrodes or by the use of a combination of magnetic and electric fields. I would like to discuss here briefly the Paul and Penning trapping principles and give an example of an electrostatic storage ring device.

2.1.2.1 Paul Trap

The Paul trap is named after W. Paul who invented this ion trapping principle using a combination of static and dynamic electric fields in 1953 and received the Nobel Prize in Physics for his development in 1989. Since the potential applied to the electrodes has to change fast in time, *i.e.*, in the radio frequency range, this kind of trap is also called radio frequency (RF) ion trap. A full description of the work principle of the Paul trap can be found in Paul [146].

The ion trap after Paul consists of a hyperbolically shaped ring and two hyperbolic rotationally symmetric cap electrodes with periodically alternating potentials, ϕ_0. A schematic view is depicted in Figure 2.1. In three dimensions, the electric quadrupole

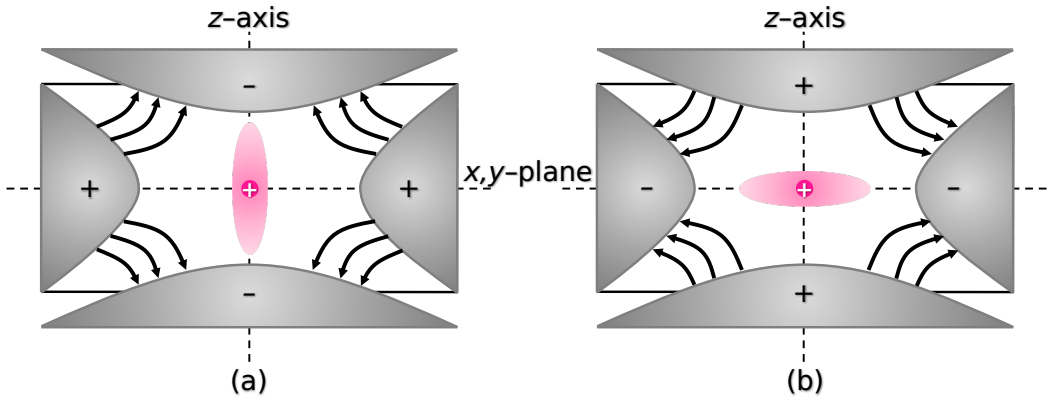

Figure 2.1: Schematic view of a Paul ion trap with a positively charged ion in the center surrounded by a cation cloud. Equipotential lines are schematically outlined between the electrodes. Panels (a) and (b) show two different trapping stages of the AC cycle.

field potential is quadratic in Cartesian coordinates,

$$\phi = \frac{\phi_0}{2r_0^2}(\alpha x^2 + \beta y^2 + \gamma z^2), \tag{2.1}$$

where r_0 is a trap specific size parameter and α, β, and γ are the weighting constants. In order to satisfy stability inside the trap, the potential has to be periodic, meaning the Laplace equation has to be fulfilled,

$$\Delta\phi \stackrel{!}{=} 0 \Rightarrow \alpha + \beta + \gamma = 0, \tag{2.2}$$

which can be satisfied with either (a) $\alpha = -\beta = 1$, $\gamma = 0$ or (b) $\alpha = \beta = 1$, $\gamma = -2$. Option (a) results in the two-dimensional electric potential used for a quadrupole mass filter,

$$\phi = \frac{\phi_0}{2r_0^2}(x^2 - y^2), \tag{2.3}$$

which will be discussed further in Section 2.2.2. Plugging in the parameter values from (b), we get the three-dimensional electric potential configuration in cylindrical coordinates

$$\phi = \frac{\phi_0}{2r_0^2}(r^2 - 2z^2) \tag{2.4}$$

for the ion trap. With the periodic potential,

$$\phi_0 = U + V \cos \omega t, \tag{2.5}$$

which is applied between the electrodes, the ion is dynamically confined on a saddle surface which rotates with angular frequency, ω. Figure 2.2 demonstrates how a particle, here depicted as a ball, is confined in the potential which changes periodically with ω. The stability map is similar to the two-dimensional case which will be discussed in more detail in Section 2.2.2.

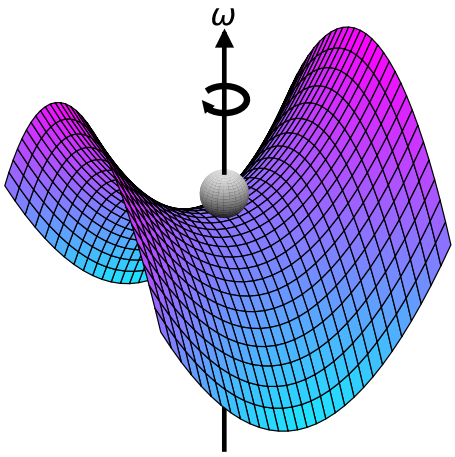

Figure 2.2: Potential surface of the Paul ion trap with a particle depicted as a ball in the center of the saddle point. The potential surface rotates periodically with angular frequency, ω.

2.1.2.2 Penning Trap

Another possibility of trapping ions is the use of a quadrupole electric field in combination with an axial magnetic field confining the charged particle in all three dimensions. This concept was introduced by H. G. Dehmelt [147] who was inspired by the Penning gauge [148] and shared the Nobel Prize in 1989 together with aforementioned W. Paul [149]. A schematic of a Penning trap with a ring and two end electrodes is depicted in Figure 2.3 (a).

Considering a charged particle with mass, m, and charge, q, in an axial homogeneous

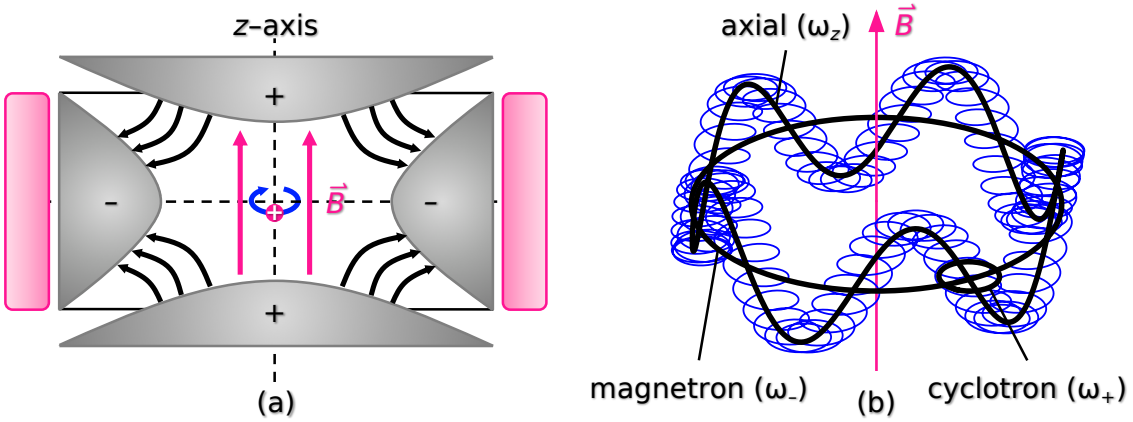

Figure 2.3: Panel (a): Schematic view of a Penning ion trap with a positively charged ion in the center of the electrodes and a magnetic field in z-direction. Equipotential lines are schematically outlined between the electrodes. Panel (b) shows the motion of the ion inside the trap, which consists of the superposition of the cyclotron, ω_+, and magnetron, ω_-, motions, and the axial oscillation with ω_z.

magnetic field, $\vec{B}$, in the z-direction,

$$\vec{B} = B\vec{e_z}, \tag{2.6}$$

the particle will be confined on a circular path in the x, y-plane, or on a helical path in three dimensions. If we additionally apply an harmonic electric quadrupole field, $\vec{E}$, with potential, ϕ, (*cf.* Equation (2.4))

$$\vec{E} = -\vec{\nabla}\phi = -\vec{\nabla}\left(\frac{\phi_0}{2r_0^2}\left(z^2 - \frac{x^2}{2} - \frac{y^2}{2}\right)\right) = \frac{\phi_0}{2r_0^2}\begin{pmatrix} x \\ y \\ -2z \end{pmatrix} \tag{2.7}$$

to the electrodes, we can express the equation of motion of the particle via the Lorentz force as

$$m\ddot{\vec{r}} = q\left(\vec{E} + \dot{\vec{r}} \times \vec{B}\right) = q\left(\frac{\phi_0}{2r_0^2}\begin{pmatrix} x \\ y \\ -2z \end{pmatrix} + \dot{\vec{r}} \times \begin{pmatrix} 0 \\ 0 \\ B \end{pmatrix}\right). \tag{2.8}$$

Solving the ordinary differential equation for the axial motion, the oscillating trajec-

tory of the particle in z-direction will be

$$z = r_z \cos\left(\omega_z t + \varphi_z\right), \quad \text{with} \quad \omega_z = \left(\frac{q\phi_0}{mr_0^2}\right)^{\frac{1}{2}}. \tag{2.9}$$

The solution for the x- and y-components of the motion,

$$m\begin{pmatrix} \ddot{x} \\ \ddot{y} \end{pmatrix} = q\left(\frac{\phi_0}{2r_0^2}\begin{pmatrix} x \\ y \end{pmatrix} + B\begin{pmatrix} \dot{y} \\ -\dot{x} \end{pmatrix}\right), \tag{2.10}$$

can be derived for strong magnetic fields, $\vec{B}$, and weak electric fields, $\vec{E}$, *i.e.*

$$\left(\frac{qB}{2m}\right)^2 > \frac{q\phi_0}{2mr_0^2}, \tag{2.11}$$

as the sum of two circular motions

$$\begin{pmatrix} x \\ y \end{pmatrix} = r_+\begin{pmatrix} \cos\left(\omega_+ t + \varphi_+\right) \\ \sin\left(\omega_+ t + \varphi_+\right) \end{pmatrix} + r_-\begin{pmatrix} \cos\left(\omega_- t + \varphi_-\right) \\ \sin\left(\omega_- t + \varphi_-\right) \end{pmatrix} \tag{2.12}$$

with

$$\omega_\pm = -\frac{qB}{2m} \pm \left(\left(\frac{qB}{2m}\right)^2 - \frac{q\phi_0}{2mr_0^2}\right)^{\frac{1}{2}}. \tag{2.13}$$

Figure 2.4 demonstrates the motions of a particle in the Penning trap along each of the axes, x, y, and z, in the x, y-plane, and the superposition of the three motions, which are also denoted

- ω_+ – cyclotron motion (fast, small radius)
- ω_z – axial oscillation (medium fast)
- ω_- – magnetron motion (slow, large radius)

and are depicted together with the schematic of the Penning trap on the right in Figure 2.3. What can be directly derived from the frequencies, ω, is that the motion inside the Penning trap depends on the mass-to-charge ratio, here $\frac{m}{q}$, of the trapped particle or ion, making this setup advantageous for mass spectrometry experiments, in which the $\frac{m}{q}$ ratio is used to distinguish between different species. The PIRENEA

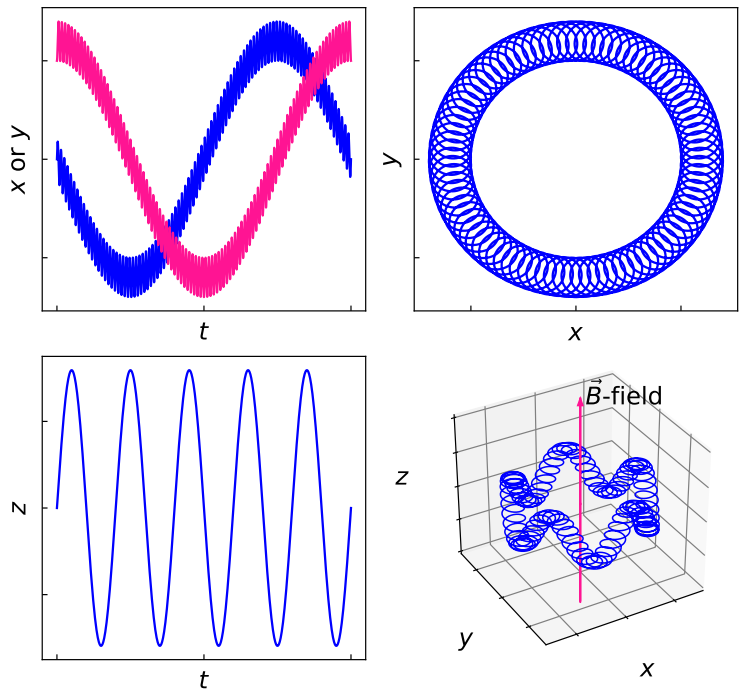

Figure 2.4: Motions of a charged particle in a Penning trap in the x, y, z-directions. On the bottom right, the superposition of all motions in all directions, *i.e.*, the cyclotron, ω_+, and magnetron, ω_-, motions, and the axial oscillation with ω_z, are shown.

setup is a special case of a Penning trap with an alternative geometry including open cylinders as electrodes and can simultaneously be operated as a Fourier Transform ion cyclotron resonance mass spectrometer [150, 151] as will be described in Section 2.2.3.

2.1.2.3 Electrostatic Storage Rings

Electrostatic storage rings also make use of magnetic and electric fields to store charged particles and ions. A magnetic field can bend the trajectory of an ion depending on its momentum, whereas an electric field deflects the ion depending on its kinetic energy. For ions with the same kinetic energy, the deflection is independent of the mass of the ion, meaning that electrostatic storage rings have no mass limitation. A thorough review of electrostatic storage rings and their use for atomic and molecular physics can be found in Schmidt [152].

The first electrostatitc storage ring for heavy ions, ELISA, was constructed at the Aarhus University, Denmark, in 1997 [153], and is followed by many more, such as the

ESRing at the KEK-High Energy Accelerator Research Organization in Japan [154], the CSR project at the Max-Planck-Institut für Kernphysik in Heidelberg, Germany [155], the tabletop Mini-Ring at the Lyon University, France [156], and the double rings, DESIREE, at the Stockholm University, Sweden [157]. Especially the tabletop electrostatic storage device Mini-Ring has demonstrated its potential in the examination of the photophysics of PAHs, in particular of their cooling mechanisms. For example, Martin *et al.* [61, 135] have investigated the radiative cooling decay rates of anthracene cations interacting with photons and found a fast radiative cooling mechanism to potentially affect the lifetime of PAHs in interstellar conditions. Moreover, between infrared vibrational emission and Poincaré fluorescence, the latter was found to predominantly contribute to the cooling [158], but also fragmentation kinematics studies can be addressed using an electrostatic storage ring [159].

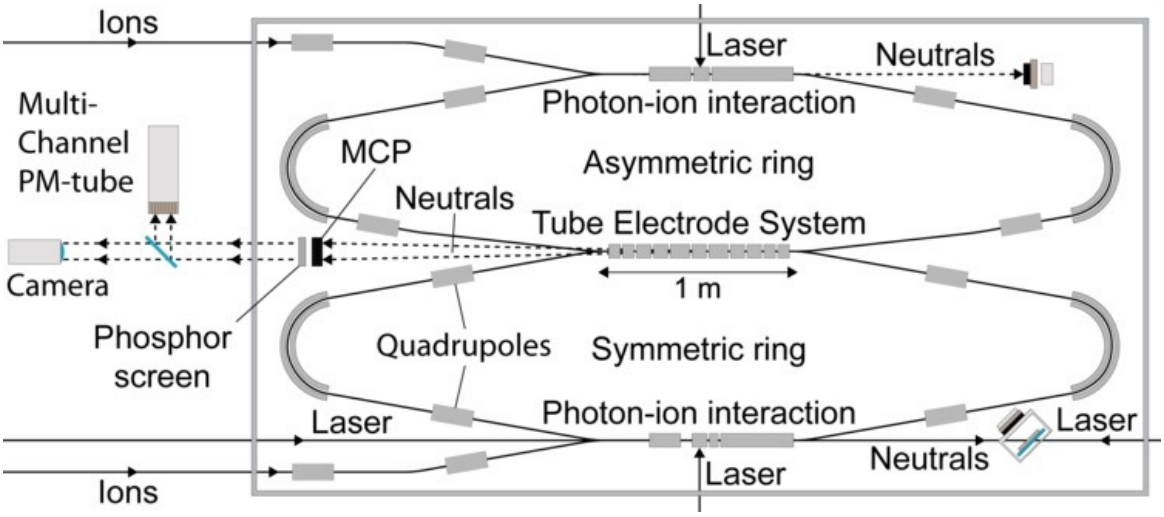

Figure 2.5: Schematic of the double electrostatic ion ring experiment, DESIREE, available at the Stockholm University, Sweden. Taken and adapted from desiree-infrastructure.com/desiree.

In the framework of a collaboration with the Mini-Ring team from the University of Lyon, I had the opportunity to participate in a DESIREE beamtime measurement on the cooling of the cationic PAH isomers, anthracene and phenanthrene. On this account, I would like to briefly present DESIREE, which is shown in Figure 2.5.

DESIREE stands for Double ElectroStatic Ion Ring ExpEriment, and is a cryogenic double storage ring. When using the double ring capability, high energetic, in the keV energy range, beams of positively and negatively charged ions can be fed into the

respective rings and merged in the tube electrode, enabling the study of cation-anion collisions down to the meV energy range which is similar to what can be reached in the ISM. The single ring configuration is also useful for the study of the photophysics of PAHs in astrophysical conditions combining long ion storage times and a cryogenic environment. For example, Stockett *et al.* [160] have shown that the multiple photon photodissociation action spectrum of the coronene cation as a function of storage time reveals the rate at which hot-band absorptions are quenched by radiative cooling in the experiment via infrared emission from vibrational transitions. The authors observed that the spectrum recorded after more than 10 s of radiative cooling is close to the one which was recorded in the PIRENEA setup (see Section 2.2.3) in which cooling with He buffer gas at 35 K has been achieved [132].

2.2 Mass Spectrometry Techniques

Once ions have been produced, trapped, stored, and/or processed by the interaction with light, they can be analyzed by mass spectrometers. Ions with different masses or charges can be separated using different separation techniques which all are related to the mass-to-charge ratio, m/z, of the ions. These include the kinetic energy or momentum of the ions in electric or magnetic sector mass analyzers, respectively, their velocity, which is used in time-of-flight mass spectrometers such as the AROMA setup [161], or according to their trajectory stability in quadrupoles and their resonance frequency in ion traps and Fourier Transform ion cyclotron resonance mass spectrometers. The mass analyzers employed to carry out this thesis work are presented in the following sections.

2.2.1 Mass Selection and Resolution

Positively or negatively charged molecules with mass, m, and charge, $q = z\,e$, with $z = \pm 1, \pm 2, \ldots$ and the elementary charge, e, can be distinguished according to their mass-to-charge ratio, $\frac{m}{q}$, or more commonly written as m/z. According to the type of detector, an intensity or number of counts, *i.e.*, a relative abundance of the ions is recorded as a function of m/z yielding a characteristic mass spectrum.

Two peaks in the mass spectrum can be resolved according to the resolving power,

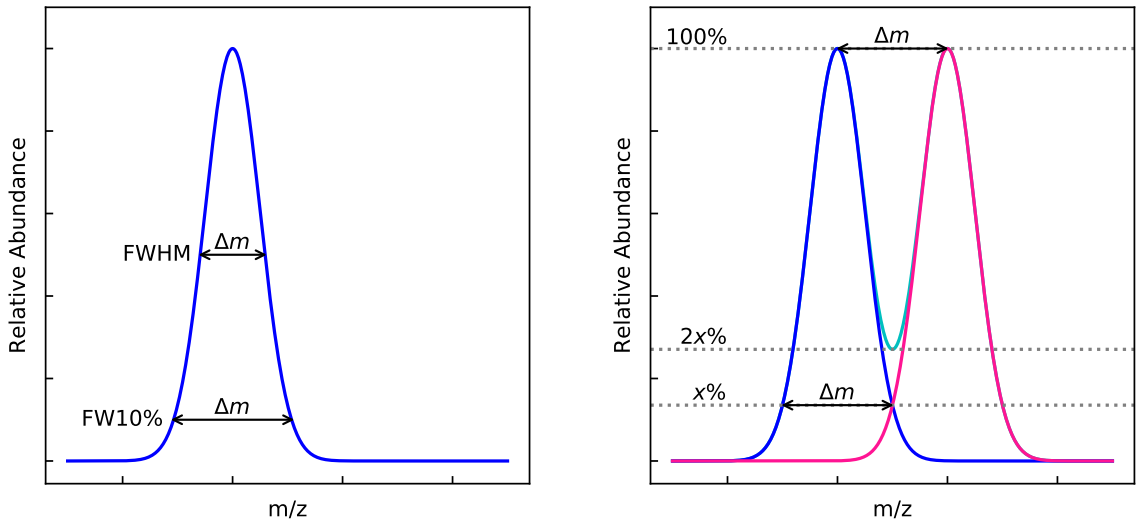

Figure 2.6: Definition of the mass difference, Δm, which determines the resolving power, $R = \frac{m}{\Delta m}$. The left panel shows the definition at a given height of the peak, whereas the right panel depicts the definition for two present mass peaks.

R. For the smallest mass-to-charge difference, Δm, between two mass peaks with $m/z = m_0$ and $m/z = m_0 + \Delta m$, the resolving power, R, is defined as

$$R = \frac{m_0}{\Delta m}. \tag{2.14}$$

Figure 2.6 depicts typical possibilities of the definition of Δm which can be determined by the use of the full width at half maximum (FWHM) or the full width at a given percentage of the relative abundance, e.g. at 10 % (FW10 %), of an isolated peak (left panel in Figure 2.6). For two peaks with a similar relative abundance, Δm is defined as the difference between the two peaks and can be determined at x % of the peak height or at $2x$ %, *i.e.*, the valley between the peaks.

2.2.2 Quadrupole Mass Spectrometry

A quadrupole mass analyzer consists of four perfectly parallel rods to which an oscillating potential, ϕ_0, is applied as firstly described by Paul and Steinwedel [162]. The potential can be written as

$$\phi_0 = U + V \cos \omega t, \tag{2.15}$$

where U is the direct potential, V is the amplitude of the radio frequency voltage, ω is the angular frequency and time, t. A charged molecule entering the space between the rods will interact with the applied potentials and either be pushed away from or drawn toward the rods depending on the sign of charge. The experimental setup for a quadrupole mass analyzer is schematically presented in Figure 2.7, depicting the trajectory of an ion traveling with a constant velocity along the z-axis. In x- and y-directions the ion is subjected to accelerations induced by the forces of the electric fields. The ion will pass the quadrupole mass analyzer if its trajectory is stable in x and y, hence if the ion will not hit and discharge itself on one of the rods. The equations of motions can be modified as described by Paul [146] so that they resemble the Mathieu equations, for which distinct solutions exist with

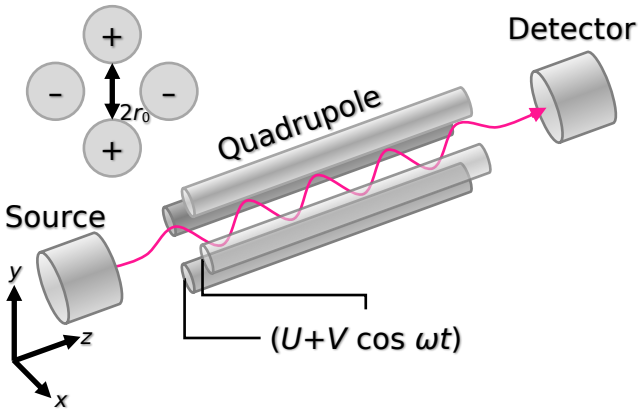

Figure 2.7: Schematic of a quadrupole mass analyzer setup consisting of an ion source, the quadrupole cylindrical rods, and a detector. The rods must be perfectly parallel and induce an electric field with oscillating potential, $\phi_0 = U + V\cos\omega t$.

$$a_u = a_x = -a_y = \frac{4eU}{m\omega^2 r_0^2} \quad \& \quad q_u = q_x = -q_y = \frac{2eV}{m\omega^2 r_0^2}, \tag{2.16}$$

where m/e is the mass-to-charge ratio of the ion, e is the elementary charge, and r_0 is the distance from the center of the space between the rods to the rods as schematically depicted in the top left corner in Figure 2.7. The stability diagram for a_u and q_u is shown in Figure 2.8. Since the ion trajectory has to be stable in both x- and y-directions, only the overlapping areas in Figure 2.8 are of interest. The first stable area is depicted in the right panel of Figure 2.8, also showing the experimentally advisable stability area, A, for positive a_u, and hence for positive direct potentials, U.

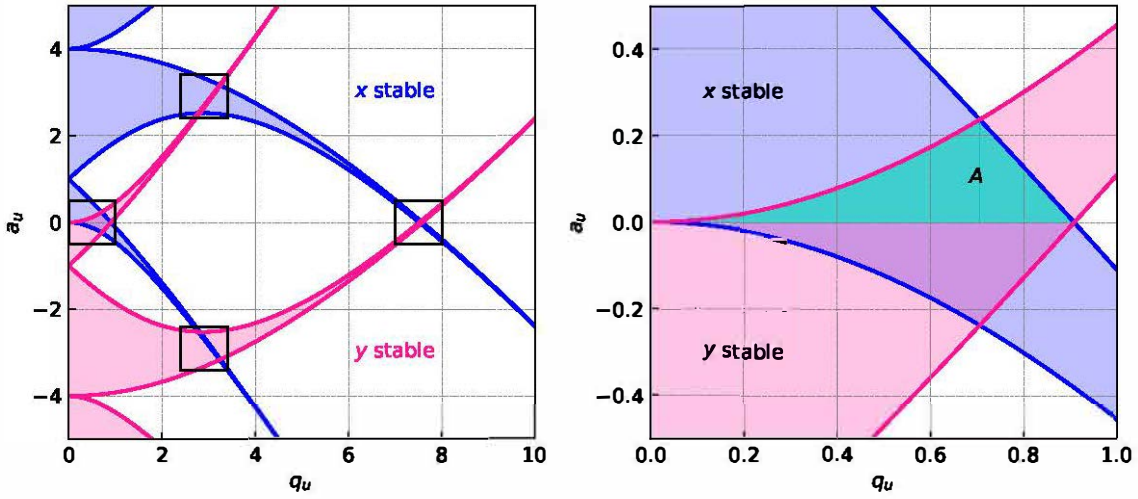

Figure 2.8: Left panel: Stability diagram for an ion inside a quadrupole along x (blue) and y (pink). The four stability areas, in which the ion trajectory is stable along x and y, are marked by rectangulars. Right panel: Zoom of the first and experimentally feasible stability region for $a_u > 0$, denoted A.

Since a_u and q_u are directly dependent on U and V, respectively, the stability diagram can be transformed to a U, V diagram representing the stable areas, A, for different masses. While keeping the $2U/V$ ratio constant, ions with different masses can successively pass through the quadrupole and be detected. Adjusting the slope of the $2U/V$ curve changes the resolution, Δm, of the quadrupole.

2.2.3 Fourier Transform Ion Cyclotron Resonance Mass Spectrometry

The PIRENEA setup, short for ***Piège à Ions pour la Recherche et l'Étude de Nouvelles Espèces Astrochimiques***, is a home-built cryogenic Fourier Transform ion cyclotron resonance (FTICR) ion trap available at the Institut de Rechereche en Astrophysique et Planétologie (IRAP), Toulouse, France, dedicated to investigate large molecules and small grains of astrophysical interest [131, 132]. PIRENEA is a special form of a Penning trap (see Section 2.1.2.2) and was constructed in order to mimic interstellar conditions, *i.e.*, a cold temperature of about $T \approx 30$ K, low pressure of $p \approx 10^{-10}$ mbar, and the presence of UV photons.

Figure 2.9 schematically depicts the experimental setup of PIRENEA, consisting of

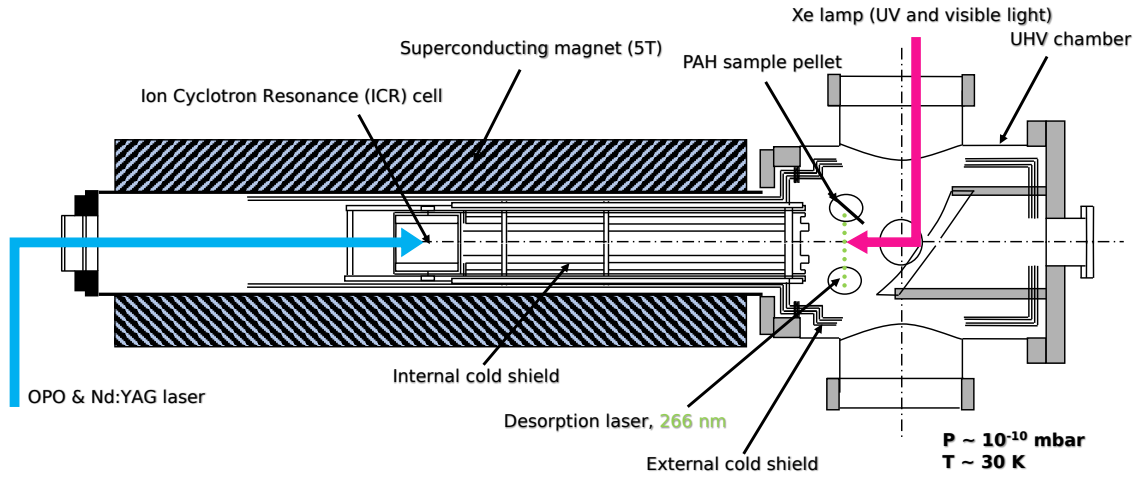

Figure 2.9: The cryogenic ion trap setup, PIRENEA, available at IRAP in Toulouse.

the ion cyclotron resonance (ICR) cell, encased by a superconducting magnet with a homogeneous cylindrical magnetic field of 5 T. Inside the ultra-high vacuum (UHV) chamber, cryogenic shields are connected to a closed cycle cryogenerator with an internal cold shield reaching 30 K in the ICR cell and an external cold shield at about 80 K. A load lock is coupled to the UHV chamber in order to easily insert and extract the samples of interest without completely breaking the vacuum. The ions are directly produced from the neutral molecule sample pellet by laser desorption (*cf.* Section 2.1.1.3) with the fourth harmonic of a Nd:YAG laser (266 nm), whose intensity and focus can be tuned in order to obtain a good parent ion cloud. The ions are then somehow guided by the magnetic field into the ICR cell and can be trapped by the application of electric potentials. This technique ensures that large molecules, for example $C_{78}H_{26}^{+}$ [133], can be inserted and studied and therefore does not rely on the solubility of the PAH sample which was a breaking point in the case of APPI (see Section 2.1.1.1).

If necessary, He gas can be introduced into the ICR cell in order to cool the ions by ion-He collisions. The mass analysis method provided by the FTICR is based on the principle of a Penning trap (*cf.* Section 2.1.2.2). The ions rotating at their cyclotron frequency induce an image current on the electrodes. The resulting measured signal can be converted into a mass spectrum by performing a Fourier Transform. Contaminating species or fragments can be directly ejected from the ICR by applying an ejection pulse to the electrodes, adopting the stored waveform inverse Fourier

Transform (SWIFT) excitation technique [163].

A photophysical interface is installed to the PIRENEA setup which consists of a xenon arc lamp (UV/Vis light, selectable by color filters), a Nd:YAG laser (Surelite I, Continuum) which can be used with different higher harmonics, and an optical parametric oscillator (OPO) laser (Panther EX OPO, Continuum) which is tunable from *ca.* 210 nm to 2 μm with interruptions (see Section 2.3.3). The different light sources can be used alone or in combination with each other and irradiate the trapped ions of interest. The most prominent process observed for PAHs in PIRENEA is photodissociation occurring from multiple photon absorption events. The detection signal is recorded as a function of employed light source with varying photon energy, irradiation time, or laser power and mass spectra are derived by Fourier Transform. Usually a sequence of ten measurements is performed on the same settings in order to increase the statistics of the outcome.

2.3 Spectroscopy Techniques in Ion Traps

Once the species of interest is trapped, the interaction with light can be studied by irradiating the ions for a certain duration. Different techniques and effects can be observed and investigated. As for now, spectroscopic signatures of PAHs are the only diagnostics to identify their presence in the ISM. The following sections are dedicated to the brief description of the spectroscopic techniques which were used throughout this PhD work and concerned trapped PAH cations.

2.3.1 Action Spectroscopy on the Bare Cation

The photophysical processes a PAH cation can undergo upon light absorption were discussed in Section 1.2. The relaxation channels of photoionization and photodissociation of the PAH cations upon light absorption can be followed by means of mass spectrometry, mass-analyzing the photoproduts. For example, PAH dications will be measured at half of the m/z of the parent cation due to the double charge ($z = 2$) and photofragments can be identified at a m/z which is smaller than the one of the parent ion. The loss of acetylene, C_2H_2, for instance, will show a photoproduct peak in the mass spectrum shifted for the acetylene mass from the parent ion m/z, *i.e.*,

at $m/z - 26$. Recording the photoproducts in dependence of the wavelength of the absorbed light means therefore to record the action the PAH cations take upon light absorption, and is thus called action spectroscopy. However, the formation of such photofragments from the bare PAH cation requires quite an amount of energy which, for PAH cations, is in the order of ∼10 eV, depending on the molecular size [e.g. 56, 126]. In order to study the spectroscopy of PAH cations in the visible or infrared range (without using tagging techniques, *cf.* Section 2.3.2), therefore requires multiple photon absorption schemes. Different absorption schemes are presented in Figure 2.10 and discussed in the following.

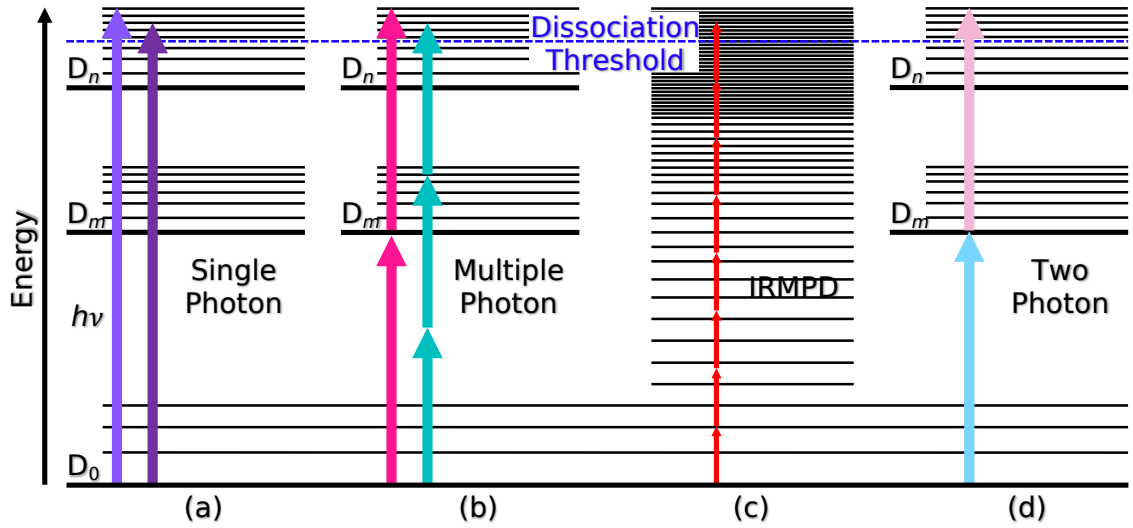

Figure 2.10: Different absorption schemes to perform action spectroscopy. (a) Single photon absorption, (b) multiple photon absorption of photons with the same wavelength, (c) infrared multiple photon absorption, and (d) two photon absorption of photons with different wavelengths.

2.3.1.1 Single Photon Absorption

In a single photon absorption scheme, PAHs are studied when they absorb only one photon with a set energy, $h\nu$, typically a photon with an energy in the vacuum ultraviolet (VUV) range[(5)]. To probe these processes as a function of the incident VUV photon energy is key in the investigation of the electronic properties of interstellar

[(5)] We refer here to vacuum ultraviolet (VUV) photons because of the experimental constraint. Please find Table B.1 indicating all mentioned UV ranges in Appendix B.

matter. The process is depicted in Figure 2.10 (a), showing the absorption of a VUV photon which in this case leads to excitation to the D_n state of the PAH cation. In gas-phase spectroscopy such as the experiments performed at the DESIRS beamline at the synchrotron SOLEIL (*cf.* Chapter 4), the absorption of a single VUV photon by a PAH cation can be tracked by recording the produced photoproducts, *i.e.*, the photofragments as well as dications or even trications which have been formed upon VUV photon absorption [126, 127, 164].

2.3.1.2 Multiple Photon Dissociation

Multiple photon dissociation (MPD) spectroscopy is based on the fragmentation of a PAH by multiple photon absorption and schematically illustrated in Figure 2.10 (b). Fragmentation occurs when the laser wavelength is tuned on an absorption band so that the absorbed energy is sufficient to dissociate the PAH. The recorded action spectrum following one or all photofragments of the PAH as a function of the laser wavelength can be related to the absorption spectrum of that PAH [132, 165]. This technique allows us to directly study the species of interest, but the destruction of a chemical bond in order to measure the photoproducts is disadvantageous. The subsequent absorption of photons during the MPD scheme leads to the heating of the ions which might affect the band profile and cause unwanted phenomena such as isomerization.

The use of infrared light to perform infrared multiple photon dissociation (IRMPD) experiments [see 166, for a review of the technique] on PAHs [95–97] as depicted in Figure 2.10 (c), requires powerful light sources such as free electron lasers (*cf.* Section 2.3.3.3).

2.3.1.3 Two Photon Absorption

To minimize the heating effects described for the MPD spectroscopy, two photon absorption schemes can be employed to investigate the spectroscopy of PAH cations. As shown in Figure 2.10 (d), two photons of two different light sources, *i.e.*, with different $h\nu$ are absorbed by the PAH cation. Here, the wavelength of the first photon to be absorbed is tuned to find absorption bands of the PAH cation. The absorption of a second additional photon then causes the PAH to reach its dissociation threshold.

By using this scheme, the effect on the spectral bands due to the heating of the ions, as can be observed in the MPD scheme, is minimized.

A technique benefiting from the two photon absorption scheme is resonance-enhanced multiple photon ionization (REMPI) spectroscopy, in which two lasers are applied in sequence to firstly excite the neutral molecule to an intermediate electronic state, and secondly, to ionize the species of interest [167, 168].

2.3.2 Predissociation Spectroscopy of the Tagged Ion

Different from the above described action spectroscopy which involves the dissociation or the ionization of the parent species is the predissociation (PD) spectroscopy of the complex formed by the ion tagged with a rare gas atom [169]. While action spectroscopy can be performed at various temperatures, this particular kind of spectroscopic technique requires cryogenic temperatures and collisionally cooled ions. These can be tagged with noble gas atoms such as He or Ne which condense onto the ions, yielding a mass-to-charge ratio which is shifted for the mass of the chemically inert atom, the so-called tag (e.g. $m/z = +4$ and $m/z = +20$ for He and Ne, respectively). The tagged complex, consisting of the ion of interest and the tag, is then submitted to tunable light. Upon resonant absorption of a single photon, the tag is detached from the complex and hence, the depletion of these complexes is measured as less tagged complexes will be detected at that photon energy. The clear advantage of this technique is the nature of the single photon absorption which happens in a linear regime and allows us to record the spectrum of cold species. Indeed, the cryogenic environment and non-heating of the ions help to narrow the resulting spectra because of less molecular dynamics and side effects such as dissociation or isomerization are prevented.

2.3.3 Light Sources

Studying the photophysics of PAHs in laboratory astrophysics with the above described spectroscopic techniques requires the production of light of various wavelengths. Even though a key task is to investigate the interaction of PAHs with UV light, other ranges of the electromagnetic spectrum are of interest to obtain spectroscopic fingerprints. Here I would like to introduce the light sources which were used

to carry out this PhD work.

2.3.3.1 Tabletop Light Sources

Multiple photon absorption schemes can be used to dissociate the PAHs. The PIRENEA setup is coupled to three different light sources, which are briefly presented in the following.

A Xe arc lamp can be used to build internal energy inside the PAH ions and study their dissociation. An elliptical mirror focuses the Xe light inside the ion trap. Xe light consists of a broad continuum between 260 nm and 1.6 μm, similar to the light produced by the sun. Long-pass color filters can be used to select a particular range of wavelength.

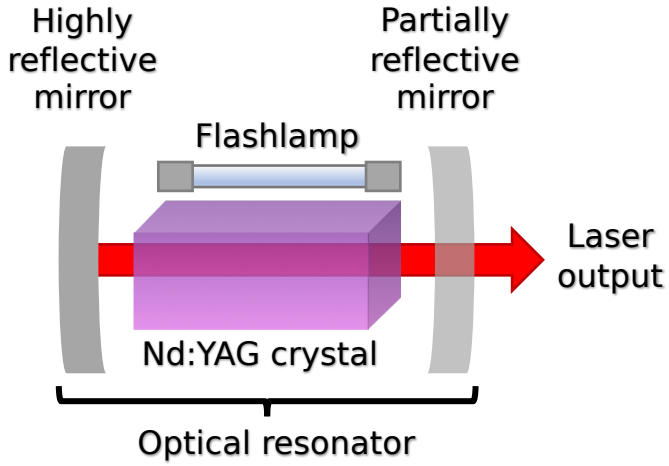

Figure 2.11: Schematic of the working principle of a Nd:YAG laser.

Nd:YAG lasers are used to laser ablate and ionize PAHs from the solid sample pellet but also in MPD experiments. As depicted in Figure 2.11, Nd:YAG lasers are optically pumped by a flashlamp or a pump diode and emit light with a wavelength of 1064 nm. The high-intensity pulses of the Nd:YAG can be efficiently frequency doubled to generate laser light at 532 nm, or higher harmonics at 355, 266, and even 213 nm. Since PAH cations have typical absorption bands in this energy range, the fourth harmonic at 266 nm is employed for laser desorption and ionization of PAHs

from the solid sample target. The typical output energy is about 4 mJ with a pulse duration of $5 - 7$ ns at this wavelength.

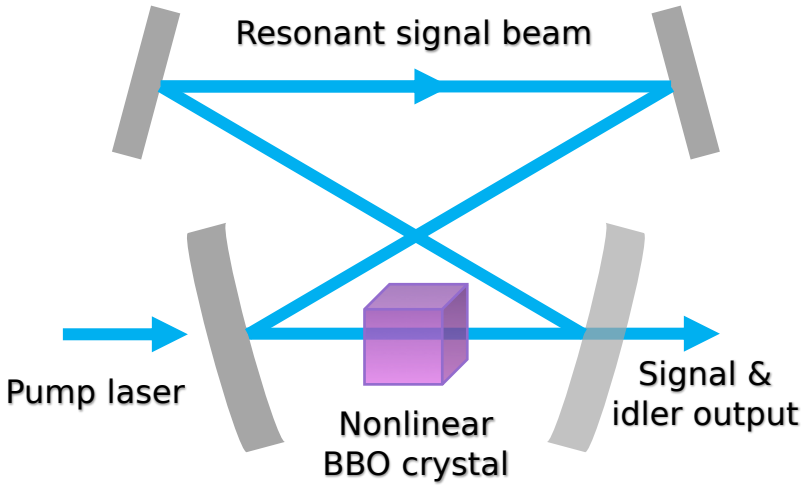

Figure 2.12: Schematic of the working principle of an OPO laser.

An optical parametric oscillator (OPO) laser relies on the nonlinear response of, for example, a barium borate (BBO) crystal when being pumped with a pump laser, e.g. a Nd:YAG laser at its third harmonic, 355 nm, and is schematically shown in Figure 2.12. Upon entering the nonlinear BBO crystal, the 355 nm photon splits into a pair of less energetic photons, being referred to as the signal and the idler output. The BBO has different indices of refraction for different polarizations of light. One index varies with respect to the incident light on the crystal angle. When tuning this angle, a signal and idler pair with a particular energy distribution can be produced. This process is called phase matching and an output of 210 nm to 2 μm with a pulse duration of 5 ns can be generated.

2.3.3.2 Synchrotron SOLEIL

The synchrotron facility located in St. Aubin, France, is called ***S**ource **O**ptimisée de **L**umière d'**É**nergie **I**ntermédiaire du **L**URE*, short SOLEIL, which translates to LURE Optimized Intermediary Energy Light Source, where LURE stands for ***L**aboratoire pour l'**U**tilisation du **R**ayonnement **É**lectromagnétique* meaning Laboratory for the

Use of Electromagnetic Radiation. In order to produce synchrotron radiation in SOLEIL, seven steps have to be followed which are schematically depicted in Figure 2.13.

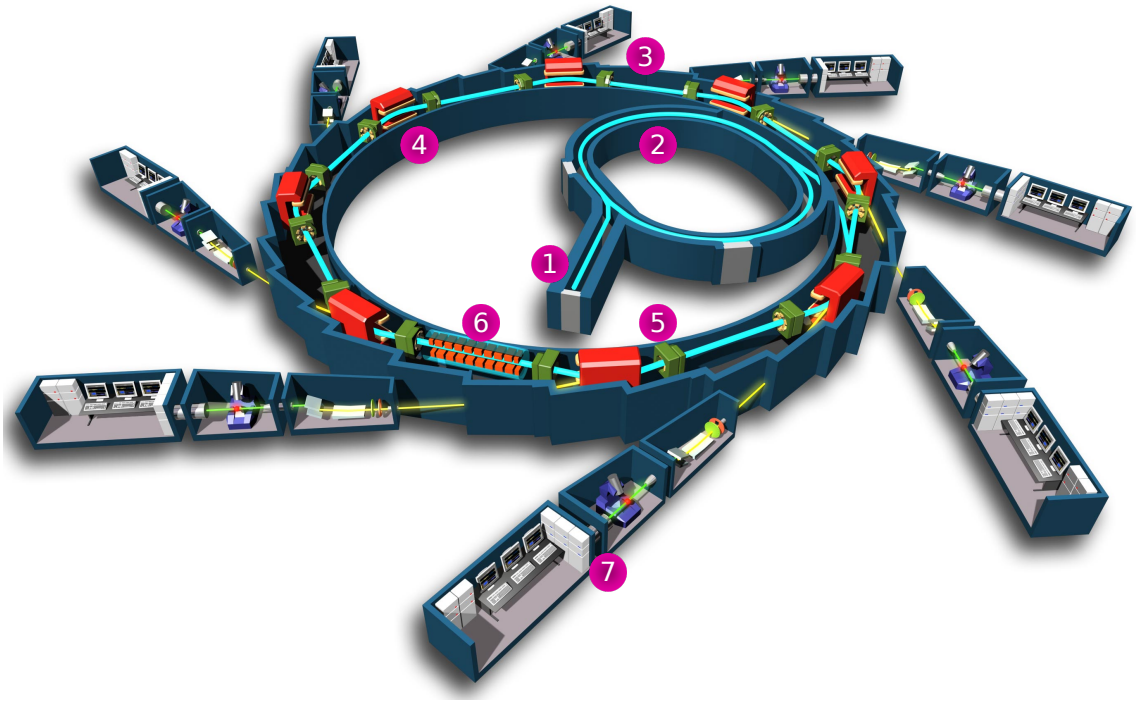

Figure 2.13: Schematic of the synchrotron SOLEIL. Copyright © EPSIM 3D/JF Santarelli, Synchrotron SOLEIL.

An electron gun emits electrons which are accelerated in a linear particle accelerator (linac) using oscillating electric potentials along a 16 m long linear beamline (1). The electrons reach an energy of 100 MeV in the linac and are subsequently inserted into a second but circular accelerator, called the booster (2). Here the electrons are accelerated to an energy of 2.75 GeV which is the operating energy value of the SOLEIL synchrotron. At this level, the electrons are injected into the storage ring (3) with a circumference of 354 m in which they are guided by bending magnets (4) and circulate for several hours. During the bending process, a part of the energy of the electrons is emitted in the form of light, the so-called synchrotron radiaton. In order to compensate for the radiated energy and to keep the electrons on a constant kinetic energy, several radiofrequency cavities (5) are installed along the storage ring. Wigglers and undulators (6) control the trajectory of the electrons. These consist of a periodic

arrangement of magnets with alternating orientation. While traveling through the periodic structure of dipole magnets, the electrons are forced on an oscillating path along their initial direction and, as accelerated charges, emit dipole radiation whose wavelength depends on the periodicity of the magnets in the wiggler. Due to relativistic effects, the synchrotron radiation is emitted in a cone along the velocity vector of the electrons. The radiation is diverted from the pathway of the electrons and collected and shaped by optic systems which are coupled to the storage ring and part of the beamlines (7), which are arranged around the storage ring in according orientation. The usual beamline consists of an optics room, an experimental area, and a control room and is specialized to perform experiments with a specific kind of light.

2.3.3.3 Free Electron Laser FELIX

The concept of synchrotron radiation is also employed when building free electron lasers, short FEL. Increasing demands on, for example, intensity and coherence of the radiation necessitate electron beams with equally enhanced specifications with respect to energetic, temporal and angular distribution. Free-electron lasers generate radiation in an undulator but solely rely on linear accelerators. Moreover, the undulators are usually either much longer (X-ray) or placed in an optical resonator (IR) and operated in different regimes which allow for the generation of radiation that is more intense and (partly) coherent.

Similarly to inside the storage ring of SOLEIL, the electrons are forced on a sinusoidal path inside the undulator and emit radiation which travels along the electron path. The resonator stores the light emitted by subsequent electron bunches, hence increasing the intracavity light intensity. As an oscillating electromagnetic field, the light exerts a force on the electrons that accelerates or decelerates the electrons depending on their phase relative to the field. This force causes the electrons to gradually arrange in packets, so-called microbunches, which have a mutual distance of exactly the wavelength of the light. Consequently, as light emitters are already spaced accordingly, the emitted radiation is increasingly coherent, and constructive interference of the radiation emitted from different microbunches further increases the overall intensity. If no resonator is available, *i.e.*, for X-rays, the process can be driven further in undulators of several 100 m in a resonant process called self-amplified spontaneous emission (SASE). It is worth to mention that, since no discrete energy levels are in-

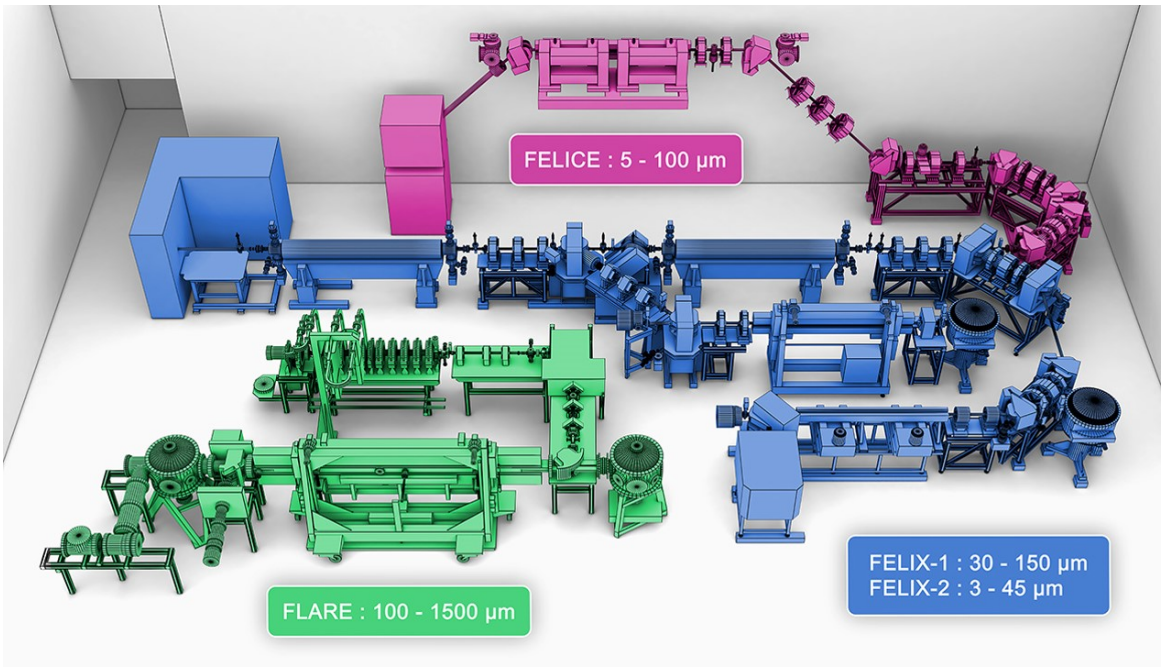

Figure 2.14: Overview of the laser hall and the three free electron lasers available at the FELIX facility at Radboud University in Nijmegen, The Netherlands. The relevant free electron laser, FELIX-2, is depicted in blue. Copyright © FELIX Laboratory, Radboud University. High resolution image kindly provided by J. Palotás.

volved, the wavelength of the radiation can be continuously tuned by variation of the electron energy and, in some cases, the gap between the undulator magnets.

A specific **FEL** for **I**nfrared e**X**periments is the FELIX laser [170], located at the Radboud University in Nijmegen, The Netherlands. The FELIX Laboratory is equipped with experiment specific FELs and their laser park is shown in Figure 2.14. The FELIX-2 laser with a spectral range of $2.7 - 45\,\mu$m ($3600 - 66\,\mathrm{cm}^{-1}$) has been employed to carry out the experiments presented in Chapter 5.

3 | Theoretical Methods

Outline

3.1 Theoretically Studying Astro-PAHs

The photophysics of astro-PAHs and their chemical evolution in the ISM were discussed in Chapter 1, justifying the requirement of theoretical studies on these systems for laboratory astrophysics applications as introduced in Section 1.3.

Compared to Hartree-Fock approximations, the density functional theory (DFT) method is less expensive in computational time and memory, enabling the calculation of characteristics of even large PAHs with basically any charge state, one of the limiting factors in the laboratory. It grants us access to the intrinsic properties of PAHs in the gas phase, in particular, geometric structures, thermodynamic quantities, and vibrational states, and is hence the quantum chemical approach of choice for this study.

During this PhD work, we used DFT as well as time-dependent DFT (TD-DFT) implemented in quantum chemical packages in order to perform harmonic vibrational analysis of vibrationally excited PAH cations and to access photoabsorption cross sections. I will thus briefly introduce the basics of DFT which supported our data analysis and interpretation. However, the focus of this PhD work lies on the laboratory approach of the investigation of astro-PAHs and a rigorous explanation of DFT is out of the scope of this thesis. A thorough description can be found, for instance, in Sholl and Steckel [171] or Koch and Holthausen [172].

3.2 Density Functional Theory

The electronic structure of molecules or ions, such as (ionic) PAHs, can be theoretically studied by quantum chemistry calculations performed at the DFT level. In the foundation of DFT, as of the Hartree and Hartree-Fock theories, lies the Born-Oppenheimer approximation. In this approximation, motions of electrons and atomic nuclei of a system are considered separately. We can make this approach because of their specific masses and inertia, as each proton and neutron of the atomic nucleus has a mass of approximately 1800 times the mass of an electron. With this *ansatz*, the Schrödinger equation will have two separate solutions, one for the electrons and one for the nuclei. This approach is called Born-Oppenheimer approximation [173].

In the following, we consider a system with M nuclei at positions $\mathbf{R}_1, \ldots, \mathbf{R}_M$ and N

electrons at positions $\mathbf{r}_1, \ldots, \mathbf{r}_N$.

3.2.1 Born-Oppenheimer Approximation

The time-dependent, non-relativistic Schrödinger equation of electrons in a potential is written in its complete form as

$$H\psi(\mathbf{r}, \mathbf{R}) = E\psi(\mathbf{r}, \mathbf{R}), \tag{3.1}$$

where ψ is called the wave function and denotes a set of solutions, or eigenstates, of the quantum system indicating the probability of finding a specific particle at a certain position. ψ is defined such that

$$|\psi|^2 = \psi^* \cdot \psi \tag{3.2}$$

is the probability density of the presence of the particle. H is the Hamiltonian which accounts for the total energy of the system, while E are the eigenvalues of the system. In molecules, the Hamiltonian can be formulated as

$$H = T_{\mathbf{r}} + T_{\mathbf{R}} + V_{\mathbf{r},\mathbf{r}} + V_{\mathbf{r},\mathbf{R}} + V_{\mathbf{R},\mathbf{R}}, \tag{3.3}$$

with the kinetic energies of the electrons and the nuclei, $T_{\mathbf{r}}$ and $T_{\mathbf{R}}$, respectively, electrostatic attractive interaction between nuclei and electrons, $V_{\mathbf{r},\mathbf{R}}$, and the repulsive potential caused by electron-electron, $V_{\mathbf{r},\mathbf{r}}$, and nucleus-nucleus, $V_{\mathbf{R},\mathbf{R}}$, interaction. If we describe the wave function as a set of k solutions with

$$\psi(\mathbf{r}, \mathbf{R}) = \sum_k \chi_k(\mathbf{R})\varphi_k(\mathbf{r}, \mathbf{R}), \tag{3.4}$$

where χ represents the weighting coefficients and φ the atomic orbitals, the electronic Schrödinger equation with $\mathbf{R}$ as its parameters can be reformulated as

$$(T_{\mathbf{r}} + V_{\mathbf{R},\mathbf{R}} + V_{\mathbf{r},\mathbf{r}}V_{\mathbf{r},\mathbf{R}})\varphi(\mathbf{r}, \mathbf{R}) = \varepsilon(\mathbf{R})\varphi(\mathbf{r}, \mathbf{R}), \tag{3.5}$$

from which we obtain the electronic eigenvalues and eigenfunctions, $\varepsilon_k(\mathbf{R})$ and $\varphi_k(\mathbf{r}, \mathbf{R})$,

respectively. Applying the Hamiltonian to this set of k solutions yields

$$H\psi(\mathbf{r},\mathbf{R}) = H\sum_k \chi_k(\mathbf{R})\varphi_k(\mathbf{r},\mathbf{R}) \tag{3.6}$$

$$= \sum_k (T_\mathbf{R} + \varepsilon_k(\mathbf{R}))\chi_k(\mathbf{R})\varphi_k(\mathbf{r},\mathbf{R}) \tag{3.7}$$

$$= E\sum_k \chi_k(\mathbf{R})\varphi_k(\mathbf{r},\mathbf{R}). \tag{3.8}$$

We can multiply from the left by $\varphi_j^*(\mathbf{r},\mathbf{R})$ and integrate over the electronic degrees of freedom. The Born-Oppenheimer approximation then lies in neglecting the term

$$\int d\mathbf{r}\varphi_j^*(\mathbf{r},\mathbf{R})T_\mathbf{R}\varphi_k(\mathbf{r},\mathbf{R}), \tag{3.9}$$

which leads us to the nuclear Schrödinger equation as

$$(T_\mathbf{R} + \varepsilon_k(\mathbf{R}))\chi(\mathbf{R}) = E\chi(\mathbf{R}). \tag{3.10}$$

From this equation we see that not the explicit electronic eigenfunctions, $\varphi(\mathbf{r},\mathbf{R})$, but only the electronic eigenvalues, $\varepsilon_k(\mathbf{R})$, are required to determine the energy of the system.

3.2.2 Electron Density

The electronic wave function solving the electronic Schrödinger equation (see Equation (3.5)) depends on $3N$ positional coordinates and N spin functions, making the determination of a ground state of all wave functions a multibody problem. Multibody problems are only analytically solvable for a few special cases, such as the hydrogen atom. Additionally, the numerical computation of the wave functions would be exceedingly expensive. To determine the electronic structure of a system, DFT relies on the probability to find any electron in a specific position. The density of the electrons, $\rho(\mathbf{r})$, is closely related to this probability and can be written as

$$\rho(\mathbf{r}) = N \cdot \int d^3r_2 \int d^3r_3 \ldots \int d^3r_N \left|\psi\left(\mathbf{r},\mathbf{r}_2,\mathbf{r}_3,\ldots,\mathbf{r}_N\right)\right|^2. \tag{3.11}$$

Assuming a simple form of ψ and using the variational principle to determine the compatible wave function

$$\delta \langle \psi | H | \psi \rangle = 0, \tag{3.12}$$

yields the lowest possible energy. In the simplest approximation, the Hartree theory, we can choose an *ansatz* for ψ which considers to be the product of one-particle wave functions, such that

$$\psi(\mathbf{r}, \mathbf{r}_2, \mathbf{r}_3, \ldots, \mathbf{r}_N) = \varphi_1(\mathbf{r}_1)\varphi_2(\mathbf{r}_2)\varphi_3(\mathbf{r}_3)\cdots\varphi_N(\mathbf{r}_N). \tag{3.13}$$

In the Hartree-Fock theory, however, the wave functions are considered to be an antisymmetrized product of the one-particle wave functions, called Slater determinant [174]. The *ansatz*,

$$\psi(\mathbf{r}, \mathbf{r}_2, \mathbf{r}_3, \ldots, \mathbf{r}_N) = \det\left(\varphi_1(\mathbf{r}_1)\varphi_2(\mathbf{r}_2)\varphi_3(\mathbf{r}_3)\cdots\varphi_N(\mathbf{r}_N)\right). \tag{3.14}$$

and the variational principle lead to

$$\rho(\mathbf{r}, \mathbf{R}) = \sum_k \varphi_k^*(\mathbf{r}, \mathbf{R})\varphi_k(\mathbf{r}, \mathbf{R}). \tag{3.15}$$

The energy of the system can be described with the Hartree-Fock exact exchange functional, $E_{\mathrm{X}}^{\mathrm{HF}}$.

Using the above described electron density, DFT is based on theorems made by Hohenberg and Kohn [175], which are

(i) The ground state energy of a system of interacting electrons is one unique functional of the electron density.

(ii) The electron density minimizing the functional over the entire range is linked to the complete solution of the Schrödinger equation.

Theorem (i) describes a unique connection between the ground state wave function and the ground state electron density, meaning that the ground state electron density is assigned with an energy eigenvalue, $E[\rho(\mathbf{r})]$. This relation allows us to reduce the eigenvalue equation from a $3N$-dimensional to a 3-dimensional problem.

Theorem (ii) gives the decisive properties of the functional. In practice, this is achieved using the variational principle. The electron density will be iteratively varied until the approximated functional describing the ground state energy will be minimal. The electron density obtained in this way will then be the relevant ground state density.

3.2.3 Exchange-Correlation Functional

Kohn and Sham [176] suggested that the above introduced functional can be written as an expression of the one-electron wave functions, $\psi(\mathbf{r})$, as

$$E[\rho(\mathbf{r})] = \underbrace{T_{\mathbf{r}} + V(\mathbf{r},\mathbf{R}) + V(\mathbf{R},\mathbf{R}) + E_{\text{Hartree}}[\rho(\mathbf{r})]}_{E_{\text{known}}[\rho(\mathbf{r})]} + E_{\text{XC}}[\rho(\mathbf{r})]. \tag{3.16}$$

Here, the terms included in $E_{\text{known}}[\rho(\mathbf{r})]$ are the ones representing the kinetic energy of the non-interacting electrons, the Coulomb interaction of the electrons with the positive nuclei, and the Coulomb term of the interaction in pairs between two electrons and two nuclei. The interesting term is $E_{\text{XC}}[\rho(\mathbf{r})]$ which is the exchange-correlation functional taking into account all other quantum effects, electron correlations and exchange energy. Plugging this relation into the electronic Schrödinger equation (see Equation (3.5)) yields the Kohn-Sham equation,

$$\left(T_{\mathbf{r}} + V(\mathbf{r},\mathbf{R}) + E_{\text{Hartree}}[\rho(\mathbf{r})] + E_{\text{XC}}[\rho(\mathbf{r})] - \varepsilon'\right)\varphi'_k(\mathbf{r},\mathbf{R}) = 0, \tag{3.17}$$

with an auxiliary set of eigenfunctions, $\varphi'_k(\mathbf{r},\mathbf{R})$, which produces the same total energy and identical electron density as the 'real' set of electronic eigenfunctions, $\varphi_k(\mathbf{r},\mathbf{R})$. The eigenfunctions, $\varphi'_k(\mathbf{r},\mathbf{R})$, are also called Kohn-Sham-eigenfunctions.

If we solve this equation, we get an exact expression for the electron density and the system can be described without approximations. However, the challenging point of DFT is the determination of the unknown exchange-correlation energy, $E_{\text{XC}}[\rho(\mathbf{r})]$, and different approaches exist. The variety of exchange-correlation functionals, $E_{\text{XC}}[\rho(\mathbf{r})]$, used in DFT is large. During this work, we utilized three different functionals to carry out electronic structure and harmonic IR spectra calculations.

The local density approximation (LDA) functional consists in the assumption that the exchange and correlation energies of an infinitesimal volume of the system can be approximated to those of an homogeneous electron gas with constant density, which is equal to the local one in the variable system. Integration over these contributions yields the functional.

The frequently used BLYP functional combining the generalized gradient approximations, the Becke [177] exchange functional, $E_{\mathrm{X}}^{\mathrm{GGA}}$, with the correlation functional, $E_{\mathrm{C}}^{\mathrm{GGA}}$, by Lee *et al.* [178], introduces a dependence not only on the local electron density of the system but also its derivatives.

The popular B3LYP functional, $E_{\mathrm{XC}}^{\mathrm{B3LYP}}$, [179, 180] is a hybrid functional as it combines the above described exchange-correlation functionals with the Hartree-Fock exact exchange functional, $E_{\mathrm{X}}^{\mathrm{HF}}$. In this specific case it is a mixture with the local spin-density approximation exchange, $E_{\mathrm{X}}^{\mathrm{LDA}}$, and correlation, $E_{\mathrm{C}}^{\mathrm{LDA}}$, [181], given by the relation

$$E_{\mathrm{XC}}^{\mathrm{B3LYP}} = E_{\mathrm{X}}^{\mathrm{LDA}} + a_0 \left(E_{\mathrm{X}}^{\mathrm{HF}} - E_{\mathrm{X}}^{\mathrm{LDA}}\right) + a_{\mathrm{X}} \left(E_{\mathrm{X}}^{\mathrm{GGA}} - E_{\mathrm{X}}^{\mathrm{LDA}}\right) + E_{\mathrm{C}}^{\mathrm{LDA}} + a_{\mathrm{c}} \left(E_{\mathrm{C}}^{\mathrm{GGA}} - E_{\mathrm{C}}^{\mathrm{LDA}}\right), \tag{3.18}$$

with the weighting coefficients $a_0 = 0.20, a_{\mathrm{X}} = 0.72$, and $a_{\mathrm{C}} = 0.81$ as proposed by Becke [182, 183].

3.2.4 Basis Sets

In DFT but also, for example, in Hartree-Fock methods, basis set functions are used to represent the electronic wave functions. The quantitative description of the wave functions requires a conversion to numerically solvable ones to implement them in computer codes. In the concept of basis sets, the wave functions are expressed as a linear combination of the functions of the basis set.

One of the oldest kind of basis set functions used in molecular quantum chemistry are atomic orbitals (LCAOs), but also basis sets with plane waves, mostly used for periodic systems as, for instance in Quantum Espresso [184], or wavelets for the BigDFT [185] code are employed. During this work, discrete grids in the quantum chemical package Octopus [186, 187] and Gaussian functions, implemented in Gaussian [188] but also

in NWChem [189], Orca [190], and the Turbomole [191] codes, were utilized as basis sets.

In the case of Gaussian basis sets, one benefits from the fact that a Gaussian multiplied by a Gaussian is still a Gaussian, simplifying a lot of calculations. A draw back using Gaussians is their difficulty to reproduce cusps in some eigenfunctions. The discrete grid approach following short-scale variations in the wave functions of core electrons, however, requires either an extremely dense grid, which would make the calculations computationally heavy, or a variable spacing, which is very complicated to perform. In the quantum chemical package OCTOPUS, this problem is bypassed by the assumption that core electrons do not significantly participate in the chemistry and photophysics of the molecule, so that pseudopotentials mimicking the core electrons can be used.

In principle, the functions of basis sets are infinite. However, to make calculations tractable, the basis set has to be cut into a subset of the infinite basis set, causing truncation errors due to the now finite basis set. For some constellations of basis sets and applications, these truncation errors are systematic and correction scaling factors, which are determined empirically, can be applied. For instance, when performing harmonic vibrational analysis using DFT and employing a Gaussian basis set, the determination and application of an appropriate scaling factor is indispensable.

3.2.5 Potential Energy Surface

Illustrated as a potential energy surface (PES), the energy of a system can be described in dependence of the positions of the atoms. In order to optimize the geometry of a molecule (or a molecular ion), a minimum of the PES has to be found. This can be achieved by full diagonalization of the Hessian matrix of the system and thus harmonic frequency calculations, resulting in the theoretical IR spectra presented in Chapter 5, to characterize the obtained geometry as a minimum or a first order saddle point with zero-point vibrational energies (ZPEs).

The Born-Oppenheimer approximation [173] introduced in Section 3.2.1 leading to the two separated Schrödinger equations for nuclei and electrons is only a good approach as long as the PES, or electronic hypersurfaces, for the involved electronic states are far enough from each other. An example of a random potential energy surface, $\varepsilon_k(\mathbf{R})$, is depicted in Figure 3.1.

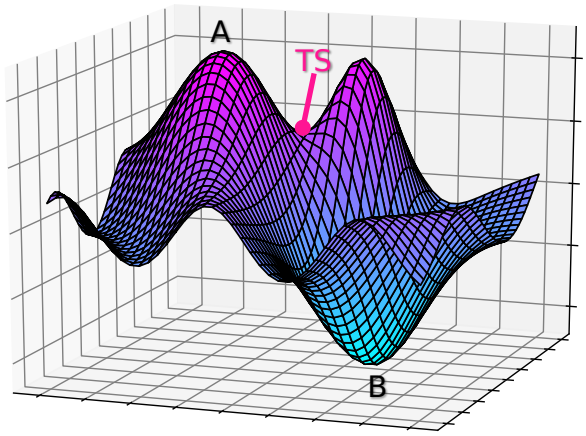

Figure 3.1: An example of a potential energy surface, $\varepsilon_k(\mathbf{R})$, with a second order saddle point at position A, a minimum at position B, and a transition state TS.

3.2.6 Counting States

Estimating quantities in an internal thermodynamical equilibrium in a microcanoncial ensemble, for example in unimolecular dissociation studies, the knowledge of the density of states, $\rho(E)$, is required. If the degrees of freedom and therefore the states are decoupled, we can obtain $\rho(E)$ by explicitly enumerating them up to a given energy. Taking advantage of the decoupling, one degree of freedom can be singled out together with its respective density of states, as

$$\rho(E) = \int dE' \rho^{(1)}(E') \rho^*(E - E'). \tag{3.19}$$

With this relation, we can build iteratively the density of states following an algorithm implemented in the model by Mulas *et al.* [192, 193] which is based on the work of Beyer and Swinehart [194] and Stein and Rabinovitch [195]. As an example, the density of states of the coronene and the dicoronylene cations are depicted in Figure 3.2.

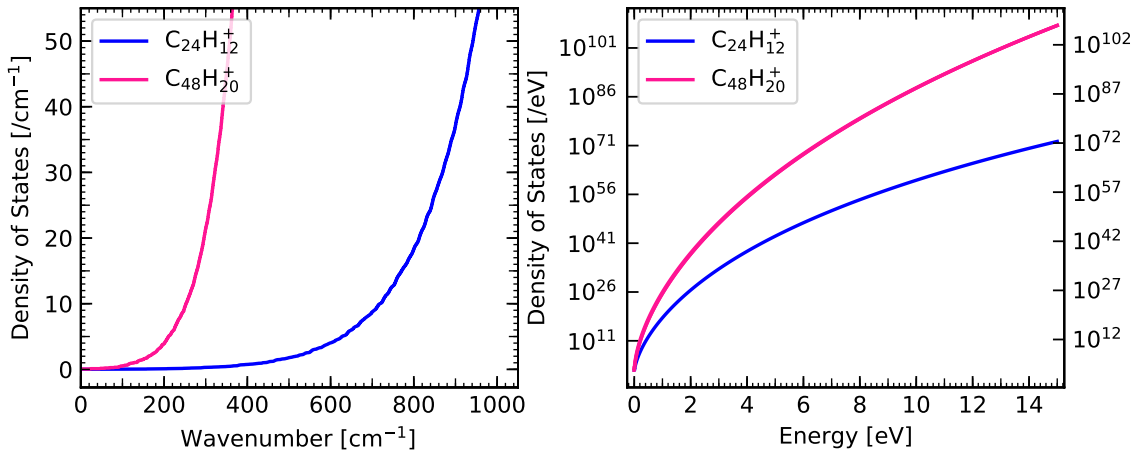

Figure 3.2: Comparison between the density of states of cationic coronene, $C_{24}H_{12}^+$, and dicoronylene, $C_{48}H_{20}^+$, computed by the model based on Mulas *et al.* [192, 193].

3.3 Time-Dependent Density Functional Theory

As a ground state theory, static DFT is not suited to predict energies for excited states. With the theorem by Runge and Gross [196] which describes that the state of a given time-dependent system is uniquely determined by the charge density, a similar approach of non-interacting electrons can be made. It states that the electrons only evolve under the effect of a potential that is solely a function of the density. This approach results in the time-dependent Kohn-Sham equations

$$\frac{i\partial\varphi_k(\mathbf{r},t,\mathbf{R})}{\partial t} = \left(T_\mathbf{r} + V(\mathbf{r},\mathbf{R}) + E_{\text{Hartree}}[n] + E_{\text{XC}}[n]\right)\varphi_k(\mathbf{r},t,\mathbf{R}). \tag{3.20}$$

Exactly as in the case of static DFT, this theorem only states the existence and unicity of $E_{\text{XC}}[n]$, however, its form is not defined. Usually, the TD-DFT implementations make the assumption that $E_{\text{XC}}[n]$ is approximately local in time, meaning that it depends on the density at the same moment in time. This is called the adiabatic approximation of TD-DFT and enables us to use basically all exchange-correlation functionals which were initially developed for static DFT.

During this PhD work, TD-DFT was utilized to compute photoabsorption cross sections, $\sigma_{\text{abs, theo}}$, of the cationic PAH species studied and presented in Chapter 4.

4 Large PAH Cations under VUV Irradiation

Outline

4.1 Introduction

The relevance of molecular data describing and quantifying the interaction of isolated PAHs with ultraviolet (UV) light has been discussed in Chapter 1, but so far their relaxation processes have been poorly investigated. Especially data on larger PAHs is missing, but the photophysical reactions caused by UV photon absorption in a PAH play a key role in the physics and chemistry of the interstellar medium (ISM). After the absorption of a UV photon, an isolated PAH can undergo different relaxation processes: photoionization (contributing to the interstellar gas heating through photoelectric effect), photodissociation, and radiative cooling [164]. The latter includes infrared (IR) emission, which results in the aromatic infrared bands (AIBs) observed in many astronomical objects [35, 197]. The PAH population in the diffuse ISM [198], in circumstellar disks [53], and in reflection nebulae [54], is governed by these processes. Due to their photostability against UV irradiation, astro-PAHs are expected to be large molecules with ∼50 carbon atoms or more [54], dominating the AIB emission in bright PDRs [199] in their neutral, cationic or even dicationic stage [55, 200].

In this chapter, we refer to vacuum UV (VUV) photons because of the experimental constraint. The range of VUV light includes both FUV and EUV photons which have been discussed in Chapter 1. Table B.1 indicates all mentioned UV ranges and can be found in Appendix B.

The branching ratio between the two relaxation processes of photoionization and photodissociation of medium-sized PAH cations with number of carbon atoms, N_C, of 16 to 24 have previously been investigated using the DESIRS VUV beamline at the synchrotron SOLEIL [133]. Up to an energy of 13.6 eV which is crucial for H I regions, dissociation was observed to be the dominant channel for all examined PAH cations. As suggested by the study of the large hexa-peri-hexabenzocoronene (HBC) cation, $C_{42}H_{18}^+$, photoionization is expected to be the significant relaxation channel for larger PAHs [136]. We therefore extend the study to the photoprocessing of larger PAH cations to quantify the importance of photoionization as the molecular size of the PAH increases. The investigated PAH cations range in size from 30 to 48 carbon atoms and were studied over the $9.5 - 20.0$ eV VUV photon energy range. We report their branching ratio between photoionization and dissociation. In addition, we aimed to derive their photoionization yield which is an important parameter in the modeling

of the charge balance of PAHs [37], but also in the evaluation of their contribution to the photoelectric heating rate of the interstellar gas [7, 8]. This work was the basis of the publication Wenzel *et al.* [127].

4.2 Beamline DESIRS with LTQ Ion Trap

The photophysical properties of large PAH cations under VUV irradiation have been studied using the Thermo Scientific^{TM} LTQ XL^{TM} linear ion trap (LTQ ion trap) available at the DESIRS beamline at the synchrotron SOLEIL in St. Aubin, France. During the campaign with the general working title 'Photoprocessing of astro-PAHs' in September 2017, experiments have been carried out at the undulator-based DESIRS beamline available at the synchrotron SOLEIL. DESIRS is short for ***D****ichroïsme* ***E****t* ***S****pectroscopie par* ***I****nteraction avec le* ***R****ayonnement* ***S****ynchrotron* which translates to Dichroism and Spectroscopy through Interaction with Synchrotron Radiation and described in detail in reference [201]. The main characteristics of DESIRS are the wide tunability of photon energy in the vacuum ultraviolet (VUV), a range of $5 - 40\,\mathrm{eV}$, a high spectral purity and photon flux. In addition, the VUV light is fully polarizable. DESIRS consists of three branches, of which one is employed for ultra-high resolution absorption spectroscopy using a Fourier Transform VUV spectrometer and two monochromatized ones for photodynamics, electron or ion spectroscopy, and dichroism experiments. The VUV light is monochromatized by the use of a monochromator chamber which is, dependent on the photon energy range, filled with noble gases such as argon (Ar) or krypton (Kr) which have a photon cut-off above 16 and 14 eV, respectively. Experiments on PAHs and PAH clusters have been performed on the photoelectron photoion coincidence double imaging spectrometer (PEPICO) which is permanently coupled to one of the branches, for example by Bréchignac *et al.* [202], Rouillé *et al.* [203], and Joblin *et al.* [204]. The other monochromatized branch is open for users moving their own experimental setups to the DESIRS beamline but is usually coupled to a commercial linear ion trap which is schematically depicted in Figure 4.1. Dependent on the photon energy range, the synchrotron radiation is gas filtered to suppress the undulator higher harmonics. It enters a normal-incidence monochromator (NIM) which tunes the wavelength and is focused into the LTQ ion trap with a spot size of approximately $0.055\,\mathrm{cm}^2$. A beam shutter couples the light

into the commercial linear ion trap and can be opened and closed for set irradiation times, normally a few hundred ms.

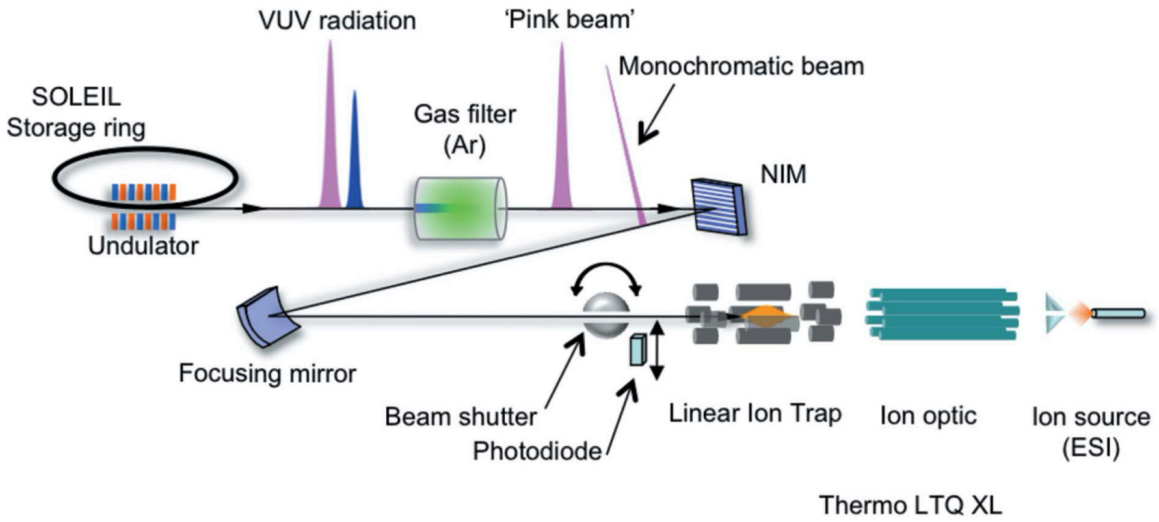

Figure 4.1: Schematic of the Thermo Scientific LTQ ion trap at the DESIRS beamline coupled to the synchrotron SOLEIL. Taken from Milosavljević *et al.* [205].

The Thermo Scientific^{TM} LTQ XL^{TM} linear ion trap (LTQ ion trap) is a commercial setup coupled to the DESIRS beamline at the synchrotron SOLEIL and described in detail by Milosavljević *et al.* [205]. As depicted in Figure 4.1, the LTQ ion trap consists of an ion source, typically an electrospray ionization (ESI) or an atmospheric pressure photoionization (APPI) source, ion optics (an octopole) guiding and selecting the ions of interest and the linear ion trap. The APPI source ensures a soft production of cations from a solution containing neutrals which are subsequently filtered by the octopole, ejecting fragments, contaminants, and most of the isotopes from the ion cloud so that only the species of interest is trapped at room temperature. Helium is led into the trap up to a pressure of $p \approx 10^{-3}$ mbar which thermalizes the ions by ion-He collisions. Once the beam shutter opens for the set irradiation time, the ions interact with synchrotron photons and their photoproducts are mass-analyzed and recorded.

4.3 Experimental Methods and Data Analysis

Four large PAH cations with number of carbon atoms, N_C, ranging from 30 to 48 were investigated in this study, namely (a) benzobisanthene, $C_{30}H_{14}^+$, (b) ovalene, $C_{32}H_{14}^+$, (c) dibenzophenanthropentaphene (DBPP), $C_{36}H_{18}^+$, and (d) dicoronylene, $C_{48}H_{20}^+$. Samples (a) and (c) originated from the PAH Research Institute in Greifenberg (Dr. Werner Schmidt) and sample (b) was purchased from Janssen Chimica (Belgium). Sample (d) was synthesized following the procedure reported by Cataldo *et al.* [206] (see Appendix D). Their molecular structures are depicted in Figure 4.2.

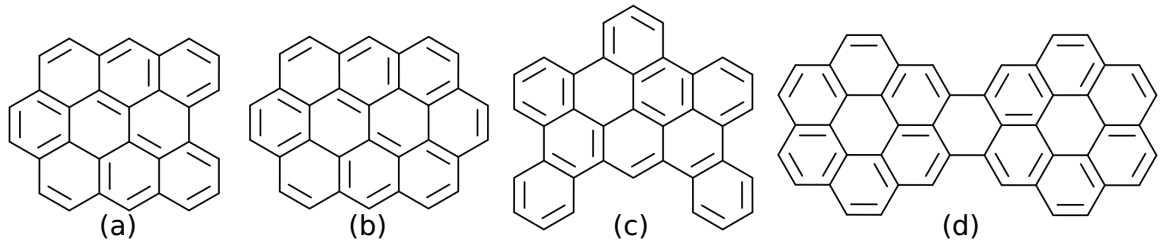

Figure 4.2: Molecular structures of the studied PAH cations, namely (a) benzobisanthene, $C_{30}H_{14}^+$, (b) ovalene, $C_{32}H_{14}^+$, (c) DBPP, $C_{36}H_{18}^+$, and (d) dicoronylene, $C_{48}H_{20}^+$.

4.3.1 Acquisition of Mass Spectra

Neutral PAH solutions were drawn back up into a syringe which is mounted onto the Thermo Scientific™ LTQ XL™ linear ion trap (LTQ ion trap). Emptying the syringe is performed at a set syringe velocity which was kept constant for each experiment, usually to values of about $4 - 10\,\frac{\mu l}{\mathrm{min}}$. The neutral PAH solutions were fed into the atmospheric pressure photoionization (APPI) source in which the PAHs were ionized by UV photon absorption from a Kr discharge lamp. This procedure ensures the soft creation of cations without fragmentation. The cations were guided through ion optics into the linear LTQ ion trap in which a constant He pressure of $p \approx 10^{-3}$ mbar is held. The ions were cooled by the collisions with He atoms and the PAH cation of interest, the so-called parent ion, was isolated through mass selection and ejection of other species from the trap. The VUV synchrotron radiation was tuned from $9.5 - 20.0$ eV in steps of 0.1, 0.2, 0.3 or 0.5 eV depending on the photon energy range. High harmonics of the VUV synchrotron radiation with fundamental photon energies lower than 16 eV were filtered out by a monochromator chamber filled with Ar gas

at a pressure of 0.23 mbar. Above 16 eV no such gas filtering is necessary. The photon rate was in the range of $0.8 - 2.8 \cdot 10^{12}$ photons s^{-1} and was tuned by changing (i) the irradiation time from 0.8 to 0.2 s for the lower and higher photon energy ranges, respectively, and (ii) the monochromator exit slit width from 200 μm at low energies to 70 μm at high energies, in order to limit possible two photon consecutive absorption processes. For the largest investigated PAH cation, dicoronylene, values of 400 and 100 μm at low and high energies, respectively, were used to improve the signal-to-noise ratio. The photon flux was assumed to be linearly proportional to both the irradiation time and the monochromator exit slit width. The probability of two photon absorption processes could be estimated based on the formation of triply charged parent ions, yielding only very small relative intensities below 2 % of the total number of photoproducts.

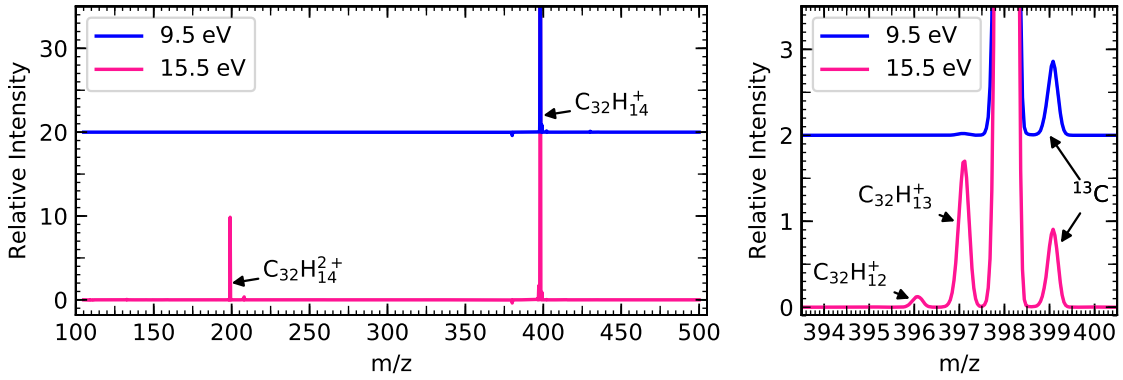

Figure 4.3: Mass spectra of the ovalene parent cation, m/z = 398, at two different photon energies. At 9.5 eV, none of the photoionization or photodissociation channels are opened, whereas at 16.5 eV the doubly ionized parent ion at m/z = 398 is observed as well as the photofragments where ovalene has lost one or two hydrogen atoms, m/z = 397 and 396, respectively.

Depending on the acquisition time, a few hundred, N, mass spectra, x, were recorded for each photon energy step. Averaging these mass spectra for each photon energy yielded one mean mass spectrum, $\bar{x}$, per photon energy with an absolute standard error of $\Delta\bar{x} = \frac{\sigma}{\sqrt{N}}$, where σ is the standard deviation as

$$\sigma = \sqrt{\frac{1}{N-1}\sum_{i=1}^{N}(x_i - \bar{x})^2}. \tag{4.1}$$

The error bars, Δf, in Figures 4.5 and 4.6 result from error propagation for a function, $f \rightarrow f(x_1, x_2, ..., x_N)$, according to

$$\Delta f = \sqrt{\sum_{i=1}^{N} \left(\frac{\partial f}{\partial x_i} \Delta x_i \right)^2}. \tag{4.2}$$

Following the same procedure, we also recorded blank mass spectra at each photon energy by selecting an isolated mass close to but different enough from each parent ion. This allowed us to perform background subtraction which eliminates contamination peaks from the mass spectra. As an example, the background subtracted mass spectra for ovalene with $m/z = 398$ recorded at photon energies of 9.5 eV and 15.5 eV are depicted in Figure 4.3. The parent ion, $C_{32}H_{14}^+$, is well isolated, the $^{13}CC_{31}H_{14}^+$ isotopic parent ion has a residual of less than 1 % remaining in the ion trap. By increasing the photon energy, three main secondary ions can be observed. In the ovalene example shown in Figure 4.3, these are namely the –H and –2H/H_2 fragments, $C_{32}H_{13}^+$ and $C_{32}H_{12}^+$, respectively, as well as the doubly ionized parent ion, the dication, $C_{32}H_{14}^{2+}$.

4.3.2 Photon Flux Calibration

The photon rate and therefore the photon flux at the synchrotron SOLEIL facility changes with photon energy. Hence, it is important to carefully record the photon flux in order to correct the peak intensities of the photoproducts, *i.e.*, the secondary ions, S. The photon rate, φ, depends on

$$\varphi = \frac{\lambda I}{hcR} = \frac{I}{ER}, \tag{4.3}$$

where h is the Planck constant, c is the speed of light, I is the measured current, R is the photodiode response, and λ and E are the photon wavelength and energy, respectively. The left panel of Figure 4.4 depicts the photodiode response in A/W and the current in A from which the photon rate, φ, in photons s^{-1} as a function of photon energy in eV can be determined following Equation (4.3).

The result is presented in the right panel of Figure 4.4. The signal drop emerging shortly before reaching 16 eV is caused by the absorption of the Ar gas which filters higher harmonics of the synchrotron radiation. The signal above 16 eV was recorded

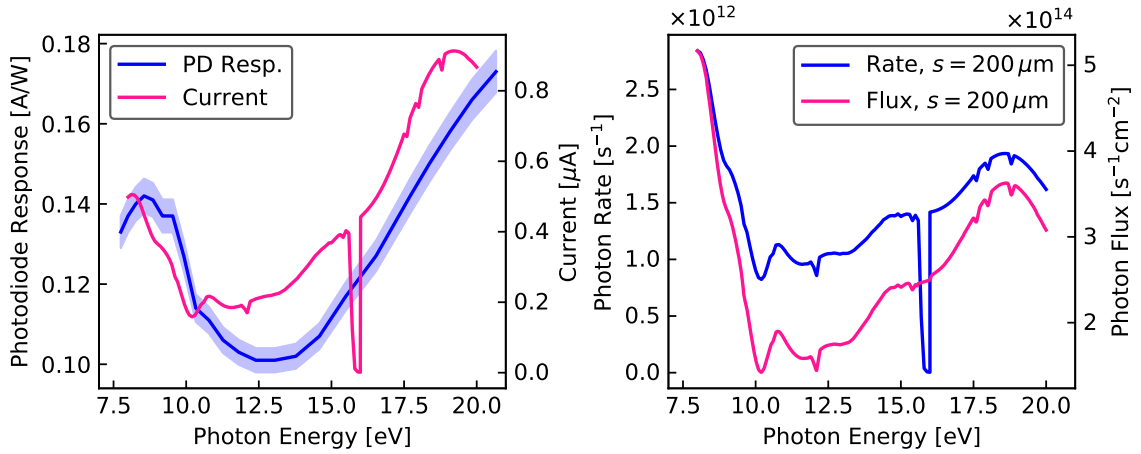

Figure 4.4: Left panel: The measured photodiode response (PD Resp.) and current. Right panel: The photon rate, φ, determined following Equation (4.3) and the estimated photon flux, ϕ, both for a monochromator exit slit width of 200 μm.

after evacuating the monochromator chamber and the data points where the signal had dropped were masked. In a last step, the photon rate is divided by the spot size of the beam in the ion trap, which covers roughly a surface of 0.055 cm^2, but which is also photon energy dependent. The resulting photon flux, ϕ, in photons $\mathrm{s}^{-1}\mathrm{cm}^{-2}$ is reported in the right panel of Figure 4.4.

4.3.3 Detector Gain Efficiency

When processing the recorded mass spectra, we have to analyze the recorded photoproducts carefully. Due to detector characteristics, doubly ionized molecules are detected more efficiently than singly ionized molecules. Therefore, the peak intensities which can be derived from the mass spectra have to be scaled by the detector gain efficiency, ε, to retrieve values that scale with actual ion abundances. Thermo Scientific$^{\mathrm{TM}}$ provides $\varepsilon_+ = 0.29$ for parent ions and fragments, $\varepsilon_{2+} = 0.42$ for dications and a value of $\varepsilon_{3+} = 0.54$ for trications. There is some gain change with mass but this is a minor correction for the range of studied masses and is thus not taken into account. The total number of ions in the trap, P_0, in uncalibrated values, can then be calculated with

$$P_0 = \frac{P_t}{\varepsilon_+} + \frac{S_\mathrm{F}}{\varepsilon_+} + \frac{S_\mathrm{I}}{\varepsilon_{2+}}, \tag{4.4}$$

where $\frac{P_t}{\varepsilon_+}$ is the number of parent ions after irradiation time, t, and $\frac{S_\mathrm{F}}{\varepsilon_+}$ and $\frac{S_\mathrm{I}}{\varepsilon_{2+}}$ are the corrected peak intensities of fragments and dications, respectively. We will need this relation and the detector gain efficiencies in the following.

4.4 Results and Discussion

The following sections present and discuss the results of the photophysical investigation of the four large PAH cations, namely (a) benzobisanthene, $C_{30}H_{14}^+$, (b) ovalene, $C_{32}H_{14}^+$, (c) DBPP, $C_{36}H_{18}^+$, and (d) dicoronylene, $C_{48}H_{20}^+$, as depicted in Figure 4.2. We report action spectra and branching ratios of the ionization and fragmentation relaxation processes, and aim to derive experimental cross sections which are compared to theoretically calculated photoabsorption cross sections. Finally, we present photoionization yields of the four studied PAH cations.

4.4.1 Action Spectra

From the recorded mass spectra, peak intensities of parent ions and their photoproducts can be deduced. The secondary ions produced upon VUV irradiation consist of the dication with peak intensity S_I, and the photofragments with summed peak intensity S_F, including the H and $2H/H_2$ loss channels. Building the action spectra requires to derive normalized photoproduct intensities for S_I and S_F, which can be obtained by first dividing them by P_0 and then correcting for the variation of the photon flux, $\phi(\nu)$. Indeed, the latter evolved in energy due to spectral shape variations and changes made in the irradiation time, t, and monochromator exit slit width, s, so that the total photoproduct intensity remains smaller than *ca.* 12 % of P_t, as seen in the mass spectra. This led to

$$S_\mathrm{I,F}^\mathrm{norm}(\nu) = \frac{S_\mathrm{I,F}(\nu)}{\phi_\mathrm{norm}(\nu)\, t(\nu)\, s(\nu)}, \tag{4.5}$$

where $\phi_\mathrm{norm}(\nu)$ is normalized to be 1 at its maximum at 9.5 eV. Note that the obtained intensities are in arbitrary units (see Figure 4.5) and not in percentage of the total number of ions because of the scaling by the relative photon flux.

The resulting relative intensities for the photoionization (dication, denoted I) and

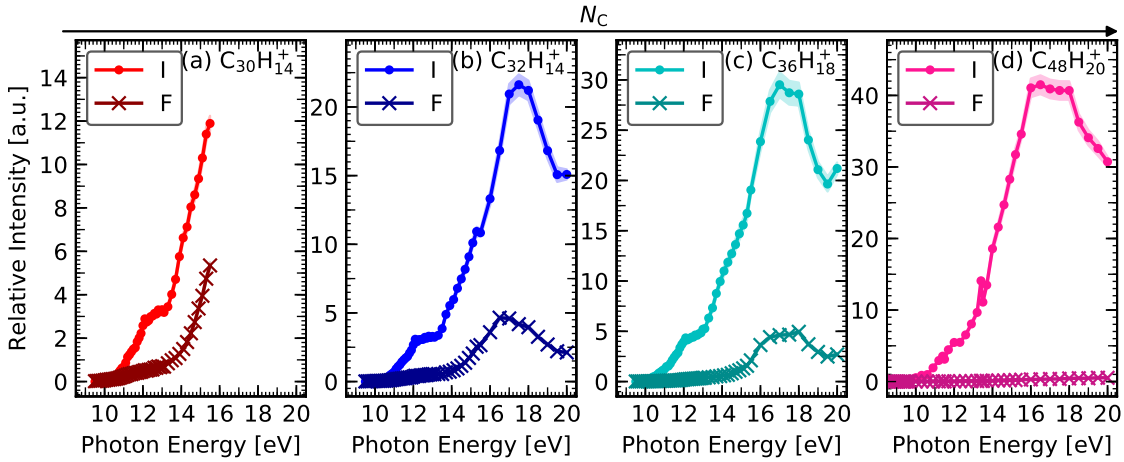

Figure 4.5: Relative intensities of the studied PAH cations as a function of photon energy, (a) benzobisanthene, (b) ovalene, (c) DBPP, and (d) dicoronylene after absorption of a single VUV photon.

Table 4.1: Theoretical adiabatic ionization potentials, IP^{2+}, compared to measured appearance energies, AE^{2+}, for doubly ionized PAH cations, $PAH^+ \rightarrow PAH^{2+}$. We also list here our recorded appearance energies for AE^{3+} as obtained from the ionization of $PAH^{2+} \rightarrow PAH^{3+}$.

Molecule	**Formula**	**IP^{2+} [eV]**	**AE^{2+} [eV]**	**AE^{3+} [eV]**
Benzobisanthene	$C_{30}H_{14}^+$	9.66[a]	10.2 ± 0.1	14.1 ± 0.2
Ovalene	$C_{32}H_{14}^+$	9.82[a]	10.0 ± 0.1	13.9 ± 0.2
DBPP	$C_{36}H_{18}^+$	9.94[b]	10.0 ± 0.1	13.9 ± 0.2
Dicoronylene	$C_{48}H_{20}^+$	8.84[a]	9.1 ± 0.2	–[c]

[a] Taken from Malloci *et al.* [79].
[b] Calculated specifically for this work according to Malloci *et al.* [74].
[c] Trication peak out of mass range.

photodissociation (fragments, denoted F) relaxation channels of the four studied PAH cations are shown in Figure 4.5. For these large PAHs, photoionization starts abruptly and at lower energies than photodissociation and is the dominating process at all photon energies. The photon energy at which photoionization appears, the appearance energy, AE^{2+}, can be deduced from the dication curves presented in Figure 4.5. The AE^{2+} which are required to form PAH dications from their parent monocations are listed in Table 4.1 and compared to the theoretically computed adiabatic ionization

potentials, IP^{2+}, which were extracted from the Theoretical Spectral Database of PAHs[6] [74, 79]. Considering the accuracy of 0.3 eV for the calculated values, both experimental and theoretical values are found to be consistent and the trend of a slow decrease of IP^{2+} with $N_C \geq 30$ carbon atoms reported by Malloci *et al.* [142] is confirmed. The dissociation channel, F, remains small, below 6, for all investigated PAH cations at all photon energies. A special case is the dicoronylene cation whose action spectrum is depicted in Figure 4.5 (d) and whose photodissociation remains below 1 over the whole photon energy range studied.

4.4.2 Competition between Ionization and Dissociation

Branching ratios can directly be obtained from the experimentally recorded mass spectra and apart from the detector gain efficiency, ε, for differently charged species, no scaling procedure is required. Figure 4.6 depicts the branching ratios for the three different photoproducts created from the parent ion, P^+, upon VUV photon absorption. The photoproducts are the dication, P^{2+}, and the photofragments when losing one or two hydrogen atoms, $P^+ - H$ and $P^+ - 2H/H_2$, respectively.

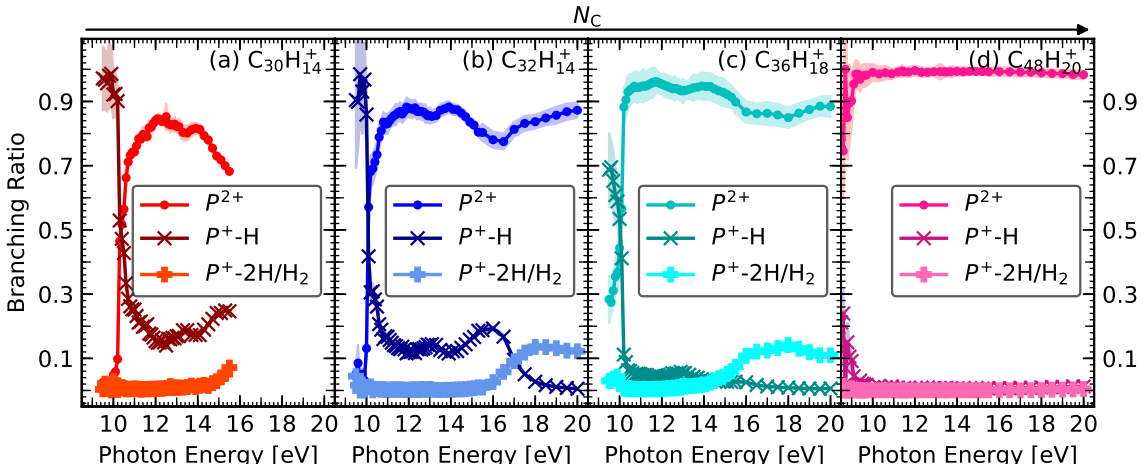

Figure 4.6: Branching ratios of the studied PAH cations as a function of photon energy, (a) benzobisanthene, $C_{30}H_{14}^+$, (b) ovalene, $C_{32}H_{14}^+$, (c) DBPP, $C_{36}H_{18}^+$, and (d) dicoronylene, $C_{48}H_{20}^+$, after absorption of a single VUV photon.

Figure 4.6 demonstrates how the branching ratio for photoionization increases with increasing number of carbon atoms, N_C, reaching a minimal value of 0.98 for the

[6] http://astrochemistry.oa-cagliari.inaf.it/database/

largest studied cation, dicoronylene. This is in line with the ionization branching ratio of about 0.97 at 20 eV which was derived by Zhen *et al.* [136] for the HBC cation, $C_{42}H_{18}^{+}$. However, our ionization branching ratio of 0.87 ± 0.02 for the ovalene cation differs from the finding of a value of 0.70 ± 0.10 at 20 eV of Zhen *et al.* [136], which can be interpreted as being caused by the low mass resolution achieved in their experiment which impacted both the isolation of the ^{12}C parent isotopomer before VUV irradiation and the quantification of the abundance of –H fragments in the photoproducts.

In contrast to ionization, the branching ratio for dissociation decreases with increasing N_C, *cf.* from panel (a) to (d) in Figure 4.6. This trend of large PAHs differs from the earlier study of medium-sized PAH cations for which a larger fraction of fragments was observed [126]. For all studied PAH cations the $2H/H_2$ loss channel opens at higher photon energies than the H loss channel. Only for the less compactly structured DBPP cation the $2H/H_2$ branching ratio reaches higher values than the one for H loss, making DBPP a possible candidate for the catalysis of H_2 formation.

4.4.3 Theoretical Photoabsorption Cross Sections

The emission of photoelectrons by PAHs plays a key role in the heating of the gas in astrophysical environments. An important parameter in astrophysical models is therefore the ionization yield that quantifies the electron emission rate upon absorption of VUV photons by PAHs. Obtaining the yield requires to divide experimentally obtained relaxation process cross sections by the photoabsorption cross section. For the latter we do not have experimental data which is why these were calculated by the use of time-dependent density functional theory (TD-DFT) with the real-time, real-space method of Yabana and Bertsch [186], as implemented in the Octopus computer code [187].

We followed very closely the method used and described in Malloci *et al.* [79], who already calculated the photoabsorption cross sections for (a) benzobisanthene, (b) ovalene, and (d) dicoronylene. Cross sections for (c) DBPP are missing in the database, but also the ones for the former molecules had to be recalculated, as we have to consider relatively high photon energies of up to 20 eV. We also took the chance to verify at these energies the convergence of the calculations with respect to the simulation

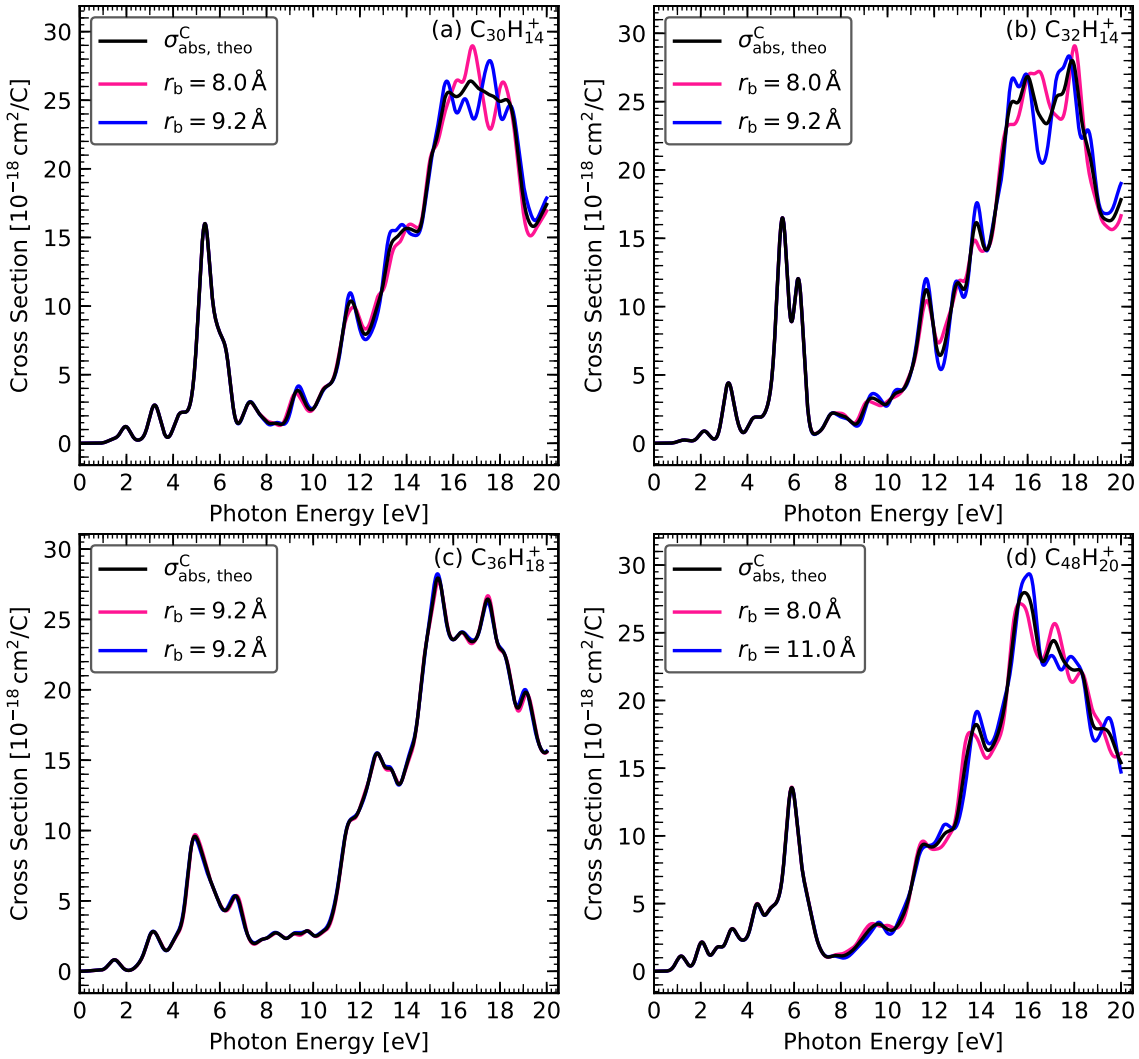

Figure 4.7: Theoretical photoabsorption cross sections, $\sigma^{C}_{abs,\,theo}$, as computed by TD-DFT for the (a) benzobisanthene, (b) ovalene, (c) DBPP, and (d) dicoronylene cations. The pink and blue curves were calculated with the so-called 'minimum' simulation box with a spherical radius of $r_b = 8.0$ Å and a spherical simulation box with a radius of (a) and (b) $r_b = 9.2$ Å or (d) $r_b = 11.0$ Å, respectively. For (c) DBPP, we found two stable geometries and therefore calculated $\sigma^{C}_{abs,\,theo}$ for both geometries with a spherical box shape with $r_b = 9.2$ Å. The black curves are the average between the two calculations.

box shape, size, and grid spacing, the real-space equivalent of more conventional basis-set convergence for e.g. Gaussian-based DFT. The calculated photoabsorption cross sections include the transitions to discrete bound electron states and transitions to

the continuum of unbound electrons, which are artificially turned into discrete ones by the use of the finite simulation box. In this case, more highly excited electronic states are expected to be distributed over a larger volume with a significant electron density at larger distances from the nuclei of the molecule. In order to represent these states properly, they will therefore need a larger simulation box. It is indeed known [207] and mentioned in the OCTOPUS documentation, that as a rule of thumb larger simulation boxes are needed to obtain converged values for the energies of higher lying electronic excited states. We therefore chose to consider substantially larger simulation box sizes, and denser grid spacings, to achieve convergence up to ∼20 eV, as required for this work. For our purposes, we found that a so-called "minimal" simulation box consisting of the union of spheres with a radius of $r_\mathrm{b} = 8$ Å centered on every atom of the molecule, or a sphere of similar total volume, and a grid spacing of 0.18 Å were needed to achieve convergence. Hence, two different converged spectra for each species were computed and averaged to smooth out the contribution of free electron states and retain discrete ones. Finally, we divided the obtained photoabsorption cross sections, $\sigma_{\mathrm{abs,\,theo}}$, of each PAH cation by its respective number of carbon atoms, N_C, yielding $\sigma^\mathrm{C}_{\mathrm{abs,\,theo}}$. The resulting $\sigma^\mathrm{C}_{\mathrm{abs,\,theo}}$ are presented in Figure 4.7.

4.4.4 Experimental Photoproduct Cross Sections

The absorption of a photon by a PAH leads to different relaxation channels. The photoabsorption cross section, σ_abs, can be decomposed into the sum of the cross sections for each relaxation channel as

$$\sigma_\mathrm{abs} = \sigma_\mathrm{I+F} + \sigma_\mathrm{rad}, \tag{4.6}$$

where $\sigma_\mathrm{I+F}$ is the cross section leading to the production of secondary products due to ionization or fragmentation and σ_rad is the cross section for the creation of a hot ion that will relax its internal energy by radiative cooling and/or collisions with the buffer gas, *i.e.*, He in our experiment. The latter processes cannot be traced in this experiment and only $\sigma_\mathrm{I+F}$ can be estimated as following.

When a parent ion, P, absorbs a photon with energy, $h\nu$, and produces a secondary

ion, S, the reaction pathway can be expressed as

$$P + h\nu \rightarrow S, \tag{4.7}$$

which means that the decay of parent ions, P, follows the same rate, k, as the production of secondary ions, S, yielding

$$\mathrm{d}P = -\mathrm{d}S = -kP\mathrm{d}t \tag{4.8}$$

with irradiation time, t. Considering the absorbed photons to be monochromatic, the rate, k, can be written as

$$k = \phi\sigma_{\mathrm{I+F}}, \tag{4.9}$$

where ϕ is the photon flux in photons $\mathrm{cm}^{-2}\mathrm{s}^{-1}$ and $\sigma_{\mathrm{I+F}}$ the cross section in cm^2. Plugging Equation (4.9) into Equation (4.8) and directly integrating over an irradiation time interval from 0 to t, we get

$$\sigma_{\mathrm{I+F}} = \frac{1}{\phi t}\ln\left(\frac{\varepsilon_+ P_0}{P_t}\right), \tag{4.10}$$

with the total number of ions, P_0, and measured parent ions, $\frac{P_t}{\varepsilon_+}$, after irradiation time, t. The relation for P_0 derived in Section 4.3.3 from Equation (4.4) can be inserted in Equation (4.10) and yield

$$\sigma_{\mathrm{I+F}} = \frac{\gamma}{\phi t}\ln\left(1 + \frac{S_{\mathrm{F}}}{P_t} + \frac{\varepsilon_+ S_{\mathrm{I}}}{\varepsilon_{2+} P_t}\right), \tag{4.11}$$

in which we also introduced a form factor, γ, which describes the overlap of the photon beam and the ion cloud inside the ion trap. In order to determine absolute cross sections, the photon flux, ϕ, and the form factor, γ, have to be well-known. This is not the case for the measurements we performed in September 2017, which is why we are introducing two approaches in order to determine absolute cross sections.

4.4.4.1 Approach 1 - Introduction of a Proportionality Factor

We consider having a rate of photon absorption events given by $\Gamma_{\mathrm{Dico}}\,\phi\,\sigma_{\mathrm{I+F}}\,P$, where Γ_{Dico} is the (non-energy dependent) proportionality factor relating the photon flux, ϕ,

to the actual photon flux arriving in the ion trap and $\sigma_{\mathrm{I+F}}$ the total absorption cross section. With $Y_{\mathrm{I+F}}$ being the total yield of ionization and fragmentation processes, we can write Equation (4.11) as

$$\sigma_{\mathrm{I+F}} = \frac{1}{\Gamma_{\mathrm{Dico}}\phi Y_{\mathrm{I+F}} t} \ln\left(1 + \frac{S_{\mathrm{F}}}{P_t} + \frac{\varepsilon_+ S_{\mathrm{I}}}{\varepsilon_{2+} P_t}\right). \tag{4.12}$$

If we now choose a specific case in which we can assume that $Y_{\mathrm{I+F}} \approx 1$, such as e.g. irradiating dicoronylene parent ions with 18 eV photons (*cf.* Figure 4.5 (d)), we can equate this experimentally measured value of $\sigma_{\mathrm{I+F}}$ to its theoretically calculated absolute value, and solve for Γ_{Dico}, so that

$$\Gamma_{\mathrm{Dico}} \approx \frac{1}{\sigma_{\mathrm{abs,\,theo}}\phi t} \ln\left(1 + \frac{S_{\mathrm{F}}}{P_t} + \frac{\varepsilon_+ S_{\mathrm{I}}}{\varepsilon_{2+} P_t}\right), \tag{4.13}$$

which then can be used as the fixed proportionality factor between the measured photon flux, ϕ, and the actual average photon flux for all photon energies and all parent ions. With Γ_{Dico}, we can use this equation for all parent ions at all photon energies to obtain

$$\sigma_{\mathrm{I+F}}(h\nu)\, Y_{\mathrm{I+F}}(h\nu) = \frac{1}{\Gamma_{\mathrm{Dico}}\phi t} \ln\left(1 + \frac{S_{\mathrm{F}}}{P_t} + \frac{\varepsilon_+ S_{\mathrm{I}}}{\varepsilon_{2+} P_t}\right). \tag{4.14}$$

We can now write any specific process, e.g. a given fragmentation, following the above equations, as

$$\begin{aligned} \mathrm{d}S_{\mathrm{F}} &= \Gamma_{\mathrm{Dico}}\, \phi\, \sigma_{\mathrm{I+F}}\, Y_{\mathrm{F}}\, P\, \mathrm{d}t & (4.15)\\ &= \Gamma_{\mathrm{Dico}}\, \phi\, \sigma_{\mathrm{I+F}}\, Y_{\mathrm{F}}\, P_0 \exp\left(-\Gamma_{\mathrm{Dico}}\phi\sigma_{\mathrm{I+F}} Y_{\mathrm{I+F}} t\right) \mathrm{d}t & (4.16)\\ &= -\frac{Y_{\mathrm{F}}}{Y_{\mathrm{I+F}}} \mathrm{d}P, & (4.17) \end{aligned}$$

which can be readily integrated on both sides yielding

$$S_{\mathrm{F}}(t) - S_{\mathrm{F}}(0) = S_{\mathrm{F}} = (P_0 - P_t)\, \frac{Y_{\mathrm{F}}(h\nu)}{Y_{\mathrm{I+F}}(h\nu)}. \tag{4.18}$$

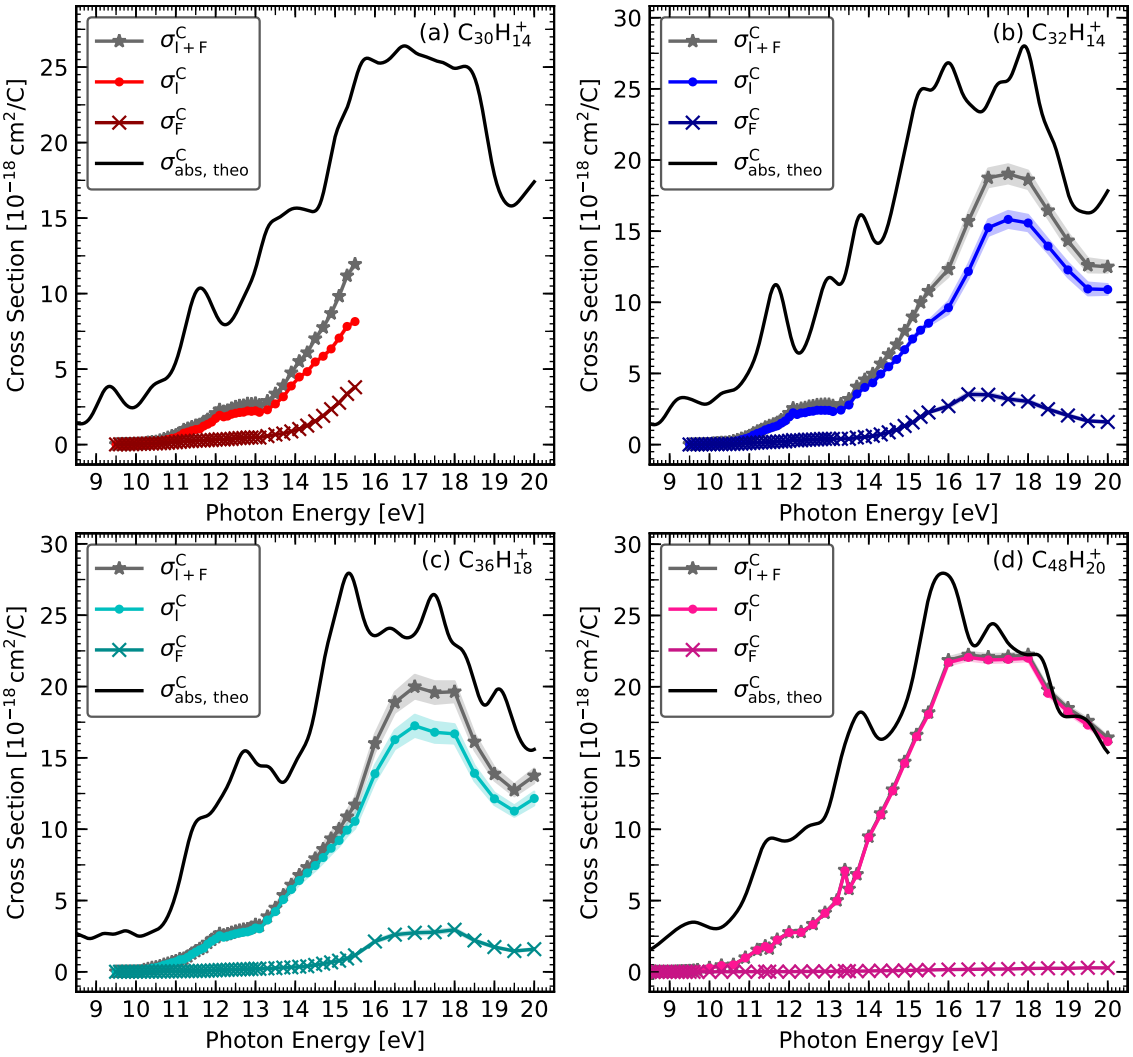

Figure 4.8: Experimentally obtained ionization and dissociation cross sections, $\sigma_{\mathrm{I}}^{\mathrm{C}}$ and $\sigma_{\mathrm{F}}^{\mathrm{C}}$, respectively, and their sum, $\sigma_{\mathrm{I+F}}^{\mathrm{C}}$, of the studied PAH cations as a function of photon energy, (a) benzobisanthene, (b) ovalene, (c) DBPP, and (d) dicoronylene, after absorption of a single VUV photon, compared to the by TD-DFT computed theoretical photoabsorption cross section, $\sigma_{\mathrm{abs,\,theo}}^{\mathrm{C}}$.

In order to solve for the yield of this specific process, Equation (4.18) transforms to

$$Y_{\mathrm{F}}(h\nu) = Y_{\mathrm{I+F}}(h\nu)\frac{S_{\mathrm{F}}}{P_0 - P_t} = Y_{\mathrm{I+F}}(h\nu)\frac{S_{\mathrm{F}}}{S_{\mathrm{F}} + S_{\mathrm{I}}}, \tag{4.19}$$

and finally

$$\sigma_{\mathrm{F}}(h\nu) = \sigma_{\mathrm{I+F}}(h\nu)\, Y_{\mathrm{F}}(h\nu) = \frac{1}{\Gamma_{\mathrm{Dico}}\phi t} \ln\left(1 + \frac{S_{\mathrm{F}}}{P_t} + \frac{\varepsilon_+ S_{\mathrm{I}}}{\varepsilon_{2+} P_t}\right) \frac{S_{\mathrm{F}}}{S_{\mathrm{F}} + S_{\mathrm{I}}}. \tag{4.20}$$

Analogously following the same procedure, we obtain for the ionization process and the formation of dication cross section

$$\sigma_{\mathrm{I}}(h\nu) = \sigma_{\mathrm{I+F}}(h\nu)\, Y_{\mathrm{I}}(h\nu) = \frac{1}{\Gamma_{\mathrm{Dico}}\phi t} \ln\left(1 + \frac{S_{\mathrm{F}}}{P_t} + \frac{\varepsilon_+ S_{\mathrm{I}}}{\varepsilon_{2+} P_t}\right) \frac{S_{\mathrm{I}}}{S_{\mathrm{F}} + S_{\mathrm{I}}}. \tag{4.21}$$

Figure 4.8 depicts the resulting cross sections for all four investigated PAH cations, using the theoretically calculated photoabsorption cross section of dicoronylene as an upper limit for the experimentally determined ones. Comparing the experimental cross sections to the calculated ones, we notice that with this approach our experimental cross sections seem to be underestimated. We therefore try to improve our attempt to derive absolute values of the experimental cross sections with a second approach.

4.4.4.2 Approach 2 - Determination via a Known Cross Section

The photon flux, ϕ, and the form factor, γ, describing the overlap of the photon beam and the ion cloud inside the ion trap were carefully determined by Douix *et al.* [208], in which the buckminsterfullerene cation, C_{60}^+, was measured and its absolute photoionization cross section, $\sigma_{\mathrm{I}}^{C_{60}^+}$, was determined following Equation (4.11), where the term $\frac{S_{\mathrm{F}}}{P_t}$ was zero due to the non-dissociation of C_{60}^+. If an absolute cross section for species A is known, it can be used to determine the cross sections of species B, if A and B are measured in the same conditions, because from Equation (4.11) we get

$$\frac{\sigma^B}{\sigma^A} = \frac{\ln\left(1 + \frac{S_{\mathrm{F}}^B}{P_t^B} + \frac{\varepsilon_+ S_{\mathrm{I}}^B}{\varepsilon_{2+} P_t^B}\right)}{\ln\left(1 + \frac{S_{\mathrm{F}}^A}{P_t^A} + \frac{\varepsilon_+ S_{\mathrm{I}}^A}{\varepsilon_{2+} P_t^A}\right)}, \tag{4.22}$$

and therefore

$$\sigma^B = \sigma^A \cdot \frac{\ln\left(1 + \frac{S_{\mathrm{F}}^B}{P_t^B} + \frac{\varepsilon_+ S_{\mathrm{I}}^B}{\varepsilon_{2+} P_t^B}\right)}{\ln\left(1 + \frac{S_{\mathrm{F}}^A}{P_t^A} + \frac{\varepsilon_+ S_{\mathrm{I}}^A}{\varepsilon_{2+} P_t^A}\right)}. \tag{4.23}$$

For the second approach to yield absolute cross sections, we trapped C_{60}^+ and ovalene, $C_{32}H_{14}^+$, and recorded their photoproducts peak intensities under the same irradiation conditions used for our studied PAHs except dicoronylene as explained below. We could therefore derive the value of $\frac{\gamma}{\phi t}$ by calculating the ratio between the two curves according to Equation (4.23) which then can be used to scale the recorded photoproduct evolutions of our PAHs in order to determine experimental cross sections, σ_{I+F}

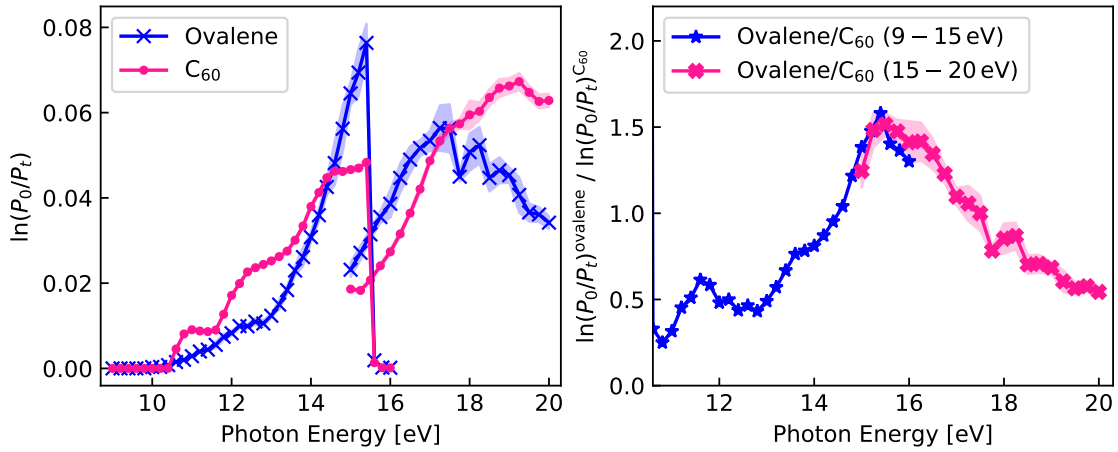

Figure 4.9: Left panel: The $\ln\left(1+\frac{S_F}{P_t}+\frac{\varepsilon_+ S_I}{\varepsilon_{2+} P_t}\right)$ from Equation (4.10) for the ovalene (blue) and C_{60} (pink) cation, and right panel: Their ratio according to Equation (4.22).

With the ratio from Figure 4.9, we can determine the cross section of ionization and fragmentation, σ_{I+F}, for ovalene by scaling to the C_{60}^+ reference curve[7] from Douix *et al.* [208]. The result is presented in Figure 4.10.

Since C_{60}^+ is only ionized above $\sim 10.5\,eV$, we cannot access the values of the cross sections below this value (*cf.* Figure 4.10). Nevertheless, the shapes of the cross sections in both approaches are very similar. We therefore scaled our experimental cross sections from approach 1 to these new cross sections and replaced the low photon energy values with values from approach 1. Additionally, to simplify the comparison between species, we divide σ_{I+F} of each PAH cation by its respective N_C, yielding σ_{I+F}^C. The photoionization cross sections, σ_I^C, and photodissociation cross sections, σ_F^C, were then derived by multiplying the σ_{I+F}^C with the branching ratios depicted in

[7] The absolute photoionization cross section of C_{60}^+, $\sigma_I^{C_{60}^+}$, can be accessed through `http://zenodo.org/record/1001072/`

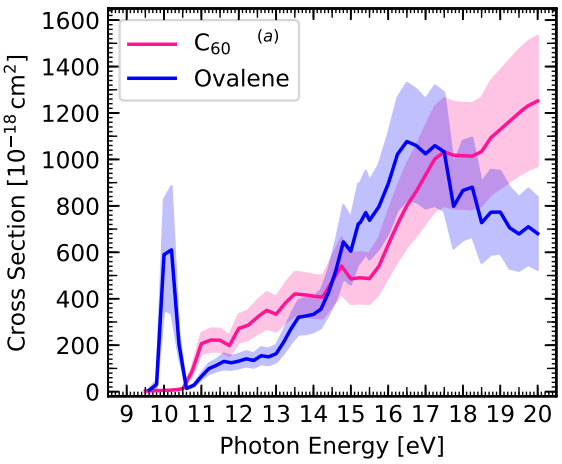

Figure 4.10: The experimental cross section, $\sigma_{\mathrm{I+F}}$, of the ovalene cation obtained from the experimental ionization cross section of C_{60}^{+} from Douix *et al.* [208].

Figure 4.6. The resulting experimental cross sections with respect to the respective N_{C} are displayed in Figure 4.11 for the (a) benzobisanthene, (b) ovalene, (c) DBPP, and (d) dicoronylene cations. The dicoronylene cation, the largest PAH of this study, could not be investigated at the same conditions as the others due to its low solubility which made it difficult to experimentally handle this molecule. For this reason, both the syringe flow rate and the monochromator exit slit width, s, were increased in order to get a sufficient signal. In order to correct at best for these changes, we applied corrections to the $\frac{\gamma}{\phi t}$ factor in Equation (4.11) by assuming that not only the photon flux but also the beam overlap with the ion cloud scales linearly with s. The solid, black curves in Figure 4.11 represent the theoretically calculated photoabsorption cross sections, $\sigma^{\mathrm{C}}_{\mathrm{abs,\,theo}}$, for the studied PAH cations.

Comparing the experimentally and theoretically obtained cross sections, we find that above 14 eV, the cross sections are globally consistent. The values of $\sigma^{\mathrm{C}}_{\mathrm{I+F}}$ are found to be systematically larger than those of $\sigma^{\mathrm{C}}_{\mathrm{abs,\,theo}}$, especially around the peak at 17 eV. In addition, there is a trend of increasing $\sigma^{\mathrm{C}}_{\mathrm{I+F}}$ at the peak with increasing N_{C}. Due to a less accurate calibration procedure, the case of $C_{48}H_{20}^{+}$ has to be considered with caution. On the contrary to the experimental cross sections, the values of $\sigma^{\mathrm{C}}_{\mathrm{abs,\,theo}}$ stay close to each other, which is expected from the proportionality of the photoabsorption cross sections with N_{C}. Still, it is not yet possible to access how precise the calculated cross sections are. The comparison with an experimental photoabsorption

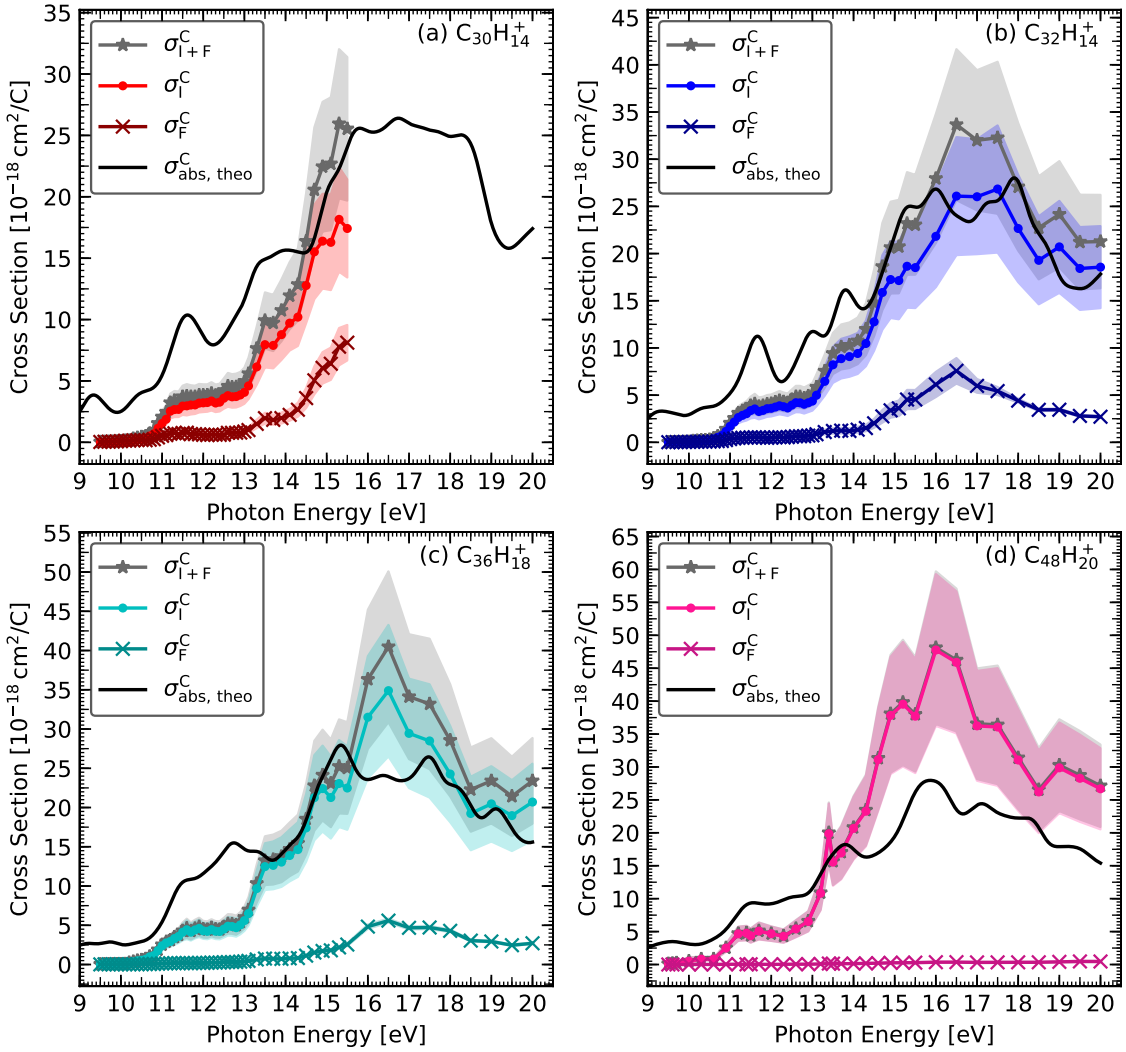

Figure 4.11: Experimentally obtained ionization and dissociation cross sections, $\sigma_{\mathrm{I}}^{\mathrm{C}}$ and $\sigma_{\mathrm{F}}^{\mathrm{C}}$, respectively, and their sum, $\sigma_{\mathrm{I+F}}^{\mathrm{C}}$, of the studied PAH cations as a function of photon energy, (a) benzobisanthene, (b) ovalene, (c) DBPP, and (d) dicoronylene, after absorption of a single VUV photon, compared to the by TD-DFT computed theoretical photoabsorption cross section, $\sigma_{\mathrm{abs,\,theo}}^{\mathrm{C}}$.

cross section at high energies (up to 30 eV) has been done so far only for neutral anthracene, $C_{14}H_{10}$ [74].

Below 14 eV, we can see the presence of a plateau from 11.3 to 12.9 eV, for both $\sigma_{\mathrm{I+F}}^{\mathrm{C}}$ and $\sigma_{\mathrm{I}}^{\mathrm{C}}$, whereas $\sigma_{\mathrm{abs,\,theo}}^{\mathrm{C}}$ exhibits strong bands, indicating that, in this photon energy range, direct ionization is not the dominant process and there is a strong coupling

between electronic states and with nuclear states. This implies that a large fraction of the absorbed photons lead to vibrational excitation of the parent ion which will subsequently relax by radiative cooling since no fragmentation is observed. Such a relaxation scheme could be, at least partially, promoted by long-lived Rydberg states for which radiative cooling with σ_{rad} can be an efficient relaxation channel [123]. Such states could involve autoionization (AI) resonances as was clearly observed in the photoelectron spectroscopy of neutral coronene [202]. In our data, only the peak at 13.4 eV observed in $\sigma_{\mathrm{I}}^{\mathrm{C}}$ of the dicoronylene cation provides evidence for AI resonances. The energy steps used in our scans were, however, too large to catch efficiently these possibly narrow AI resonances and determine how frequently they occur.

Although we can discuss qualitatively the contribution of σ_{rad} at energies below 14 eV, this is not the case at higher energies, implying that the maximum values that can be achieved for the photoionization yield are unknown.

4.4.5 Photoionization Yields

In Figure 4.11 we present the experimental cross sections for photoionization, $\sigma_{\mathrm{I}}^{\mathrm{C}}$, compared to the theoretically computed photoabsorption cross sections, $\sigma_{\mathrm{abs,\,theo}}^{\mathrm{C}}$. By dividing the $\sigma_{\mathrm{I}}^{\mathrm{C}}$ by $\sigma_{\mathrm{abs,\,theo}}^{\mathrm{C}}$, we get the photoionization yields for each PAH cation describing processes for $\mathrm{PAH}^{+} \rightarrow \mathrm{PAH}^{2+}$ transitions. The yields are displayed in the right panel of Figure 4.12.

At energies below 14 eV, the presence of bands in $\sigma_{\mathrm{abs,\,theo}}^{\mathrm{C}}$, which are not present in $\sigma_{\mathrm{I}}^{\mathrm{C}}$, can induce spectral features in the photoionization yields, as for example the 12 eV peak obtained for $\mathrm{C_{32}H_{14}^{+}}$, which are as precise as the calculated spectrum. Still, Figure 4.12 shows that the photoionization yields display comparable features for the studied molecules, with a rise starting at the ionization thresholds, AE^{2+}, the plateau in the 11.3 to 12.9 eV range similarly to what was observed in the ionization cross section, $\sigma_{\mathrm{I}}^{\mathrm{C}}$, as depicted in the left panel of Figure 4.12, followed by another rise to reach the maximum value. There is some uncertainty on this maximum value because of the unknown contribution from σ_{rad}. We made the hypothesis that the contribution of σ_{rad} at high photon energies of 20 eV is minor and that the photoionization yields are limited by the photoionization branching ratio, which never reaches unity as shown in Figure 4.6. The mean values at high energies of the photoionization yields were

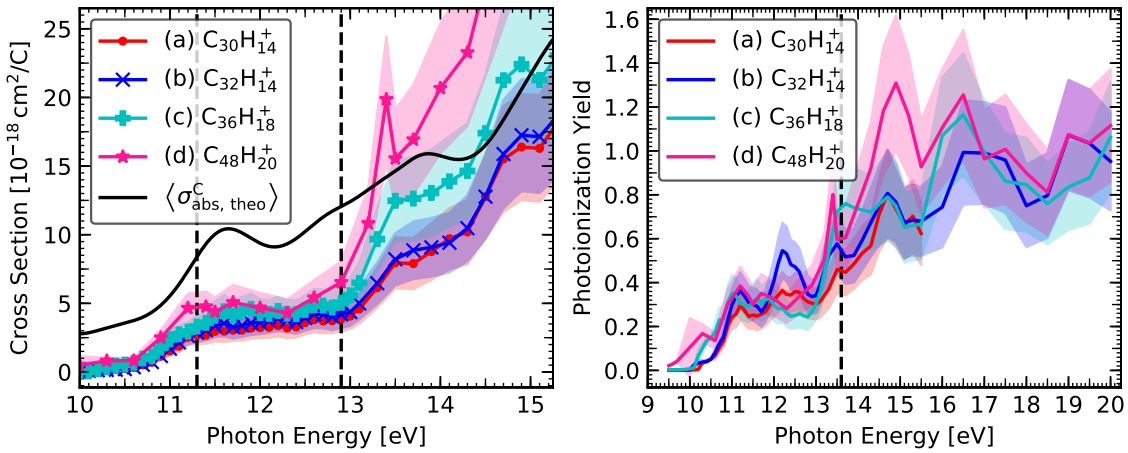

Figure 4.12: Left panel: Experimentally obtained photoionization cross sections per C atom, σ_I^C, of the studied PAH cations as a function of photon energy, (a) benzobisanthene, (b) ovalene, (c) DBPP, and (d) dicoronylene after absorption of a single VUV photon. The average of the calculated photoabsorption cross sections, $\langle \sigma^C_{abs,\,theo} \rangle$, is also presented. The dashed vertical lines mark the transitions between the different ionization regimes. Right panel: Photoionization yields for $PAH^+ \rightarrow PAH^{2+}$ processes deduced from Figure 4.11 by dividing the photoionization cross sections, σ_I^C, by the computed photoabsorption cross sections, $\sigma^C_{abs,\,theo}$, for each PAH cation. The dashed vertical line marks the 13.6 eV cut-off in H I regions.

thus scaled using the ionization branching ratio at 20 eV.

5 | Isomer Diversity in the –H Fragments of Methylated PAH Cations

Outline

5.1 Introduction

Recent theoretical studies have suggested that the –H fragment of methylated PAH cations could exhibit the same isomerization processes as those involved in the dissociative ionization of toluene [209], namely a tropylium-like and a benzylium-like species. Methylated PAHs are expected to be abundant in space [45] and the isomerization process will impact their chemical evolution in photodissociation regions. In order to disentangle tropylium- and benzylium-like cations that are formed in the dissociative ionization of methylated PAHs, we employed infrared predissociation (IRPD) spectroscopy of fragment ions tagged with Ne taking advantage of the cryogenic 22-pole ion trap FELion available at the FELIX Laboratory. In this kind of experiment we demonstrate the potential of the IRPD spectroscopy to disentangle isomeric forms. In particular, this technique prevents further isomerization processes after the initial formation of the fragment ions, which might happen in multiple photon dissociation studies such as IRMPD spectroscopy.

5.2 Motivation

Parneix *et al.* [210] have used molecular modeling to investigate, in the case of two PAHs, pyrene and coronene, the competition between isomerization and relaxation at various degrees of dehydrogenation. This competition is usually not considered, although it can have consequences on the structure of astro-PAHs. In this specific case, Parneix *et al.* [210] reported that it can lead to the formation of pentagonal cycles and that this isomerization into a pentagon-hexagon pair can be competitive with dehydrogenation reactions in neutral PAHs, which should therefore be implemented in astrophysical models. A similar rearrangement was observed by Chen *et al.* [211], who performed molecular dynamics simulations to probe the various structures during the dissociation of coronene and coronene-related species, such as 1-hydrocoronene or 1-methylcoronene. In another theoretical study, Rapacioli *et al.* [140] proposed that the –H fragment of the 1-methylpyrene cation, $C_{17}H_{11}^+$, is possibly abundant in two isomeric forms, *i.e.*, the pyrene-like $PyrC_7^+$ with a tropylium cycle and the 1-pyrenemethylium, $PyrCH_2^+$, which both are depicted in Figure 5.1. An isomerization barrier of $3.5-4$ eV was calculated between the two isomers, suggesting that isomeriza-

tion between $PyrC_7^+$ and $PyrCH_2^+$ might occur under photoactivation in the ISM [140]. A first laboratory study on $C_{17}H_{11}^+$ was earlier performed by Kokkin *et al.* [212] using the PIRENEA setup (see Section 2.2.3). One of the motivations at the time was the proposal by Léger *et al.* [213] that this species or a related one can be the carrier of the DIBs at 4430 Å and 7565 Å (see Sections 1.1.4 and 1.3). The experiments carried out by Kokkin *et al.* [212] provided evidence that neither the 1-methylpyrene cation nor its –H fragment are good candidates for the DIBs. In addition, the recorded band for $C_{17}H_{11}^+$ was observed to be very broad, already suggesting a contribution of isomerization during the multiple photon dissociation scheme implemented to probe the electronic spectroscopy (see Section 2.3.1.2). We therefore aimed to investigate the possible formation of the two isomers under experimental conditions by using infrared spectroscopy.

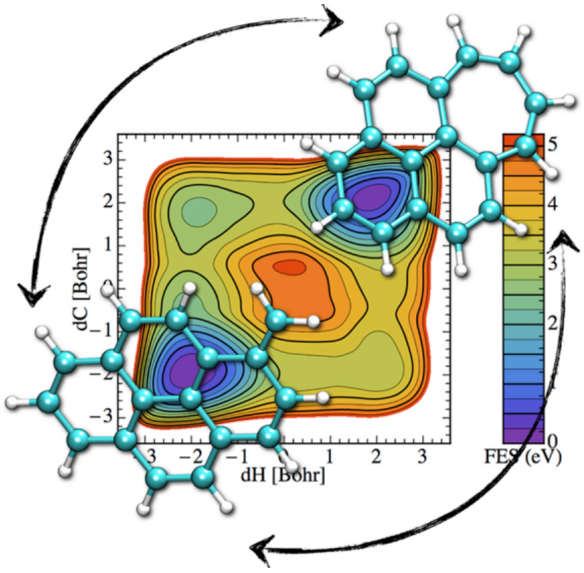

Figure 5.1: Calculated potential energy surface of the isomerization pathways between $PyrC_7^+$ (top right) and $PyrCH_2^+$ (bottom left). Taken from Rapacioli *et al.* [140].

Indeed, during a first FELIX campaign in 2017, we investigated the –H fragment of the 1-methylpyrene cation by means of IRMPD spectroscopy, which is often used to study the structure of molecular ions including PAHs [95–97]. The experiments were carried out using the cryogenic ion trap instrument FELion in combination with the free electron laser radiation from FELIX. An IRMPD spectrum following the major fragment of $C_{17}H_{11}^+$ corresponding to the loss of C_2H_2 (*cf.* also Figure 5.7 (b)),

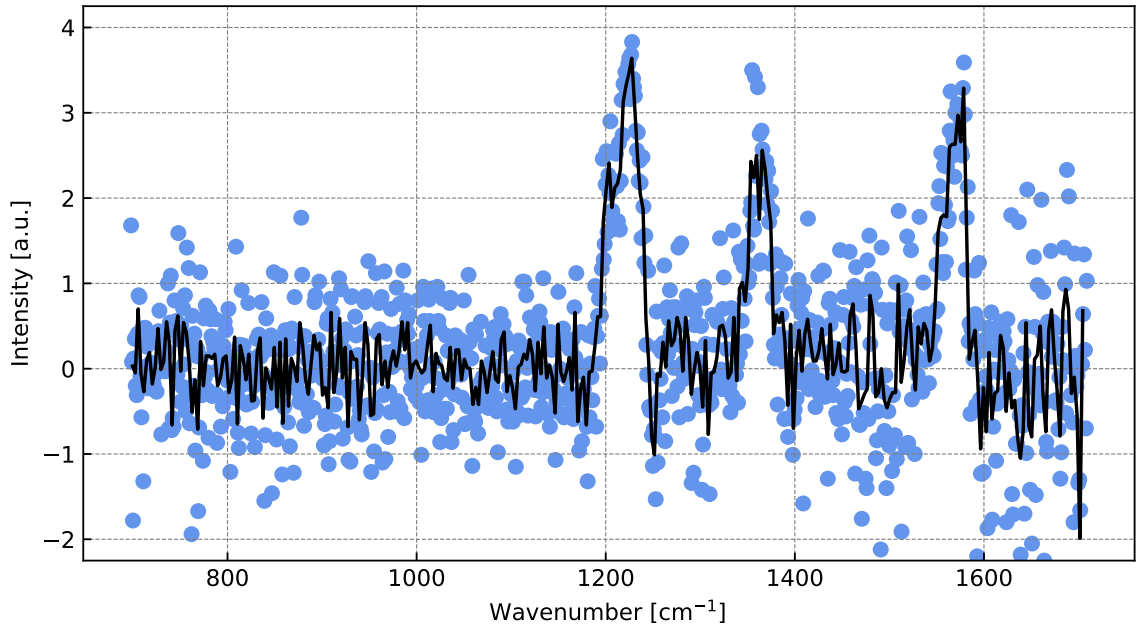

Figure 5.2: Recorded IRMPD data points (blue dots) and obtained IRMPD spectrum (black curve) of the $-C_2H_2$ fragment ($m/z = 189$) of $C_{17}H_{11}^+$. In comparison to the calculated IR spectra shown in the top panel of Figure 5.5, only features of the $PyrCH_2^+$ were observed.

$m/z = 189$, was recorded as a function of the FELIX laser wavelength and is presented in Figure 5.2.

Despite technical difficulties of the instrument at the time of measurements, leading to a decreased signal-to-noise ratio, spectral features of the $PyrCH_2^+$ isomer could be identified with IRMPD and compared to the quantum-chemical calculations (*cf.* Figure 5.5). The results have been published by Jusko *et al.* [214]. We concluded that IRMPD spectroscopy is not the technique of choice since the absorption of many IR photons can heat the ions and lead to further undesired isomerization processes inside the ion trap.

5.3 FELion Beamline at the FELIX Laboratory

Schematically depicted in Figure 5.3 is the FELion cryogenic ion trap instrument which is a home-built, cryogenically cooled 22-pole ion trap described in detail in

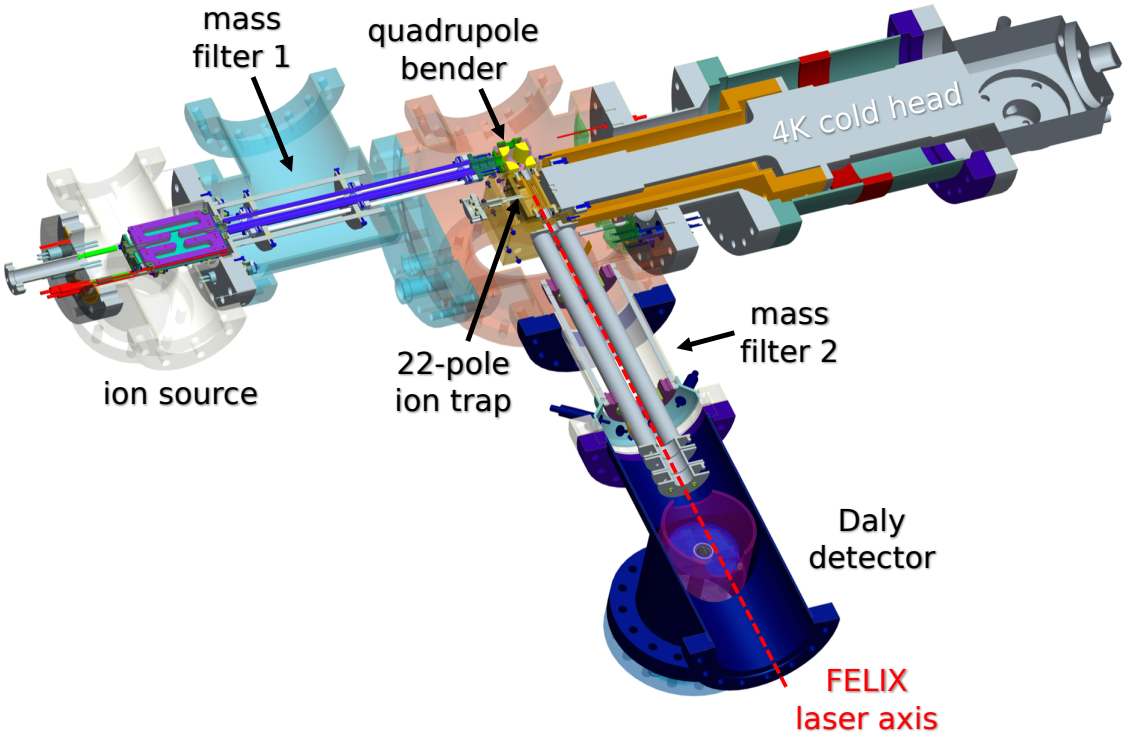

Figure 5.3: Schematic of the cryogenically cooled 22-pole ion trap, FELion, as it is available at the FELIX Laboratory. Image taken and adapted from its twin ion trap, COLTRAP, available at the University of Cologne [215].

reference [216] and available at the free electron laser FELIX Laboratory [170]. In addition to the cryogenic 22-pole ion trap, FELion consists of an electron impact ionization source (see Section 2.1.1.2) and is equipped with two quadrupole mass filters allowing the mass selection and analysis of the ions of interest, which are detected by a Daly detector. The 22-pole radio frequency ion trap is coupled to a cryogenic cold head ensuring temperatures as low as 4 K which is crucial for efficient noble gas tagging. Depending on the used precursor, an electron impact storage or non-storage ion source can be installed to FELion with electron bombardment energy in the source of up to 125 eV.

Infrared multiple photon dissociation (IRMPD) spectroscopy can be performed at various trap temperatures using the cold head in combination with a resistive

heating tape as well as noble gas, e.g. He, to thermalize the ions of interest. The trapped ions are irradiated by the focused FELIX beam to induce multiple photon absorption processes within one macropulse and therefore dissociation of the ions of interest. One of the major fragments of the ions of interest, e.g. due to acetylene, C_2H_2, loss, are mass selected by the second quadrupole mass filter while tuning the FELIX laser wavelength leading to the recording of IRMPD spectra (*cf.* Figure 5.2 and also Section 2.3.1.2).

Infrared predissociation (IRPD) spectroscopy is performed on the weakly bound complexes of the ions of interest with a noble gas atom, e.g. He or Ne. The trap has to be operated at low temperatures, *i.e.*, 4 K or $6 - 10$ K for He or Ne, respectively, in order to tag the species of interest with a noble gas atom. The depletion of these complexes is then induced by a single photon absorption process (see Section 2.3.2) and is recorded as a function of the FELIX laser wavelength yielding the IRPD spectra. The FELIX laser delivers up to 30 mJ into the 22-pole ion trap in a single macropulse with a pulse duration of about 5 μs at a 10 Hz repetition rate. Each macropulse is composed of micropulses with energies in the 10 μJ range and with a typical pulse length in the ps range. The use of FELIX is essential because of the provision of widely tunable infrared radiation with sufficient laser intensity in the required fingerprint regions between 600 and 1800 cm^{-1} of the investigated methylated PAH fragments.

5.4 Preparation of the Experiment

The preparation of these beamtime measurements required theoretical DFT calculations to predict possible isomer structures, their optimized geometries, and to compute IR spectra of the photon energy range, the IR fingerprints of these species, we aimed to examine.

5.4.1 Methylated PAH Precursors

Experiments and calculations were performed for the cationic –H fragments of three different methylated PAH precursors, namely 1-methylpyrene, $C_{17}H_{12}$, 2-methylanthracene, $C_{15}H_{12}$, and 2-methylnaphthalene, $C_{11}H_{10}$, which are commercially available

from Sigma-Aldrich. As predicted by calculations, the –H fragments of these PAH precursors are able to form at least two different isomers, consisting of a benzylium-like or tropylium-like structure which have a CH_2 group attached or incorporate the extra carbon atom inside a C_7 ring, respectively [140]. The structures of the considered isomers from the –H fragments of 1-methylpyrene, $PyrCH_2^+$ and $PyrC_7^+$, 2-methylanthracene, $AntCH_2^+$ and $AntC_7^+$, and 2-methylnaphthalene, $NapCH_2^+$ and $NapC_7^+$, are depicted in Figure 5.4.

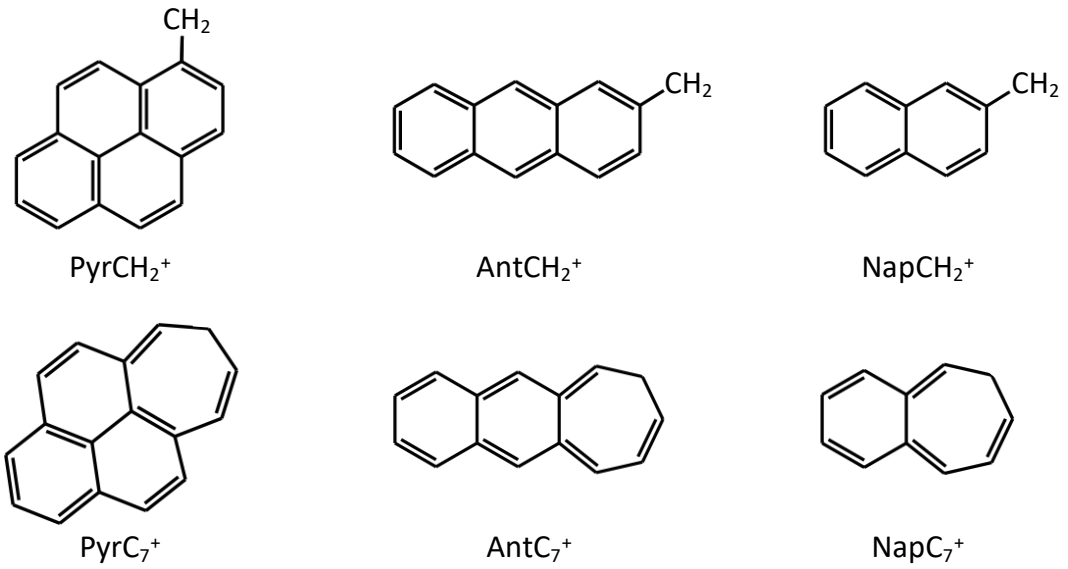

Figure 5.4: Predicted isomer structures for $C_{17}H_{11}^+$, $PyrCH_2^+$ and $PyrC_7^+$ (left); $C_{15}H_{11}^+$, $AntCH_2^+$ and $AntC_7^+$ (center); and $C_{11}H_9^+$, $NapCH_2^+$ and $NapC_7^+$ (right). The neutral precursors have the same structure as the top row but with a methyl, CH_3, instead of a methylene, CH_2, sidegroup attached.

5.4.2 Expected Results: IR Spectra

Before the experimental campaign, static density functional theory (DFT) calculations have been carried out in order to obtain theoretical harmonic IR spectra of the six possible isomers. The B3LYP exchange-correlation functional [182] provides good results for molecules of similar size and structure [217]. The geometry of each isomer was therefore optimized using the B3LYP hybrid functional in conjunction with a 6-31G(d,p) basis set [218].

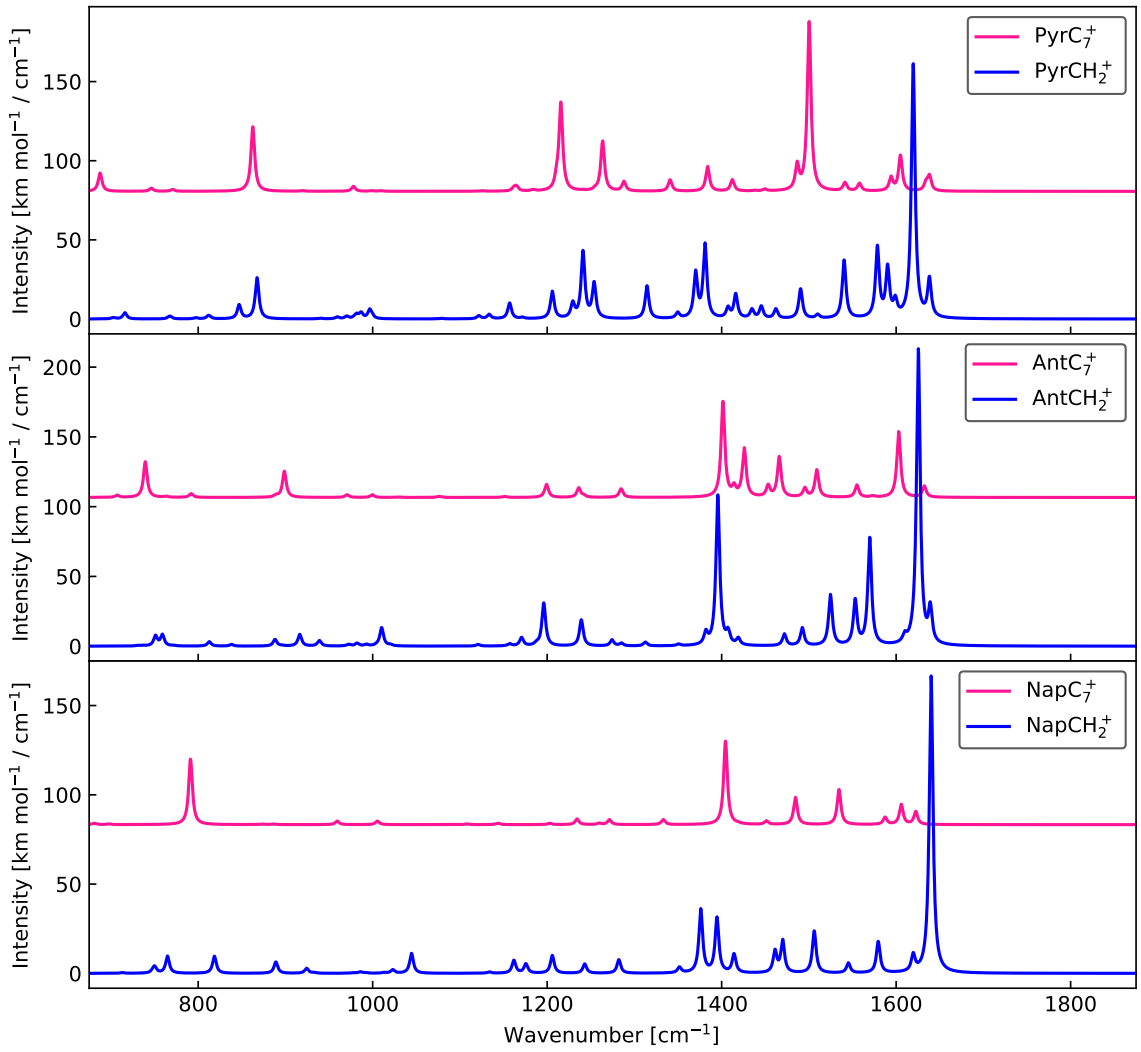

Figure 5.5: Theoretically calculated IR spectra of the proposed isomer structures of $C_{17}H_{11}^+$, $PyrCH_2^+$ and $PyrC_7^+$ (top panel); $C_{15}H_{11}^+$, $AntCH_2^+$ and $AntC_7^+$ (center panel); and $C_{11}H_9^+$, $NapCH_2^+$ and $NapC_7^+$ (bottom panel).

The geometries for $C_{17}H_{11}^+$ were found to be quasi-degenerate at this level, with $PyrC_7^+$ being more stable than $PyrCH_2^+$ by only 0.5 kJ mol^{-1} when including zero-point energy (ZPE) effect corrections. Considering the geometries for $C_{15}H_{11}^+$ and $C_{11}H_9^+$, the tropylium-like structures, $AntC_7^+$ and $NapC_7^+$, respectively, are more stable compared to the benzylium-like geometries, $AntCH_2^+$ and $NapCH_2^+$ by 3.0 kJ mol^{-1}. The values of the energy difference, ΔE, are summarized in Table 5.1.

The theoretical harmonic IR spectra presented in Figure 5.5 were obtained by full

Table 5.1: Energy differences taking into account the zero-point energy (ZPE) effects of the considered isomer geometries of $C_{17}H_{11}^+$, $C_{15}H_{11}^+$, and $C_{11}H_9^+$ in kJ mol^{-1}.

Molecule	$\mathbf{C_{17}H_{11}^+}$	$\mathbf{C_{15}H_{11}^+}$	$\mathbf{C_{11}H_9^+}$
$\boldsymbol{\Delta E}$ **[kJ mol^{-1}]**	0.5[a]	3.0[b]	3.0[b]

[a] Taken from Rapacioli *et al.* [140].
[b] Calculated at the same level of theory as presented in [140].

diagonalization of the weighted Hessian matrix and calculations were achieved with the Gaussian09 suite of programs [188]. All theoretical harmonic IR spectra were scaled by a factor in order to correct for anharmonic effects. Scaling factors applied to harmonic frequencies accounting for mode anharmonicities are in the range of 0.96 to 0.99. We determined this factor to be 0.978 by overplotting the $PyrCH_2^+$ spectrum and the experimentally obtained IRPD spectrum of $C_{17}H_{11}^+$ (*cf.* Figure 5.7 (c) and (d)).

5.5 Data Acquisition and Analysis

In order to further investigate the structure of the $C_{17}H_{11}^+$ fragment and to extend the study toward the –H fragments of the 2-methylanthracene and 2-methylnaphthalene cations (see Section 5.4.1) by means of IRPD spectroscopy, several steps have to be followed, which are schematically depicted in Figure 5.6.

First, the neutral precursors have to be ionized by electron bombardment in the ion source. The –H fragments are directly produced by the dissociative ionization of the neutral precursors and mass-selected by the first quadrupole mass filter. The ion trap is cooled down to approximately 6 K and a first mass spectrum in non-trapping and non-tagging mode is recorded by the use of the second quadrupole mass filter in order to identify the parent ion, P^+, and possible fragments. Upon ion injection, high quantities of a Ne:He 1:2 gas mixture were introduced into the ion trap in order to promote ternary Ne atom attachment to the cation of interest, P^+, *i.e.*, $C_{17}H_{11}^+$, $C_{15}H_{11}^+$, or $C_{11}H_9^+$. Proof of Ne tagging was given through a second recorded mass spectrum in trapping mode which shows the peak of the tagged complex, $P^+ \cdot T$, with a mass shift of $m/z = +20$ corresponding to the mass of Ne. Even double tagging

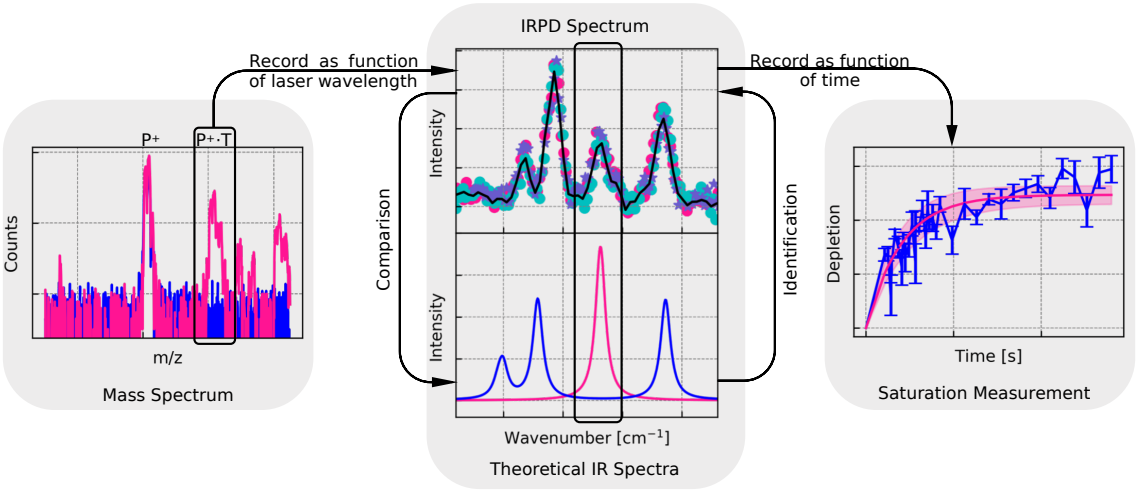

Figure 5.6: Data processing and evaluation scheme using the cryogenic ion trap FELion and the free electron laser FELIX.

can be observed for all of our species, as well as a little bit of N_2 contamination (mass shift of $m/z = +28$), which does not influence or invalidate our measurements.

Recording the intensity of the Ne tagged complex, $P^+ \cdot Ne$, while tuning the photon energy of the FELIX laser, leads to the presented IRPD spectra. In order to identify the isomers abundant in the ion trap, the measured IRPD spectrum has to be compared to the theoretically calculated IR spectra as schematically presented in the centered panel in Figure 5.6. By this comparison, resonance bands of one or more specific isomers can be identified. In order to investigate the abundance of two proposed isomers in the ion trap, time scans on resonance bands as well as background time scans (off resonance) with set laser wavelengths were performed. The depletion, D, as a function of time, t, can be written as

$$D(t) = \frac{N_{\mathrm{BG}}(t) - N(t)}{N_{\mathrm{BG}}(t)} = 1 - \frac{N(t)}{N_{\mathrm{BG}}(t)}, \tag{5.1}$$

where $N_{\mathrm{BG}}(t)$ is the number of ions (counts) off resonance and $N(t)$ is the number of ions (counts) on a resonance band. According to an exponential decay, they can be written as

$$N(t) = N_{\mathrm{a}}(t) + N_{\mathrm{n}}(t) = N_{\mathrm{a0}}\,\mathrm{e}^{-kt}\,\mathrm{e}^{-k_{\mathrm{BG}}t} + N_{\mathrm{n0}}\,\mathrm{e}^{-k_{\mathrm{BG}}t} \tag{5.2}$$

$$N_{\mathrm{BG}}(t) = (N_{\mathrm{a0}} + N_{\mathrm{n0}})\,\mathrm{e}^{-k_{\mathrm{BG}}t}, \tag{5.3}$$

where $N_{\mathrm{a}}(t)$ is the active isomer absorbing on the band, $N_{\mathrm{n}}(t)$ is the non-active isomer not absorbing on this band, k is the decay rate caused by FELIX and k_{BG} is the background decay rate, which we assume to be equal for both active and non-active isomer. If we then plug Equations (5.2) and (5.3) into Equation (5.1), we get for the depletion

$$D(t) = \frac{N_{\mathrm{a0}}}{N_{\mathrm{a0}} + N_{\mathrm{n0}}} \left(1 - \mathrm{e}^{-kt}\right), \tag{5.4}$$

with characteristics

$$\lim_{t \to 0} D(t) = 0 \tag{5.5}$$

$$\lim_{t \to \infty} D(t) = \frac{N_{\mathrm{a0}}}{N_{\mathrm{a0}} + N_{\mathrm{n0}}} =: A. \tag{5.6}$$

We can therefore fit an exponential decay function according to Equation (5.4) to our time scan data in order to determine A, the abundance of the active isomer (values 0 to 1), and k (> 0), the active isomer decay rate, as schematically shown in the right panel of Figure 5.6.

5.6 Results and Discussion

During our second campaign at the FELion setup available at the free electron laser FELIX and following the procedure presented in the precedent Section 5.5, we investigated the –H fragments of three different methylated PAH cations. The results are presented in Figures 5.7, 5.9, and 5.10 for $C_{17}H_{11}^{+}$, $C_{15}H_{11}^{+}$, and $C_{11}H_{9}^{+}$, respectively, in which panel (a) shows the initially proposed isomer structures, (b) the mass spectra of the non-trapping / non-tagging (Trap OFF) and the trapping mode (Trap ON), (c) the experimentally recorded IRPD spectra, where different colors correspond to different measurement sequences which contributed to the averaged spectrum (solid black curve), (d) the theoretically calculated IR spectra of the two proposed isomer structures, (e) and (f) saturation depletion measurements on two selected bands with exponential decay fit.

5.6.1 –H Fragment of 1-Methylpyrene: $C_{17}H_{11}^+$

The results for the $C_{17}H_{11}^+$ cation, $m/z = 215$, are presented in the following.

Table 5.2: Experimental mid-IR band positions recorded for $C_{17}H_{11}^+$ and calculated positions for the $PyrCH_2^+$ and $PyrC_7^+$ isomers. The intensities correspond to the maximum of the convoluted spectra.

$PyrCH_2^+$			**$PyrC_7^+$**		
Experiment IRPD	**Theory B3LYP-DFT**		**Experiment IRPD**	**Theory B3LYP-DFT**	
$\bar{\nu}\,[\mathrm{cm}^{-1}]$	$\bar{\nu}\,[\mathrm{cm}^{-1}]$	$I\,[\frac{\mathrm{km\,mol}^{-1}}{\mathrm{cm}^{-1}}]$	$\bar{\nu}\,[\mathrm{cm}^{-1}]$	$\bar{\nu}\,[\mathrm{cm}^{-1}]$	$I\,[\frac{\mathrm{km\,mol}^{-1}}{\mathrm{cm}^{-1}}]$
724	716	4	–	687	12
–	847	9	–	863	41
870	867	26	–	1164	4
972	970	2	–	1216	56
–	982	4	–	1264	32
–	987	5	–	1288	6
–	997	6	–	1341	7
1155	1157	10	–	1384	16
1207	1206	18	–	1412	7
1229	1230	12	–	1487	19
1239	1241	43	–	1500	107
–	1254	24	–	1541	6
1311	1315	21	–	1558	5
–	1350	5	–	1594	10
1368	1370	31	–	1605	23
1379	1381	48	–	1638	11
–	1408	8			
1413	1416	16			
–	1435	7			
–	1445	8			
–	1462	7			
–	1490	19			
1535	1540	37			
1570	1579	47			
1590	1590	35			
–	1599	15			
1620	1620	161			
–	1638	27			

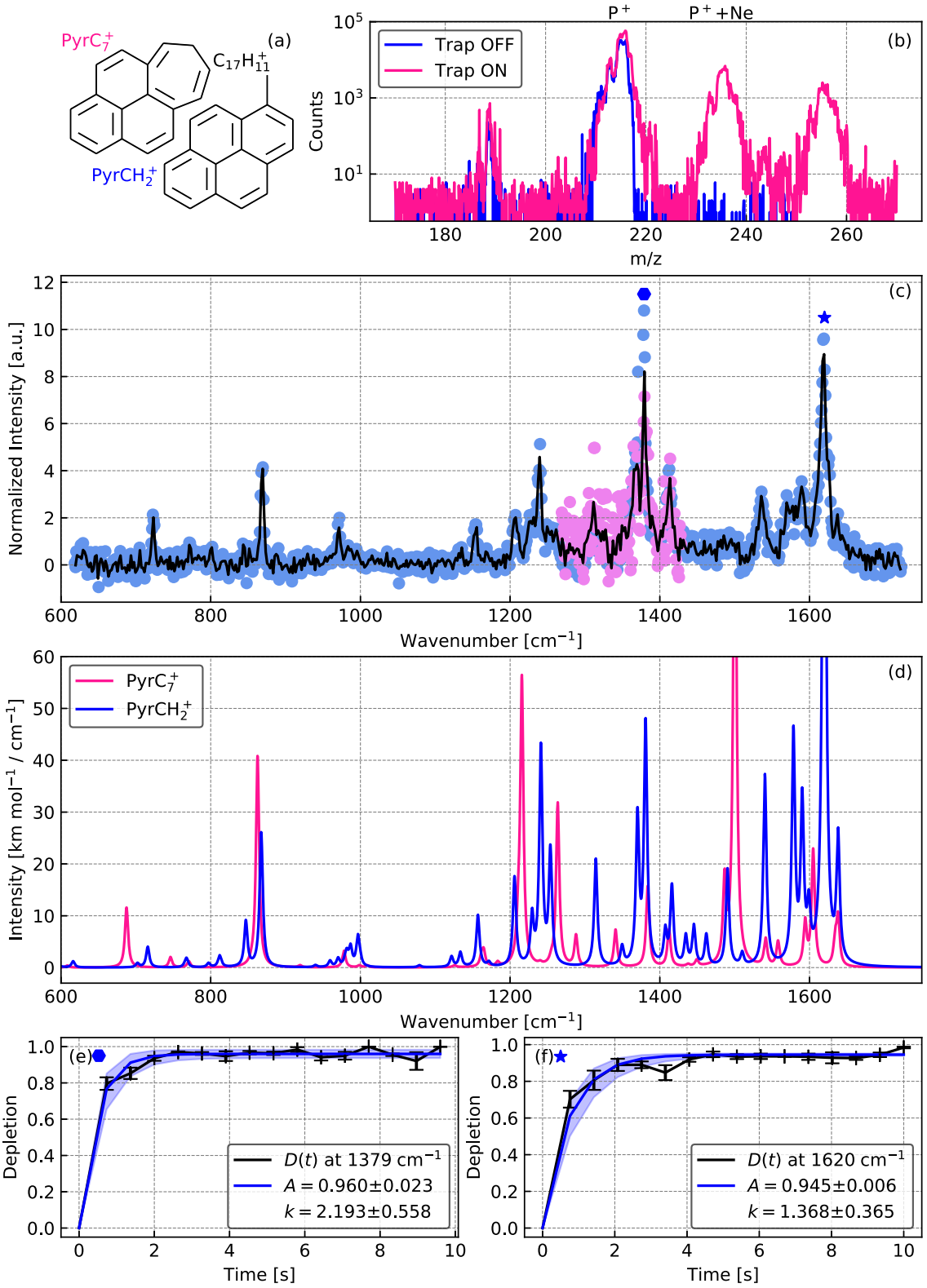

Figure 5.7: Results for $C_{17}H_{11}^+$, $m/z = 215 + 20$, obtained using FELion at FELIX. (a) Considered possible isomeric structures. (b) Mass spectra. (c) IRPD spectrum. (d) Theoretical IR spectra. (e) and (f) Saturation depletion measurements for the bands marked in (c). Details are provided in the main text.

The experiments for the $C_{17}H_{11}^+$ cation, $m/z = 215$, were performed with an electron impact energy of $-56.7\,\text{eV}$, yielding a production of $\sim 10^5$ parent ions (see Figure 5.7). The Ne tagging efficiency was about 12 % for the singly tagged and 4 % for the doubly tagged complexes. Mass spectra were recorded with a 0.1 mass resolution (see Section 2.2.1) and are presented in Figure 5.7 (b).

Recording the Ne tagged complex at $m/z = 235$ and tuning the FELIX laser wavelength with a wavenumber step size of $1\,\text{cm}^{-1}$, IRPD spectra were produced with a trapping time of 1.6 s and 4 iterations for each data point shown in Figure 5.7 (c). Comparing the recorded and averaged IRPD spectrum to the calculated IR spectra of the two proposed isomer structures, many bands of the $PyrCH_2^+$ can be identified, whereas no features of the $PyrC_7^+$ can be observed, as reported in Table 5.2.

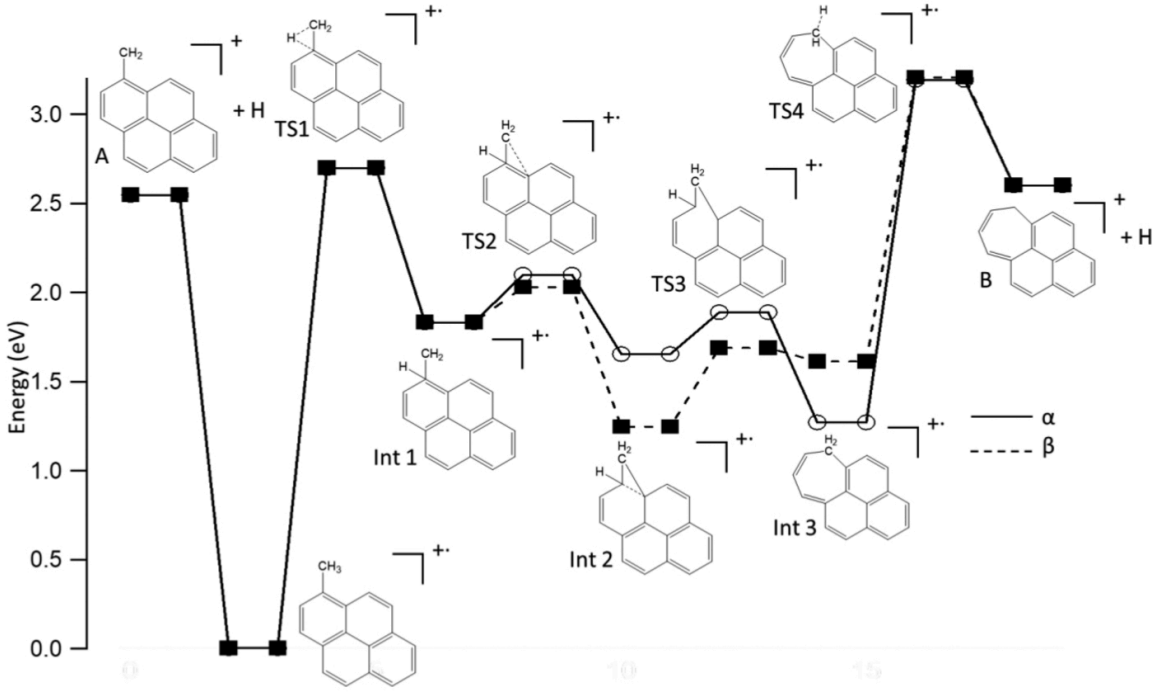

Figure 5.8: Calculated possible reaction pathways for the dissociation of the ionized 1-methylpyrene, $C_{17}H_{12}^+$, indicating that the formation of $PyrCH_2^+$ is more likely to happen than $PyrC_7^+$. Computed by and taken from West *et al.* [130].

Saturation depletion measurements on two strong resonance bands, $1379\,\text{cm}^{-1}$ and $1620\,\text{cm}^{-1}$, were performed in order to test the isomer depletion. The results are depicted in Figure 5.7 (e) and (f), respectively, from which the exponential decay fit parameter, A, suggesting the abundance of the tested isomer in the mixture, can be

deduced. In this case, A corresponds to $(96.0 \pm 2.3)\,\%$ or $(94.5 \pm 0.6)\,\%$ of $PyrCH_2^+$, yielding to the conclusion that mainly $PyrCH_2^+$ is formed by the dissociative ionization of 1-methylpyrene.

This observation can be rationalized by the fact that the formation of $PyrC_7^+$ is unlikely to happen according to the calculated reaction pathways depicted in Figure 5.8 which were computed by DFT calculations performed by West *et al.* [130].

5.6.2 –H Fragment of 2-Methylanthracene: $C_{15}H_{11}^+$

The $C_{15}H_{11}^+$ cation was formed by electron bombardment with a constant electron energy of $-18.0\,\text{eV}$ and mass spectra were recorded with a resolution of 0.05, clearly showing the parent ion peak at $m/z = 191$ with $\sim 10^5$ ions (see Figure 5.9 (b)).

Successful trapping and tagging was performed by introducing the He:Ne gas mixture, yielding a tagging efficiency of the Ne tagged complex ($m/z = 211$) of about $10.5\,\%$ as shown in the mass spectrum in Figure 5.9 (b) with a trapping time of $1.63\,\text{s}$. Following this peak and varying the FELIX laser wavelength gave the recorded and averaged IRPD spectrum with a wavenumber step size of 0.5 and $1\,\text{cm}^{-1}$ depicted in Figure 5.9 (c). Each data point presented corresponds to the average of 4 iterations. Comparing the IRPD spectrum to the theoretically calculated IR spectra for the two proposed isomer structures, several bands can be identified, which are reported in Table 5.3. The saturation depletion measurements at band positions $756\,\text{cm}^{-1}$ and $1519\,\text{cm}^{-1}$ yielded very similar abundances of $(73.8 \pm 2.7)\,\%$ and $(67.3 \pm 5.2)\,\%$, respectively, which could lead to the conclusion that we measured resonance bands of only one isomer structure. Comparing the band positions to the calculated IR spectra, we can identify this structure to be the $AntCH_2^+$ isomer. Nevertheless, quantities of the $AntC_7^+$ isomer seem to be present in the ion trap because of the identification of several bands as reported in Table 5.3 and the fact that we were not able to deplete the ions to $\sim 100\,\%$. The similar values of the depletion saturation measurements could also account for an 1:1 isomer mixture inside the ion trap and hence a smearing and overlap of the respective bands.

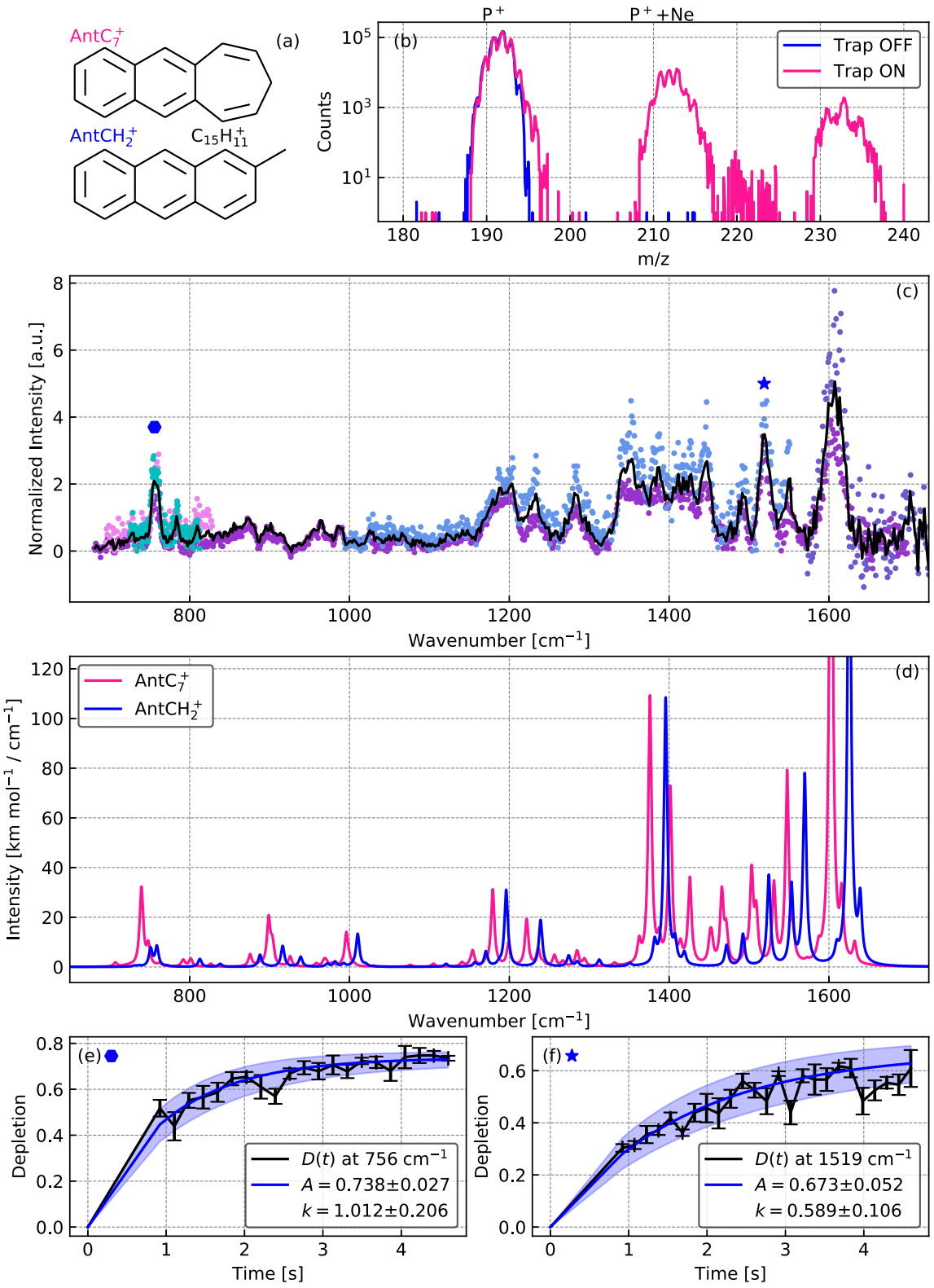

Figure 5.9: Results for $C_{15}H_{11}^+$, $m/z = 191 + 20$, obtained using FELion at FELIX. (a) Considered possible isomeric structures. (b) Mass spectra. (c) IRPD spectrum. (d) Theoretical IR spectra. (e) and (f) Saturation depletion measurements for the bands marked in (c). Details are provided in the main text.

Table 5.3: Experimental mid-IR band positions recorded for $C_{15}H_{11}^+$ and calculated positions for the $AntCH_2^+$ and $AntC_7^+$ isomers. The intensities correspond to the maximum of the convoluted spectra.

$AntCH_2^+$			**$AntC_7^+$**		
Experiment IRPD	**Theory B3LYP-DFT**		**Experiment IRPD**	**Theory B3LYP-DFT**	
$\bar{\nu}\,[\mathrm{cm}^{-1}]$	$\bar{\nu}\,[\mathrm{cm}^{-1}]$	$I\,[\frac{\mathrm{km\,mol}^{-1}}{\mathrm{cm}^{-1}}]$	$\bar{\nu}\,[\mathrm{cm}^{-1}]$	$\bar{\nu}\,[\mathrm{cm}^{-1}]$	$I\,[\frac{\mathrm{km\,mol}^{-1}}{\mathrm{cm}^{-1}}]$
–	751	8	–	739	26
756	759	9	783	792	3
809	813	3	–	899	19
875	888	5	964	971	2
–	917	9	1204	1199	9
–	939	4	1234	1236	7
–	1010	13	1283	1285	6
–	1171	6	–	1401	69
1188	1196	31	1412	1414	11
1234	1239	19	1428	1426	36
–	1274	5	1447	1453	10
–	1382	12	–	1466	29
–	1396	108	–	1495	7
–	1407	14	–	1509	20
–	1419	7	–	1555	9
–	1472	9	1607	1603	47
1492	1492	13	–	1632	8
1519	1525	37			
1550	1553	34			
–	1570	78			
–	1610	11			
–	1625	213			
–	1639	32			

5.6.3 –H Fragment of 2-Methylnaphthalene: $C_{11}H_9^+$

Similarly to the previous measurements, experiments were performed on the $C_{11}H_9^+$ cation which was produced by the dissociation and ionization in the electron impact source with an electron energy of −17.0 eV (see Figure 5.10).

Table 5.4: Experimental mid-IR band positions recorded for $C_{11}H_9^+$ and calculated positions for the $NapCH_2^+$ and $NapC_7^+$ isomers. The intensities correspond to the maximum of the convoluted spectra.

$NapCH_2^+$			**$NapC_7^+$**		
Experiment IRPD	**Theory B3LYP-DFT**		**Experiment IRPD**	**Theory B3LYP-DFT**	
$\bar{\nu}\,[\mathrm{cm}^{-1}]$	$\bar{\nu}\,[\mathrm{cm}^{-1}]$	$I\,[\frac{\mathrm{km\,mol}^{-1}}{\mathrm{cm}^{-1}}]$	$\bar{\nu}\,[\mathrm{cm}^{-1}]$	$\bar{\nu}\,[\mathrm{cm}^{-1}]$	$I\,[\frac{\mathrm{km\,mol}^{-1}}{\mathrm{cm}^{-1}}]$
760	750	4	791	791	31
771	765	10	–	960	2
818	818	10	–	1005	2
–	889	6	1153	1143	1
–	924	3	1276	1271	3
1021	1023	2	1336	1333	3
1035	1044	11	1405	1404	47
1165	1162	7	1454	1451	2
–	1176	6	–	1485	15
1208	1206	10	–	1534	20
1244	1243	5	–	1587	4
1276	1282	8	1603	1606	11
1349	1352	4	–	1623	7
1376	1376	36			
–	1395	32			
–	1414	11			
–	1461	14			
–	1470	19			
–	1506	24			
–	1545	6			
–	1579	18			
–	1620	12			
1630	1640	167			

Mass spectra were achieved with a mass resolution of 0.1 and are shown in Fig-

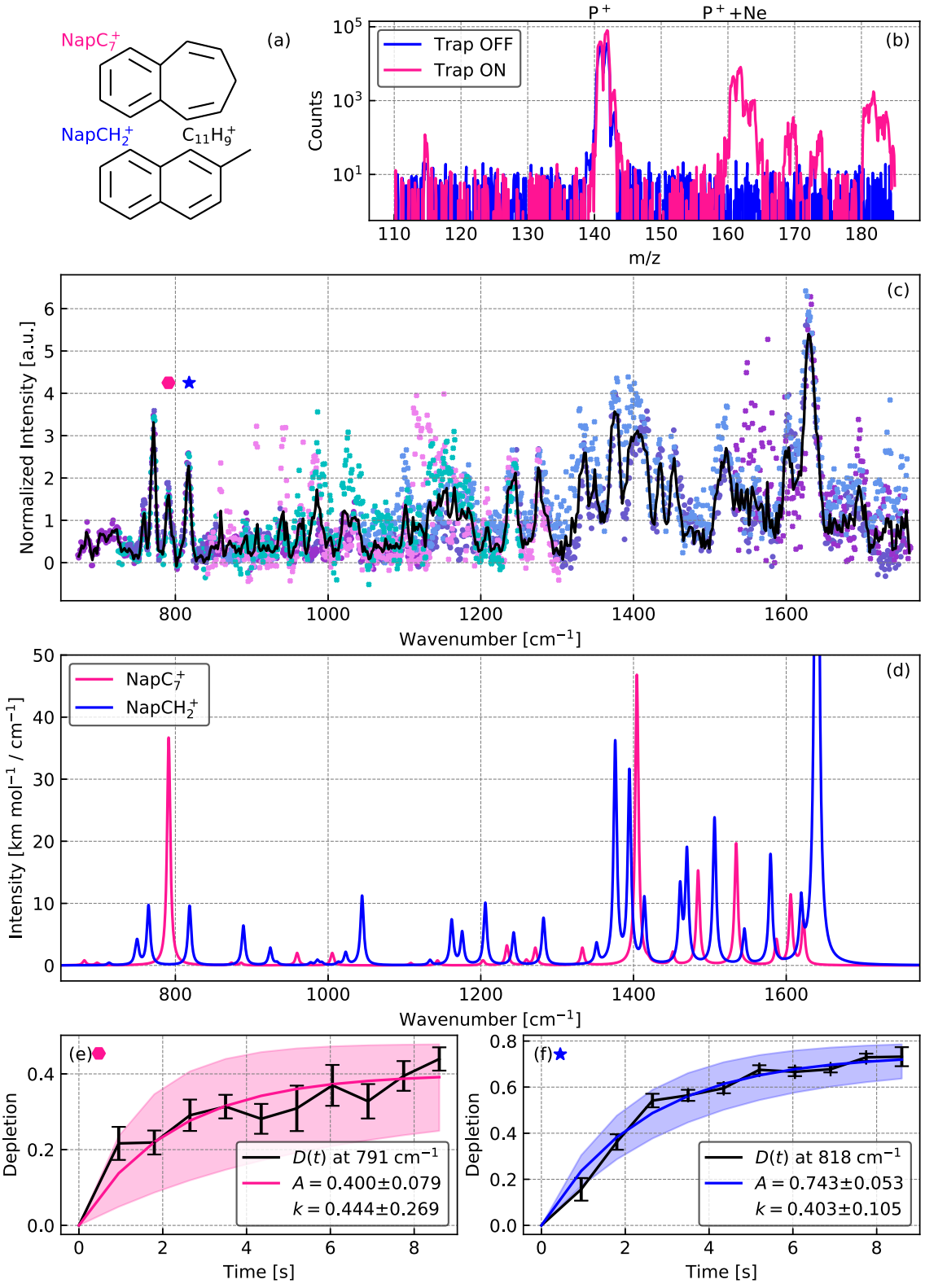

Figure 5.10: Results for $C_{11}H_9^+$, $m/z = 141 + 20$, obtained using FELion at FELIX. (a) Considered possible isomeric structures. (b) Mass spectra. (c) IRPD spectrum. (d) Theoretical IR spectra. (e) and (f) Saturation depletion measurements for the bands marked in (c). Details are provided in the main text.

ure 5.10 (b), clearly depicting the parent ion at $m/z = 141$ and the Ne tagged complex at $m/z = 161$ with a tagging efficiency of 11 %. With a trapping time of 1.6 s and a wavenumber step size of 1 cm^{-1}, several IRPD spectra were recorded with 4 iterations for each data point presented in Figure 5.10 (c), yielding the averaged IRPD spectrum for the $C_{11}H_9^+$ cation (black solid curve).

Figure 5.10 (d) depicts the theoretically calculated IR spectra of the two proposed isomer structures and the band positions are reported in Table 5.4, suggesting that both isomers are present in the trap. This assumption is supported by the saturation depletion measurements presented in Figure 5.10 (e) and (f). These were performed on resonance for band positions at 791 cm^{-1} and 818 cm^{-1} corresponding to $NapC_7^+$ and $NapCH_2^+$, respectively. According to the exponential decay fit, the isomer mixture is composed of $(40.0 \pm 7.9\,\%)$ of $NapC_7^+$ and $(74.3 \pm 5.3\,\%)$ of $NapCH_2^+$. These values leave us with two possible conclusions. We could argue, that within the error, the 100 % composition of the isomer mixture is given with the consideration of the two proposed isomers. On the other hand, it is possible that a third different isomer is abundant in the ion trap. Since these measurements have been performed during a beamtime at FELion at FELIX, we cannot remeasure saturation depletion on another band. Instead, we continued to investigate this possibility theoretically.

5.6.4 Isomer Diversity for $C_{11}H_9^+$

The IRPD spectrum of $C_{11}H_9^+$ as reported in Figure 5.10 (c) shows many bands which can partially be associated to the two initially proposed isomer structures, namely $NapC_7^+$ and $NapCH_2^+$ (*cf.* Figure 5.10 (a)). Nevertheless, the saturation depletion measurements yielded abundances of $(40.0 \pm 7.9\,\%)$ and $(74.3 \pm 5.3\,\%)$, respectively, adding up to more than 100 %. This prompted us to further examine the possibility of the formation of different structures with the same chemical formula of $C_{11}H_9^+$.

Molecular dynamics simulations with the electronic structure computed at the density functional based tight binding (DFTB) level were performed by Dr. Aude Simon (see Section 1.3.2) in order to get insights into the possible structures of the dissociation products of $NapCH_3^+$. These consisted in 1620 simulations of 500 ps. The internal energy of $NapCH_3^+$ was fixed at about 14 eV, which is the lowest energy for which sufficient dissociation is observed in a reasonable computational time. As depicted in

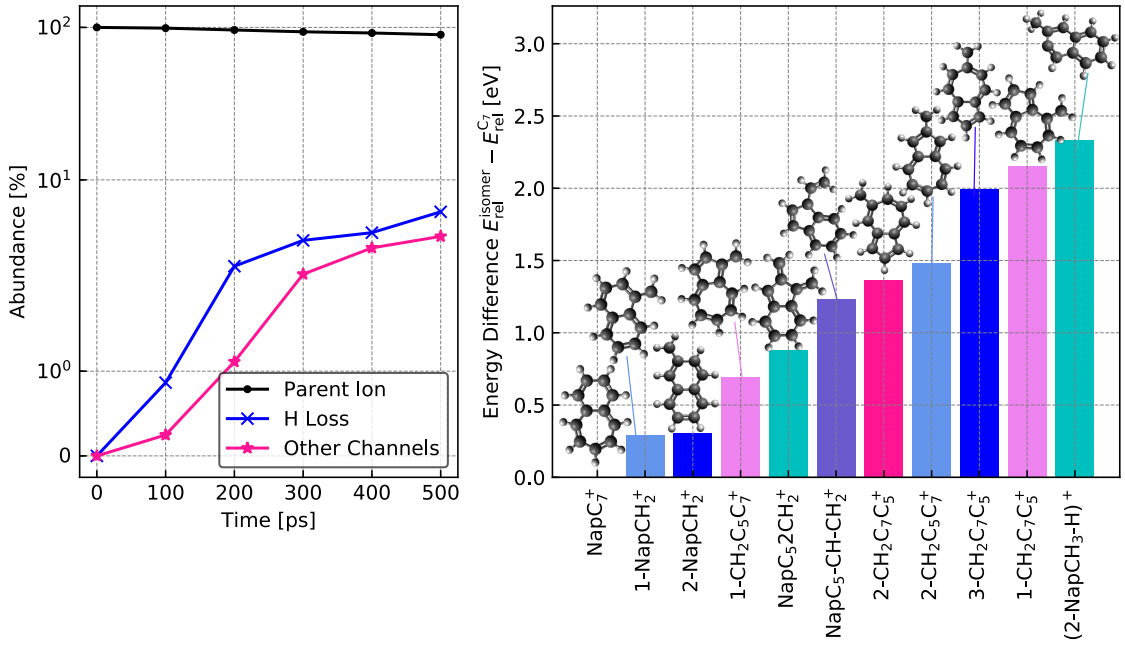

Figure 5.11: Left panel: Dynamics of the dissociation process of $C_{11}H_{10}^+$, $NapCH_3^+$. Right panel: Energy differences of the isomer structures compared to the lowest energy structure, $NapC_7^+$.

the left panel of Figure 5.11, the loss of an H atom from the methyl sidegroup was observed to be the major channel. Several isomeric structures of the dehydrogenated species were observed to be formed and were further reoptimized at the DFT level. The possible isomer structures of $C_{11}H_9^+$ are presented in the right panel of Figure 5.11 in order of energy difference. The energy reported here is set in relation to the lowest energy structure, $NapC_7^+$, meaning the energy of $NapC_7^+$ was set to zero. We see that the 1-$NapCH_2^+$ and the 2-$NapCH_2^+$ isomer structures are quasi-degenerate with an energy difference of only $0.02\,\mathrm{eV\,mol^{-1}}$. It would be of interest to estimate an isomerization barrier between these two isomers.

In order to complement the theoretical investigation of other possible isomer structures, the theoretical IR spectra of all proposed structures (*cf.* Figure 5.11, right panel) were calculated accordingly in the harmonic approximation at the DFT level and are presented in Figure 5.12. The IR spectra are reported in the same relative energy order as in Figure 5.11 and can directly be compared to the experimentally obtained IRPD spectrum of $C_{11}H_9^+$ which is shown in Figure 5.10 (c).

Showing similar features in the IR spectra as the 2-$NapCH_2^+$, especially in the $750-$

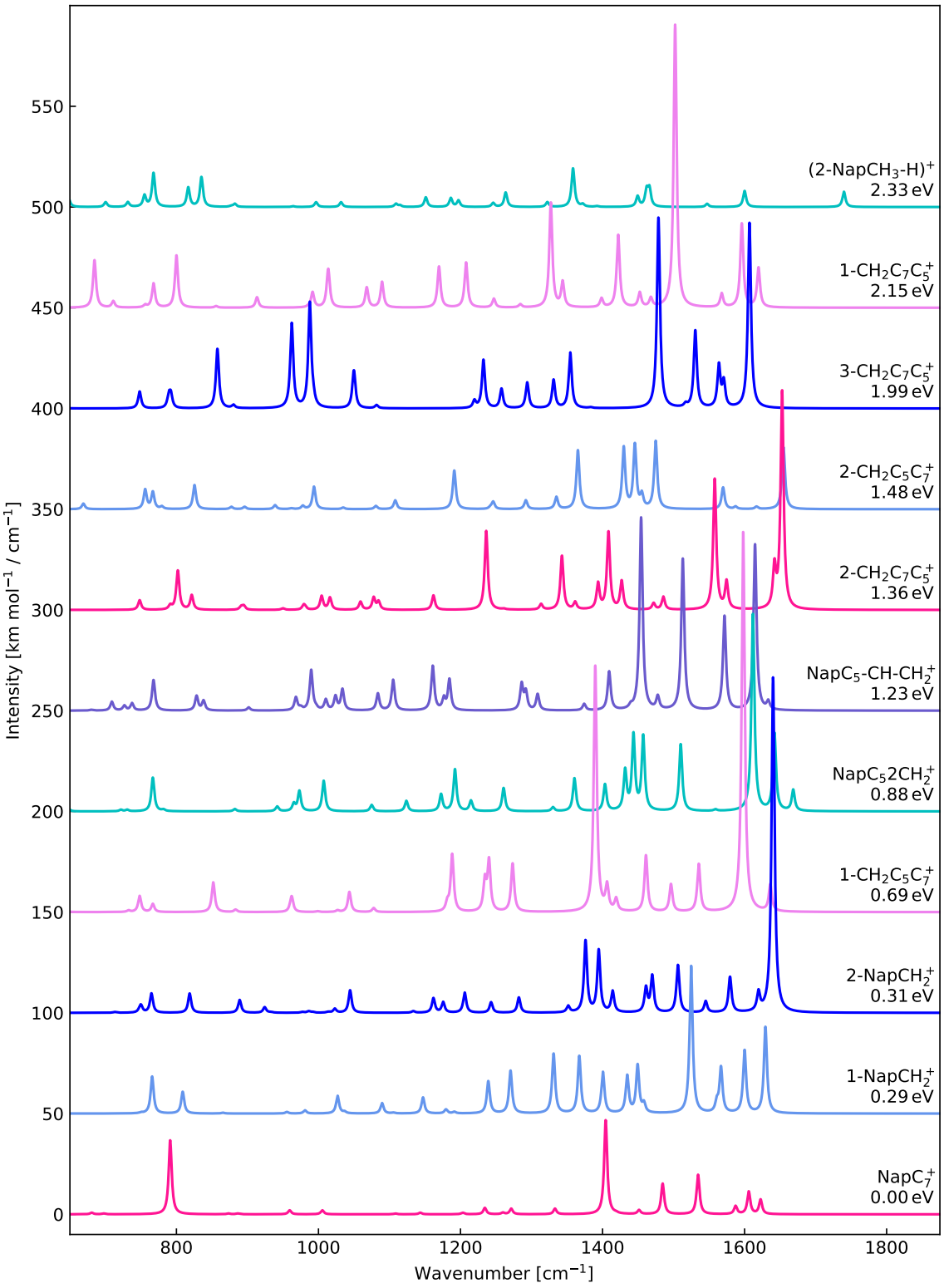

Figure 5.12: Theoretical harmonic IR spectra of $C_{11}H_9^+$ isomer structures which are presented in Figure 5.11 in order of relative energy.

850 cm^{-1} range, we cannot exclude the presence of 1-NapCH_2^+ in the ion trap. However, the spectroscopic evidence is not conclusive enough.

5.7 Evolution with Size

The here presented study on the –H fragments of methylated PAH cations gives insights into the possibility of formation of isomers of these species upon dissociative ionization of their neutral precursor molecule. Our findings are summarized below.

5.7.1 Summary of Results

Of the investigated –H fragments of the methylated PAH cations, namely fragments of 1-methylpyrene, 2-methylanthracene, and 2-methylnaphthalene, we observed different behavior in the formation of isomers according to the molecular size of the examined species.

In the case of $C_{17}H_{11}^+$, we mostly observed the formation of PyrCH_2^+. In fact, none of the observed bands could be attributed to PyrC_7^+. This is in line with our IRMPD spectrum (*cf.* Figure 5.2) which was recorded in an earlier campaign, as well as with DFT calculations performed by West *et al.* [130] (*cf.* Figure 5.8). We tested the idea put forward by West *et al.* [130] that the formation of the 7-membered carbon ring can be prevented by the ring strain imposed on the C_7 ring in the compact pyrene molecule by choosing two acene-like precursors. Due to their structure, such ring strain should be relaxed in the 2-methylanthracene and the 2-methylnaphthalene fragments.

The IRPD spectrum of $C_{15}H_{11}^+$ shows many features which can be attributed to both possible isomers, AntCH_2^+ and AntC_7^+. However, our saturation depletion measurements of $C_{15}H_{11}^+$ on two different resonance bands were not conclusive enough to confirm the formation of a C_7 ring in this ion.

Only for the smallest species studied, $C_{11}H_9^+$, we can clearly confirm the presence of a 7-membered carbon ring, NapC_7^+, together with the expected 2-NapCH_2^+. In this particular case, however, we cannot exclude the potential presence of a third isomer, namely 1-NapCH_2^+ (see Section 5.6.4).

Together with the results of $C_7H_7^+$ obtained by Jusko *et al.* [209] who confirmed the formation of both the tropylium and the benzylium cation, we conclude that the

possibility to form the two different isomers upon electron impact decreases with the molecular size of the examined species.

5.7.2 Toward Changing the Isomer Mixture

According to recent calculations of Rapacioli *et al.* [140], the isomer $PyrC_7^+$ might be formed not as a product of the dissociative ionization of 1-methylpyrene, but through an isomerization process starting from $PyrCH_2^+$ (and vice versa) when overcoming a barrier of $3.5 - 4\,\text{eV}$. For our smallest parent ion, $C_{11}H_9^+$, a similar isomerization energy barrier was determined to be $\sim 3\,\text{eV}$. In order to examine the isomerization between the two isomeric structures, we tried to probe the isomerization energy barrier by tuning the electron energy of the electron impact ionization source. This was successfully performed by Jusko *et al.* [209] who modified the ratio of the isomers in the dissociative ionization of toluene. Figure 5.13 depicts the relative depletion of the fingerprint region of $NapC_7^+$ and $NapCH_2^+$ between 740 and $845\,\text{cm}^{-1}$ recorded with different electron energies, E_{e^-}. Apart from the lower signal for an electron energy of $-13.0\,\text{eV}$, the band ratios and, thus, the isomer ratio do not change for any of the tested electron energy configurations.

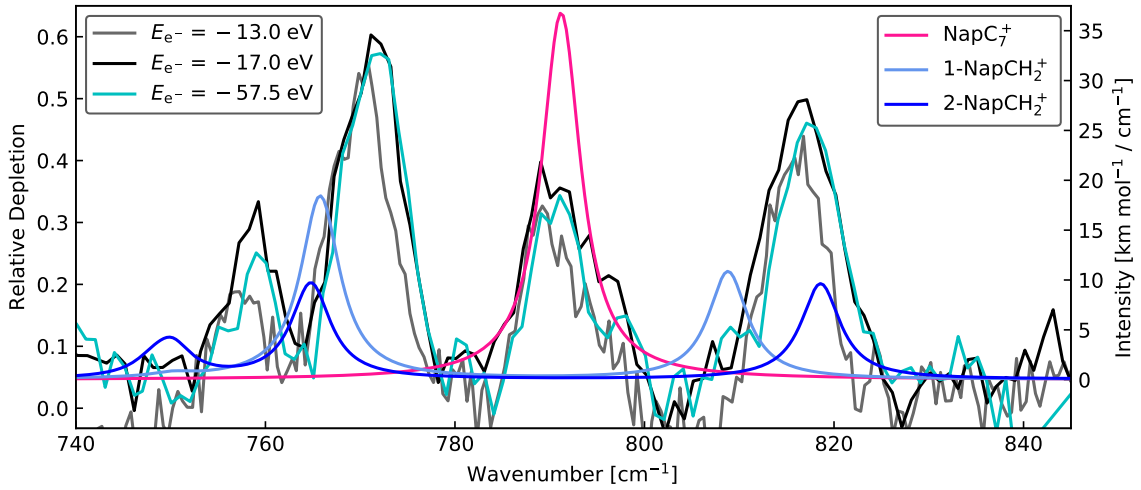

Figure 5.13: Relative depletion of $C_{11}H_9^+$ recorded for different electron energies in the electron impact ionization source in comparison to the theoretically calculated IR spectra of the three lowest energy geometries.

As a second more controlled approach to overcome the isomerization energy barrier,

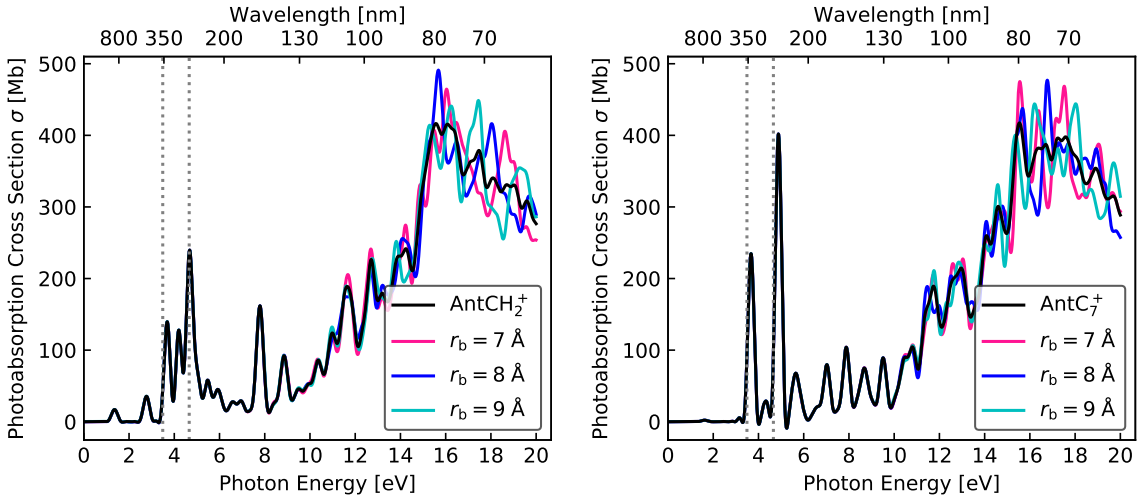

Figure 5.14: Theoretically calculated photoabsorption cross sections of the isomeric structures of $C_{15}H_{11}^+$, $AntCH_2^+$ and $AntC_7^+$, for three different radii, r_B, of the simulation sphere. The black curve corresponds to the averaged photoabsorption cross sections and the dotted lines depict the third and fourth harmonic of a Nd:YAG laser.

we had proposed to use a pump laser coupled to the FELion ion trap. Depicted in Figure 5.14 are the photoabsorption cross sections of $AntCH_2^+$ and $AntC_7^+$ which were calculated by the use of the real time, real space implementation of time dependent density function theory (TD-DFT) from the OCTOPUS code [142]. Please note that this method was presented in Section 3.3 and discussed in detail in Section 4.4.3. The different colors correspond to different simulation box sizes, which in this case were selected to be spheres with varying radii, $r_b = 7, 8, \text{or } 9$ Å. Since it was suggested that isomerization of the –H fragment of the 1-methylpyrene cation might occur under photoactivation in the ISM [140], it would be interesting to try to pump the isomerization process of $C_{15}H_{11}^+$. For this purpose, a Nd:YAG laser either in its third (355 nm) or fourth harmonic (266 nm) could be used. The dotted lines in Figure 5.14 depict the photon energies of these two harmonics and show that the two proposed isomeric structures easily absorb this energy. Unfortunately for the run in June and July 2019, the setup was not yet readily equipped with a Nd:YAG laser, hence, this method to overcome the isomerization energy barrier remains untested up to date.

6 | Astrophysical Relevance and Perspectives

Outline

6.1 Astrophysical Implications

This PhD work concentrated on studying different aspects of energy relaxation in the case of isolated PAH cations, which can be of relevance when modeling the chemical evolution of these species in astrophysical environments. The study of the interaction of large PAH cations with VUV photons presented in Chapter 4 has direct astrophysical implications. The two relaxation channels which could be examined, *i.e.*, photoionization and photodissociation, were quantified by recording action spectra and deducing absolute cross section values. We found that the photoionization branching ratio increases with increasing number of carbon atoms, N_C, and that even the formation of trications is possible for photon energies slightly above 13.6 eV. The variation of the charge state of the astro-PAH population is expected to affect both the UV extinction curve [119] and the AIB emission spectra [38]. For example, the cavity around the star in NGC 7023 is expected to be an environment containing large PAH^+ and PAH^{2+} [55, 219], possibly impacting the heating of the gas by photoelectric effect and the AIB emission. Some first IR action spectra of large PAH cations and dications have been recorded by Zhen *et al.* [101, 102], providing promising results about large ionized PAHs being good candidates as carriers of the AIBs. On this account, we provide recipes that can be used in models to quantify the charge state of large PAH cations and their photoionization yield in Sections 6.1.1 and 6.1.2, respectively, which were also part of the publication by Wenzel *et al.* [127].

In Chapter 5, we focused on a more fundamental aspect, which concerns the isomeric structures of the –H fragments of methylated PAHs. These have been probed thanks to the IRPD spectroscopy of cold PAH ions tagged with Ne that is available at the FELion setup at the free electron laser facility, FELIX. Methylated PAHs are expected to be present in space [45] and the formation of their photofragments in various isomeric forms has to be considered since it impacts their IR signatures and therefore our ability to identify them in astronomical spectra, as we discuss in Section 6.1.3.

6.1.1 Charge State of Astro-PAHs

Modeling studies on the charge state of astro-PAHs have considered that these species could reach the dication and marginally the trication states [8, 38, 55]. In Section 4.4.1 and Table 4.1 we reported the appearance energies, AE^{2+} and AE^{3+}, for ionization

processes as $PAH^+ \rightarrow PAH^{2+}$ and $PAH^{2+} \rightarrow PAH^{3+}$, respectively. We combine these experimental ionization onsets with the ones found by Zhen *et al.* [133] and experimentally obtained ionization potentials, IP^{exp}, describing processes from $PAH^0 \rightarrow PAH^+$ from Clar *et al.* [220] and Hager and Wallace [221]. We compare these experimental values to the adiabatic ionization potentials, IP^+, IP^{2+}, and IP^{3+}, as obtained from calculations [142] in Figure 6.1.

This data set can be described following a formalism which starts from a classical model of the energy it takes to remove one electronic charge from a small, conducting particle. The analytical description given by Weingartner and Draine [222] considers conducting spheres in addition to an empirical correction term to account for quantum effects as well as for the planar (instead of spherical) PAH geometry. It aims to estimate the first and second ionization potentials of PAHs as a function of their charge, z, and effective radius, a, with

$$\mathrm{IP}^{(z+1)+} = W + \frac{1}{4\pi\varepsilon_0}\left[\left(z+\frac{1}{2}\right)\frac{e^2}{a} + (z+2)\frac{e^2}{a}\frac{0.03\,\mathrm{nm}}{a}\right]\frac{1\,\mathrm{C}}{e} \tag{6.1}$$

where ε_0 is the vacuum permittivity in $\frac{\mathrm{F}}{\mathrm{nm}}$, e is the elementary charge in C, W is the work function of bulk graphite, $W = 4.4\,\mathrm{eV}$, and a is proportional to N_C via the relation

$$a = \sqrt[3]{\frac{N_\mathrm{C}}{468}}. \tag{6.2}$$

Adjusting Equation (6.1) [see 222, Equation (2)] for $z = 1$ and $z = 2$ to the $IP^{(z+1)+}$ and $AE^{(z+1)+}$ values reported in Figure 6.1, we find that a value of $W = 3.9\,\mathrm{eV}$ fits our data better than the work function value of $W = 4.4\,\mathrm{eV}$ of bulk graphite. This is in line with W values of about 4.0 eV as calculated for similarly sized PAHs by Kvashnin *et al.* [223]. This adjustment corresponds to a vertical shift and somehow depends on the considered data set, experimental or theoretical. For instance, we see that our reported values for $AE^{(z+1)+}$ are systematically slightly above the DFT values (*cf.* Table 4.1). However, the empirical formula, Eq. (6.1) which was adjusted for $z = 0, 1$ by Weingartner and Draine [222] appears also to be appropriate for $z = 2$ yielding a satisfactory model for all z values considered ($z = 0, 1, 2$).

From Figure 6.1 and Equation (6.1), it is obvious that a certain fraction of absorbed photons in H I regions is able to induce photoionization of the studied PAH cations.

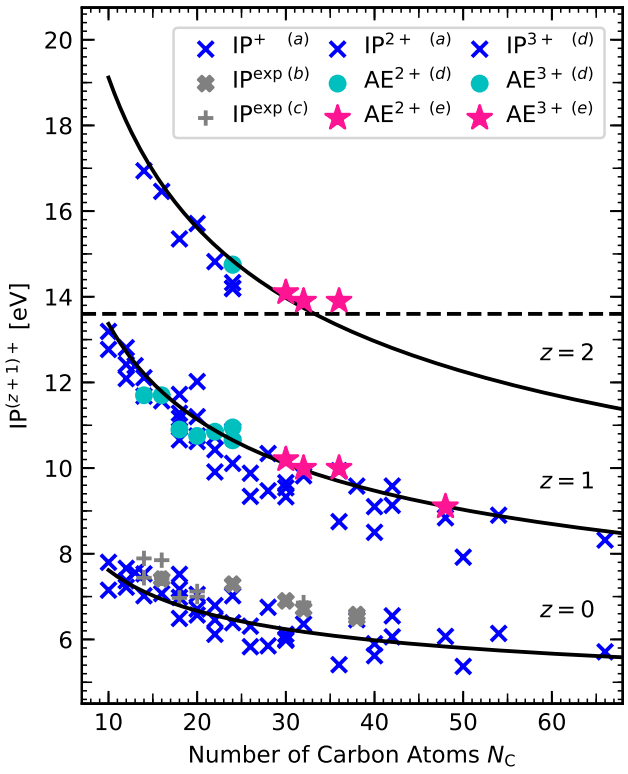

Figure 6.1: Theoretically calculated adiabatic ionization potentials, $\mathrm{IP}^{(z+1)+}$, experimentally obtained $\mathrm{IP}^{\mathrm{exp}}$, and appearance energies, $\mathrm{AE}^{(z+1)+}$, as a function of number of carbon atoms, N_C. They correspond to transitions from $\mathrm{PAH}^{z+} \rightarrow \mathrm{PAH}^{(z+1)+}$ for $z = 0, 1, 2$. The black curves are adapted from Weingartner and Draine [222] as an estimate of the $\mathrm{IP}^{(z+1)+}$ evolution as a function of PAH size and charge, z (see Equation (6.1) and text for details). The dashed horizontal line marks the 13.6 eV photon energy cut-off for H I regions.

[a] Taken from Malloci *et al.* [79].
[b] Taken from Clar *et al.* [220].
[c] Taken from Hager and Wallace [221].
[d] Taken from Zhen *et al.* [133].
[e] This work.

Considering the theoretically computed absorption and experimental ionization cross sections, which have been presented in Section 4.4.4.2 and shown in Figure 4.11, and taking into account the radiation field of the prototypical NGC 7023 NW PDR [5], it can be estimated that typically one over three photons in the $[10 - 13.6]$ eV range which are absorbed by PAH cations with $N_\mathrm{C} = 30 - 36$ will lead to photoionization.

The fraction of ionizing events will increase with increasing carbon number as the ionization potential shifts to lower energies the larger the PAH (*cf.* Equation (6.1)). For our largest PAH studied, $C_{48}H_{20}^+$, the ionization fraction reaches a value of 0.5. In this context, we also note that the formation of C_{60}^{2+} will be more difficult to achieve than that of a PAH^{2+} of similar size, because the corresponding cations have relatively similar absorption cross sections but the value of AE^{2+} for C_{60}^+ is with (10.5 ± 0.1) eV as obtained by Douix *et al.* [208] significantly higher compared to 8.7 eV for a PAH^+ with $N_C = 60$ as can be deduced from Figure 6.1.

6.1.2 Photoionization Yield for Astrophysical Modeling

Photoionization yields of the four large PAH cations studied can be derived by dividing their experimental photoionization cross section, σ_I^C, by the theoretically computed photoabsorption cross section, $\sigma_{abs,\,theo}^C$. The precision of both the experimental and theoretical cross sections can impact the structure and the values of the photoionization yields which are presented in Figure 4.12. As can be seen from Figure 4.11 and the left panel of Figure 4.12, at energies below 14 eV, the presence of bands in $\sigma_{abs,\,theo}^C$, which are not present in σ_I^C, can induce spectral features in the photoionization yields, such as the peak obtained for $C_{32}H_{14}^+$ at 12 eV, which are therefore as precise as the calculated spectrum. Still, the photoionization yields displayed in the left panel of Figure 6.2 show comparable features for the studied PAH cations, with a rise starting at the appearance energies for ionization, AE^{2+}, the plateau in the 11.3 to 12.9 eV range followed by another rise to reach the maximum. As discussed in Section 4.4.4.2, the maximum values of the photoionization yields are subjected to uncertainty because of the unknown contribution from σ_{rad}. In the following, we made the hypothesis that the contribution of σ_{rad} at high photon energies, *i.e.*, 20 eV, is minor and that the photoionization yields are limited by the photoionization branching ratio, which never reaches unity as shown in Figure 4.6. The mean values at high energies of the photoionization yields were thus scaled using the photoionization branching ratio value at 20 eV.

Previously, photoionization yields have also been derived for neutral PAHs from experimental studies performed by Verstraete *et al.* [122] and Jochims *et al.* [123]. The latter authors have proposed a *rule of thumb* to facilitate the implementation of this

yield into astrophysical models, consisting of a linear function of the photon energy with dependence on the ionization potential, IP^+. We propose to use a similar approach to describe the evolution of the presented photoionization yield of PAH cations with carbon number. The resulting function, Y^+_{ion}, is based on the above described ionization regimes which occur in different energy ranges as

$$Y^+_{\mathrm{ion}}[N_{\mathrm{C}}](h\nu) = \begin{cases} 0 & h\nu < \mathrm{IP}^{2+} \\ \frac{\alpha}{11.3\,\mathrm{eV} - \mathrm{IP}^{2+}}(h\nu - \mathrm{IP}^{2+}) & \mathrm{IP}^{2+} \leq h\nu < 11.3\,\mathrm{eV} \\ \alpha & \text{for} \quad 11.3\,\mathrm{eV} \leq h\nu < 12.9\,\mathrm{eV} \\ \frac{\beta(N_{\mathrm{C}}) - \alpha}{2.1\,\mathrm{eV}}\,(h\nu - 12.9\,\mathrm{eV}) + \alpha & 12.9\,\mathrm{eV} \leq h\nu < 15.0\,\mathrm{eV} \\ \beta(N_{\mathrm{C}}) & h\nu \geq 15.0\,\mathrm{eV}, \end{cases} \tag{6.3}$$

where $\alpha = 0.3$ is the value of the plateau and β depends on N_{C} with

$$\beta(N_{\mathrm{C}}) = \begin{cases} 0.59 + 8.1 \cdot 10^{-3} N_{\mathrm{C}} & \text{for} \quad 32 \leq N_{\mathrm{C}} < 50 \\ 1 & N_{\mathrm{C}} \geq 50. \end{cases} \tag{6.4}$$

The reported $\beta(N_{\mathrm{C}})$ function is based on the photoionization branching ratio values at 20 eV as deduced from Figure 4.6. Neglecting a possible contribution of σ_{rad} to the photoabsorption cross section, the β values can be considered as maximum values to be reached by the respective PAH cation. The $\beta(N_{\mathrm{C}})$ function was found to increase linearly with N_{C} for the studied size range as expressed by Equation (6.4). Extrapolation to larger sizes leads to a β value of 1 for $N_{\mathrm{C}} \geq 50$. This trend differs from the case of neutral PAHs for which Jochims *et al.* [123] concluded that the maximum of $\beta = 1$ is independent of size which was in agreement with previous measurements by Verstraete *et al.* [122].

In the right panel of Figure 6.2, examples of $Y^+_{\mathrm{ion}}[N_{\mathrm{C}}](h\nu)$ are displayed, which were calculated from Equations (6.3) and (6.4), illustrating the variability of $Y^+_{\mathrm{ion}}[N_{\mathrm{C}}](h\nu)$ with the size of the PAH. According to $\beta(N_{\mathrm{C}})$ from Equation (6.4), no significant variation of the photoionization yield is expected for PAH cations with $N_{\mathrm{C}} \geq 50$. In their PAH evolution model, Andrews *et al.* [55] have considered the yield of PAH cations based on the *rule of thumb* given by Jochims *et al.* [123] for neutrals but considering the appropriate photoionization potential for cations to dications, *i.e.*, values of IP^{2+}. To illustrate the impact that this approximation may have on the model results, we report in Figure 6.2 these estimated yields and compare them with

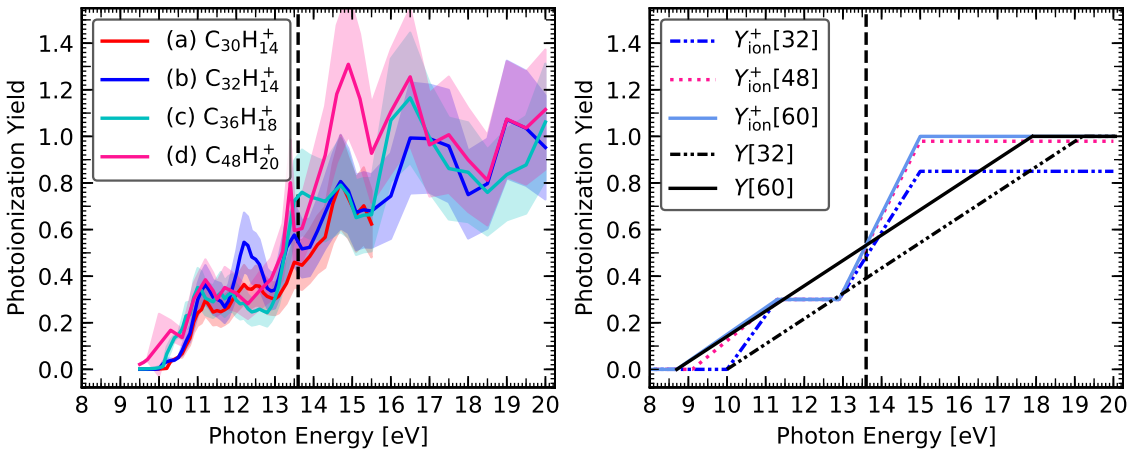

Figure 6.2: Left panel: Photoionization yields of the studied cations derived from the experimental ionization and theoretical absorption cross sections (*cf.* Figure 4.11) and scaled as explained in Section 6.1.2. Right panel: Photoionization yields, $Y_{\rm ion}^+[N_{\rm C}](h\nu)$, calculated from Equations (6.3) and (6.4) for PAH cations with $N_{\rm C} = 32$, 48, and 60 atoms. For comparison, the photoionization yields, $Y[N_{\rm C}](h\nu)$, for $N_{\rm C} = 32$ and 60, are displayed. They were estimated using the Equations (4) and (5) from Jochims *et al.* [123] adapted for neutral PAHs but taking into account the shift of the ionization potential to IP^{2+}, which is relevant for cations. The dashed vertical line marks the 13.6 eV photon energy cut-off for H I regions.

our recommended yields by integrating from IP^{2+} to 13.6 eV. We found that for a medium-sized PAH, as represented by $N_{\rm C} = 32$, our integrated yield is larger by 35 % compared to the previously available one, whereas for large PAHs, as represented by $N_{\rm C} = 60$, it is smaller by 11 %. These simple estimates are however not conclusive and astrophysical models have to be run to evaluate the impact on the photoionization of the PAH population in specific astronomical environments.

6.1.3 Methyl and Methylene Sidegroups attached to PAHs

As shown by Joblin *et al.* [45], methylated PAHs are good candidates to account for the 3.40 μm emission band, which is observed as a satellite of the 3.29 μm band in the AIB spectra. The photodissociation of these species is expected to lead to the –H fragments. We have shown in Chapter 5 that the formation of the methylene structure, the benzylium-like –H fragment isomer with a CH_2 instead of a CH_3 sidegroup attached, is the one observed as the PAH grows in molecular size. This observation

is also rationalized by DFT calculations [130].

In our experiments, only the smallest PAH studied, 2-methylnaphthalene, led to the formation of a 7-membered ring –H fragment isomer. We can neglect the consideration of this smallest tropylium-like isomer, $NapC_7^+$, in the astrophysical context as we only expect large PAHs to be carriers of the AIBs [54]. Based on DFT calculations, Yang *et al.* [224, 225] tried to address the differences in band intensity and position of the C–H stretching features in the $3.2 - 3.5\,\mu$m region by attaching different sidegroups to PAHs. Their structural study implies that due to the sidegroup attached, the band positions of the 3.3 and $3.4\,\mu$m aromatic and aliphatic C–H feature might shift. Still, the authors have not considered the features related to the formation of CH_2 sidegroups, which are expected to be formed upon photodissociation of methylated PAHs. We therefore present here the theoretically computed $3.1 - 3.5\,\mu$m spectral region of the three studied methylated PAH cations and their methylene fragments. Figure 6.3 (a) – (c) displays the calculated IR spectra for the methyl- and methylene-derivatives of the pyrene-, anthracene-, and naphthalene-like cations, respectively. Panel (d) of Figure 6.3 depicts the averaged spectra of the two main groups. The satellite band close to $3.4\,\mu$m which is due to the aliphatic C–H stretch of the CH_3 sidegroups can be clearly observed.

The spatial evolution of the emission bands at 3.29 and $3.40\,\mu$m in the prototypical PDR NGC 7023 has been studied with the use of AKARI-IRC IR spectra by Pilleri *et al.* [226]. Two of these spectra measured at positions P1 and P2, where P1 is closer to the star HD 200775 than P2, are shown in the bottom panel (b) of Figure 6.4. At position P2, the bands at 3.29 and $3.40\,\mu$m can be clearly observed and the $3.29\,\mu$m shows a shoulder-like shape on the blue side of the spectrum. When getting closer to the star, at position P1, the spectrum evolves. The two main differences are (i) the disappearance of the $3.40\,\mu$m band which belongs to the aliphatic C–H stretch of the CH_3 group, and (ii) the increase of the shoulder at $\sim 3.29\,\mu$m. For comparison, our averaged calculated IR spectra for the CH_3 and CH_2 sidegroup PAHs from Figure 6.3 (d) are displayed in Figure 6.4 (a). It is not possible to compare these two spectra in detail since they involve different PAH sizes but also very different physical conditions: DFT spectra are calculated at 0 K whereas the AIBs result from the cooling of very hot PAHs (see Section 1.1.5.1). Still, we can note some general trends in the spectrum of the CH_2 sidegroup species relative to their parent methylated PAH

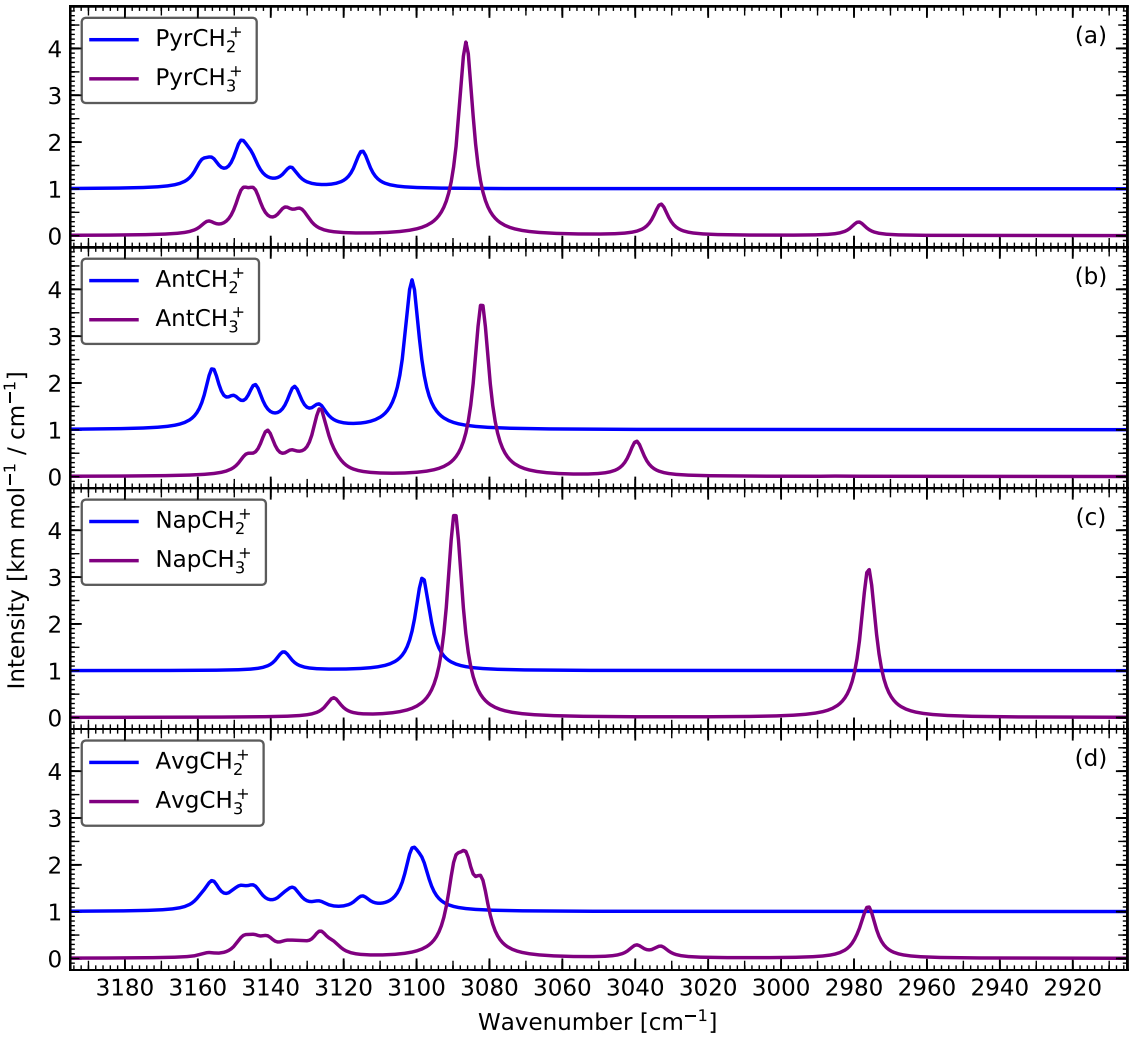

Figure 6.3: Theoretically calculated IR spectra of three methylated PAHs and their –H fragments in which they lost an H atom from their methyl sidegroup, for (a) 1-methylpyrene, $C_{17}H_{12}^{+}$, (b) 2-methylanthracene, $C_{15}H_{12}^{+}$, (c) 2-methylnaphthalene, $C_{11}H_{10}^{+}$, and (d) the average of both the CH_3 and the CH_2 group cations.

cations. On the one hand, no features are present on the red side of the aromatic C–H stretch, including the range of the 3.4 μm band. On the other hand, there is an increasing contribution of bands on the blue side of the aromatic C–H stretch range. Although we cannot strictly identify the contribution of the CH_2 sidegroup PAHs in the AIB spectra, the observed evolution of the AKARI-IRC spectra when getting closer to the star, from position P2 to P1, is consistent with the photodissociation of

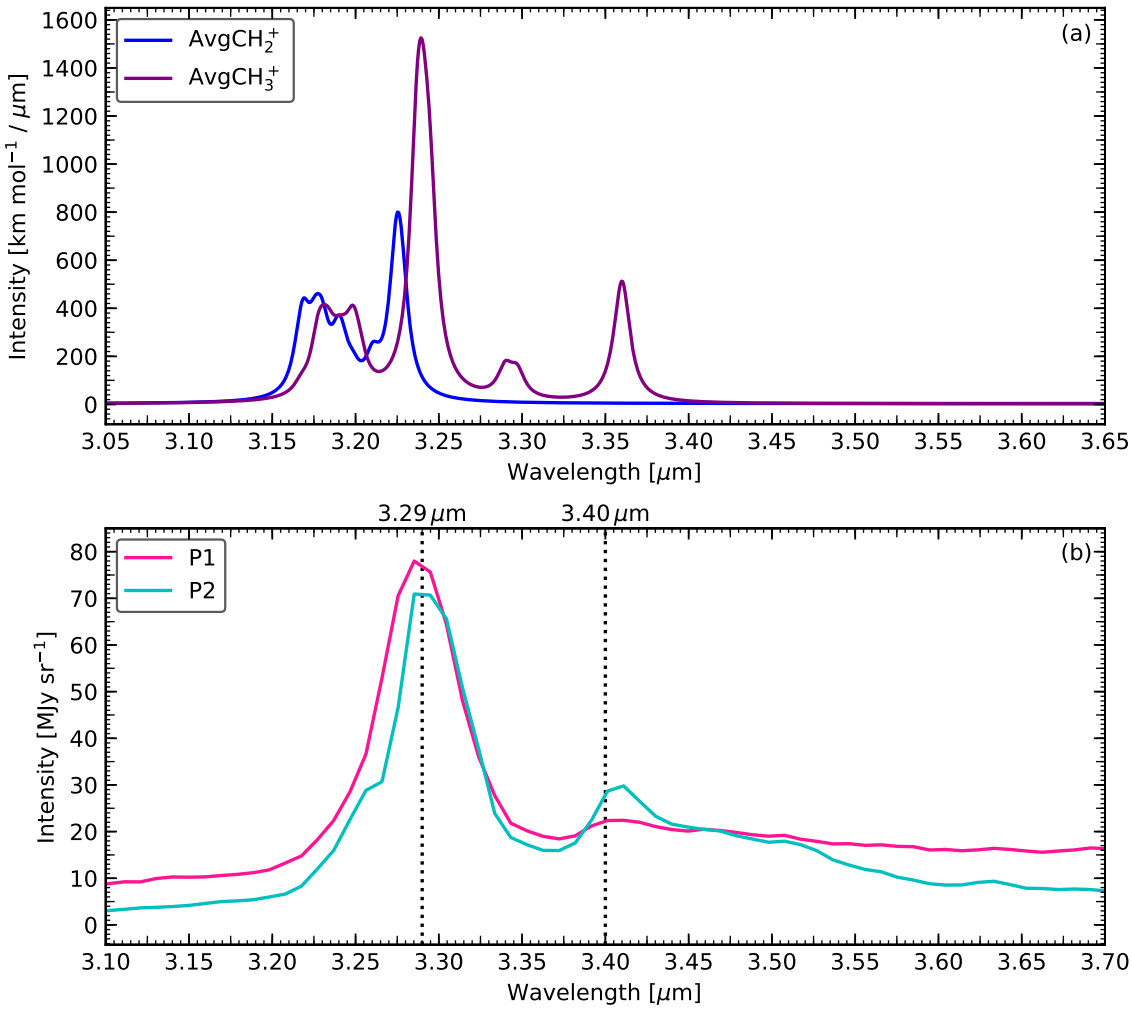

Figure 6.4: (a) Averaged theoretically calculated IR spectra of the three methylated PAH cations with CH_3 sidegroups and their –H fragments with CH_2 sidegroup. (b) AKARI-IRC spectra observed at two positions, P1 and P2, near the star HD 200775 with P1 being closer to the star than P2. Taken from Pilleri *et al.* [226]. The vertical dotted lines mark the 3.29 μm and 3.40 μm emission feature positions.

the CH_3 sidegroup PAHs and the formation of methylene-PAH species.

6.2 Laboratory Astrophysics Perspectives

The focus of this PhD work was the investigation of relaxation processes of energized PAHs as a function of photon energy and molecular properties. We examined especially their ionization and dissociation upon VUV photon absorption and probed the formation of different isomers from the dissociative ionization of methylated PAHs. For the former, this study provides a quantitative analysis of the photoionization and photodissociation of large PAH cations, providing the branching ratio between these two processes and action spectra. Additionally, we derived experimental cross sections and proposed estimates for the PAH charge state and the photoionization yield to be used in astrophysical models.

This work opens many perspectives. For instance, it emphasized the need to obtain accurate values of the photoabsorption cross sections, both from TD-DFT calculations and from experiments. It would also be of interest to extend this study to even larger PAH cations such as, for instance, circumcoronene, $C_{54}H_{18}$, circumovalene, $C_{66}H_{20}$, and circumcircumcoronene, $C_{96}H_{24}$, as these have been considered in models and are expected to survive in interstellar conditions [54]. For this purpose, a different ionization technique than APPI would have to be employed because these large PAHs are insoluble in solvents.

With experiments using FELion, it can be of interest to extend the measurements in the range of the C–H stretches. For our beamshifts, the FELIX laser was optimized for the $600 - 1800\,\mathrm{cm}^{-1}$ range to investigate the various isomeric species of interest. Tuning FELIX to the right photon energy is time-consuming and can thus only be performed once per beamshift. It was therefore not possible to experimentally probe at the same time the $3.0 - 3.5\,\mu$m region and one would need dedicated beamshifts for this task. Additionally, the presented theoretical IR spectra were calculated for harmonic frequencies and their band positions strongly depend on the applied scaling factor, here 0.978 (see Section 5.4.2), which shall correct for anharmonic effects at 0 K. The choice of this anharmonicity factor is not trivial and anharmonic calculations [see for example 94, 227–229] have to be performed in order to properly evaluate this region and to support the interpretation of possible future experiments on these systems.

In general, isomerization processes of molecules in the ISM are of relevance as they can be photoactivated by stellar radiation [210], but not much is yet known about them

and the competition between fragmentation and isomerization has yet to be evaluated to be used in astrophysical models. Efforts to identify isomers and to characterize isomerization processes of PAHs in the laboratory have been attempted [141, 161, 230], but these studies have to be supported by molecular dynamics simulations in order to evaluate the formation of isomeric structures as has been performed in the case of the –H fragment of the 1-methylpyrene cation [214]. The use of cryogenic ion trap setups such as FELion unlocks the investigation of these isomers by freezing them after formation and tagging them with a noble gas atom to record their spectroscopic fingerprints. The spectroscopy of the cold tagged ions can be performed, either to reveal their different isomeric structures without heating the ions, or to obtain spectroscopic information of astro-PAHs in correlation with the identification of potential carriers of the DIBs, which has been successfully performed in the case of C_{60}^+ [25, 231].

During this PhD and as a preparation for the collaboration concerning an experimental campaign on the radiative cooling of PAH isomers at DESIREE, an electronic spectrum of the cold phenanthrene cation has been recorded using an MPD scheme with the cryogenic PIRENEA setup, displaying an absorption band at ∼460 nm (see Appendix A). Although the probed ions are expected to be cold, the shape and position of the observed band could be affected by the MPD scheme because of the heating following the sequential absorption of photons by the ions. Complementary experiments making use of a one-photon absorption scheme as those performed at FELion are needed to investigate this point.

The study of astro-PAHs through laboratory astrophysics has motivated the use of complex experimental setups to investigate their physical and chemical properties in conditions that approach those found in astrophysical environments. It inspires and requires the construction of more and more sophisticated machines such as, for instance, the new PIRENEA2[(8)] setup. PIRENEA2 is a cryogenic tandem mass spectrometer that will be dedicated to study the interaction of cosmic dust analogs and PAHs with photons and gas under interstellar conditions [232]. This setup is currently being assembled and tested in a collaboration between the two research laboratories, IRAP and LCAR, in Toulouse.

[(8)] http://nanocosmos.iff.csic.es/?page_id=49

Conclusions [en]

This PhD thesis is part of laboratory astrophysics studies aiming to gather new molecular data to better model the chemical evolution of PAHs in PDRs upon UV irradiation. More specifically, we have scrutinized two main aspects. One focused on the competition between ionization and fragmentation of large PAH cations, another concerned the possibility of isomerization of the –H fragments of methylated PAH cations.

During our SOLEIL campaign, we used a linear ion trap coupled to the synchrotron radiation in order to study the interaction of trapped PAH cations with UV photons. In particular, we examined the ionization and dissociation channels for four large PAH cations ranging in size from 30 to 48 carbon atoms and absorbing VUV photons in the 9 to 20 eV range. We presented their action spectra and branching ratios, and aimed to determine their photoionization and photodissociation cross sections by utilizing a reference cross section. We conclude that

- below 13.6 eV, the formation of a hot ion with subsequent radiative cooling is the dominant relaxation channel. This is followed by photoionization with a yield which reaches approximately 0.5 at 13.6 eV. The photoionization yield features a plateau extending over an energy range of $11.3 - 12.9$ eV with a value of approximately 0.3. This suggests that there is a strong coupling between electronic and nuclear states in this energy range. It would be of interest to investigate the dynamics of the relaxation of these excited electronic states using fs pump-probe experiments [62].

- at 20 eV, dissociation is observed for all studied PAH cations, implying that the photoionization yield does not reach a value of 1, which is different from

what was observed in previous studies on neutrals. We found that the photoionization branching ratio increases with molecular size and reaches 0.98 for the largest studied cation, dicoronylene, $C_{48}H_{20}^{+}$. Additionally, we were not able to quantify the possible contribution of the formation of a hot ion that would subsequently relax by radiative cooling in isolated conditions, which would further lower the maximum of the photoionization yield. It would be interesting to further investigate the difference observed between neutrals and cations in order to unveil this charge effect.

From the astrophysical point of view, we proposed recipes to determine the ionization potential of PAH cations as a function of their N_C and their photoionization yield as a function of the absorbed photon energy. These recipes can be extended to larger molecular sizes of typically $N_C = 100$. Combining the photoionization yield with photoabsorption cross sections that are readily available from calculations using TD-DFT can be useful for models describing the chemical evolution of PAHs in PDRs.

For the FELIX beamtime, our aim was to shed light on a more fundamental aspect related to the isomerization of the –H fragments of methylated PAH cations. We studied the fragments of three methylated PAHs and experimentally probed their composition by means of vibrational predissociation spectroscopy of cold ions tagged (complexed) with Ne atoms. We were able to clearly identify the formation of different isomers in the case of the –H fragment of the 2-methylnaphthalene. In addition to the usually observed methylene sidegroup structure, at least one isomer with the tropylium-like form with a 7-membered ring was found to be present. Regarding the methylated anthracene precursor, the presence of the tropylium-like isomer remained ambiguous. In the case of 1-methylpyrene, however, it was clearly not present. Because of the available experimental conditions, the studied fragments were produced by dissociative ionization induced by electron bombardment. It would be of interest to repeat the measurements in the case of fragments formed by laser irradiation. Molecular dynamics simulations and DFT calculations can also help to interpret these data by identifying dissociation pathways and determining isomerization barriers.

Concerning the astrophysical regions considered in this work, the PDRs, we do not expect these small methylated PAHs to be abundant, as they would not survive the local UV radiation field. Nevertheless, we discussed how attached methyl and methy-

lene sidegroups to PAHs can impact the AIB spectrum in the $3.1 - 3.5\,\mu$m range by comparing their calculated IR spectra to the evolution of the spectra observed by AKARI-IRC in the prototypical PDR NGC 7023 as a function of the distance to the star HD 200775.

In summary, our work contributes to the view we can have on the evolution of astro-PAHs under UV irradiation. Still, the identification of specific species in this population remains open. A key issue concerns the formation of these molecules in astrophysical environments, most likely in the envelopes of evolved stars. This is a question at the heart of the NANOCOSMOS[(9)] project and some progress is expected in the coming years [233, 234]. In combination with the wealth of spectral and spatial information, which will soon be delivered by the *James Webb* Space Telescope, we can then expect to improve our understanding of the PAH population in the ISM, aiming at the identification of specific molecules and a better characterization of their role in the physics and chemistry of PDRs.

[(9)] `http://nanocosmos.iff.csic.es/`

Conclusions [fr]

Cette thèse fait partie des études d'astrophysique de laboratoire visant à recueillir de nouvelles données moléculaires pour mieux modéliser l'évolution chimique des PAH dans les PDR sous l'irradiation UV. Plus précisément, nous avons examiné deux aspects principaux. L'un porte sur la compétition entre ionisation et fragmentation pour des cations PAH de grande taille, l'autre concerne la possibilité d'isomérisation des fragments –H de cations de PAH méthylés.

Lors de la campagne à SOLEIL, nous avons utilisé un piège à ions linéaire couplé au rayonnement synchrotron afin d'étudier l'interaction de cations PAH piégés avec des photons UV. Plus spécifiquement, nous avons examiné les voies d'ionisation et de dissociation pour quatre PAH de grande taille entre 30 et 48 atomes de carbone, qui absorbent des photons VUV dans la gamme de 9 à 20 eV. Nous avons présenté leurs spectres d'action et les rapports de branchement, et avons cherché à déterminer leurs sections efficaces de photoionisation et de photodissociation en utilisant une section efficace de référence. Nous avons conclu que

- en dessous de 13,6 eV, la formation d'un ion chaud suivie de son refroidissement radiatif est le canal de relaxation dominant. Vient ensuite la photoionisation dont le rendement atteint environ 0,5 à 13,6 eV. Le rendement de photoionisation présente un plateau s'étendant sur une gamme d'énergie de $11{,}3 - 12{,}9$ eV avec une valeur d'environ 0,3. Dans ce domaine d'énergie, il semble exister un couplage fort entre états électroniques et états nucléaires. Il serait intéressant de sonder la dynamique de relaxation de ces états électroniques excités par des expériences de type pompe-sonde fs [62],
- à 20 eV, une contribution de la dissociation est observée pour tous les cations

PAH étudiés, ce qui implique que le rendement de photoionisation n'atteint pas une valeur de 1, ce qui diffère de ce qui a été observé précédemment pour des PAH neutres. Nous avons trouvé que le rapport de branchement de la photoionisation augmente avec la taille moléculaire et atteint 0,98 pour le plus grand PAH cation étudié, le dicoronylène, $C_{48}H_{20}^{+}$. De plus, nous n'avons pas pu quantifier la contribution possible de la formation d'un ion chaud qui se déesexciterait uniquement par refroidissement radiatif dans des conditions isolées, ce qui abaisserait encore le maximum du rendement de photoionisation. Il serait intéressant d'investiguer la différence observée entre neutres et cations afin de mieux comprendre cet effet de charge.

Du point de vue astrophysique, nous avons proposé des recettes afin de déterminer le potentiel d'ionisation de cations PAH en fonction de leur nombre d'atomes de carbone (N_C) ainsi que le rendement de photoionisation en fonction de l'énergie des photons absorbés. Ces recettes peuvent être étendues à des tailles moléculaires plus grandes, typiquement $N_C = 100$. La combinaison de ce rendement de photoionisation avec des sections efficaces de photoabsorption, qui sont relativement simplement calculées en utilisant la théorie de la TD-DFT, peut être utile pour les modèles décrivant l'évolution chimique des PAH dans les PDR.

Lors de la campagne à FELIX, notre objectif a été de mieux comprendre un aspect plus fondamental lié à l'isomérisation du fragment –H des cations PAH méthylés. Nous avons étudié les fragments de trois PAH méthylés et sondé expérimentalement leur composition au moyen de spectroscopie vibrationnelle de prédissociation impliquant des ions froids complexés avec des atomes de Ne. Nous avons pu identifier clairement la formation de différents isomères dans le cas du fragment –H du 2-méthylnaphthalène. En plus de la structure comprenant un groupement méthylène qui est habituellement observée, au moins un isomère de type tropylium avec un cycle à 7 atomes de carbone a été mis en évidence. Avec le méthylanthracène comme précurseur, la présence de l'isomère de type tropylium est restée ambigüe. Dans le cas du 1-méthylpyrène, cependant, cet isomère n'est clairement pas présent. En raison des conditions expérimentales disponibles, les fragments étudiés ont été produits par ionisation dissociative induite par bombardement électronique. Il serait intéressant de répéter les mesures pour des fragments formés par irradiation laser. Les simulations

de dynamique moléculaire et les calculs DFT peuvent également aider à interpréter les données obtenues en identifiant des chemins possibles de dissociation et en déterminant des barrières d'isomérisation.

Concernant les environnements astrophysiques considérés dans ce travail que sont les PDR, nous ne nous attendons pas à ce que ces petits PAH méthylés y soient abondants, car ils ne survivraient pas à l'irradiation par le champ de rayonnement UV local. Néanmoins, nous avons discuté de l'impact des groupements de type méthyl et méthylène sur le spectre AIB dans la région $3{,}1-3{,}5\,\mu$m en comparant les spectres IR calculés à l'évolution des spectres observés par AKARI-IRC dans la PDR prototype NGC 7023 en fonction de la distance à l'étoile HD 200775.

En résumé, nos travaux contribuent à la vision que nous pouvons avoir de l'évolution des astro-PAH sous irradiation UV. L'identification de molécules spécifiques reste néanmoins ouverte. Un problème clé concerne leur formation dans les environnements astrophysiques, très probablement dans les enveloppes des étoiles évoluées. C'est une question au coeur du projet NANOCOSMOS[(10)] et des progrès sont attendus dans les années à venir [233, 234]. En combinaison avec la richesse des informations spectrales et spatiales, qui seront bientôt fournies par le télescope spatial *James Webb*, nous pouvons donc nous attendre à améliorer notre compréhension de la population des astro-PAH, dans le but d'identifier ces molécules et de mieux caractériser leur rôle dans la physico-chimie des PDR.

[(10)] `http://nanocosmos.iff.csic.es/`

References

[1] T. P. Snow and B. J. McCall. *Diffuse Atomic and Molecular Clouds.* Annual Review of Astronomy and Astrophysics, **44**, 1, 367–414 (2006). 6, 7, 171

[2] A. A. Boogert, P. A. Gerakines, and D. C. Whittet. *Observations of the Icy Universe.* Annual Review of Astronomy and Astrophysics, **53**, 1, 541–581 (2015). 7

[3] E. Herbst and E. F. van Dishoeck. *Complex Organic Interstellar Molecules.* Annual Review of Astronomy and Astrophysics, **47**, 1, 427–480 (2009). 8, 10

[4] D. J. Hollenbach and A. G. G. M. Tielens. *Photodissociation Regions in the Interstellar Medium of Galaxies.* Reviews of Modern Physics, **71**, 1, 173–230 (1999). 9, 10

[5] C. Joblin, E. Bron, C. Pinto, P. Pilleri, F. Le Petit, M. Gerin, J. Le Bourlot, A. Fuente, O. Berné, J. R. Goicoechea, E. Habart, M. Köhler, D. Teyssier, Z. Nagy, J. Montillaud, C. Vastel, J. Cernicharo, M. Röllig, V. Ossenkopf-Okada, and E. A. Bergin. *Structure of Photodissociation Fronts in Star-Forming Regions Revealed by Herschel Observations of High-J CO Emission Lines.* Astronomy & Astrophysics, **615**, A129 (2018). 9, 116

[6] H. J. Habing. *The Interstellar Radiation Density between 912 Å and 2400 Å.* Bulletin of the Astronomical Institutes of the Netherlands, **19**, 421 (1968). 9

[7] E. L. O. Bakes and A. G. G. M. Tielens. *The Photoelectric Heating Mechanism for Very Small Graphitic Grains and Polycyclic Aromatic Hydrocarbons.* The Astrophysical Journal, **427**, 822–838 (1994). 10, 65

[8] J. C. Weingartner and B. T. Draine. *Dust Grain–Size Distributions and Extinction in the Milky Way, Large Magellanic Cloud, and Small Magellanic Cloud.* The Astrophysical Journal, **548**, 1, 296–309 (2001). 10, 65, 114

[9] V. Wakelam, E. Bron, S. Cazaux, F. Dulieu, C. Gry, P. Guillard, E. Habart, L. Hornekær, S. Morisset, G. Nyman, V. Pirronello, S. D. Price, V. Valdivia, G. Vidali, and N. Watanabe. *H_2 Formation on Interstellar Dust Grains: The Viewpoints of Theory, Experiments, Models and Observations.* Molecular Astrophysics, **9**, 1–36 (2017). 10

[10] A. G. G. M. Tielens and D. Hollenbach. *Photodissociation Regions - Part Two - a Model for the Orion Photodissociation Region.* The Astrophysical Journal, **291**, 747 (1985). 10

[11] A. Sternberg and A. Dalgarno. *The Infrared Response of Molecular Hydrogen Gas to Ultraviolet Radiation - High-Density Regions.* The Astrophysical Journal, **338**, 197–233 (1989).

[12] M. J. Kaufman, M. G. Wolfire, D. J. Hollenbach, and M. L. Luhman. *Far-Infrared and Submillimeter Emission from Galactic and Extragalactic Photodissociation Regions.* The Astrophysical Journal, **527**, 2, 795–813 (1999).

[13] F. Le Petit, C. Nehmé, J. Le Bourlot, and E. Roueff. *A Model for Atomic and Molecular Interstellar Gas: The Meudon PDR Code.* The Astrophysical Journal Supplement Series, **164**, 2, 506 (2006).

[14] M. Röllig, N. P. Abel, T. Bell, F. Bensch, J. Black, G. J. Ferland, B. Jonkheid, I. Kamp, M. J. Kaufman, J. L. Bourlot, F. L. Petit, R. Meijerink, O. Morata, V. Ossenkopf, E. Roueff, G. Shaw, M. Spaans, A. Sternberg, J. Stutzki, W.-F. Thi, E. F. van Dishoeck, P. A. M. van Hoof, S. Viti, and M. G. Wolfire. *A Photon Dominated Region Code Comparison Study.* Astronomy & Astrophysics, **467**, 1, 187–206 (2007). 10

[15] D. P. Gilra. *Composition of Interstellar Grains.* Nature, **229**, 5282, 237–241 (1971). 10

[16] M. Compiègne, L. Verstraete, A. Jones, J.-P. Bernard, F. Boulanger, N. Flagey, J. L. Bourlot, D. Paradis, and N. Ysard. *The Global Dust SED: Tracing the*

Nature and Evolution of Dust with DustEM. Astronomy & Astrophysics, **525**, A103 (2011). 11, 12, 161

[17] E. L. Fitzpatrick and D. Massa. *An Analysis of the Shapes of Interstellar Extinction Curves. V. The IR-through-UV Curve Morphology.* The Astrophysical Journal, **663**, 1, 320 (2007). 11

[18] L. Verstraete and A. Léger. *The Visible and Ultraviolet Absorption of Large Polycyclic Aromatic Hydrocarbons.* Astronomy and Astrophysics, **266**, 513–519 (1992). 11

[19] A. Li and B. T. Draine. *Infrared Emission from Interstellar Dust. II. The Diffuse Interstellar Medium.* The Astrophysical Journal, **554**, 2, 778–802 (2001). 11

[20] P. Jenniskens and F.-X. Désert. *A Survey of Diffuse Interstellar Bands (3800 – 8680 Å).* Astronomy & Astrophysics Supplement Series, **106**, 1, 39–78 (1994). 11

[21] M. L. Heger. *Further Study of the Sodium Lines in Class B Stars.* Lick Observatory Bulletin, **10**, 141–145 (1922). 11

[22] B. J. McCall and R. E. Griffin. *On the Discovery of the Diffuse Interstellar Bands.* Proceedings of the Royal Society A: Mathematical, Physical and Engineering Sciences, **469**, 2151, 20120604 (2013). 11

[23] L. M. Hobbs, D. G. York, T. P. Snow, T. Oka, J. A. Thorburn, M. Bishof, S. D. Friedman, B. J. McCall, B. Rachford, P. Sonnentrucker, and D. E. Welty. *A Catalog of Diffuse Interstellar Bands in the Spectrum of HD 204827.* The Astrophysical Journal, **680**, 2, 1256–1270 (2008). 11

[24] L. M. Hobbs, D. G. York, J. A. Thorburn, T. P. Snow, M. Bishof, S. D. Friedman, B. J. McCall, T. Oka, B. Rachford, P. Sonnentrucker, and D. E. Welty. *Studies of the Diffuse Interstellar Bands. III. HD 183143.* The Astrophysical Journal, **705**, 1, 32–45 (2009). 11

[25] E. K. Campbell, M. Holz, D. Gerlich, and J. P. Maier. *Laboratory Confirmation of C_{60}^+ as the Carrier of Two Diffuse Interstellar Bands.* Nature, **523**, 7560, 322–323 (2015). 11, 15, 20, 124

[26] M. A. Cordiner, H. Linnartz, N. L. J. Cox, J. Cami, F. Najarro, C. R. Proffitt, R. Lallement, P. Ehrenfreund, B. H. Foing, T. R. Gull, P. J. Sarre, and S. B. Charnley. *Confirming Interstellar C_{60}^{+} Using the Hubble Space Telescope.* The Astrophysical Journal, **875**, 2, L28 (2019). 11, 20

[27] T. R. Geballe. *The Diffuse Interstellar Bands – A Brief Review.* Journal of Physics: Conference Series, **728**, 062005 (2016). 11

[28] F.-X. Désert, F. Boulanger, and J. L. Puget. *Interstellar Dust Models for Extinction and Emission.* Astronomy & Astrophysics, **237**, 215–236 (1990). 12

[29] B. T. Draine and A. Li. *Infrared Emission from Interstellar Dust. IV. The Silicate-Graphite-PAH Model in the Post-Spitzer Era.* The Astrophysical Journal, **657**, 810–837 (2007). 15

[30] R. Siebenmorgen, N. V. Voshchinnikov, and S. Bagnulo. *Dust in the Diffuse Interstellar Medium - Extinction, Emission, Linear and Circular Polarisation.* Astronomy & Astrophysics, **561**, A82 (2014).

[31] A. P. Jones, M. Köhler, N. Ysard, M. Bocchio, and L. Verstraete. *The Global Dust Modelling Framework THEMIS.* Astronomy & Astrophysics, **602**, A46 (2017). 12

[32] K. Sellgren. *The Near-Infrared Continuum Emission of Visual Reflection Nebulae.* The Astrophysical Journal, **277**, 623–633 (1984). 12

[33] A. Léger and J. L. Puget. *Identification of the "Unidentified" IR Emission Features of Interstellar Dust?* Astronomy & Astrophysics, **500**, 279 (1984). 12, 14

[34] L. J. Allamandola, A. G. G. M. Tielens, and J. R. Barker. *Polycyclic Aromatic Hydrocarbons and the Unidentified Infrared Emission Bands: Auto Exhaust along the Milky Way.* The Astrophysical Journal, **290**, L25 (1985). 12, 14, 19

[35] E. Peeters. *Astronomical Observations of the PAH Emission Bands.* European Astronomical Society Publications Series, **46**, 13–27 (2011). 13, 14, 64, 161

[36] F. Pauzat, D. Talbi, and Y. Ellinger. *UIR Bands: Computational Experiments on the IR Spectra of Naphthalene Derivatives as Models for PAHs.* Astronomy and Astrophysics, **293**, 263–277 (1995). 15

[37] E. L. O. Bakes, A. G. G. M. Tielens, C. W. Bauschlicher Jr., D. M. Hudgins, and L. J. Allamandola. *Theoretical Modeling of Infrared Emission from Neutral and Charged Polycyclic Aromatic Hydrocarbons. II.* The Astrophysical Journal, **560**, 1, 261 (2001). 65

[38] E. L. O. Bakes, A. G. G. M. Tielens, and C. W. Bauschlicher Jr. *Theoretical Modeling of Infrared Emission from Neutral and Charged Polycyclic Aromatic Hydrocarbons. I.* The Astrophysical Journal, **556**, 1, 501 (2001). 114

[39] O. Berné, C. Joblin, Y. Deville, J. D. Smith, M. Rapacioli, J. P. Bernard, J. Thomas, W. Reach, and A. Abergel. *Analysis of the Emission of Very Small Dust Particles from Spitzer Spectro-Imagery Data Using Blind Signal Separation Methods.* Astronomy & Astrophysics, **469**, 2, 575–586 (2007).

[40] F. Galliano, E. Dwek, and P. Chanial. *Stellar Evolutionary Effects on the Abundances of Polycyclic Aromatic Hydrocarbons and Supernova-Condensed Dust in Galaxies.* The Astrophysical Journal, **672**, 1, 214 (2008).

[41] C. Boersma, J. Bregman, and L. J. Allamandola. *The Charge State of Polycyclic Aromatic Hydrocarbons across Reflection Nebulae: PAH Charge Balance and Calibration.* The Astrophysical Journal, **832**, 1, 51 (2016).

[42] S. Foschino, O. Berné, and C. Joblin. *Learning Mid-IR Emission Spectra of Polycyclic Aromatic Hydrocarbon Populations from Observations.* Astronomy & Astrophysics, **632**, A84 (2019). 15

[43] D. M. Hudgins, C. W. Bauschlicher Jr., and L. J. Allamandola. *Variations in the Peak Position of the 6.2 μm Interstellar Emission Feature: A Tracer of N in the Interstellar Polycyclic Aromatic Hydrocarbon Population.* The Astrophysical Journal, **632**, 316–332 (2005). 15

[44] C. W. Bauschlicher, E. Peeters, and L. J. Allamandola. *The Infrared Spectra of Very Large Irregular Polycyclic Aromatic Hydrocarbons (PAHs): Observational*

Probes of Astronomical PAH Geometry, Size, and Charge. The Astrophysical Journal, **697**, 1, 311–327 (2009). 15

[45] C. Joblin, A. G. G. M. Tielens, L. J. Allamandola, and T. R. Geballe. *Spatial Variation of the 3.29 and 3.40 Micron Emission Bands within Reflection Nebulae and the Photochemical Evolution of Methylated Polycyclic Aromatic Hydrocarbons.* The Astrophysical Journal, **458**, 610 (1996). 15, 22, 88, 114, 119

[46] J. Cami, J. Bernard-Salas, E. Peeters, and S. E. Malek. *Detection of C_{60} and C_{70} in a Young Planetary Nebula.* Science, **329**, 5996, 1180–1182 (2010). 15

[47] K. Sellgren, M. W. Werner, J. G. Ingalls, J. D. T. Smith, T. M. Carleton, and C. Joblin. *C_{60} in Reflection Nebulae.* The Astrophysical Journal Letters, **722**, 1, L54 (2010).

[48] D. A. García-Hernández, A. Manchado, P. García-Lario, L. Stanghellini, E. Villaver, R. A. Shaw, R. Szczerba, and J. V. Perea-Calderón. *Formation of Fullerenes in H-Containing Planetary Nebulae.* The Astrophysical Journal, **724**, 1, L39–L43 (2010).

[49] K. Sellgren, M. W. Werner, J. G. Ingalls, J. D. T. Smith, T. M. Carleton, and C. Joblin. *Confirmation of C_{60} in the Reflection Nebula NGC 7023.* EAS Publications Series, **46**, 209–214 (2011).

[50] O. Berné, G. Mulas, and C. Joblin. *Interstellar C_{60}^+.* Astronomy & Astrophysics, **550**, L4 (2013). 15

[51] T. Allain, S. Leach, and E. Sedlmayr. *Photodestruction of PAHs in the Interstellar Medium. I. Photodissociation Rates for the Loss of an Acetylenic Group.* Astronomy & Astrophysics, **305**, 602 (1996). 16

[52] V. Le Page, T. P. Snow, and V. M. Bierbaum. *Hydrogenation and Charge States of PAHs in Diffuse Clouds. I. Development of a Model.* The Astrophysical Journal Supplement Series, **132**, 2, 233 (2001). 18

[53] R. Visser, V. C. Geers, C. P. Dullemond, J.-C. Augereau, K. M. Pontoppidan, and E. F. van Dishoeck. *PAH Chemistry and IR Emission from Circumstellar Disks.* Astronomy & Astrophysics, **466**, 1, 229–241 (2007). 64

[54] J. Montillaud, C. Joblin, and D. Toublanc. *Evolution of Polycyclic Aromatic Hydrocarbons in Photodissociation Regions - Hydrogenation and Charge States.* Astronomy & Astrophysics, **552**, A15 (2013). 18, 21, 64, 120, 123

[55] H. Andrews, A. Candian, and A. G. G. M. Tielens. *Hydrogenation and dehydrogenation of interstellar PAHs: Spectral characteristics and H_2 formation.* Astronomy & Astrophysics, **595**, A23 (2016). 16, 64, 114, 118

[56] B. West, B. Lowe, and P. M. Mayer. *Unimolecular Dissociation of 1-Methylpyrene Cations: Why Are 1-Methylenepyrene Cations Formed and Not a Tropylium-Containing Ion?* The Journal of Physical Chemistry A, **122**, 20, 4730–4735 (2018). 17, 44

[57] A. Léger, L. D'Hendecourt, and D. Défourneau. *Physics of IR Emission by Interstellar PAH Molecules.* Astronomy and Astrophysics, **216**, 148–164 (1989). 17

[58] C. Joblin, P. Boissel, A. Leger, L. D'Hendecourt, and D. Defourneau. *Infrared Spectroscopy of Gas-Phase PAH Molecules. II. Role of the Temperature.* Astronomy & Astrophysics, **299**, 835 (1995). 17

[59] A. M. Tokmachev, M. Boggio-Pasqua, D. Mendive-Tapia, M. J. Bearpark, and M. A. Robb. *Fluorescence of the Perylene Radical Cation and an Inaccessible D_0/D_1 Conical Intersection: An MMVB, RASSCF, and TD-DFT Computational Study.* The Journal of Chemical Physics, **132**, 4, 044306 (2010). 17

[60] A. Léger, P. Boissel, and L. d'Hendecourt. *Predicted Fluorescence Mechanism in Highly Isolated Molecules: The Poincaré Fluorescence.* Physical Review Letters, **60**, 10, 921–924 (1988). 17, 21

[61] S. Martin, J. Bernard, R. Brédy, B. Concina, C. Joblin, M. Ji, C. Ortega, and L. Chen. *Fast Radiative Cooling of Anthracene Observed in a Compact Electrostatic Storage Ring.* Physical Review Letters, **110**, 6, 063003 (2013). 17, 21, 37

[62] A. Marciniak, V. Despré, T. Barillot, A. Rouzée, M. C. E. Galbraith, J. Klei, C.-H. Yang, C. T. L. Smeenk, V. Loriot, S. N. Reddy, A. G. G. M. Tielens,

S. Mahapatra, A. I. Kuleff, M. J. J. Vrakking, and F. Lépine. *XUV Excitation Followed by Ultrafast Non-Adiabatic Relaxation in PAH Molecules as a Femto-Astrochemistry Experiment.* Nature Communications, **6**, 1, 1–6 (2015). 18, 21, 125, 129

[63] D. R. Hartree. *The Wave Mechanics of an Atom with a Non-Coulomb Central Field. Part II. Some Results and Discussion.* Mathematical Proceedings of the Cambridge Philosophical Society, **24**, 1, 111–132 (1928). 18

[64] D. R. Hartree. *The Wave Mechanics of an Atom with a Non-Coulomb Central Field. Part I. Theory and Methods.* Mathematical Proceedings of the Cambridge Philosophical Society, **24**, 1, 89–110 (1928).

[65] V. Fock. *Näherungsmethode zur Lösung des quantenmechanischen Mehrkörperproblems.* Zeitschrift für Physik, **61**, 1, 126–148 (1930). 18

[66] D. J. DeFrees and A. D. McLean. *Molecular Orbital Predictions of the Vibrational Frequencies of Some Molecular Ions.* The Journal of Chemical Physics, **82**, 1, 333–341 (1985). 18

[67] Y. Yamaguchi, M. Frisch, J. Gaw, H. F. Schaefer, and J. S. Binkley. *Erratum: Analytic Evaluation and Basis Set Dependence of Intensities of Infrared Spectra [J. Chem. Phys. 84, 2262 (1986)].* The Journal of Chemical Physics, **85**, 10, 6251–6251 (1986). 18

[68] Y. Yamaguchi, M. Frisch, J. Gaw, H. F. Schaefer, and J. S. Binkley. *Analytic Evaluation and Basis Set Dependence of Intensities of Infrared Spectra.* The Journal of Chemical Physics, **84**, 4, 2262–2278 (1986). 18

[69] F. Pauzat, D. Talbi, M. D. Miller, D. J. DeFrees, and Y. Ellinger. *Theoretical IR Spectra of Ionized Naphthalene.* The Journal of Physical Chemistry, **96**, 20, 7882–7886 (1992). 18

[70] F. Pauzat, D. Talbi, and Y. Ellinger. *The PAH Hypothesis: A Computational Experiment on the Combined Effects of Ionization and Dehydrogenation on the IR Signatures.* Astronomy and Astrophysics, **319**, 318–330 (1997). 18

[71] S. R. Langhoff. *Theoretical Infrared Spectra for Polycyclic Aromatic Hydrocarbon Neutrals, Cations, and Anions.* The Journal of Physical Chemistry, **100**, 8, 2819–2841 (1996). 19

[72] C. W. Bauschlicher Jr., D. M. Hudgins, and L. J. Allamandola. *The Infrared Spectra of Polycyclic Aromatic Hydrocarbons Containing a Five-Membered Ring: Symmetry Breaking and the B3LYP Functional.* Theoretical Chemistry Accounts: Theory, Computation, and Modeling (Theoretica Chimica Acta), **103**, 2, 154–162 (1999). 19

[73] C. W. Bauschlicher and E. L. O. Bakes. *Infrared Spectra of Polycyclic Aromatic Hydrocarbons (PAHs).* Chemical Physics, **262**, 2, 285–291 (2000).

[74] G. Malloci, G. Mulas, and C. Joblin. *Electronic Absorption Spectra of PAHs up to Vacuum UV - Towards a Detailed Model of Interstellar PAH Photophysics.* Astronomy & Astrophysics, **426**, 1, 105–117 (2004). 19, 20, 72, 73, 83

[75] A. Ricca, C. W. Bauschlicher, C. Boersma, A. G. G. M. Tielens, and L. J. Allamandola. *The Infrared Spectroscopy of Compact Polycyclic Aromatic Hydrocarbons Containing up to 384 Carbons.* The Astrophysical Journal, **754**, 1, 75 (2012). 19

[76] C. W. Bauschlicher, C. Boersma, A. Ricca, A. L. Mattioda, J. Cami, E. Peeters, F. S. de Armas, G. P. Saborido, D. M. Hudgins, and L. J. Allamandola. *The NASA Ames Polycyclic Aromatic Hydrocarbon Infrared Spectroscopic Database: The Computed Spectra.* The Astrophysical Journal Supplement Series, **189**, 2, 341–351 (2010). 19

[77] C. W. Bauschlicher, A. Ricca, C. Boersma, and L. J. Allamandola. *The NASA Ames PAH IR Spectroscopic Database: Computational Version 3.00 with Updated Content and the Introduction of Multiple Scaling Factors.* The Astrophysical Journal Supplement Series, **234**, 2, 32 (2018).

[78] C. Boersma, C. W. Bauschlicher, A. Ricca, A. L. Mattioda, J. Cami, E. Peeters, F. S. de Armas, G. P. Saborido, D. M. Hudgins, and L. J. Allamandola. *The NASA Ames PAH IR Spectroscopic Database Version 2.00: Updated Content,*

Web Site, And On(Off)Line Tools. The Astrophysical Journal Supplement Series, **211**, 1, 8 (2014). 19

[79] G. Malloci, C. Joblin, and G. Mulas. *Theoretical Evaluation of PAH Dication Properties.* Astronomy & Astrophysics, **462**, 2, 627–635 (2007). 19, 72, 73, 74, 116

[80] D. M. Hudgins, S. A. Sandford, and L. J. Allamandola. *Infrared Spectroscopy of Polycyclic Aromatic Hydrocarbon Cations. 1. Matrix-Isolated Naphthalene and Perdeuterated Naphthalene.* The Journal of Physical Chemistry, **98**, 16, 4243–4253 (1994). 19

[81] D. M. Hudgins and L. J. Allamandola. *Infrared Spectroscopy of Matrix-Isolated Polycyclic Aromatic Hydrocarbon Cations. 3. The Polyacenes Anthracene, Tetracene, and Pentacene.* The Journal of Physical Chemistry, **99**, 22, 8978–8986 (1995).

[82] D. M. Hudgins and L. J. Allamandola. *Infrared Spectroscopy of Matrix-Isolated Polycyclic Aromatic Hydrocarbon Cations. 2. The Members of the Thermodynamically Most Favorable Series through Coronene.* The Journal of Physical Chemistry, **99**, 10, 3033–3046 (1995).

[83] D. M. Hudgins and L. J. Allamandola. *Infrared Spectroscopy of Matrix-Isolated Polycyclic Aromatic Hydrocarbon Cations. 4. The Tetracyclic PAH Isomers Chrysene and 1,2-Benzanthracene.* The Journal of Physical Chemistry A, **101**, 19, 3472–3477 (1997).

[84] D. M. Hudgins, C. W. Bauschlicher, L. J. Allamandola, and J. C. Fetzer. *Infrared Spectroscopy of Matrix-Isolated Polycyclic Aromatic Hydrocarbon Ions. 5. PAHs Incorporating a Cyclopentadienyl Ring.* The Journal of Physical Chemistry A, **104**, 16, 3655–3669 (2000).

[85] J. Szczepanski, D. Roser, W. Personette, M. Eyring, R. Pellow, and M. Vala. *Infrared Spectrum of Matrix-Isolated Naphthalene Radical Cation.* The Journal of Physical Chemistry, **96**, 20, 7876–7881 (1992).

[86] J. Szczepanski and M. Vala. *Laboratory Evidence for Ionized Polycyclic Aromatic Hydrocarbons in the Interstellar Medium.* Nature, **363**, 6431, 699–701 (1993).

[87] J. Szczepanski and M. Vala. *Infrared Frequencies and Intensities for Astrophysically Important Polycyclic Aromatic Hydrocarbon Cations.* The Astrophysical Journal, **414**, 646–655 (1993).

[88] J. Szczepanski, C. Chapo, and M. Vala. *Visible and Infrared Spectra of Matrix-Isolated Perylene Cations.* Chemical Physics Letters, **205**, 4, 434–439 (1993).

[89] J. Szczepanski, J. Drawdy, C. Wehlburg, and M. Vala. *Vibrational and Electronic Spectra of Matrix-Isolated Tetracene Cations.* Chemical Physics Letters, **245**, 6, 539–548 (1995).

[90] J. Szczepanski, C. Wehlburg, and M. Vala. *Vibrational and Electronic Spectra of Matrix-Isolated Pentacene Cations and Anions.* Chemical Physics Letters, **232**, 3, 221–228 (1995). 19

[91] C. Joblin, F. Salama, and L. Allamandola. *Photoinduced Fluorescence from the Perylene Cation Isolated in Ne and Ar Matrices.* The Journal of Chemical Physics, **102**, 24, 9743–9745 (1995). 19

[92] S. Chakraborty, G. Mulas, K. Demyk, and C. Joblin. *Experimental Approach to the Study of Anharmonicity in the Infrared Spectrum of Pyrene from 14 to 723 K.* The Journal of Physical Chemistry A, **123**, 19, 4139–4148 (2019). 19

[93] F. Calvo, M. Basire, and P. Parneix. *Temperature Effects on the Rovibrational Spectra of Pyrene-Based PAHs.* The Journal of Physical Chemistry A, **115**, 32, 8845–8854 (2011). 19

[94] C. J. Mackie, T. Chen, A. Candian, T. J. Lee, and A. G. G. M. Tielens. *Fully Anharmonic Infrared Cascade Spectra of Polycyclic Aromatic Hydrocarbons.* The Journal of Chemical Physics, **149**, 13, 134302 (2018). 19, 123

[95] J. Oomens, A. J. A. van Roij, G. Meijer, and G. von Helden. *Gas-Phase Infrared Photodissociation Spectroscopy of Cationic Polyaromatic Hydrocarbons.* The Astrophysical Journal, **542**, 1, 404–410 (2000). 19, 45, 89

[96] J. Oomens, B. G. Sartakov, A. G. G. M. Tielens, G. Meijer, and G. von Helden. *Gas-Phase Infrared Spectrum of the Coronene Cation.* The Astrophysical Journal, **560**, 1, L99–L103 (2001).

[97] J. Oomens, A. G. G. M. Tielens, B. G. Sartakov, G. von Helden, and G. Meijer. *Laboratory Infrared Spectroscopy of Cationic Polycyclic Aromatic Hydrocarbon Molecules.* The Astrophysical Journal, **591**, 968–985 (2003). 19, 45, 89

[98] J. Gao, G. Berden, and J. Oomens. *Laboratory Infrared Spectroscopy of Gaseous Negatively Charged Polyaromatic Hydrocarbons.* The Astrophysical Journal, **787**, 2, 170 (2014). 19

[99] H. Knorke, J. Langer, J. Oomens, and O. Dopfer. *Infrared Spectra of Isolated Protonated Polycyclic Aromatic Hydrocarbon Molecules.* The Astrophysical Journal, **706**, 1, L66–L70 (2009). 19

[100] J. Palotás, J. Martens, G. Berden, and J. Oomens. *The Infrared Spectrum of Protonated Buckminsterfullerene* $C_{60}H^+$. Nature Astronomy, pp. 1–6 (2019). 19

[101] J. Zhen, P. Castellanos, J. Bouwman, H. Linnartz, and A. G. G. M. Tielens. *Infrared Spectra of Hexa-peri-hexabenzocoronene Cations:* HBC^+ *and* HBC^{2+}. The Astrophysical Journal, **836**, 1, 28 (2017). 19, 114

[102] J. Zhen, A. Candian, P. Castellanos, J. Bouwman, H. Linnartz, and A. G. G. M. Tielens. *Laboratory Gas-phase Infrared Spectra of Two Astronomically Relevant PAH Cations: Diindenoperylene,* $C_{32}H_{16}^+$ *and Dicoronylene,* $C_{48}H_{20}^+$. The Astrophysical Journal, **854**, 1, 27 (2018). 19, 114

[103] A. Léger and L. D'Hendecourt. *Are Polycyclic Aromatic Hydrocarbons the Carriers of the Diffuse Interstellar Bands in the Visible?* Astronomy and Astrophysics, **146**, 81–85 (1985). 19

[104] G. P. van der Zwet and L. J. Allamandola. *Polycyclic Aromatic Hydrocarbons and the Diffuse Interstellar Bands.* Astronomy and Astrophysics, **146**, 76–80 (1985).

[105] F. Salama, E. L. O. Bakes, L. J. Allamandola, and A. G. G. M. Tielens. *Assessment of the Polycyclic Aromatic Hydrocarbon–Diffuse Interstellar Band Proposal.* The Astrophysical Journal, **458**, 621 (1996).

[106] F. Salama, G. A. Galazutdinov, J. Krełowski, L. J. Allamandola, and F. A. Musaev. *Polycyclic Aromatic Hydrocarbons and the Diffuse Interstellar Bands: A Survey.* The Astrophysical Journal, **526**, 1, 265–273 (1999). 19

[107] H. W. Kroto and M. Jura. *Circumstellar and Interstellar Fullerenes and Their Analogues.* Astronomy and Astrophysics, **263**, 275–280 (1992). 19

[108] M. K. Crawford, A. G. G. M. Tielens, and L. J. Allamandola. *Ionized Polycyclic Aromatic Hydrocarbons and the Diffuse Interstellar Bands.* The Astrophysical Journal Letters, **293**, L45–L48 (1985). 19

[109] F. Salama, C. Joblin, and L. J. Allamandola. *Electronic Absorption Spectroscopy of Matrix-Isolated Polycyclic Aromatic Hydrocarbon Cations. II. The Phenanthrene Cation ($C_{14}H_{10}^{+}$) and its 1-Methyl Derivative.* The Journal of Chemical Physics, **101**, 12, 10252–10262 (1994). 20, 169, 178

[110] R. Ruiterkamp, T. Halasinski, F. Salama, B. H. Foing, L. J. Allamandola, W. Schmidt, and P. Ehrenfreund. *Spectroscopy of Large PAHs - Laboratory Studies and Comparison to the Diffuse Interstellar Bands.* Astronomy & Astrophysics, **390**, 3, 1153–1170 (2002).

[111] T. M. Halasinski, J. L. Weisman, R. Ruiterkamp, T. J. Lee, F. Salama, and M. Head-Gordon. *Electronic Absorption Spectra of Neutral Perylene ($C_{20}H_{12}$), Terrylene ($C_{30}H_{16}$), and Quaterrylene ($C_{40}H_{20}$) and Their Positive and Negative Ions: Ne Matrix-Isolation Spectroscopy and Time-Dependent Density Functional Theory Calculations.* The Journal of Physical Chemistry A, **107**, 19, 3660–3669 (2003). 20

[112] L. Biennier, F. Salama, M. Gupta, and A. O'Keefe. *Multiplex Integrated Cavity Output Spectroscopy of Cold PAH Cations.* Chemical Physics Letters, **387**, 4, 287–294 (2004). 20

[113] X. Tan and F. Salama. *Cavity Ring-Down Spectroscopy of Jet-Cooled 1-Pyrenecarboxyaldehyde ($C_{17}H_{10}O$) and 1-Methylpyrene ($C_{17}H_{12}$) Cations.* Chemical Physics Letters, **422**, 4, 518–521 (2006). 20

[114] X. Tan and F. Salama. *Cavity Ring-Down Spectroscopy and Theoretical Calculations of the $S_1\,(^1B_{3u}) \leftarrow S_0\,(^1A_g)$ Transition of Jet-Cooled Perylene.* The Journal of Chemical Physics, **122**, 8, 084318 (2005). 20

[115] G. Rouillé, M. Arold, A. Staicu, S. Krasnokutski, F. Huisken, T. Henning, X. Tan, and F. Salama. *$S_1\,(^1A_1) \leftarrow S_0\,(^1A_1)$ Transition of Bbenzo[g,h,i]perylene in Supersonic Jets and Rare Gas Matrices.* The Journal of Chemical Physics, **126**, 17, 174311 (2007). 20

[116] F. Salama, G. A. Galazutdinov, J. Krełowski, L. Biennier, Y. Beletsky, and I.-O. Song. *Polycyclic Aromatic Hydrocarbons and The Diffuse Interstella Bands: A Survey.* The Astrophysical Journal, **728**, 2, 154 (2011). 20

[117] C. Joblin, A. Leger, and P. Martin. *Contribution of Polycyclic Aromatic Hydrocarbon Molecules to the Interstellar Extinction Curve.* The Astrophysical Journal Letters, **393**, L79–L82 (1992). 20

[118] G. Malloci, G. Mulas, C. Cecchi-Pestellini, and C. Joblin. *Dehydrogenated Polycyclic Aromatic Hydrocarbons and UV Bump.* Astronomy & Astrophysics, **489**, 3, 1183–1187 (2008). 20

[119] C. Cecchi-Pestellini, G. Malloci, G. Mulas, C. Joblin, and D. A. Williams. *The Role of the Charge State of PAHs in Ultraviolet Extinction.* Astronomy & Astrophysics, **486**, 3, L25–L29 (2008). 20, 114

[120] G. Mulas, A. Zonca, S. Casu, and C. Cecchi-Pestellini. *Modeling Galactic Extinction with Dust and "Real" Polycyclic Aromatic Hydrocarbons.* The Astrophysical Journal Supplement Series, **207**, 1, 7 (2013). 20

[121] E. Posenitskiy, M. Rapacioli, B. Lepetit, D. Lemoine, and F. Spiegelman. *Non-Adiabatic Molecular Dynamics Investigation of the Size Dependence of the Electronic Relaxation in Polyacenes.* Physical Chemistry Chemical Physics, **21**, 23, 12139–12149 (2019). 21

[122] L. Verstraete, A. Leger, L. D'Hendecourt, D. Defourneau, and O. Dutuit. *Ionization Cross-Section Measurements for Two PAH Molecules - Implications for the Heating of Diffuse Interstellar Gas.* Astronomy & Astrophysics, **237**, 436 (1990). 21, 117, 118

[123] H. W. Jochims, H. Baumgärtel, and S. Leach. *Photoionization Quantum Yields of Polycyclic Aromatic Hydrocarbons.* Astronomy & Astrophysics, **314**, 1003–1009 (1996). 84, 117, 118, 119, 168

[124] H. W. Jochims, E. Rühl, H. Baumgärtel, S. Tobita, and S. Leach. *VUV Peaks in Absorption Spectra and Photoion Yield Curves of Polycyclic Aromatic Hydrocarbons and Related Compounds.* International Journal of Mass Spectrometry and Ion Processes, **167-168**, 35–53 (1997). 21

[125] S. Tobita, S. Leach, H. W. Jochims, E. Rühl, E. Illenberger, and H. Baumgärtel. *Single- and Double-Ionization Potentials of Polycyclic Aromatic Hydrocarbons and Fullerenes by Photon and Electron Impact.* Canadian Journal of Physics, **72**, 11-12, 1060–1069 (1994). 21

[126] J. Zhen, S. Rodriguez Castillo, C. Joblin, G. Mulas, H. Sabbah, A. Giuliani, L. Nahon, S. Martin, J.-P. Champeaux, and P. M. Mayer. *VUV Photo-Processing of PAH Cations: Quantitative Study on the Ionization Versus Fragmentation Processes.* The Astrophysical Journal, **822**, 2, 113 (2016). 21, 44, 45, 74

[127] G. Wenzel, C. Joblin, A. Giuliani, S. R. Castillo, G. Mulas, M. Ji, H. Sabbah, S. Quiroga, D. Peña, and L. Nahon. *Astrochemical Relevance of VUV Ionization of Large PAH Cations.* Astronomy & Astrophysics, **641**, A98 (2020). 21, 45, 65, 114

[128] B. West, C. Joblin, V. Blanchet, A. Bodi, B. Sztáray, and P. M. Mayer. *On the Dissociation of the Naphthalene Radical Cation: New iPEPICO and Tandem Mass Spectrometry Results.* The Journal of Physical Chemistry A, **116**, 45, 10999–11007 (2012). 21

[129] B. West, F. Useli-Bacchitta, H. Sabbah, V. Blanchet, A. Bodi, P. M. Mayer, and C. Joblin. *Photodissociation of Pyrene Cations: Structure and Energetics from $C_{16}H_{10}^+$ to C_{14}^+ and Almost Everything in Between.* The Journal of Physical Chemistry A, **118**, 36, 7824–7831 (2014). 21

[130] B. West, S. Rodriguez Castillo, A. Sit, S. Mohamad, B. Lowe, C. Joblin, A. Bodi, and P. M. Mayer. *Unimolecular Reaction Energies for Polycyclic Aromatic*

Hydrocarbon Ions. Physical chemistry chemical physics: PCCP, **20**, 10, 7195–7205 (2018). 21, 100, 101, 109, 120, 167

[131] C. Joblin, P. Boissel, and P. de Parseval. *Polycyclic Aromatic Hydrocarbon Lifetime in Cometary Environments*. Planetary and Space Science, **45**, 12, 1539–1542 (1997). 21, 41, 177

[132] F. Useli-Bacchitta, A. Bonnamy, G. Mulas, G. Malloci, D. Toublanc, and C. Joblin. *Visible Photodissociation Spectroscopy of PAH Cations and Derivatives in the PIRENEA Experiment*. Chemical Physics, **371**, 1–3, 16–23 (2010). 38, 41, 45, 177

[133] J. Zhen, G. Mulas, A. Bonnamy, and C. Joblin. *An optical spectrum of a large isolated gas-phase PAH cation: $C_{78}H_{26}^{+}$*. Molecular Astrophysics, **2**, 12–17 (2016). 21, 42, 64, 115, 116

[134] P. Boissel, P. de Parseval, P. Marty, and G. Lefèvre. *Fragmentation of Isolated Ions by Multiple Photon Absorption: A Quantitative Study*. The Journal of Chemical Physics, **106**, 12, 4973–4984 (1997). 21

[135] S. Martin, M. Ji, J. Bernard, R. Brédy, B. Concina, A. R. Allouche, C. Joblin, C. Ortega, G. Montagne, A. Cassimi, Y. Ngono-Ravache, and L. Chen. *Fast Radiative Cooling of Anthracene: Dependence on Internal Energy*. Physical Review A, **92**, 5, 053425 (2015). 21, 37

[136] J. Zhen, P. Castellanos, D. M. Paardekooper, N. Ligterink, H. Linnartz, L. Nahon, C. Joblin, and A. G. G. M. Tielens. *Laboratory Photo-Chemistry of PAHs: Ionization Versus Fragmentation*. The Astrophysical Journal, **804**, 1, L7 (2015). 21, 64, 74

[137] S. Rodriguez Castillo, A. Simon, and C. Joblin. *Investigating the Importance of Edge-Structure in the Loss of H/H_2 of PAH Cations: The Case of Dibenzopyrene Isomers*. International Journal of Mass Spectrometry, **429**, 189–197 (2018). 22

[138] A. Simon and M. Rapacioli. *Energetic Processing of PAHs: Isomerisation and Dissociation*. In *Chemical Modelling*, pp. 195–216. The Royal Society of Chemistry (2018). 22

[139] A. Simon, M. Rapacioli, G. Rouaut, G. Trinquier, and F. X. Gadéa. *Dissociation of Polycyclic Aromatic Hydrocarbons: Molecular Dynamics Studies.* Philosophical Transactions of the Royal Society A: Mathematical, Physical and Engineering Sciences, **375**, 2092, 20160195 (2017). 22

[140] M. Rapacioli, A. Simon, C. C. M. Marshall, J. Cuny, D. Kokkin, F. Spiegelman, and C. Joblin. *Cationic Methylene–Pyrene Isomers and Isomerization Pathways: Finite Temperature Theoretical Studies.* The Journal of Physical Chemistry A, **119**, 51, 12845–12854 (2015). 22, 88, 89, 93, 95, 110, 111, 166

[141] H. A. B. Johansson, H. Zettergren, A. I. S. Holm, N. Haag, S. B. Nielsen, J. A. Wyer, M.-B. S. Kirketerp, K. Støchkel, P. Hvelplund, H. T. Schmidt, and H. Cederquist. *Unimolecular dissociation of anthracene and acridine cations: The importance of isomerization barriers for the C_2H_2 loss and HCN loss channels.* The Journal of Chemical Physics, **135**, 8, 084304 (2011). 23, 124, 178

[142] G. Malloci, C. Joblin, and G. Mulas. *On-Line Database of the Spectral Properties of Polycyclic Aromatic Hydrocarbons.* Chemical Physics, **332**, 2, 353–359 (2007). 29, 73, 111, 115

[143] A. Giuliani, A. R. Milosavljević, K. Hinsen, F. Canon, C. Nicolas, M. Réfrégiers, and L. Nahon. *Structure and Charge-State Dependence of the Gas-Phase Ionization Energy of Proteins.* Angewandte Chemie International Edition, **51**, 38, 9552–9556 (2012). 29

[144] L. C. Short, S.-S. Cai, and J. A. Syage. *APPI-MS: Effects of Mobile Phases and VUV Lamps on the Detection of PAH Compounds.* Journal of the American Society for Mass Spectrometry, **18**, 4, 589–599 (2007). 29

[145] D. Gerlich. *Inhomogeneous RF Fields: A Versatile Tool for the Study of Processes with Slow Ions.* In *Advances in Chemical Physics*, pp. 1–176. John Wiley & Sons, Ltd (2007). 30

[146] W. Paul. *Electromagnetic Traps for Charged and Neutral Particles.* Reviews of Modern Physics, **62**, 3, 531–540 (1990). 31, 40

[147] H. G. Dehmelt. *Radiofrequency Spectroscopy of Stored Ions I: Storage**Part II: Spectroscopy Is Now Scheduled to Appear in Volume V of This Series.* In D. R.

Bates and I. Estermann (Editors), *Advances in Atomic and Molecular Physics*, volume 3, pp. 53–72. Academic Press (1968). 33

[148] F. M. Penning. *Ein neues Manometer für niedrige Gasdrucke, insbesondere zwischen* 10^{-3} *und* 10^{-5} *mm*. Physica, **4**, 2, 71–75 (1937). 33

[149] H. J. Kluge. *Penning Trap Mass Spectrometry of Radionuclides*. International Journal of Mass Spectrometry, **349–350**, 26–37 (2013). 33

[150] A. G. Marshall. *Fourier Transform Ion Cyclotron Resonance Mass Spectrometry*. Accounts of Chemical Research, **18**, 10, 316–322 (1985). 36

[151] A. G. Marshall, C. L. Hendrickson, and G. S. Jackson. *Fourier Transform Ion Cyclotron Resonance Mass Spectrometry: A Primer*. Mass Spectrometry Reviews, **17**, 1, 1–35 (1998). 36

[152] H. T. Schmidt. *Electrostatic Storage Rings for Atomic and Molecular Physics*. Physica Scripta, **T166**, 014063 (2015). 36

[153] S. P. Møller. *ELISA, and Electrostatic Storage Ring for Atomic Physics*. Nuclear Instruments and Methods in Physics Research Section A: Accelerators, Spectrometers, Detectors and Associated Equipment, **394**, 3, 281–286 (1997). 36

[154] T. Tanabe, K. Chida, K. Noda, and I. Watanabe. *An Electrostatic Storage Ring for Atomic and Molecular Science*. Nuclear Instruments and Methods in Physics Research Section A: Accelerators, Spectrometers, Detectors and Associated Equipment, **482**, 3, 595–605 (2002). 37

[155] M. Lange, M. Froese, S. Menk, J. Varju, R. Bastert, K. Blaum, J. R. C. López-Urrutia, F. Fellenberger, M. Grieser, R. von Hahn, O. Heber, K.-U. Kühnel, F. Laux, D. A. Orlov, M. L. Rappaport, R. Repnow, C. D. Schröter, D. Schwalm, A. Shornikov, T. Sieber, Y. Toker, J. Ullrich, A. Wolf, and D. Zajfman. *A Cryogenic Electrostatic Trap for Long-Time Storage of keV Ion Beams*. Review of Scientific Instruments, **81**, 5, 055105 (2010). 37

[156] J. Bernard, G. Montagne, R. Brédy, B. Terpend-Ordacière, A. Bourgey, M. Kerleroux, L. Chen, H. T. Schmidt, H. Cederquist, and S. Martin. *A "Tabletop"*

Electrostatic Ion Storage Ring: Mini-Ring. Review of Scientific Instruments, **79**, 7, 075109 (2008). 37

[157] R. D. Thomas, H. T. Schmidt, G. Andler, M. Björkhage, M. Blom, L. Brännholm, E. Bäckström, H. Danared, S. Das, N. Haag, P. Halldén, F. Hellberg, A. I. S. Holm, H. a. B. Johansson, A. Källberg, G. Källersjö, M. Larsson, S. Leontein, L. Liljeby, P. Löfgren, B. Malm, S. Mannervik, M. Masuda, D. Misra, A. Orbán, A. Paál, P. Reinhed, K.-G. Rensfelt, S. Rosén, K. Schmidt, F. Seitz, A. Simonsson, J. Weimer, H. Zettergren, and H. Cederquist. *The Double Electrostatic Ion Ring Experiment: A Unique Cryogenic Electrostatic Storage Ring for Merged Ion-Beams Studies.* Review of Scientific Instruments, **82**, 6, 065112 (2011). 37

[158] M. Ji, J. Bernard, L. Chen, R. Brédy, C. Ortéga, C. Joblin, A. Cassimi, and S. Martin. *Cooling of Isolated Anthracene Cations Probed with Photons of Different Wavelengths in the Mini-Ring.* The Journal of Chemical Physics, **146**, 4, 044301 (2017). 37

[159] R. Brédy, C. Ortéga, M. Ji, L. Chen, J. Bernard, A. R. Allouche, C. Joblin, A. Cassimi, and S. Martin. *PAH Radiative Cooling and Fragmentation Kinematics Studied within an Electrostatic Ring.* Journal of Physics: Conference Series, **583**, 1, 012042 (2015). 37

[160] M. H. Stockett, M. Björkhage, H. Cederquist, H. T. Schmidt, and H. Zettergren. *Storage Time Dependent Photodissociation Action Spectroscopy of Polycyclic Aromatic Hydrocarbon Cations in the Cryogenic Electrostatic Storage Ring DESIREE.* Faraday Discussions, **217**, 0, 126–137 (2019). 38

[161] H. Sabbah, A. Bonnamy, D. Papanastasiou, J. Cernicharo, J.-A. Martín-Gago, and C. Joblin. *Identification of PAH Isomeric Structure in Cosmic Dust Analogs: The AROMA Setup.* The Astrophysical Journal, **843**, 1, 34 (2017). 38, 124

[162] W. Paul and H. Steinwedel. *Notizen: Ein Neues Massenspektrometer Ohne Magnetfeld.* Zeitschrift für Naturforschung A, **8**, 7, 448–450 (1953). 39

[163] A. G. Marshall, T. C. L. Wang, and T. L. Ricca. *Tailored Excitation for Fourier Transform Ion Cyclotron Mass Spectrometry.* Journal of the American Chemical Society, **107**, 26, 7893–7897 (1985). 43

[164] C. Joblin, G. Wenzel, S. Rodriguez Castillo, A. Simon, H. Sabbah, A. Bonnamy, D. Toublanc, G. Mulas, M. Ji, A. Giuliani, and L. L. Nahon. *Photo-Processing of Astro-PAHs.* Journal of Physics: Conference Series (2019). 45, 64

[165] D. Rolland, A. A. Specht, M. W. Blades, and J. W. Hepburn. *Resonance Enhanced Multiphoton Dissociation of Polycyclic Aromatic Hydrocarbons Cations in an RF Ion Trap.* Chemical Physics Letters, **373**, 3, 292–298 (2003). 45

[166] J. Oomens, B. G. Sartakov, G. Meijer, and G. von Helden. *Gas-Phase Infrared Multiple Photon Dissociation Spectroscopy of Mass-Selected Molecular Ions.* International Journal of Mass Spectrometry, **254**, 1, 1–19 (2006). 45

[167] F. Güthe, H. Ding, T. Pino, and J. P. Maier. *Diagnosis of a Benzene Discharge with a Mass-Selective Spectroscopic Technique.* Chemical Physics, **269**, 1, 347–355 (2001). 46

[168] D. L. Kokkin, T. P. Troy, M. Nakajima, K. Nauta, T. D. Varberg, G. F. Metha, N. T. Lucas, and T. W. Schmidt. *The Optical Spectrum of a Large Isolated Polycyclic Aromatic Hydrocarbon: Hexa-peri-hexabenzocoronene, $C_{42}H_{18}$.* The Astrophysical Journal Letters, **681**, 1, L49 (2008). 46

[169] A. M. Ricks, G. E. Douberly, and M. A. Duncan. *The Infrared Spectrum of Protonated Naphthalene and Its Relevance for the Unidentified Infrared Bands.* The Astrophysical Journal, **702**, 1, 301–306 (2009). 46

[170] D. Oepts, A. F. G. van der Meer, and P. W. van Amersfoort. *The Free-Electron-Laser User Facility FELIX.* Infrared Physics & Technology, **36**, 1, 297–308 (1995). 51, 91

[171] D. Sholl and J. A. Steckel. *Density Functional Theory: A Practical Introduction.* John Wiley & Sons (2011). 54

[172] W. Koch and M. C. Holthausen. *A Chemist's Guide to Density Functional Theory.* John Wiley & Sons (2015). 54

[173] M. Born and R. Oppenheimer. *Zur Quantentheorie der Molekeln.* Annalen der Physik, **389**, 20, 457–484 (1927). 54, 60

[174] J. C. Slater. *The Self Consistent Field and the Structure of Atoms.* Physical Review, **32**, 3, 339–348 (1928). 57

[175] P. Hohenberg and W. Kohn. *Inhomogeneous Electron Gas.* Physical Review, **136**, 3B, B864–B871 (1964). 57

[176] W. Kohn and L. J. Sham. *Self-Consistent Equations Including Exchange and Correlation Effects.* Physical Review, **140**, 4A, A1133–A1138 (1965). 58

[177] A. D. Becke. *Density-Functional Exchange-Energy Approximation with Correct Asymptotic Behavior.* Physical Review A, **38**, 6, 3098–3100 (1988). 59

[178] C. Lee, W. Yang, and R. G. Parr. *Development of the Colle-Salvetti Correlation-Energy Formula into a Functional of the Electron Density.* Physical Review B, **37**, 2, 785–789 (1988). 59

[179] K. Kim and K. D. Jordan. *Comparison of Density Functional and MP2 Calculations on the Water Monomer and Dimer.* The Journal of Physical Chemistry, **98**, 40, 10089–10094 (1994). 59

[180] P. J. Stephens, F. J. Devlin, C. F. Chabalowski, and M. J. Frisch. *Ab Initio Calculation of Vibrational Absorption and Circular Dichroism Spectra Using Density Functional Force Fields.* The Journal of Physical Chemistry, **98**, 45, 11623–11627 (1994). 59

[181] S. H. Vosko, L. Wilk, and M. Nusair. *Accurate Spin-Dependent Electron Liquid Correlation Energies for Local Spin Density Calculations: A Critical Analysis.* Canadian Journal of Physics, **58**, 8, 1200–1211 (1980). 59

[182] A. D. Becke. *A New Mixing of Hartree-Fock and Local Density-Functional Theories.* Journal of Chemical Physics, **98**, 1372–1377 (1993). 59, 93

[183] A. D. Becke. *Density-functional Thermochemistry. III. The Role of Exact Exchange.* The Journal of Chemical Physics, **98**, 7, 5648–5652 (1993). 59

[184] P. Giannozzi, S. Baroni, N. Bonini, M. Calandra, R. Car, C. Cavazzoni, D. Ceresoli, G. L. Chiarotti, M. Cococcioni, I. Dabo, A. D. Corso, S. de Gironcoli, S. Fabris, G. Fratesi, R. Gebauer, U. Gerstmann, C. Gougoussis, A. Kokalj, M. Lazzeri, L. Martin-Samos, N. Marzari, F. Mauri, R. Mazzarello, S. Paolini, A. Pasquarello, L. Paulatto, C. Sbraccia, S. Scandolo, G. Sclauzero, A. P. Seitsonen, A. Smogunov, P. Umari, and R. M. Wentzcovitch. *QUANTUM ESPRESSO: A Modular and Open-Source Software Project for Quantum Simulations of Materials.* Journal of Physics: Condensed Matter, **21**, 39, 395502 (2009). 59

[185] L. Genovese, A. Neelov, S. Goedecker, T. Deutsch, S. A. Ghasemi, A. Willand, D. Caliste, O. Zilberberg, M. Rayson, A. Bergman, and R. Schneider. *Daubechies Wavelets as a Basis Set for Density Functional Pseudopotential Calculations.* The Journal of Chemical Physics, **129**, 1, 014109 (2008). 59

[186] K. Yabana and G. F. Bertsch. *Time-Dependent Local-Density Approximation in Real Time.* Physical Review B, **54**, 7, 4484–4487 (1996). 59, 74

[187] N. Tancogne-Dejean, M. J. T. Oliveira, X. Andrade, H. Appel, C. H. Borca, G. Le Breton, F. Buchholz, A. Castro, S. Corni, A. A. Correa, U. De Giovannini, A. Delgado, F. G. Eich, J. Flick, G. Gil, A. Gomez, N. Helbig, H. Hübener, R. Jestädt, J. Jornet-Somoza, A. H. Larsen, I. V. Lebedeva, M. Lüders, M. A. L. Marques, S. T. Ohlmann, S. Pipolo, M. Rampp, C. A. Rozzi, D. A. Strubbe, S. A. Sato, C. Schäfer, I. Theophilou, A. Welden, and A. Rubio. *OCTOPUS, a Computational Framework for Exploring Light-Driven Phenomena and Quantum Dynamics in Extended and Finite Systems.* The Journal of Chemical Physics, **152**, 1, 124119 (2020). 59, 74

[188] M. J. Frisch, G. W. Trucks, H. B. Schlegel, G. E. Scuseria, M. A. Robb, J. R. Cheeseman, G. Scalmani, V. Barone, B. Mennucci, G. A. Petersson, H. Nakatsuji, M. Caricato, X. Li, H. P. Hratchian, A. F. Izmaylov, J. Bloino, G. Zheng, J. L. Sonnenberg, M. Hada, M. Ehara, K. Toyota, R. Fukuda, J. Hasegawa, M. Ishida, T. Nakajima, Y. Honda, O. Kitao, H. Nakai, T. Vreven, J. A. Montgomery, Jr., J. E. Peralta, F. Ogliaro, M. Bearpark, J. J. Heyd, E. Brothers, K. N. Kudin, V. N. Staroverov, R. Kobayashi, J. Normand, K. Raghavachari, A. Rendell, J. C. Burant, S. S. Iyengar, J. Tomasi, M. Cossi, N. Rega, J. M.

Millam, M. Klene, J. E. Knox, J. B. Cross, V. Bakken, C. Adamo, J. Jaramillo, R. Gomperts, R. E. Stratmann, O. Yazyev, A. J. Austin, R. Cammi, C. Pomelli, J. W. Ochterski, R. L. Martin, K. Morokuma, V. G. Zakrzewski, G. A. Voth, P. Salvador, J. J. Dannenberg, S. Dapprich, A. D. Daniels, Ö. Farkas, J. B. Foresman, J. V. Ortiz, J. Cioslowski, and D. J. Fox. *Gaussian 09 Revision D.01*. Gaussian Inc. Wallingford CT (2016). 59, 95

[189] M. Valiev, E. J. Bylaska, N. Govind, K. Kowalski, T. P. Straatsma, H. J. J. Van Dam, D. Wang, J. Nieplocha, E. Apra, T. L. Windus, and W. A. de Jong. *NWChem: A Comprehensive and Scalable Open-Source Solution for Large Scale Molecular Simulations*. Computer Physics Communications, **181**, 9, 1477–1489 (2010). 60

[190] F. Neese. *The ORCA Program System*. WIREs Computational Molecular Science, **2**, 1, 73–78 (2012). 60

[191] R. Ahlrichs, M. Bär, M. Häser, H. Horn, and C. Kölmel. *Electronic Structure Calculations on Workstation Computers: The Program System Turbomole*. Chemical Physics Letters, **162**, 3, 165–169 (1989). 60

[192] G. Mulas. *A MonteCarlo Model of the Rotation of a Big, Isolated Molecule in the ISM*. Astronomy and Astrophysics, **338**, 243–261 (1998). 61, 62, 164

[193] G. Mulas, G. Malloci, C. Joblin, and D. Toublanc. *A General Model for the Identification of Specific PAHs in the Far-IR*. Astronomy & Astrophysics, **460**, 1, 93–104 (2006). 61, 62, 164

[194] T. Beyer and D. F. Swinehart. *Algorithm 448: Number of Multiply-Restricted Partitions*. Communications of the ACM, **16**, 6, 379 (1973). 61

[195] S. E. Stein and B. S. Rabinovitch. *Accurate Evaluation of Internal Energy Level Sums and Densities Including Anharmonic Oscillators and Hindered Rotors*. The Journal of Chemical Physics, **58**, 6, 2438–2445 (1973). 61

[196] E. Runge and E. K. U. Gross. *Density-Functional Theory for Time-Dependent Systems*. Physical Review Letters, **52**, 12, 997–1000 (1984). 62

[197] C. Joblin and A. G. G. M. Tielens (Editors). *PAHs and the Universe: A Symposium to Celebrate the 25th Anniversary of the PAH Hypothesis*, volume 46. EAS, EDP Sciences, Toulouse, France (2011). 64

[198] V. Le Page, T. P. Snow, and V. M. Bierbaum. *Hydrogenation and Charge States of Polycyclic Aromatic Hydrocarbons in Diffuse Clouds. II. Results.* The Astrophysical Journal, **584**, 1, 316 (2003). 64

[199] H. Andrews, C. Boersma, M. W. Werner, J. Livingston, L. J. Allamandola, and A. G. G. M. Tielens. *PAH Emission at the Bright Locations of PDRs: The GrandPAH Hypothesis.* The Astrophysical Journal, **807**, 1, 99 (2015). 64

[200] A. G. G. M. Tielens. *The Physics and Chemistry of the Interstellar Medium.* Cambridge University Press (2005). 64

[201] L. Nahon, N. de Oliveira, G. A. Garcia, J.-F. Gil, B. Pilette, O. Marcouillé, B. Lagarde, and F. Polack. *DESIRS: A State-of-the-Art VUV Beamline Featuring High Resolution and Variable Polarization for Spectroscopy and Dichroism at SOLEIL.* Journal of Synchrotron Radiation, **19**, 4, 508–520 (2012). 65

[202] P. Bréchignac, G. A. Garcia, C. Falvo, C. Joblin, D. Kokkin, A. Bonnamy, P. Parneix, T. Pino, O. Pirali, G. Mulas, and L. Nahon. *Photoionization of Cold Gas Phase Coronene and Its Clusters: Autoionization Resonances in Monomer, Dimer, and Trimer and Electronic Structure of Monomer Cation.* The Journal of Chemical Physics, **141**, 16, 164325 (2014). 65, 84

[203] G. Rouillé, S. A. Krasnokutski, D. Fulvio, C. Jäger, T. Henning, G. A. Garcia, X.-F. Tang, and L. Nahon. *Dissociative Photoionization of Polycyclic Aromatic Hydrocarbon Molecules Carrying an Ethynyl Group.* The Astrophysical Journal, **810**, 2, 114 (2015). 65

[204] C. Joblin, L. Dontot, G. A. Garcia, F. Spiegelman, M. Rapacioli, L. Nahon, P. Parneix, T. Pino, and P. Bréchignac. *Size Effect in the Ionization Energy of PAH Clusters.* The Journal of Physical Chemistry Letters, **8**, 15, 3697–3702 (2017). 65

[205] A. R. Milosavljević, C. Nicolas, J.-F. Gil, F. Canon, M. Réfrégiers, L. Nahon, and A. Giuliani. *VUV Synchrotron Radiation: A New Activation Technique for*

Tandem Mass Spectrometry. Journal of Synchrotron Radiation, **19**, 2, 174–178 (2012). 66, 164

[206] F. Cataldo, O. Ursini, G. Angelini, and S. Iglesias-Groth. *On the Way to Graphene: The Bottom-Up Approach to Very Large PAHs Using the Scholl Reaction.* Fullerenes, Nanotubes and Carbon Nanostructures, **19**, 8, 713–725 (2011). 67, 169, 187

[207] N. N. Matsuzawa, A. Ishitani, D. A. Dixon, and T. Uda. *Time-Dependent Density Functional Theory Calculations of Photoabsorption Spectra in the Vacuum Ultraviolet Region.* The Journal of Physical Chemistry A, **105**, 20, 4953–4962 (2001). 76

[208] S. Douix, D. Duflot, D. Cubaynes, J.-M. Bizau, and A. Giuliani. *Photoionization of the Buckminsterfullerene Cation.* The Journal of Physical Chemistry Letters, **8**, 1, 7–12 (2017). 80, 81, 82, 117, 165

[209] P. Jusko, A. Simon, G. Wenzel, S. Brünken, S. Schlemmer, and C. Joblin. *Identification of the Fragment of the 1-Methylpyrene Cation by Mid-IR Spectroscopy.* Chemical Physics Letters, **698**, 206–210 (2018). 88, 109, 110

[210] P. Parneix, A. Gamboa, C. Falvo, M. A. Bonnin, T. Pino, and F. Calvo. *Dehydrogenation Effects on the Stability of Aromatic Units in Polycyclic Aromatic Hydrocarbons in the Interstellar Medium: A Computational Study at Finite Temperature.* Molecular Astrophysics, **7**, 9–18 (2017). 88, 123

[211] T. Chen, Y. Luo, and A. Li. *Fragmentation and Isomerization of Polycyclic Aromatic Hydrocarbons in the Interstellar Medium: Coronene as a Case Study.* Astronomy & Astrophysics, **633**, A103 (2020). 88

[212] D. L. Kokkin, A. Simon, C. Marshall, A. Bonnamy, and C. Joblin. *A Novel Approach to the Detection and Characterization of PAH Cations and PAH-Photoproducts.* Proceedings of the International Astronomical Union, **9**, S297, 286–290 (2013). 89

[213] A. Léger, L. D'Hendecourt, and D. Défourneau. *Proposed Identification for the (Common) Carrier of the 4430 Å and 7565 Å DIBs.* Astronomy and Astrophysics, **293** (1995). 89

[214] P. Jusko, A. Simon, S. Banhatti, S. Brünken, and C. Joblin. *Direct Evidence of the Benzylium and Tropylium Cations as the Two Long-Lived Isomers of $C_7H_7^+$.* ChemPhysChem, **19**, 23, 3182–3185 (2018). 90, 124, 178

[215] O. Asvany, S. Brünken, L. Kluge, and S. Schlemmer. *COLTRAP: a 22-pole ion trapping machine for spectroscopy at 4 K.* Applied Physics B, **114**, 1, 203–211 (2014). 91, 166

[216] P. Jusko, S. Brünken, O. Asvany, S. Thorwirth, A. Stoffels, L. van der Meer, G. Berden, B. Redlich, J. Oomens, and S. Schlemmer. *The FELion Cryogenic Ion Trap Beam Line at the FELIX Free-Electron Laser Laboratory: Infrared Signatures of Primary Alcohol Cations.* Faraday Discussions, **217**, 0, 172–202 (2019). 91

[217] K. S. Kharnaior, M. Devi, and R. H. Duncan Lyngdoh. *Generation of $C_7H_7^+$ cations with isomerization reactions.* Computational and Theoretical Chemistry, **1091**, 150–164 (2016). 93

[218] M. J. Frisch, J. A. Pople, and J. S. Binkley. *Self-consistent Molecular Orbital Methods 25. Supplementary Functions for Gaussian Basis Sets.* The Journal of Chemical Physics, **80**, 7, 3265–3269 (1984). 93

[219] B. A. Croiset, A. Candian, O. Berné, and A. G. G. M. Tielens. *Mapping PAH Sizes in NGC 7023 with SOFIA.* Astronomy & Astrophysics, **590**, A26 (2016). 114

[220] E. Clar, J. M. Robertson, R. Schloegl, and W. Schmidt. *Photoelectron Spectra of Polynuclear Aromatics. 6. Applications to Structural Elucidation: "Circumanthracene".* Journal of the American Chemical Society, **103**, 6, 1320–1328 (1981). 115, 116

[221] J. W. Hager and S. C. Wallace. *Two-Laser Photoionization Supersonic Jet Mass Spectrometry of Aromatic Molecules.* Analytical Chemistry, **60**, 1, 5–10 (1988). 115, 116

[222] J. C. Weingartner and B. T. Draine. *Photoelectric Emission from Interstellar Dust: Grain Charging and Gas Heating.* The Astrophysical Journal Supplement Series, **134**, 2, 263 (2001). 115, 116, 168

[223] D. G. Kvashnin, P. B. Sorokin, J. W. Brüning, and L. A. Chernozatonskii. *The Impact of Edges and Dopants on the Work Function of Graphene Nanostructures: The Way to High Electronic Emission from Pure Carbon Medium.* Applied Physics Letters, **102**, 18, 183112 (2013). 115

[224] X. J. Yang, R. Glaser, A. Li, and J. X. Zhong. *The Carriers of the Interstellar Unidentified Infrared Emission Features: Constraints From The Interstellar C–H Stretching Features at* $3.2 - 3.5\,\mu m$. The Astrophysical Journal, **776**, 2, 110 (2013). 120

[225] X. J. Yang, A. Li, R. Glaser, and J. X. Zhong. *The C–H Stretching Features at* $3.2 - 3.5\,\mu m$ *of Polycyclic Aromatic Hydrocarbons with Aliphatic Sidegroups.* The Astrophysical Journal, **825**, 1, 22 (2016). 120

[226] P. Pilleri, C. Joblin, F. Boulanger, and T. Onaka. *Mixed Aliphatic and Aromatic Composition of Evaporating Very Small Grains in NGC 7023 Revealed by the* $3.4/3.3\,\mu m$ *Ratio.* Astronomy & Astrophysics, **577**, A16 (2015). 120, 122, 169

[227] G. Mulas, C. Falvo, P. Cassam-Chenaï, and C. Joblin. *Anharmonic Vibrational Spectroscopy of Polycyclic Aromatic Hydrocarbons (PAHs).* The Journal of Chemical Physics, **149**, 14, 144102 (2018). 123

[228] T. Chen, C. Mackie, A. Candian, T. J. Lee, and A. G. G. M. Tielens. *Anharmonicity and the Infrared Emission Spectrum of Highly Excited Polycyclic Aromatic Hydrocarbons.* Astronomy & Astrophysics, **618**, A49 (2018).

[229] A. K. Lemmens, D. B. Rap, J. M. M. Thunnissen, C. J. Mackie, A. Candian, A. G. G. M. Tielens, A. M. Rijs, and W. J. Buma. *Anharmonicity in the Mid-Infrared Spectra of Polycyclic Aromatic Hydrocarbons: Molecular Beam Spectroscopy and Calculations.* Astronomy & Astrophysics, **628**, A130 (2019). 123

[230] Y. Ling and C. Lifshitz. *Time-Dependent Mass Spectra and Breakdown Graphs. 21.* $C_{14}H_{10}$ *Isomers.* The Journal of Physical Chemistry A, **102**, 4, 708–716 (1998). 124

[231] H. Linnartz, J. Cami, M. Cordiner, N. L. J. Cox, P. Ehrenfreund, B. Foing, M. Gatchell, and P. Scheier. C_{60}^{+} *as a Diffuse Interstellar Band Carrier; a*

Spectroscopic Story in 6 Acts. Journal of Molecular Spectroscopy, **367**, 111243 (2020). 124

[232] P. Schmitt-Kopplin and B. Kanawati. *Fundamentals and Applications of Fourier Transform Mass Spectrometry.* Elsevier (2019). 124

[233] L. Martínez, G. Santoro, P. Merino, M. Accolla, K. Lauwaet, J. Sobrado, H. Sabbah, R. J. Pelaez, V. J. Herrero, I. Tanarro, M. Agúndez, A. Martín-Jimenez, R. Otero, G. J. Ellis, C. Joblin, J. Cernicharo, and J. A. Martín-Gago. *Prevalence of Non-Aromatic Carbonaceous Molecules in the Inner Regions of Circumstellar Envelopes.* Nature Astronomy, **4**, 1, 97–105 (2020). 127, 131

[234] G. Santoro, L. Martínez, K. Lauwaet, M. Accolla, G. Tajuelo-Castilla, P. Merino, J. M. Sobrado, R. J. Peláez, V. J. Herrero, I. Tanarro, Á. Mayoral, M. Agúndez, H. Sabbah, C. Joblin, J. Cernicharo, and J. Á. Martín-Gago. *The Chemistry of Cosmic Dust Analogues from C, C_2, and C_2H_2 in C-Rich Circumstellar Envelopes.* The Astrophysical Journal, **895**, 2, 97 (2020). 127, 131

List of Figures

List of Tables

List of Acronyms

Acronym	Definition
AIB	Aromatic Infrared Band
APPI	Atmospheric Pressure PhotoIonization
BG	Big Grain
CID	Collision Induced Dissociation
CNM	Cold Neutral Medium
CRDS	Cavity Ring-Down Spectroscopy
CRESU	Cinétique de Réaction en Ecoulement Supersonique Uniforme
DESIREE	Double ElectroStatic Ion Ring ExpEriment
DFT	Density Functional Theory
DIB	Diffuse Interstellar Band
ESI	ElectroSpray Ionization
FELIX	Free Electron Laser for Infrared eXperiments
FIR	Far InfraRed
FT	Fourier Transform
FTICR	Fourier Transform Ion Cyclotron Resonance
FUV	Far UltraViolet
FWHM	Full Width at Half Maximum
HIM	Hot Ionized Medium
IC	Internal Conversion
ICR	Ion Cyclotron Resonance
ISC	InterSystem Crossing
IR	InrfraRed
IRMPD	InrfraRed Multiple Photon Dissociation
ISM	InterStellar Medium
IVR	Internal Vibrational Redistribution
LURE	Laboratoire d'Utilisation du Rayonnement Électromagnétique
MIR	Mid InfraRed

Acronym	Definition
MIS	Matrix Isolation Spectroscopy
MIS	Milieu InterStellaire
MPD	Multiple Photon Dissociation
MS	Mass Spectrometry
NIR	Near InfraRed
OPO	Optical Parametric Oscillator
PAH	Polycyclic Aromatic Hydrocarbon
PES	PhotoElectron Spectroscopy
PDR	PhotoDissociation Region or Photon-Dominated Region
PEPICO	PhotoElectron PhotoIon Coincidence
PIRENEA	Piège à Ions pour la Recherche et l'Étude de Nouvelles Espèces Astrochimiques
QMS	Quadrupole Mass Spectrometry
REMPI	Resonance-Enhanced MultiPhoton Ionization
SIFT	Selected Ion Flow Tube
SOLEIL	Source Optimisée de Lumière d'Energie Intermédiaire du LURE
SVP	Split Valence Polarization
SWIFT	Stored Waveform Inverse Fourier Transform
TD-DFT	Time-Dependent Density Functional Theory
TOF	Time Of Flight
TPIMS	Time-Resolved PhotoIonization Mass Spectrometry
TRPD	Time-Resolved PhotoDissociation
UIE or UIR	Unidentified Infrared Emission
UV	UltraViolet
VIS	Visible
VR	Vibrational Relaxation
VSG	Very Small Grain
VUV	Vacuum UltraViolet
WIM	Warm Ionized Medium
WNM	Warm Neutral Medium

Units and Physical Constants

Atomic mass unit	$1\,\mathrm{u} = 1.66057 \cdot 10^{-27}\,\mathrm{kg}$
Electric dipole moment unit	$1\,\mathrm{D} = 3.33 \cdot 10^{-30}\,\mathrm{C\,m}$
Energy units	$1\,\mathrm{eV} = 1.602 \cdot 10^{-19}\,\mathrm{J} = 23.08\,\frac{\mathrm{kcal}}{\mathrm{mol}}$
	$1\,\mathrm{eV} = 96.013\,\frac{\mathrm{kJ}}{\mathrm{mol}} = 0.0367\,\mathrm{H}$
Pressure units	$1\,\mathrm{Torr} = 1.333\,\mathrm{mbar} = 133.3\,\mathrm{Pa}$
Spectral flux density unit	$1\,\mathrm{Jy} = 10^{-26}\,\mathrm{W\,m^{-2}\,Hz^{-1}}$

Avogadro constant	$N_\mathrm{A} = 6.028 \cdot 10^{23}\,\mathrm{mol^{-1}}$
Boltzmann constant	$k_\mathrm{B} = 1.38 \cdot 10^{-23}\,\frac{\mathrm{kg \cdot m^2}}{\mathrm{K \cdot s^2}}$
Elementary charge	$e = 1.602 \cdot 10^{-19}\,\mathrm{C}$
Ideal gas constant	$R = k_\mathrm{B} \cdot N_\mathrm{A} = 8.314\,\frac{\mathrm{J}}{\mathrm{mol\,K}}$
Planck constant	$h = 6.626 \cdot 10^{-34}\,\mathrm{J\,s} = 4.136 \cdot 10^{-15}\,\mathrm{eV\,s}$
Speed of light	$c = 2.99792458 \cdot 10^{8}\,\frac{\mathrm{m}}{\mathrm{s}}$
Vacuum permittivity	$\varepsilon_0 = 8.854 \cdot 10^{-12}\,\frac{\mathrm{F}}{\mathrm{m}}$

A | MPD Spectroscopy of Phenanthrene using PIRENEA

In preparation of an isomerization through radiative cooling study recently conducted at DESIREE, we investigated the multiple photon dissociation (MPD) action spectrum of the gas-phase phenanthrene cation (Phen+), $C_{14}H_{10}^+$. The main photofragments resulted from the loss of H, $2H/H_2$, and C_2H_2 as can be seen in the example mass spectrum with the OPO tuned at 460 nm as displayed in Figure A.1. By following these loss channels as a function of laser wavelength over the range of $420 - 480$ nm using the PIRENEA cryogenic ion trap setup [131, 132] which is described in Section 2.2.3, we could record the MPD spectrum which is presented in Figure A.2.

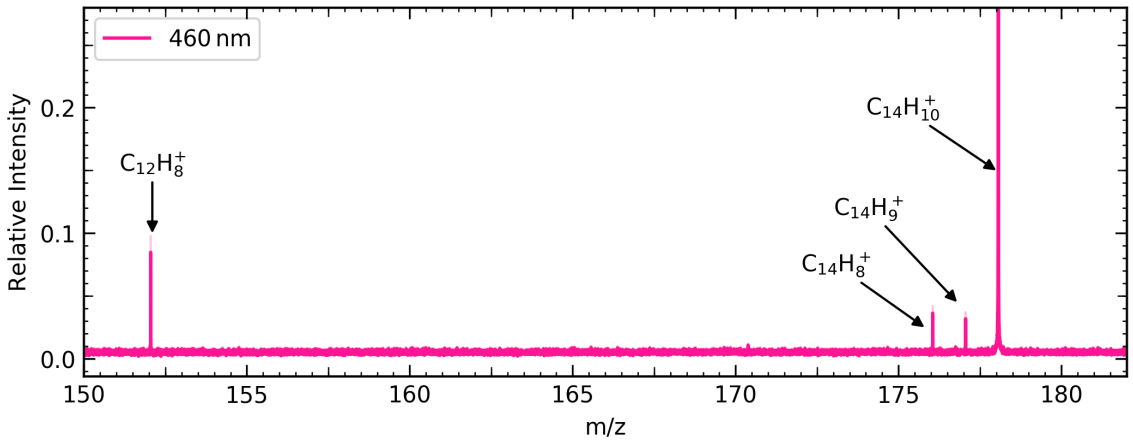

Figure A.1: Mass spectrum of the phenanthrene cation, $C_{14}H_{10}^+$, which had absorbed multiple photons with a wavelength of 460 nm. The main photofragments are $C_{14}H_9^+$, $C_{14}H_8^+$, and $C_12H_8^+$.

The dissociation yield, Y_D, is expressed as

$$Y_D = \frac{\sum_i^3 F_i}{P + \sum_i^3 F_i}, \tag{A.1}$$

where F_i denotes the intensity of the three photofragments due to H, $2H/H_2$, and C_2H_2 loss, and P the parent cation signal intensity. Each data point is the average of ten subsequent measurements recorded per photon wavelength step yielding the indicated error bar. The action spectrum is normalized to the laser power.

In comparison to the Phen+ in Ne matrix absorption spectrum of a previous study by Salama *et al.* [109], a fairly large shift of 10 nm of the 460 nm-band is observed toward higher photon energies in our spectrum, which is an uncommon difference when comparing these two techniques. In infrared multiple photon dissociation (IRMPD) experiments, isomerization processes were found to significantly affect the spectra, *cf.* Chapter 5 and Jusko *et al.* [214]. In fact, theoretical calculations have shown that the unimolecular dissociation of Phen+ involves several isomers [141].

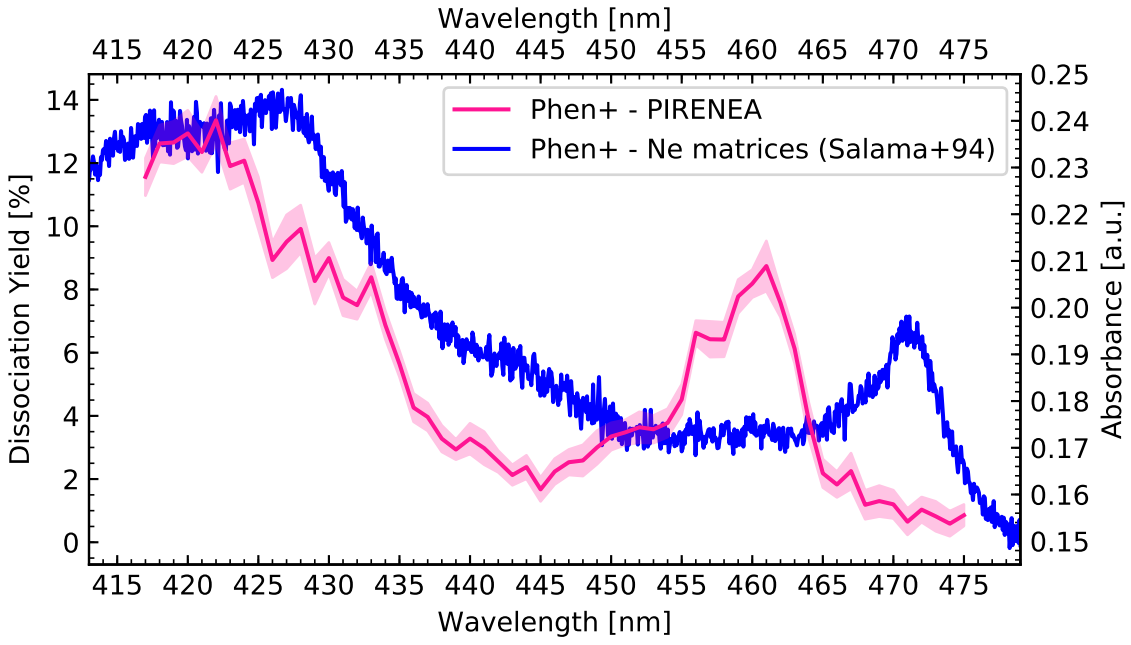

Figure A.2: Multiple photon dissociation spectrum of the phenanthrene cation, $C_{14}H_{10}^+$, obtained using PIRENEA. For comparison, the phenanthrene cation in Ne matrix absorption spectrum from Salama *et al.* [109] is also presented.

The observed bandshift for Phen+ might therefore reveal isomerization processes upon absorption of multiple photons. In the PIRENEA setup, this can happen during the MPD spectroscopy but also before at the production stage of the gas-phase cations, which involves laser desorption ionization (*cf.* Section 2.3.1.2). This hypothesis could be tested by performing the MPD spectroscopy experiment using PIRENEA on phenanthrene's isomer, anthracene, and complementary molecular dynamics simulations regarding this issue.

B | Ultraviolet Light Ranges

Table B.1: The electromagnetic spectrum ranges of ultraviolet radiation as recommended by the ISO standard, ISO-21348[a].

Name	Abbreviation	Photon Energy [eV]	Wavelength [nm]
Near ultraviolet	NUV	$3.10 - 4.13$	$400 - 300$
Middle ultraviolet	MUV	$4.13 - 6.20$	$300 - 200$
Far ultraviolet	FUV	$6.20 - 10.16$	$200 - 122$
Hydrogen Lyman-α	Ly-α	$10.16 - 10.25$	$122 - 121$
Extreme ultraviolet	EUV	$10.25 - 124$	$121 - 10$
Vacuum ultraviolet	VUV	$6.20 - 124$	$200 - 10$

[a] `http://www.spacewx.com/pdf/SET_21348_2004.pdf`

C | Public Blog Post: Secondment to Hiden Analytical

One of the industrial partners within EUROPAH is Hiden Analytical, a company with a more than 35-year long history of design, development and manufacture of quadrupole mass spectrometers for advanced research applications and specialist process monitoring. The application possibilities of Hiden's mass spectrometers and advanced systems including mass spectrometry range from vacuum, gas, plasma to surface science and if the solution to your problem is not included in Hiden's product range, yet, they provide for client interactive development of solutions meeting your specific requirements. As an ESR within EUROPAH I had the opportunity to accomplish a 2-month internship as a secondment at Hiden Analytical in order to gain experience working in an industrial environment. Director Peter Hatton and I were in contact for several weeks in order to figure out a schedule and a project plan for my time at his company. My secondment began in mid-March, right after the EPoLM-4 meeting many of us ESRs attended in Madrid.

My first week started off with a detailed introduction into the world of Hiden's quadrupole mass spectrometers and their wide range of applications. Paul Jones, Production Director, heartilywelcomed me to the Hiden team and introduced me to his coworkers as well as many different instruments and systems. Paul has worked at Hiden for over 26 years and is responsible for the day to day production. This includes managing customer orders, ensuring that all parts from the quadrupole assembling, the vacuum build, and the electronics department come together in time for being tested and finally shipped to the customer. Paul has to estimate and communicate the shipping date to the customer which means he has to consider difficulties and make sure everything concerning the production of the ordered mass spectrometer system

runs smoothly. He relies on his colleagues' knowledge who have a total of more than hundreds of years of experience. Paul considers himself very lucky to have gotten the opportunity to work in such a stable and pleasant environment and these positive vibes are exactly what he sends out every day. During this first week, I learned a lot about the concept of quadrupole mass spectrometry, how to master Hiden's own software in order to run their mass spectrometers and system testing in general. The largest part of my secondment at Hiden was a characterization project of differently coated silicon samples using the TPD Workstation and the SIMS Workstation.

My supervisor for the temperature programmed desorption (TPD) experiments was Dr. David Lundie who is Product Manager for Advanced Systems at Hiden. His industry-based PhD research topic catalysis opened the doors to Hiden, where he develops new solutions for temperature programmed processes since 2003. Once a newly developed advanced system is sold to the customer, David is also responsible for the installation and training of the costumer for this new product at the customer's site. This means David regularly travels to various places including not only Europe, but also North America, Asia and Australia, which is one of the tasks he enjoys the most about his job. David trained me on the Hiden TPD Workstation, an advanced experimental system consisting of an ultrahigh vacuum chamber, a load lock system, primary and turbomolecular pumps, as well as a quadrupole mass spectrometer which can measure mass-to-charge ratios from 1 to 300 amu, specialized for TPD experiments in which the species desorbing from a heated surface are collected by a mass spectrometer. The TPD Workstation is widely used for analyzing the surface, interlayer and bulk desorption properties of semiconductor and metal samples. Once I was familiar with the instrument, we probed six different samples for the desorption of hydrogen, water and carbon monoxide, which play an important role in the production and characterization of solar cells. Since the TPD Workstation provides a very high resolution and sensitivity, the formation of sharp peaks was observable in the spectra. By having a closer look on the used samples, we noticed that during the heating some of the samples' coatings developed blisters which can be seen by the use of a microscope but also by eye.

We decided to further investigate the blistering with help from the secondary ion mass spectrometer (SIMS) specialists Dr. Graham Cooke and Dr. Kareem El-Abiary who are responsible for developing and maintaining the SIMS Workstation. Graham

first came in contact with SIMS during his PhD in semiconductor analysis and since 2006 he develops new SIMS related instruments at Hiden. One of his first big accomplishments was the design and manufacture of a cesium cluster ion gun which is an important feature for the SIMS Workstation. But as Principal Scientist, Graham is also responsible for liaising with his Hiden colleagues about SIMS related problems and the support and service of ca. thirty big SIMS instruments distributed around the globe, which he proceeds through Skype or Team Viewer sessions as well as visits to the customer's site. For this large variety, Graham appreciates his job; "You never quite know what will happen each day", he says. The variety and the supportive environment are also Kareem's favorites about his job at Hiden. Similarly to David, Kareem graduated in catalysis and started his career with a knowledge transfer partnership which means he worked 50 % in research and 50 % in industry. Kareem is fairly new to the company as he started as a trainee in 2017 but evolved to be Hiden's SIMS Application Specialist now. His main responsibilities include customer support regarding operating the different SIMS stations and testing of costumer's samples. Together with Graham, he also tests upgrades and new components for the SIMS Workstation and writes technical sheets and application notes which are helpful features for those who attend conferences in order to inform about Hiden's products.

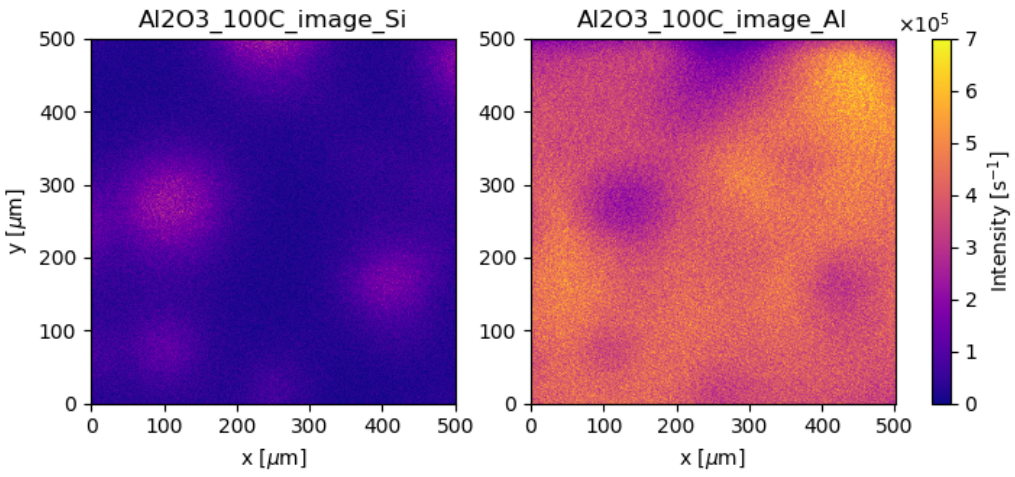

Figure C.1: Surface images taken with SIMS. On the left, the bulk material, silicon, which is more intense within the blisters (lighter areas) is depicted. On the right, the image of the surface material tracker, aluminum, shows a lack of surface material in the exact same areas.

Graham and Kareem introduced me to the SIMS Workstation which was designed to perform high sensitivity analysis of surfaces and thin solids. In SIMS experiments, a primary ion beam is directed to a sample positioned in an ultrahigh vacuum chamber. When impinging the surface, the primary ions sputter small amounts off the sample's surface. These small amounts composed of elements and molecules – the secondary ions – can then be detected and identified with a Hiden quadrupole mass spectrometer. As the primary ions sputter more and more off the sample over time, depth profiles can be recorded yielding insights into the concentrations of impurities or layers within the bulk sample. We made use of that technique in order to further investigate the blistering of our coated silicon samples. Positive oxygen ions are very surface sensitive which we used to record surface images presented in Figure C.1 that show the blisters as a lack of surface material compared to a significant signal of bulk material which should not be visible for a uniformly coated sample. Depth profiles recorded with the help of the cesium cluster ion gun revealed that the bulk material may have diffused into the surface coating during the TPD measurements which makes further discussions with the customer on how to prevent this process in the future indispensable.

My supervisors at Hiden chose an interesting and exciting research topic within an industrial environment and professional partnership for me. I appreciate to have learned so much about the different quadrupole mass spectrometers, the TPD and SIMS experiments as well as Hiden's corresponding TPD and SIMS Workstations. My time at Hiden provided me with insights into the work of a scientist in a manufacturing company and it was a great pleasure to work together with such an experienced team.

D | Synthesis of Dicoronylene, $C_{48}H_{20}$

Dicoronylene was synthesized by our collaborators S. Quiroga and D. Peña from the Centro de Investigación en Química Biolóxica e Materiais Moleculares (CiQUS) and Departamento de Química Orgánica, Universidade de Santiago de Compostela, Spain, following the procedure reported by Cataldo *et al.* [206]. A mixture of coronene (0.060 g, 0.199 mmol), $AlCl_3$ (4.20 g, 31.2 mmol), NaCl (0.817 g, 14.0 mmol), and CuCl (0.043 g, 0.440 mmol) was stirred at 195 °C for 2 h. Then, aqueous solution of HCl (10 %, 20 ml) was slowly added resulting in the precipitation of a red solid. This solid was filtrated and washed with aqueous solution of HCl (10 %, 20 ml), hot water (20 ml) and acetone (3 × 20 ml). The resulting solid was dried to obtain dicoronylene as a red solid (54 mg, 40 %).

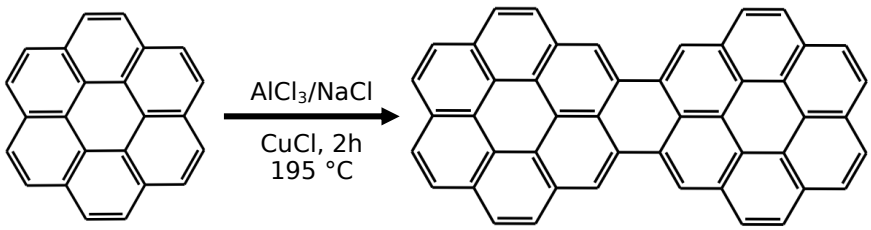

Figure D.1: Schematic of the synthesis of dicoronylene, $C_{48}H_{20}$, from coronene, $C_{24}H_{12}$, following the procedure reported by Cataldo *et al.* [206].

Acknowledgement

S. Quiroga and D. Peña acknowledge financial support from the Spanish Agencia Estatal de Investigación (MAT2016-78293-C6-3-R; AEI/FEDER, UE), Xunta de Galicia (Centro Singular de Investigación de Galicia accreditation 2016–2019, ED431G/09), the European Regional Development Fund-ERDF, and the European FET-OPEN project SPRING, Grant Agreement no. 863098.